Dipl.-Ing. Marcus Hiemer

Model Based Detection and Reconstruction of Road Traffic Accidents

universitätsverlag karlsruhe

Marcus Hiemer

Model Based Detection and Reconstruction of Road Traffic Accidents

Model Based Detection and Reconstruction of Road Traffic Accidents

von
Dipl.-Ing. Marcus Hiemer

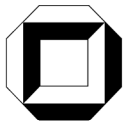

universitätsverlag karlsruhe

Dissertation, Universität Karlsruhe (TH), Fakultät für Elektrotechnik und Informationstechnik, 2004

Impressum

Universitätsverlag Karlsruhe
c/o Universitätsbibliothek
Straße am Forum 2
D-76131 Karlsruhe

www.uvka.de

Print on Demand

ISBN 3-937300-34-1

Model Based Detection and Reconstruction of Road Traffic Accidents

Zur Erlangung des akademischen Grades eines

DOKTOR-INGENIEURS

von der Fakultät für
Elektrotechnik und Informationstechnik
der Universität Fridericiana Karlsruhe

genehmigte

DISSERTATION

von
Dipl.-Ing. Marcus Hiemer
aus Tettnang

Tag der mündlichen Prüfung:	09.11.2004
Hauptreferent:	Prof. Dr.-Ing. Uwe Kiencke
Korreferent:	Prof. G. L. Gissinger
Karlsruhe:	05.10.2004

Vorwort

Die vorliegende Arbeit entstand während meiner Tätigkeit als wissenschaftlicher Mitarbeiter am Institut für Industrielle Informationstechnik (IIIT) der Universität Karlsruhe (TH). Aufgrund der Industriekooperation mit dem Unternehmen Mitsubishi Electric Corporation in Himeji, Japan, ist die Arbeit in englischer Sprache verfasst.

Herrn Prof. Dr. U. Kiencke, Leiter des Instituts für Industrielle Informationstechnik, danke ich für die Initiierung und Betreuung der Arbeit sowie für die Übernahme des Hauptreferats. Für die Übernahme des Korreferats und das Interesse an der Arbeit danke ich Herrn Prof. G. L. Gissinger von der ESSAIM, Université de Haute Alsace.

Den Mitarbeitern der Mitsubishi Electric Corporation, insbesondere Herrn Takanori Matsunaga, danke ich für die fachliche Unterstützung.

Dank sagen möchte ich auch den Mitarbeitern des Instituts für das angenehme und freundschaftliche Arbeitsklima. Ein besonderer Dank gilt meinen Zimmernachbarn. Des Weiteren möchte ich Holger Jäkel, Jörg Barrho, Julian Baumann, Thomas Rambow, Anne von Vietinghoff, Thorsten Huck und Marko Babic für die sorgfältige Durchsicht des Manuskripts danken. Nicht vergessen möchte ich Werner Nold, Stefan Seelinger und Herrmann Dilger, die mich vor allem bei der Ausstattung des Testfahrzeugs stets mit allen Kräften unterstützten.

Ohne das Engagement meiner Diplomanden und Studienarbeiter wäre die vorliegende Arbeit sicher nicht in dieser Form entstanden. Daher gilt mein Dank allen Studenten, die ihren Beitrag zum Gelingen dieser Dissertation geleistet haben.

Mein besonderer, ganz herzlicher Dank gilt den Menschen in meinem privaten Umfeld, die mir während meiner Promotion ein ständiger Rückhalt waren und die somit ganz wesentlich zum Gelingen dieses Lebensabschnitts beigetragen haben. Allen voran sei hier meine Frau Ulla genannt.

Zu guter Letzt danke ich meinen Eltern dafür, dass sie mich stets förderten und mir das Studium und damit auch diese Promotion ermöglichten.

Marcus Hiemer — Karlsruhe, im Oktober 2004

Wer fragt, ist ein Narr für eine Minute.
Wer nicht fragt, ist ein Narr sein Leben lang.

Konfuzius

Inhaltsverzeichnis

1 Introduction, Motivation and State of the Art

The number of motor vehicles in Germany has constantly grown during the last decades. As a result of the increased traffic density, more than 2.5 million road traffic accidents occur on Germany's roads each year. In 2003, in more than 335000 of these accidents, persons were injured with 6618 fatalities among them, [57]. Therefore, accident reconstruction is crucial to solve the question of liability for these accidents. After an accident has occurred the police reports about the accident scene. Accident investigators afterwards conclude about causes and the question of guilt.
Independent reconstruction experts claim that nowadays due to the growing vehicle fleet, the police often does not have sufficient time to report the accident situation accurately, [37].
Furthermore, in Europe more and more vehicles are equipped with electronic control systems. The Antilock Braking System (ABS) avoids locking wheels by controlling wheel slip. Typical brake traces left on the road surface are missing when ABS is active. Among others, brake traces are the most important aids for accident investigators to reconstruct the vehicle motion leading to an accident. For vehicles equipped with Vehicle Dynamics Control (VDC) systems the situation is even more complex. State of the art systems brake wheels selectively to stabilize the car. The latest systems even interfere into the steering system to manipulate the steering angle automatically, [45]. The question whether the control system interfered or whether the driver has acted appropriately cannot be answered clearly any more.

1.1 Accident Statistics

The annual economic costs of road traffic accidents in the USA exceeded 200 billion Euro in 2000, [59]. In Germany, the economic costs are bigger than 35 billion Euro with more than half of this sum being caused by accidents with injury or fatality. Accidents with severely injured or killed

persons economically play the most important role, [11]. That is the reason, why the focus is on these accidents.
In 2003, 29% of all accidents with injuries occurred on rural roads (without highways) with 63% of all victims being killed there. This confirms that accidents occurring outside cities are significantly more severe, because vehicles are averagely loaded with more people. Additionally, the vehicle speed is significantly increased. Speeding is still the main cause of all vehicle accidents in Germany, [57].
Among all German country road accidents since 1985 about 35% are single car accidents, [10]. In this context, country roads are regarded as roads outside cities excluding two-lane highways. Single car accidents are often vehicle rollovers or tree collisions and represent an outstanding group of accidents. 90% of all single car accidents are caused by misbehavior of the driver, [61].
In the USA and in Germany young adults between 18 and 25 years represent the group with the highest fatality rate. Regarding all accidents with injured people, averagely 1.3 driver mistakes occur, [57]. For young people with a lack of driving experience, this number is even higher.
That means that accidents with a high fatality rate are often caused by driver errors. These accidents often result from laterally critical drive situations. In such accident situations, electronic control systems attempt to support the driver. In order to solve the question of liability, accident causes must be investigated.

1.2 Patent Inquiry about Event Data Recording Devices

The idea of recording accident relevant data in a memory for later analysis bases on the principle of flight recorders installed in aeroplanes since the 1950s. There is an abundance of data recording devices patented which focus on various different aspects. The following overview therefore presents only a portion of the ideas patented by companies all over the world.
Some ideas focus on acquiring data *after* a crash only. DaimlerChrysler patent EP 839698 A2 is a multi-functional optical recording device for theft prosecution after accidents. Mannesmann Kienzle Patent DE 4303470 C decreases the triggering threshold for accident detection after switching off the ignition in order to record parking accidents.
The patented systems also distinguish in the data sources for the accident relevant data. Some of the systems (as for instance DE 4303470 C) use proprietary sensors, whereas others use the data provided by the ECU (Fuji

patent JP 2001260953 A) or by sensors and other onboard calculators (for instance PSA patent FR 2799557 A1).
In order to acquire data about the vehicle exterior, data sources additional to the inertial sensors are used. Among others Sumitomo Electric's system (JP 2000128031 A) additionally uses a camera and a hyperboloid mirror to gain a complete view around the car. Hitachi (JP 9123876 A) and Toyota (JP 8235491 A) use data from a navigation system to enhance the information about an accident. Temic Telefunken applied for a patent (DE 19729960 A) with a system triggering the recording of data by evaluating relative distances and speeds to adjacent vehicles.
The system of Schimmelpfennig Company patented with the patent number DE 4132981 C2 uses at least two sensors and reproduces the vehicle motion by solving a set of differential equations.
The list of patents could be continued regarding other aspects. The presented selection shall give an impression about the activity in the development of event data recording devices.

1.3 Evolution and State of the Art of Event Data Recorders

In the United states event data recorders (EDR) have been used for many years to record crash related scenarios. In the early 1970s an analog device called Disc Recorder was installed in about 1000 US American vehicles.
The current use of EDRs in highway vehicles is generally limited to original equipment manufacturers (OEM) and a few small aftermarket suppliers. Among the OEMs, General Motors (GM) is in the lead in developing EDR technology. Therefore, as an example the evolution of GM EDRs will be described more detailed.
General Motors event data recorders are tightly connected to the airbag system. The first generation of EDRs including the Diagnostic and Energy Reserve Module (DERM) was introduced in 1990. It records airbag status data and additionally airbag sensor information.
The Sensing and Diagnostic Module (SDM) installed first in the 1994 model year represents the next step in the evolution of event data recorders. The most important novelty of the SDM is the computation and storage of the change in longitudinal vehicle velocity.
Certain 1999 and newer GM vehicles have a SDM installed with the added capability to record vehicle system status data such as vehicle speed, engine rotations per minute, throttle position or brake switch status for the five seconds proceeding an airbag deployment or near-deployment. The SDM's

longitudinal accelerometer is low-pass filtered at approximately 400Hz. It contains 32kBytes of ROM for program code, 512 bytes of RAM and 512 bytes EEPROM. Every $312\mu s$ the algorithm samples the accelerometer data and when two successive samples exceed two Gs of deceleration, the algorithm is activated, [29]. Once each second, the SDM takes the most recent sensor data values and stores them in a recirculating buffer (RAM), one storage location for each parameter for a total of five seconds. After algorithm enable shortly after impact, buffer refreshing is suspended.
The most popular aftermarket product in Europe is Siemens VDO's Crash Data Recorder. It samples the vehicle speed, longitudinal and lateral acceleration and changes in direction with a frequency of 500 Hz for a time period of 30 seconds pre- and 15 seconds post crash. In addition, static variables like lights, indicators, brakes, etc. are recorded. The employed sensors are proprietary.
Every OEM and every aftermarket supplier uses its own data format. Therefore, the IEEE has created the P1616 Motor Vehicle Event Data Recorders Standards Project, [46]. The standard will define what data will have to be captured and how that information should be obtained, recorded and transmitted. The data will then be available not only to the OEMs but also to the public and might improve EDR based accident reconstruction.

1.4 Goal of this Thesis

The most severe accidents occur on country roads. Often there are no accident witnesses. Control interventions of electronic systems are probable. In order to reconstruct such accidents appropriately, the focus of this thesis is on vehicle dynamics whereas existing event data recorders mainly concentrate on describing the crash phase. These event data recorders mostly solely use proprietary sensors which increases the costs. Alternatively, they are connected to the airbag system, [13], and get information from the sensors processed by this system. However, the accuracy of accident data is limited, [48]. The recording of data is mainly triggered by exceeding a longitudinal acceleration threshold.
The model based system presented in this thesis provides more information about the accident, because non-measurable parameters and state variables can be estimated. Additionally, this approach increases the accuracy of the sensor signals, as models are used to eliminate systematic sensor errors. However, to limit extra costs, no additional sensors than the ones installed in modern cars are employed. Furthermore, pre-accident situations are recognized before a crash occurs based on the vehicle dynamics behavior

of the car. The trigger mechanism is significantly improved. Moreover, the following requirements for accident reconstruction are better covered by a model based system:
The vehicle dynamics and the vehicle trajectory can be reconstructed more accurately because important non-measurable variables are determined by the system.
Conclusions about the driver's behavior in critical driving situations can be drawn. Very often, drivers do not act and react appropriately before an accident. Therefore, assessing the drivers's behavior by analyzing the driver inputs and the resulting vehicle dynamic outputs is a basic requirement which can only be met by a model based EDR.
Finally, the vehicle environment significantly influences the behavior of driver and vehicle in the road traffic. By estimating environmental quantities like the friction, conclusions about the state of the site around the accident can be drawn.
An overview of the complete model based system for detection and reconstruction of road traffic accidents is given in Chapter 2. There, the general approach is described to meet the above mentioned requirements.

2 Overview of the Complete System

The following chapter is mainly based on the patent applications 543456 JP 01 (Japan) and 543456 US 01 (USA) and describes a model based EDR. That is the reason why the individual blocks and leads in Fig. 2.1 are enumerated.

2.1 General Configuration

Fig. 2.1 shows the structure of the complete system. In order to save costs, existing sensor data from in vehicle networks (for instance CAN bus) and from the electrical system are employed. The EDR acts only as a "listener" to record existing sensor signals. The CAN bus or a comparable bus system therefore need not be reprogrammed. The EDR can simply be "hooked" to the network and starts recording the data, assuming that the CAN message identifiers are made available to the system.
European middle and upper class vehicles are by default equipped with an ABS and a vehicle dynamics control system like DSC or ESP. These systems use a variety of sensors, for example wheel speed sensors (ABS), a yaw rate sensor and a lateral acceleration sensor (VDC). Additionally, the model based EDR employs a longitudinal acceleration sensor (e.g. used in VDC systems, [71], or in seat belt locking systems, [21]). The longitudinal wheel forces are measured or estimated in cars with ABS (for braking) and with an engine management system (for the drive forces). Cars equipped with the electro-hydraulic brake (EHB) will contain accurate wheel force signals. That means that all of the quantities required by the system are available in modern cars.
The acquired data are preprocessed in order to be applied to the vehicle model and estimation unit (see Fig. 2.1). The data acquisition and preprocessing as well as the applied sensors are described in Chapter 6 where the test environment is presented. In the vehicle model and estimation unit, the state space models describing the vehicle motion are executed. The underlying models will be presented in Chapter 3. The results from the model calculations are saved in a memory in case an accident occurs. Therefore,

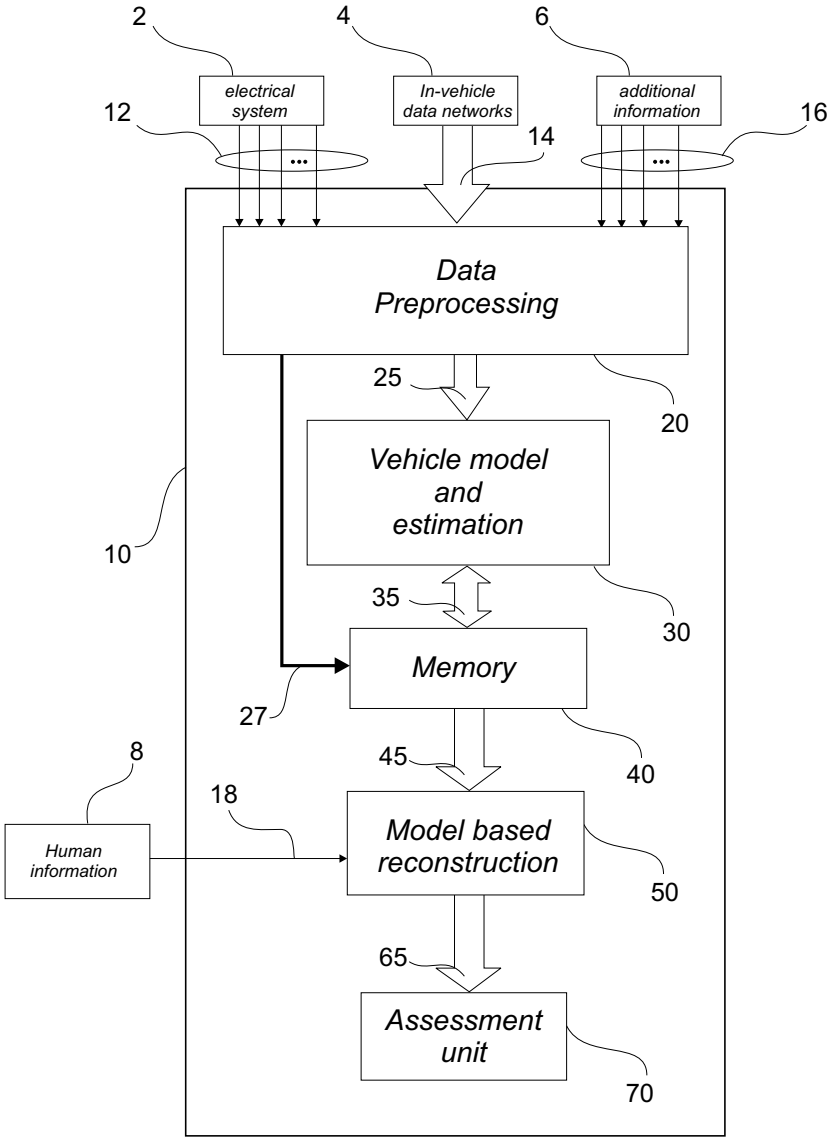

Figure 2.1: General overview of a model based EDR

an accident situation must be detected and a trigger signal must be generated to avoid that accident relevant data in the memory are overwritten again (block 40 in Fig. 2.1). The principle of accident detection is described in Chapter 4 and an overview is illustrated in Fig. 4.22. In the model based reconstruction unit the vehicle motion and the driver's behavior as well as external influences are reproduced based on the available sensor signals (Chapter 5). Due to the limited amount of employed sensor signals (for instance no camera is used in this thesis) human information from the police and from eye witnesses is required for complete accident reconstruction. In the assessment unit, finally, conclusions about the accident are drawn. From the huge variety of accident situations, as an example the steering behavior of the driver in critical situations is selected and described in Section 5.9.

2.2 Core of the System

The core of the model based event data recorder is shown in Fig. 2.2. It shows the sub-models of the vehicle model and estimation unit as well as the model based reconstruction unit. As a convention, in the entire thesis the indices ij are wildcards: i for "F" or "R": front/rear and j for "L" or "R": left/right. This expresses that a quantity, for instance a force, etc. occurs on all four wheels. If the indices are not used, then the quantity in general is described. However, the quantity can still occur on all four wheels.
In the steering model (Section 3.1.2), the steering wheel angle δ_S applied by the driver is transformed to the wheel turn angle δ_W which is an input into the state space models.
The velocity estimator described in Section 5.1 outputs an estimation of the velocity $\hat{v}_{CoG}$ in the center of gravity (CoG) which is determined by means of a fuzzy system. Figs. 5.2 and 5.6 give a more detailed overview. Here, the redundancy of the acceleration sensor signal (a_X) and the wheel speed sensor signals ω_{Rij} is used by weighting the individual sensors according to their reliability. A similar principle is implemented in the yaw rate estimator, see Fig. 5.11 in Section 5.2, to estimate the yaw rate $\dot{\psi}_{Fuz}$. The redundant signals $\dot{\psi}_S$ and ω_{Rij} from gyroscope and wheel speed sensors are fused. Using the estimated velocity $\hat{v}_{CoG}$ as well as the yaw rate $\dot{\psi}_{Fuz}$ the vehicle trajectory $\underline{x}(t)$ can be calculated. The trajectory reconstruction block is shown in more detail in Fig. 5.15 and described in Section 5.3. The trajectory represents one part of complete vehicle motion reproduction. The estimated center of gravity velocity $\hat{v}_{CoG}$ is also applied to the wheel model in Section 3.1. In the wheel model (overview given by Fig. 3.1), among others, the tire side slip angle (TSSA) α is determined.
Most of the sub-models require the forces acting on the vehicle to determine accident relevant quantities. The rolling friction force F_R calculated in the respective block is a resistance force which has significant influence on the vehicle motion at higher speeds. It is approximated in Section 3.3.2 by means of a velocity polynomial. The other main quantity influencing the vehicle motion at high speeds is the wind force F_{WX}. In the wind force calulation block, the well known quadratic approximation equation with the velocity v_{CoG} is described in Section 3.3.3.
Knowing these two main resistance forces and the longitudinal wheel forces F_{Lij} available on the in-vehicle networks, the longitudinal force balance can be evaluated to estimate the vehicle mass m_{CoG} (Section 5.5, especially Fig. 5.38). Mass changes significantly influence the vehicle model accuracy. Therefore, this time-varying parameter is adapted. The control port in the

mass estimation block of Fig. 2.2 indicates that mass estimation is activated only in certain driving situations.
The vehicle motion depends on the vertical wheel forces F_{Zij} which are changing with longitudinal and lateral accelerations a_X and a_Y. The wheel loads are calculated in the vertical wheel forces block which is explained in Section 3.3.4. In the lateral wheel forces block, the wheel loads F_{Zij} and the tire side slip angles α_{ij} are considered in a non-linear approximation equation for the side wheel forces F_{Sij} (Section 3.4.2). The cornering stiffnesses c_{ij} are not constant. In the cornering stiffness adaptation block, these parameters are adapted by using the non-linear lateral wheel force approximation F_{Sij} and the tire side slip angles α_{ij} (Section 3.4.2). Like the vehicle mass m_{CoG}, the cornering stiffnesses c_{ij} are crucial parameters for the state space model and therefore represent one of the time-varying model parameters. The approach of lateral wheel force approximation and cornering stiffness adaptation can be seen in Fig. 3.16.
The ABS-cycle detection block implemented in Section 5.6 processes the wheel speed signals ω_{Rij} to assess, whether ABS was active or not. An overview of the ABS-cycle detection method is given by Fig. 5.41. The friction coefficient block described in Section 5.7 processes the longitudinal wheel forces F_{Lij}, the vertical wheel forces F_{Zij} and the wheel accelerations $\dot{\omega}_{Rij}$ and yields the friction coefficient μ. The estimation is triggered by ABS-cycle detection. With the ABS being active, normally the maximum friction is reached and the road condition can be assessed. The friction coefficient and the longitudinal and lateral wheel forces are used to check whether the calculated forces can theoretically be transmitted to the ground or not. The Kamm-circle block implemented in Section 3.4.1 yields wheel force reduction factors k_{redij}. The longitudinal wheel forces F_{Lij} and the wheel turn angle δ_W are input variables into the state space models described in Section 3.3. Additionally, the wheel force reduction factors k_{redij}, the adapted cornering stiffnesses c_{ij} and the estimated vehicle mass m_{CoG} are time-varying parameters. Based on these inputs, two state space model types are implemented: first, the linear single track model (Section 3.5) which is required as a reference model to detect accident situations online (Chapter 4). Second, the adaptive non-linear state space model (Section 3.3) describing the vehicle dynamics up to the limit of vehicle stability offline. The cause of vehicle motion and therefore the basis of this model are the forces shown in Fig. 3.7. Based upon this adaptive non-linear vehicle model, two non-linear state space observers are implemented in Sections 5.4.2 and 5.4.5 to estimate the vehicle body side slip angle (VBSSA) β. The underlying model structures for these observers are displayed in Figs. 5.22 and 5.28. To design one of these observers, the state

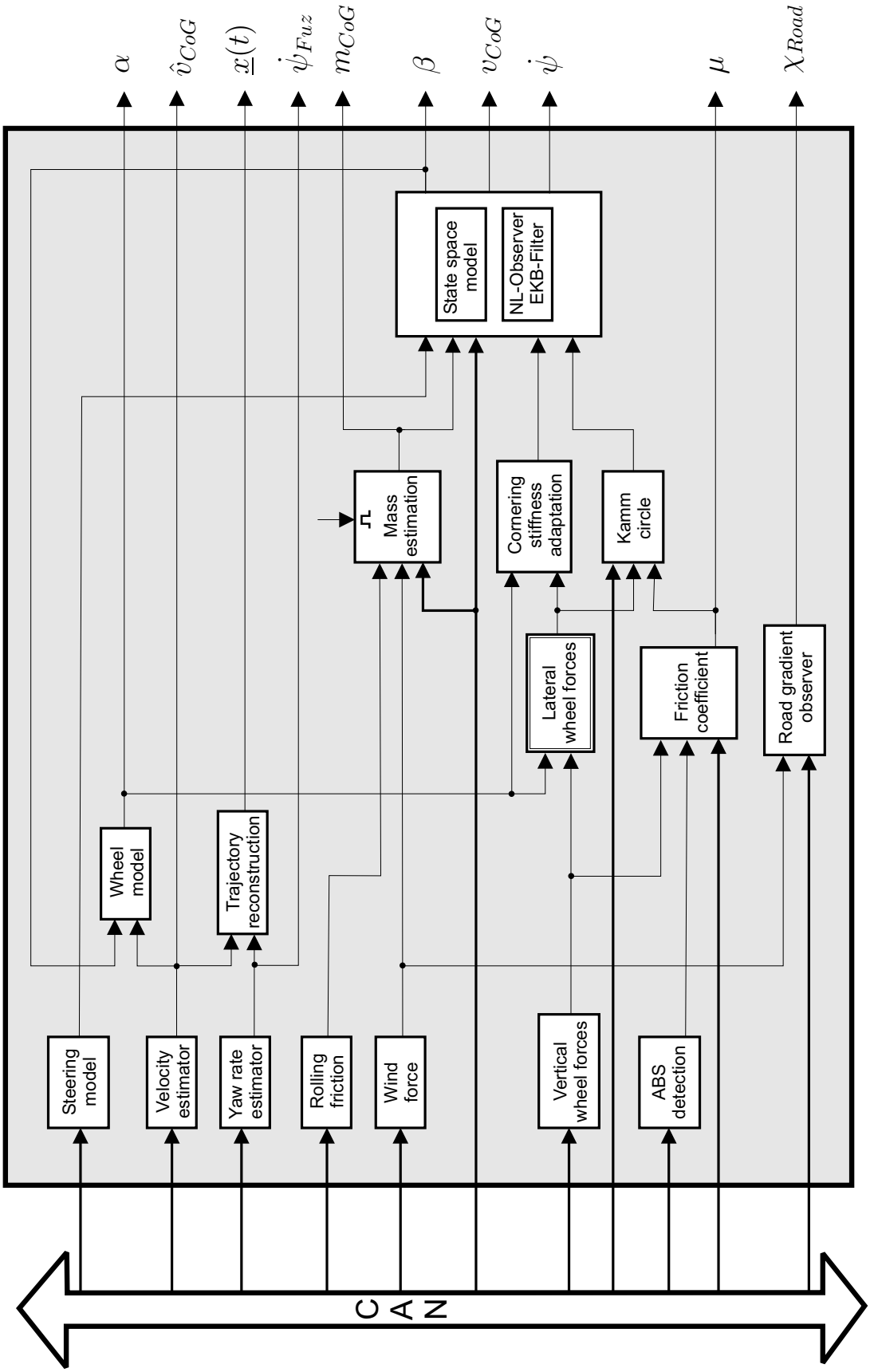

Figure 2.2: Overview over the model structure of the model based EDR

space model must be restructured (Section 5.4.3). As an alternative to the observer design, in Section 5.4.7 an extended KALMAN-BUCY-Filter was implemented to consider model inaccuracies appropriately.
Finally, a road gradient observer was implemented in Section 5.8, represented by the road gradient observer block. Here, the vehicle behavior is modeled with a linear state space observer in order to estimate the road gradient χ_{Road}. The sub-system processes the longitudinal wheel forces F_{Lij} and the wind force F_{WX}. Knowing the road gradient, the vehicle motion reproduction on the plane can be extended to the height.
The model structure shown in Fig. 2.2 generates the vehicle trajectory $\underline{x}(t)$ and the vehicle body side slip angle estimate β which is fed back to the wheel model. Knowing these two quantities, the center of gravity location as well as the vehicle heading can be calculated to provide complete information about the vehicle motion. The tire and body side slip angles α and β are measures for the stability of the car in critical situations. The vehicle mass m_{CoG} can help decide whether or not a vehicle was overloaded. Furthermore, the dynamic vehicle behavior as well as the brake distance are influenced by mass changes. The estimated maximum friction coefficient μ describes the road condition. The road gradient χ_{Road} enhances the knowledge about the vehicle motion.
With these additional quantities, the reconstruction of road traffic accidents can be achieved even when the vehicle was driven at its limits. Accident situations can be better assessed and the question of liability can be answered more accurately.

3 Vehicle Model

The vehicle model is a substantial part of a model based event data recorder. In Chapter 3, the state space models are derived to describe the vehicle motion. In a first step, the wheel forces are calculated in the wheel model of Section 3.1 based on the wheel slip. The wheel forces are the basis of the vehicle models. Afterwards, the equations of motion of the vehicle body are regarded (Section 3.2). Finally, the vehicle motion in plane is described by two vehicle model types: a non-linear two track model (Section 3.3) and a linear single track model (Section 3.5). In order to increase the accuracy of the non-linear model, several time-varying parameters are adapted (Section 3.4). After setting up the vehicle models, they are validated in Section 3.6 to analyze their applicability in a model based event data recorder.

3.1 Wheel Model

The wheel model describes the physics of the tire-road contact. The force transmission to the ground is a complex process, which is still subject to numerous research activities. In a vehicle motion reproduction system, which is planned to be installed in a large number of vehicles, simplifications have to be made because of the limited calculation capacity. For example, the determination of the friction coefficients or the lateral wheel forces are extremely sophisticated issues. That is why the wheel model is a compromise between complexity (that means calculation effort) and accuracy.

The employed wheel model is shown in Fig. 3.1. The wheel ground contact point velocities are calculated to set the basis for slip calculation. By means of the steering transmission i_S, the wheel turn angle δ_W is calculated from the steering angle δ_S given by the driver. After the derivation of approximations for the tire side slip angle, the wheel slip and the friction coefficients, this section provides solutions to calculate the wheel forces based on a friction model.

The longitudinal forces in this thesis are assumed to be measured input

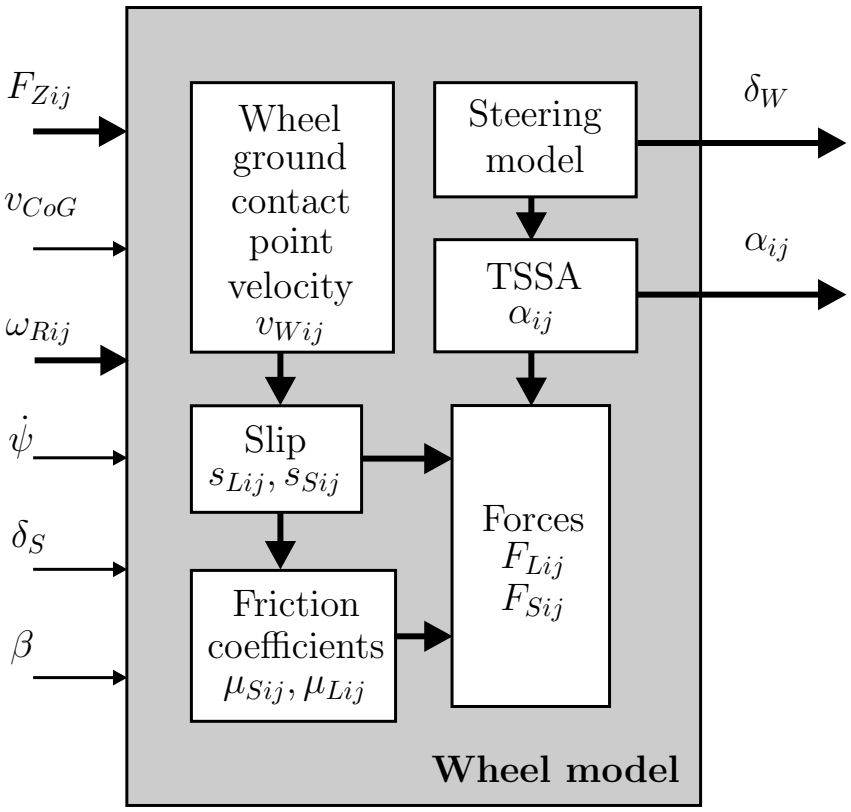

Figure 3.1: Implemented wheel model

variables into the vehicle model. The equations and relations presented in this section provide possibilities to calculate the forces, when the longitudinal forces are not measured. The wheel turn angle δ_W and the tire side slip angles α_{ij} calculated in Section 3.1 are further needed for the vehicle model. Other quantities like the side forces are approximated alternatively later on. The force model provides a possibility to calculate the wheel forces based on the friction.

3.1.1 Wheel Ground Contact Point Velocity

The wheel ground contact point velocity (WGCPV) describes the velocity of the tire relative to a fix reference point on the road surface. Under normal driving conditions the wheel ground contact point velocity deviates from the rotational equivalent velocity of the wheel. The WGCPV is required for the slip definition in Section 3.1.4. The WGCPV is determined by regarding the different curve radii of the single wheels. Assuming that the curve radius is significantly bigger than the geometric dimensions of the car, then the individual curve radii of the four wheels are parallel. In this case, the individual wheel ground contact point velocities consist of the center of gravity velocity v_{CoG} and a portion resulting from the vehicle's

yaw rate $\dot{\psi}$. Linearizing the vehicle body side slip angle β leads to the following equations for the different wheel ground contact point velocities v_{Wij}, [44]:

$$v_{WFL} = v_{CoG} - \dot{\psi}\left(\frac{b_F}{2} - l_F\beta\right) \quad , \tag{3.1}$$

$$v_{WFR} = v_{CoG} + \dot{\psi}\left(\frac{b_F}{2} + l_F\beta\right) \quad , \tag{3.2}$$

$$v_{WRL} = v_{CoG} - \dot{\psi}\left(\frac{b_R}{2} + l_R\beta\right) \quad , \tag{3.3}$$

$$v_{WRR} = v_{CoG} + \dot{\psi}\left(\frac{b_R}{2} - l_R\beta\right) \quad . \tag{3.4}$$

In Eqns. (3.1) - (3.4), l_F and l_R describe the distances of front and rear axle from the center of gravity, whereas b_F and b_R are the track of the front and the rear axle.
A method to determine the center of gravity velocity v_{CoG} is presented in Section 5.1 by means of a fuzzy estimator. Another method to determine v_{CoG} is by using GPS velocity data, [20].

3.1.2 Steering Model

In conventional steering systems, the steering wheel angle δ_S given by the driver is transformed to the wheel turn angle δ_W by a steering gear. The transmission factor of this gearbox is the steering transmission i_S. The alignment torque T_A influences the resulting wheel turn angle, [54],

$$T_A = \left(\frac{\delta_S}{i_S} - \delta_W\right) \cdot c_S \quad , \tag{3.5}$$

when considering the steering stiffness c_S. Originally, the alignment torque is caused by the wheel caster n_{LF} and the constructive caster n_C,

$$T_A = (F_{SFL} + F_{SFR}) \cdot (n_C + n_{LF}) \quad , \tag{3.6}$$

when the lateral wheel forces F_{SFL} and F_{SFR} are not acting in the middle of the wheel ground contact area. Using Eqns. (3.5) and (3.6) and isolating δ_W yields

$$\delta_W = \frac{\delta_S}{i_S} - \frac{(F_{SFL} + F_{SFR}) \cdot (n_C + n_{LF})}{c_S} \quad . \tag{3.7}$$

For most of the test drives conducted, the error is small when neglecting the alignment torque. Then, the wheel turn angle can simply be calculated by means of the steering transmission

$$\delta_W \approx \frac{\delta_S}{i_S} \quad . \tag{3.8}$$

In modern vehicles, the steering transmission i_S is not constant any more. The introduction of the active front steering system enables to adapt the steering transmission factor to the current driving situation, for instance to the vehicle speed, [18]. Then, a sum angle sensor measures the sum of the wheel turn angle portion given by the driver and the one applied by a direct current synchronous motor. In this case, Eqns. (3.7) and (3.8) cannot be applied any more, as i_S is time-varying.

3.1.3 Tire Side Slip Angles

In order to transmit lateral forces, the tire must evade laterally. That means that the direction of the tire motion deviates from the wheel plane. The angle between the wheel velocity vector $\underline{v}_W$ and the wheel plane is called the tire side slip angle α, see Fig. 3.2. Considering the geometric measures of the vehicle and its yaw motion, the individual wheel velocity directions are derived, [14]. Knowing the wheel velocity directions, the individual tire side slip angles of the four wheels are calculated. If the center of gravity is located in the middle of all wheels and if changes of l_F, l_R, b_F, b_R are neglected, the tire side slip angles of the individual wheels are

$$\alpha_{FL} = \delta_W - \arctan\left(\frac{v_{CoG}\cdot\sin\beta + l_F\cdot\dot{\psi}}{v_{CoG}\cdot\cos\beta - \frac{b_F}{2}\cdot\dot{\psi}}\right) \quad , \tag{3.9}$$

$$\alpha_{FR} = \delta_W - \arctan\left(\frac{v_{CoG}\cdot\sin\beta + l_F\cdot\dot{\psi}}{v_{CoG}\cdot\cos\beta + \frac{b_F}{2}\cdot\dot{\psi}}\right) \quad , \tag{3.10}$$

$$\alpha_{RL} = -\arctan\left(\frac{v_{CoG}\cdot\sin\beta - l_R\cdot\dot{\psi}}{v_{CoG}\cdot\cos\beta - \frac{b_R}{2}\cdot\dot{\psi}}\right) \quad , \tag{3.11}$$

$$\alpha_{RR} = -\arctan\left(\frac{v_{CoG}\cdot\sin\beta - l_R\cdot\dot{\psi}}{v_{CoG}\cdot\cos\beta + \frac{b_R}{2}\cdot\dot{\psi}}\right) \quad . \tag{3.12}$$

Merging the tire side slip angles of the two tracks and linearizing the vehicle body side slip angle ($\sin\beta \approx \beta$, $\cos\beta \approx 1$) yields the linear single track

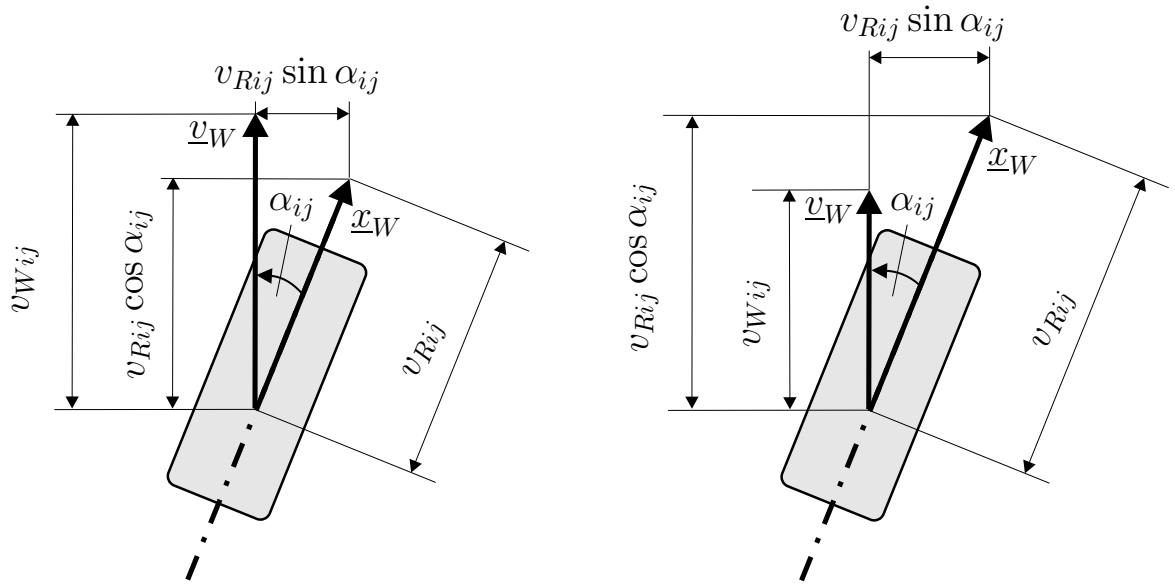

(a) Brake slip (b) Drive slip

Figure 3.2: Slip definition according to BURCKHARDT

approximation for the tire side slip angles

$$\alpha_F = \delta_W - \beta - l_F \frac{\dot{\psi}}{v_{CoG}} \quad , \tag{3.13}$$

$$\alpha_R = -\beta + l_R \frac{\dot{\psi}}{v_{CoG}} \quad . \tag{3.14}$$

Validation of the employed vehicle models shows that errors caused by linearization (Eqns. (3.13) and (3.14)) influences the model accuracy only little. The benefit of the reduced computational complexity justifies the linearization. Therefore, the linearized equations for the tire side slip angle are applied in the vehicle models of Sections 3.3 and 3.5. Information about the slip angles on all individual wheels gets lost, though.

3.1.4 Wheel Slip

The tires transmit all the drive and brake forces applied by the driver to the ground. For force transmission, the tire deforms elastically as described for instance by the brush model, [62]. Therefore, the rotational equivalent wheel velocity

$$v_{Rij} = \omega_{Rij} \cdot r_{stat} \tag{3.15}$$

and the wheel ground contact point velocity v_{Wij} relative to the ground deviate. In Eqn. (3.15), ω_{Rij} is the angular velocity of the individual wheels,

Brake slip $v_{Rij}\cos\alpha_{ij} \leq v_{Wij}$	Longitudinal slip	$s_{Lij} = \frac{v_{Rij}\cos\alpha_{ij} - v_{Wij}}{v_{Wij}}$
	Lateral slip	$s_{Sij} = \frac{v_{Rij}\sin\alpha_{ij}}{v_{Wij}}$
Drive slip $v_{Rij}\cos\alpha_{ij} > v_{Wij}$	Longitudinal slip	$s_{Lij} = \frac{v_{Rij}\cos\alpha_{ij} - v_{Wij}}{v_{Rij}\cos\alpha_{ij}}$
	Lateral slip	$s_{Sij} = \tan\alpha_{ij}$

Table 3.1: Slip definition

r_{stat} denotes the static tire radius. The normalized difference of these velocities is called wheel slip. There are several definitions of the wheel slip. For example REIMPELL, [64], defines the slip with respect to the wheel plane, whereas for instance BURCKHARDT, [12], defines it with respect to the wheel velocity direction. As the wheel moves in the direction of the wheel velocity vector $\underline{v}_W$ and not generally in the direction of the wheel plane, the BURCKHARDT definition is used in this thesis. The difference between the transformed rotational equivalent wheel velocity and the wheel ground contact point velocity is divided by the larger one of both to guarantee that the value of the slip is in the interval $[-1, +1]$. Thus, drive and brake slip must be distinguished (see Fig. 3.2). The slip can be divided into a longitudinal and a lateral component in the wheel coordinate system. The longitudinal slip s_{Lij} points in direction of the WGCPV, [12], the lateral slip component s_{Sij} perpendicular to it. This leads to the definition of the wheel slip according to Table 3.1.
The resultant slip s_{Resij} is the geometric sum of longitudinal and lateral slip:

$$s_{Resij} = \sqrt{s_{Lij}^2 + s_{Sij}^2} \quad . \tag{3.16}$$

The GPS system described in [20] is also capable to determine a suitable reference velocity. Therefore, it provides an alternative method to calculate the longitudinal and lateral slip.

3.1.5 Friction Coefficients

The determination of the friction coefficients is one of the biggest problems in vehicle dynamics research. There are several approaches to approximate the complex process of the contact between tire and road surface. The most widespread ones are probably PACEJKA'S "Magic tyre formula", [17], [60] and the DUGOFF model, [1]. An investigation of these two methods can be found in [38]. They are compared with the mentioned approach of BURCKHARDT, [12]. The result is that the PACEJKA model is the most accurate one, the DUGOFF model the one with the smallest computational effort. The BURCKHARDT formula represents an acceptable compromise between computational complexity and approximation accuracy. It is therefore used in the presented wheel model. The resultant friction coefficient μ_{Res} is a function of the slip with five approximation parameters:

$$\mu_{Res}(s_{Res}) = (c_1(1 - e^{-c_2 s_{Res}}) - c_3 s_{Res}) \cdot e^{-c_4 s_{Res} \cdot v_{CoG}}(1 - c_5 F_Z^2). \quad (3.17)$$

It can be set up for all four wheels providing μ_{Resij}. The parameters $c_1, \ldots, c_5$ depend on the characteristics of tire and road surface. Typical values can be found in [12]. Fig. 3.3 shows the friction over slip relation according to Eqn. (3.17) for different road surfaces.
The resultant slip and the resultant friction coefficient point into the same direction. This allows to define longitudinal friction coefficients μ_{Lij} and lateral friction coefficients μ_{Sij} of the individual wheels which transmit the respective forces to the road surface:

$$\mu_{Lij} = \mu_{Resij} \frac{s_{Lij}}{s_{Resij}} \quad (3.18)$$

$$\mu_{Sij} = \mu_{Resij} \frac{s_{Sij}}{s_{Resij}} \quad (3.19)$$

Eqns. (3.18) and (3.19) are used for the calculation of the longitudinal and lateral wheel forces.

3.1.6 Friction Based Wheel Forces

Approaches for the calculation of the wheel forces often require tire parameters like the longitudinal and radial tire stiffness, for instance [65]. These models are often very sophisticated with a large number of parameters. Therefore, the application of such models on standard microprocessors is impossible. In this section a simplified friction based method to describe

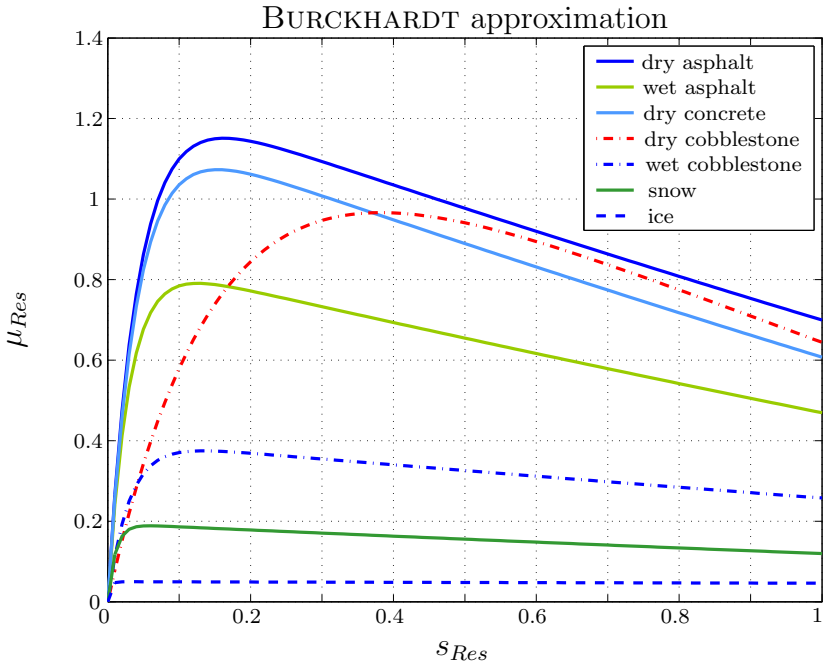

Figure 3.3: Typical μ(s)-curve for different road surfaces and a vehicle velocity $v_{CoG} = 20m/s$

the wheel forces based on Eqn. (3.17) will be presented. The friction coefficient is defined as the ratio between actually transmitted force F_{fric} and vertical wheel force F_Z:

$$\mu = \frac{F_{fric}}{F_Z} \quad . \tag{3.20}$$

This means that the longitudinal and the lateral wheel forces transmitted from the tire to the road surface can be calculated using the vertical forces and the friction coefficients determined in Section 3.1.5. As the longitudinal slip points into the direction of the wheel ground contact point velocity v_W, the forces have to be transformed from the wheel velocity coordinate system (CS) (x_{VW}, y_{VW}) into the wheel coordinate system (x_W, y_W), see Fig. 3.4(a):

$$F_{Lij} = (\mu_{Lij} \cos\alpha_{ij} + \mu_{Sij} \sin\alpha_{ij}) \cdot F_{Zij} \quad , \tag{3.21}$$

$$F_{Sij} = (\mu_{Sij} \cos\alpha_{ij} - \mu_{Lij} \sin\alpha_{ij}) \cdot F_{Zij} \quad . \tag{3.22}$$

With Eqns. (3.18) and (3.19) the resultant friction coefficient determined by means of Eqn. (3.17) can be used:

$$F_{Lij} = (s_{Lij} \cos\alpha_{ij} + s_{Sij} \sin\alpha_{ij}) \cdot \frac{\mu_{Resij}}{s_{Resij}} F_{Zij} \quad , \tag{3.23}$$

$$F_{Sij} = (s_{Sij} \cos\alpha_{ij} - s_{Lij} \sin\alpha_{ij}) \cdot \frac{\mu_{Resij}}{s_{Resij}} F_{Zij} \quad . \tag{3.24}$$

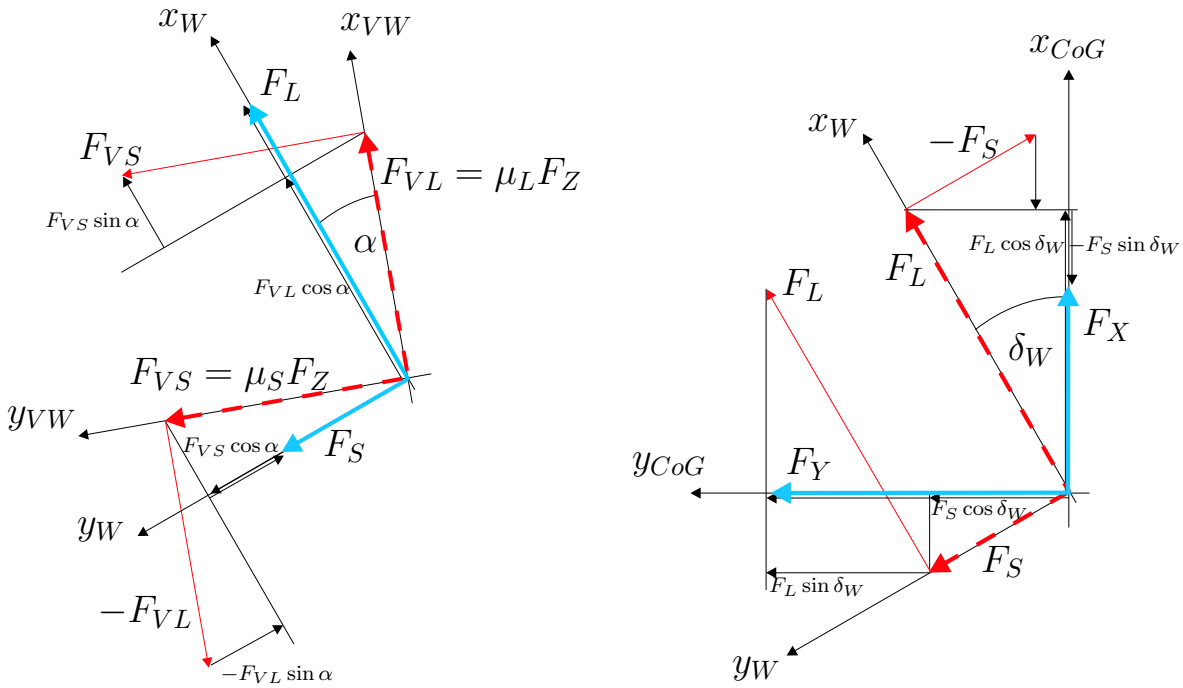

(a) Wheel velocity CS → Wheel CS

(b) Wheel CS → Center of gravity CS

Figure 3.4: Coordinate transformations of the calculated forces

In order to obtain the forces acting on the center of gravity, they are transformed into the CoG-coordinate system (x_{CoG}, y_{CoG}). For vehicles which are only front axle steered the forces in the wheel coordinate system of the rear axle are equal to those in the CoG-coordinate system:

$$F_{XRj} = F_{LRj} \quad , \tag{3.25}$$

$$F_{YRj} = F_{SRj} \quad . \tag{3.26}$$

The forces in the wheel coordinate system (x_W, y_W) of the front axle have to be transformed into the CoG-coordinate system (x_{CoG}, y_{CoG}) considering the wheel turn angle:

$$F_{XFj} = F_{LFj} \cos\delta_W - F_{SFj} \sin\delta_W \quad , \tag{3.27}$$

$$F_{YFj} = F_{SFj} \cos\delta_W + F_{LFj} \sin\delta_W \quad . \tag{3.28}$$

Fig. 3.4(b) explains this transformation of forces for one wheel of the front axle. Knowing the forces acting on the center of gravity, the force and torque balances can be set up to describe the vehicle motion in plane.

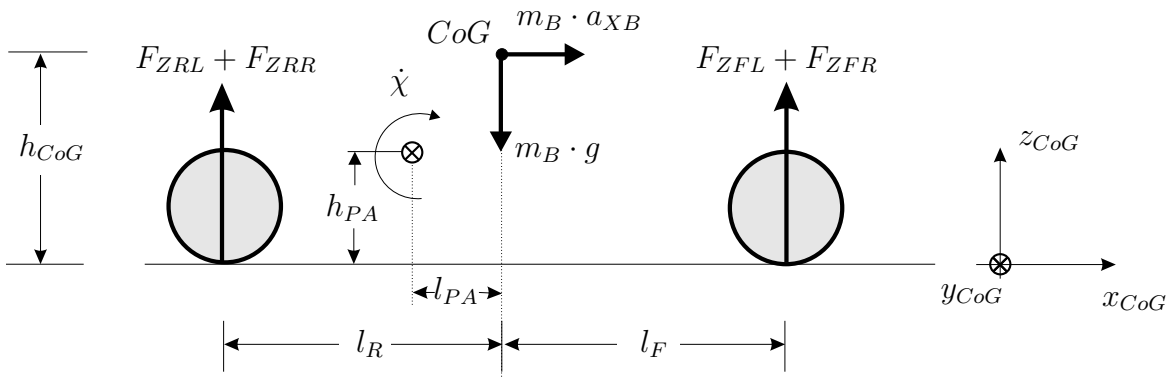

Figure 3.5: Torque balance about the pitch axis

3.2 Motions of the Vehicle Body

3.2.1 Pitch Motion

Neglecting gravitational effects due to road slope, pitching is caused by inertial forces acting on the vehicle body, when a vehicle accelerates or decelerates. The vehicle body acceleration a_{XB} directs contrarily to the measurable vehicle acceleration a_X:

$$a_{XB} = -a_X \quad . \tag{3.29}$$

When the roll axis is parallel to the vehicle's lateral axis with a longitudinal displacement l_{PA} and a height displacement $(h_{CoG} - h_{PA})$ to the center of gravity, then the torque balance about this axis is

$$\begin{aligned} J_Y \cdot \ddot{\chi} \;&=\; (F_{ZRL} + F_{ZRR}) \cdot (l_R - l_{PA}) - (F_{ZFL} + F_{ZFR}) \cdot (l_F + l_{PA}) \\ &\quad + m_B \cdot a_{XB} \cdot (h_{CoG} - h_{PA}) + m_B \cdot g \cdot l_{PA} \quad . \end{aligned} \tag{3.30}$$

The mass of the vehicle body is denoted m_B. Regarding Fig. 3.5 shows that for a braking maneuver the vehicle body accelerates in the x_{CoG}-direction. This causes an angular acceleration $\ddot{\chi}$ about the roll axis and shifts the wheel load to the front axle.

3.2.2 Roll Motion

The roll motion of the vehicle body mainly occurs in cornering situations caused by centrifugal forces. The body acceleration a_{YB} therefore can be calculated according to

$$a_{YB} = -a_Y \quad . \tag{3.31}$$

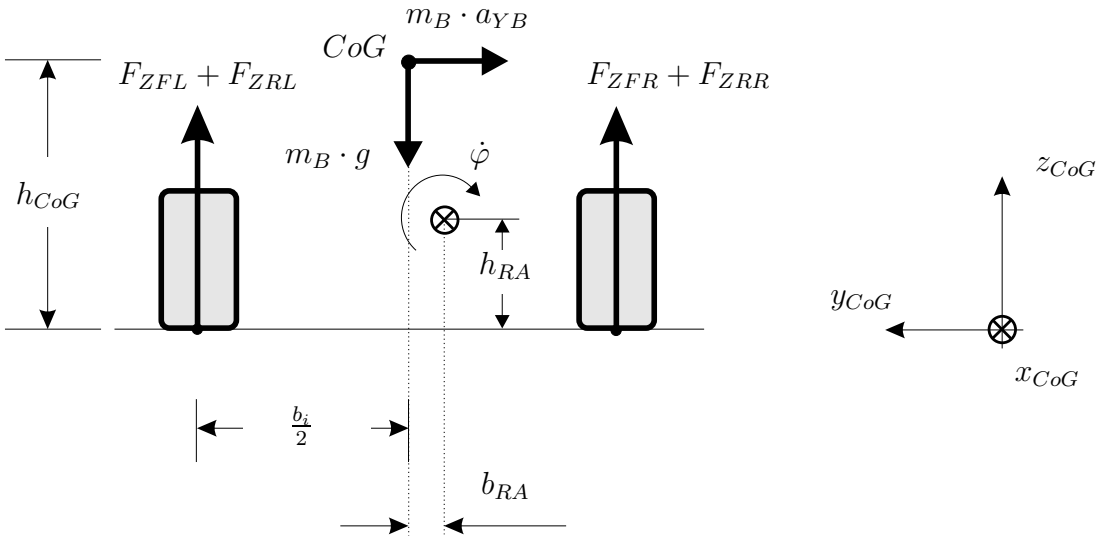

Figure 3.6: Torque balance about the roll axis

As for pitching, gravitational forces by tilted roads are not regarded. Assuming that the pitch axis is parallel to the vehicle's longitudinal axis with a lateral displacement b_{RA} and a height displacement $(h_{CoG} - h_{RA})$ to the center of gravity, then the respective torque balance is

$$\begin{aligned} J_X \cdot \ddot{\varphi} \;=\; & F_{ZFL} \cdot \left(\frac{b_F}{2} + b_{RA}\right) - F_{ZFR} \cdot \left(\frac{b_F}{2} - b_{RA}\right) \\ & + F_{ZRL} \cdot \left(\frac{b_R}{2} + b_{RA}\right) - F_{ZRR} \cdot \left(\frac{b_R}{2} - b_{RA}\right) \\ & + m_B \cdot a_{YB} \cdot (h_{CoG} - h_{RA}) - m_B \cdot g \cdot b_{RA} \quad . \end{aligned} \tag{3.32}$$

Fig. 3.6 shows the effect of a left curve: the vehicle body moves to the outer track, because the body acceleration points to the right.

3.2.3 Vertical Body Motion

Driving on uneven road surface, the vehicle body moves up and downward. The force balance is

$$m_B \cdot a_Z = F_{ZFL} + F_{ZFR} + F_{ZRL} + F_{ZRR} - m_B \cdot g \quad . \tag{3.33}$$

3.3 Non-linear Two Track Model

The main goal of this thesis is to describe the vehicle dynamics with acceptable computational costs. Moreover, vehicle models shall be used to reconstruct the vehicle motion before accidents. For these purposes, the vehicle motion in plane is of most interest. That is the reason, why the motion in plane is regarded more detailed than the body motions.
A lot of publications deal with the modeling of the vehicle dynamics in plane, for instance [2], [14], [53], [62], [78]. To describe the vehicle dynamics the vehicle's equations of motion are set up. From these equations a non-linear state space model is derived. Thereby, it is necessary to keep the structure of the model simple with a small number of input and state variables. On the other hand, the vehicle model must be as accurate as possible. As a compromise, some parameters of the state space equations are adapted according to the current driving situation (Section 3.4). Additionally, forces with only little influence for the model accuracy are neglected. Fig. 3.7 shows the most important forces, quantities of motion and some vehicle parameters of the two track model. For simplification, the center of gravity is assumed to be in the road surface and the vehicle's vertical axis lies on the CoG as well.
The force balance equations in longitudinal and lateral direction and the torque balance about the yaw axis are set up. In addition to the wheel forces F_{Lij} and F_{Sij}, rolling resistance forces are acting on each wheel. These four rolling resistance forces are unified to a resultant force F_R acting in direction of the vehicle's longitudinal axis. The centripetal force F_{CP} acts in the center of gravity perpendicular to the vehicle motion. The wind forces F_{WX} and F_{WY} are affecting the vehicle in the pressure point PP. Gravitational forces or the ascending force F_{WZ} are neglected. The wheel casters are assumed to be equal on the respective axles,

$$n_{LF} := n_{LFL} = n_{LFR} \quad \text{and} \quad n_{LR} := n_{LRL} = n_{LRR} \quad ,$$

and lateral displacements of the wheel ground contact point are neglected. Therewith, all assumptions and limitations are defined and the force balance equations in x_{CoG}- and y_{CoG}-direction are

$$\begin{aligned} m_{CoG}\dot{v}_{CoG}\cos\beta \;&=\; F_{XFL} + F_{XFR} + F_{XRL} \\ &\quad + F_{XRR} - F_{CP}\sin\beta - F_{WX} - F_R \end{aligned} \tag{3.34}$$

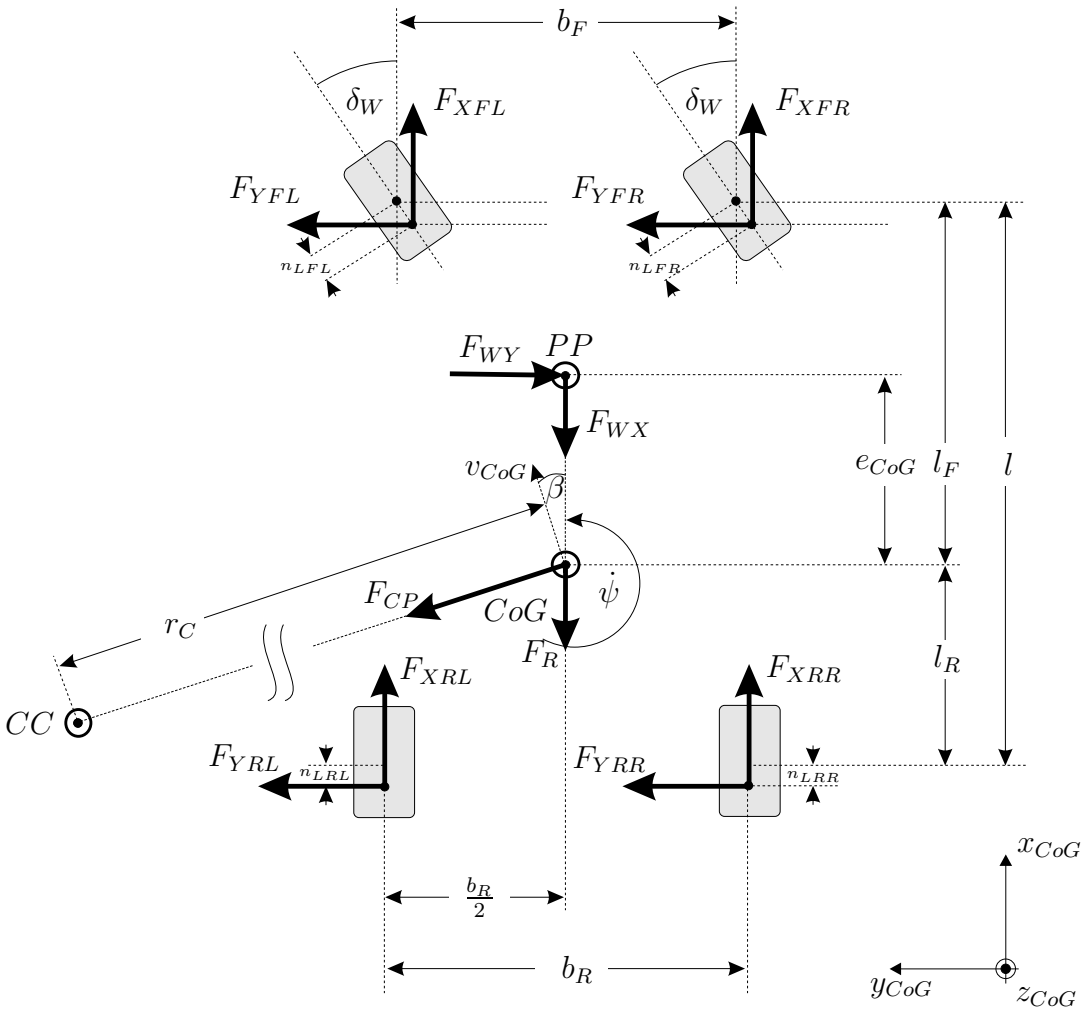

Figure 3.7: Forces and vehicle parameters of the two track model

and

$$\begin{aligned} m_{CoG}\dot{v}_{CoG}\sin\beta &= F_{YFL}+F_{YFR}+F_{YRL} \\ &\quad +F_{YRR}+F_{CP}\cos\beta-F_{WY} \quad . \end{aligned} \tag{3.35}$$

The torque balance about the z_{CoG}-axis is (see Fig. 3.7)

$$\begin{aligned} J_Z\cdot\ddot{\psi} &= (l_F-n_{LF}\cos\delta_W)(F_{YFL}+F_{YFR})-(l_R+n_{LR})(F_{YRL}+F_{YRR}) \\ &\quad +\frac{b_F}{2}(F_{XFR}-F_{XFL})+\frac{b_R}{2}(F_{XRR}-F_{XRL})-e_{CoG}F_{WY}. \end{aligned} \tag{3.36}$$

In the next section, a state space form is derived by replacing F_{CP} in Eqns. (3.34) - (3.36).

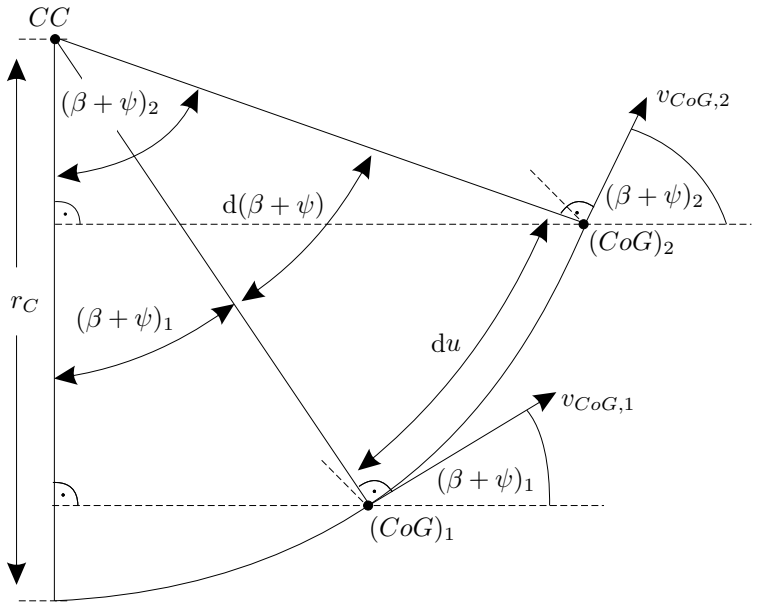

Figure 3.8: Path of the CoG with angular relations and curve radius r_C

3.3.1 Centripetal Force

According to [28], the centripetal force is

$$F_{CP} = -\frac{m_{CoG} \cdot v_{CoG}^2}{r_C} \quad , \tag{3.37}$$

where r_C describes the curve radius around the center of curvature (CC) and m_{CoG} the complete vehicle mass. According to Fig. 3.8 the inverse curve radius $1/r_C$ is the change of the course angle $d(\beta+\psi)$ with the arc length du between two successive time instants $(CoG)_1$ and $(CoG)_2$:

$$\frac{1}{r_C} = \frac{d(\beta+\psi)}{du} = \frac{d(\beta+\psi)}{dt} \cdot \frac{dt}{du} = (\dot{\beta}+\dot{\psi}) \cdot \frac{1}{v_{CoG}} \quad . \tag{3.38}$$

Then, the centripetal force according to Eqn. (3.37) can be written as

$$F_{CP} = -\frac{m_{CoG} \cdot v_{CoG}^2}{r_C} = -m_{CoG} \cdot v_{CoG} \cdot (\dot{\beta}+\dot{\psi}) \quad . \tag{3.39}$$

Inserting (3.39) into the force balances (3.34) and (3.35) yields

$$m_{CoG} \cdot \dot{v}_{CoG} \cdot \cos\beta - m_{CoG} \cdot v_{CoG} \cdot (\dot{\beta}+\dot{\psi}) \cdot \sin\beta \;=\; \sum F_X, \tag{3.40}$$

$$m_{CoG} \cdot \dot{v}_{CoG} \cdot \sin\beta + m_{CoG} \cdot v_{CoG} \cdot (\dot{\beta}+\dot{\psi}) \cdot \cos\beta \;=\; \sum F_Y, \tag{3.41}$$

with

$$\sum F_X = F_{XFL} + F_{XFR} + F_{XRL} + F_{XRR} - F_{WX} - F_R \quad , \tag{3.42}$$

$$\sum F_Y = F_{YFL} + F_{YFR} + F_{YRL} + F_{YRR} - F_{WY} \quad . \tag{3.43}$$

In order to obtain state space form $\underline{f}(\underline{x}, \underline{u})$, the state variables v_{CoG} and β shall be isolated now. Multiplying Eqn. (3.40) with $\cos\beta$ and Eqn. (3.41) with $\sin\beta$ and adding the resulting equations leads to

$$m_{CoG} \cdot \dot{v}_{CoG} \cdot \underbrace{(\cos^2\beta + \sin^2\beta)}_{=1} = \cos\beta \cdot \sum F_X + \sin\beta \cdot \sum F_Y. \tag{3.44}$$

Isolating $\dot{v}_{CoG}$ provides the first state space equation

$$\dot{v}_{CoG} = \frac{1}{m_{CoG}} \cdot \left\{ \cos\beta \cdot \sum F_X + \sin\beta \cdot \sum F_Y \right\}. \tag{3.45}$$

Using Eqn. (3.41) and (3.45) provides an equation for β

$$\cos\beta \cdot \sin\beta \sum F_X + \sin^2\beta \sum F_Y + m_{CoG} v_{CoG} (\dot{\beta} + \dot{\psi}) \cos\beta = \sum F_Y$$

$$\Leftrightarrow m_{CoG} v_{CoG} (\dot{\beta} + \dot{\psi}) \cos\beta = \underbrace{(1 - \sin^2\beta)}_{\cos^2\beta} \sum F_Y - \cos\beta \cdot \sin\beta \sum F_X.$$

Isolating $\dot{\beta}$ yields the second state space equation of the non-linear two track model:

$$\dot{\beta} = \frac{1}{m_{CoG} v_{CoG}} \cdot \left\{ \cos\beta \cdot \sum F_Y - \sin\beta \cdot \sum F_X \right\} - \dot{\psi} \quad . \tag{3.46}$$

The third state space equation from the torque balance (3.36) reads

$$\begin{aligned} \ddot{\psi} = \frac{1}{J_Z} \cdot \Big\{ & (l_F - n_{LF}\cos\delta_W)(F_{YFL} + F_{YFR}) \\ & + \frac{b_F}{2}(F_{XFR} - F_{XFL}) - (l_R + n_{LR})(F_{YRL} + F_{YRR}) \\ & + \frac{b_R}{2}(F_{XRR} - F_{XRL}) - e_{CoG} F_{WY} \Big\} \quad . \end{aligned} \tag{3.47}$$

The mass moment of inertia J_Z is approximated. Generally, it is defined as

$$J = \int_m r^2 dm \quad . \tag{3.48}$$

Assuming only two mass elements on the front axle (m_F) and on the rear axle (m_R), Eqn. (3.48) is simplified:

$$J_Z = m_F \cdot l_F^2 + m_R \cdot l_R^2 \quad . \tag{3.49}$$

If the mass distribution is unknown, then an approximation can be employed, [63]:

$$J_Z = m_{CoG} \cdot i_Z^2 \quad . \tag{3.50}$$

with $i_Z^2 = 1.3 \ldots 1.45 m^2$.
The three Eqns. (3.45), (3.46) and (3.47) describe the vehicle dynamics in plane. These equations are merged to a vector equation leading to a non-linear state space model with the state vector $\underline{x} = (v_{CoG}, \quad \beta, \quad \dot{\psi})^T$:

$$\begin{bmatrix} \dot{v}_{CoG} \\ \dot{\beta} \\ \ddot{\psi} \end{bmatrix} =: \dot{\underline{x}} = \underline{f}(v_{CoG}, \beta, \dot{\psi}, \delta_W, F_{Xij}, F_{Yij}, F_R, F_{WX}, F_{WY}). \tag{3.51}$$

The function $\underline{f}$ depends on the state variables v_{CoG}, β and $\dot{\psi}$. Furthermore, the longitudinal and lateral wheel forces F_{Xij} and F_{Yij}, the rolling resistance force F_R and the wind forces F_{WX} and F_{WY} are unknown in Eqn. (3.51). These variables are replaced stepwise in the next sections, so that $\underline{f}$ only depends on the three state variables and other measurable variables.

3.3.2 Rolling Resistance Force

When a rubber tire rotates, it is compressed when running through the wheel ground contact area. Due to the damping characteristics of the tire, a portion of this "compression energy" is transformed to thermal energy heating up the tire. The rolling resistance force is a quantity which describes this effect. It mainly occurs in the wheel ground contact area. The rolling resistance significantly depends on the vehicle velocity, and according to [64] can be approximated by a polynomial

$$F_R = F_Z \cdot \left(f_{R,0} + f_{R,1} \cdot \left(\frac{v_{CoG}}{30 \, \frac{m}{s}} \right) + f_{R,4} \cdot \left(\frac{v_{CoG}}{30 \, \frac{m}{s}} \right)^4 \right) \quad , \tag{3.52}$$

where F_Z describes the vertical wheel force calculated in Section 3.3.4. Typical values for the rolling resistance parameters $f_{R,0}$, $f_{R,1}$ and $f_{R,4}$ can be found in [52]. [32] describes a method to estimate the rolling resistance parameters with a recursive least squares approach.
The rolling resistance force is neglected in the vehicle model. Simulations show that the rolling resistance hardly influences the accuracy of the non-linear state space model.

3.3.3 Wind Force

A driving vehicle is passed by air causing a turbulent flow, [52], which can be described by a quadratic velocity dependence. Therefore, the following widespread approximation was used for the wind forces:

$$F_{WX} = c_{WX} \cdot v_{CoG}^2 \quad , \tag{3.53}$$

$$F_{WY} = c_{WY} \cdot v_{WY}^2 \quad . \tag{3.54}$$

In the vehicle models, the lateral wind force is neglected, because there is no reliable online information about the current lateral wind force v_{WY}. The constant c_{WX} holds

$$c_{WX} = c_{aer} \cdot A_L \cdot \frac{\rho_0}{2} \tag{3.55}$$

with the air density ρ_0, the vehicle front area A_L and the air drag coefficient c_{aer}.

3.3.4 Vertical Wheel Forces

In moderate driving situations the vertical wheel forces are mainly caused by earth gravitation. Then, they primarily depend on the passenger and package distribution and on the geometric measures of the vehicle. In extreme acceleration, brake or cornering situations, however, the vehicle body shifts because of inertial forces. In these situations, the individual vertical wheel forces change depending on the accelerations acting, on the spring damper characteristics of the suspension system, [69], and on kinematic interactions of the coupled wheels. Considering all of these effects results in a set of complex non-linear equations with a lot of unknown parameters which have to be identified. [32] describes the vertical wheel forces accurately by using neural networks. To avoid unnecessary complexity, the vertical wheel forces are approximated with a simple approach here. The camber angle is neglected as well as the dynamics of the vehicle body motion. The roll and pitch accelerations $\ddot{\chi}$ and $\ddot{\varphi}$ are not considered. The left sides of Eqns. (3.30) and (3.32) are zero. Furthermore, the roll and pitch axes are assumed to pass through the center of gravity. Then, h_{PA}, l_{PA}, h_{RA}, b_{RA} in Figs. 3.5 and 3.6 are zero. If, moreover, couplings between the pitch and roll dynamics are not regarded, the torque balances around the respective axes can be carried out separately. The current wheel loads depend on the longitudinal and lateral accelerations. Positive longitudinal accelerations a_X cause a pitch motion a_{XB} of the vehicle body due to its

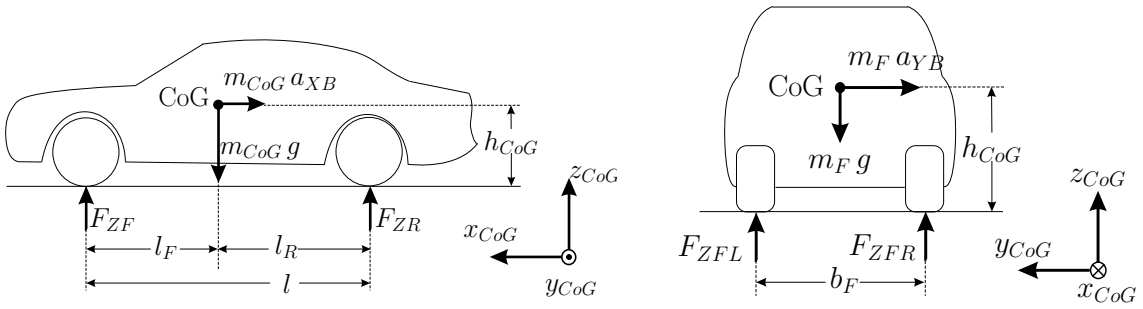

(a) Wheel load change for positive longitudinal accelerations

(b) Wheel load change on the front axle for lateral accelerations in a left curve

Figure 3.9: Wheel load changes

inertia. The pitch motion relieves the front axle and loads the rear axle (see Fig. 3.9(a)). The torque balance about the wheel ground contact point of the rear axle provides

$$F_{ZF} = m_{CoG} \cdot \left(\frac{l_R}{l}\, g - \frac{h_{CoG}}{l}\, a_{XB} \right) \quad . \tag{3.56}$$

Here, it is assumed that not only the vehicle body but the whole vehicle "rotates" around the front wheel contact point. That is the reason, why Eqn. (3.56) contains the complete vehicle mass m_{CoG} instead of the vehicle body mass m_B only.
Secondly, cornering causes lateral accelerations a_{YB} of the vehicle body, which relieves the inner vehicle track. As mentioned before, to calculate the resultant wheel loads, the front and rear axle are regarded separately. This demands to introduce two virtual masses m_F and m_R for the respective vehicle axles. According to Eqn. (3.56), for the front axle it becomes

$$m_F = \frac{F_{ZF}}{g} = \frac{m_{CoG}}{g} \cdot \left(\frac{l_R}{l}\, g - \frac{h_{CoG}}{l}\, a_{XB} \right) \quad . \tag{3.57}$$

Using the virtual mass m_F, the individual wheel loads for the front wheels can be calculated. Fig. 3.9(b) shows the affecting forces. The torque balance about the wheel ground contact point of the front right wheel yields the wheel load of the front left wheel

$$\begin{aligned} F_{ZFL} &= m_F \cdot \left(\frac{1}{2}\, g - \frac{h_{CoG}}{b_F}\, a_{YB} \right) \\ &= m_{CoG} \cdot \left(\frac{l_R}{l}\, g - \frac{h_{CoG}}{l}\, a_{XB} \right) \cdot \left(\frac{1}{2} - \frac{h_{CoG}}{b_F} \cdot \frac{a_{YB}}{g} \right) \quad . \end{aligned} \tag{3.58}$$

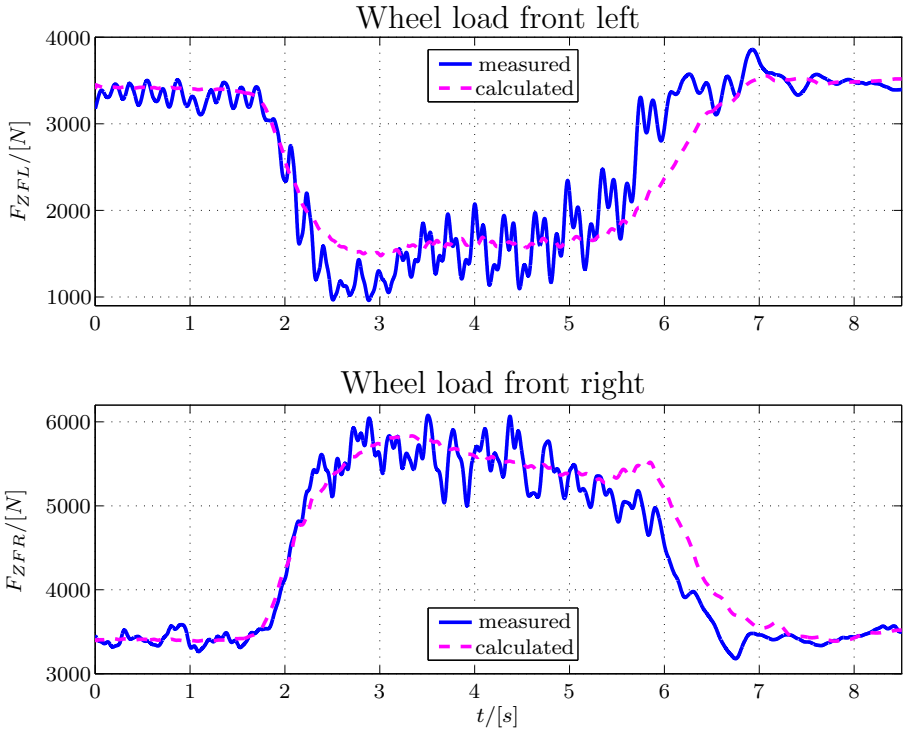

Figure 3.10: Varying wheel loads for cornering

Analogous, the wheel loads of the other wheels are calculated

$$
\begin{aligned}
F_{ZFR} &= m_{CoG} \cdot \left(\frac{l_R}{l} g - \frac{h_{CoG}}{l} a_{XB} \right) \cdot \left(\frac{1}{2} + \frac{h_{CoG}}{b_F} \cdot \frac{a_{YB}}{g} \right) \quad , \\
F_{ZRL} &= m_{CoG} \cdot \left(\frac{l_F}{l} g + \frac{h_{CoG}}{l} a_{XB} \right) \cdot \left(\frac{1}{2} - \frac{h_{CoG}}{b_R} \cdot \frac{a_{YB}}{g} \right) \quad , \\
F_{ZRR} &= m_{CoG} \cdot \left(\frac{l_F}{l} g + \frac{h_{CoG}}{l} a_{XB} \right) \cdot \left(\frac{1}{2} + \frac{h_{CoG}}{b_R} \cdot \frac{a_{YB}}{g} \right) \quad . \qquad (3.59)
\end{aligned}
$$

Fig. 3.10 shows the varying wheel loads of a cornering drive. The vehicle drives straightforward during the first phase of the drive. The wheel loads are almost constant at about $3300N$. After about $t = 1.8s$ the vehicle enters a left curve. That is why the front left wheel is relieved, whereas the right wheel is loaded. The wheel load at the right wheel rises to a value of almost $6000N$. Fig. 3.10 shows that even for extreme cornering situations with significant wheel load changes, the approximation Eqns. (3.58) - (3.59) provide very good results. The values are much better than considering static wheel loads only. This is the basis for the accurate calculation of the lateral wheel forces (see Section 3.3.6).

3.3.5 Longitudinal Wheel Forces

This thesis focuses on vehicle dynamics and accident reconstruction. Therefore, no sophisticated drivetrain and brake system models were set up. The longitudinal wheel forces are assumed to be measured or modeled inputs into the vehicle model.
The drive forces can be calculated based on the engine torque by modeling the drivetrain, e.g. [44]. In a first, rough approximation, the drive torque at the wheels is calculated with the engine torque T_E and the transmission factors of the gear box and the differential gear. This approach neglects torsion oscillations in the drivetrain, though.
The brake forces can for instance be determined by means of the main cylinder brake pressure p_{BM} and a brake model, which calculates the individual wheel cylinder brake pressures p_{BWij}, [14]. Knowing the p_{BWij} and the geometric measures as well as the friction characteristics of the brake disks allows to determine the brake forces. In future automotive applications, new brake systems like the electrohydraulic brake or the electromechanic brake, described e.g. in [69], will probably spread and provide a brake force signal.

3.3.6 Lateral Wheel Forces

Section 3.1.3 describes the deviation of the tire motion from the wheel plane. The tire must evade laterally to transform side forces. Usually, the relationship between the tire side slip angles α_{ij} and the lateral wheel forces F_{Sij} is assumed to be linear:

$$F_{Sij} = c_{ij} \cdot \alpha_{ij} \quad . \tag{3.60}$$

For the tire side slip angles, the linear state space approximations can be inserted (Eqns. (3.13) and (3.14)) leading to the following linear approximation of the lateral wheel forces on the front and on the rear axle:

$$F_{SFj} = c_{Fj} \cdot \left(\delta_W - \beta - \frac{l_F \cdot \dot{\psi}}{v_{CoG}} \right) \quad , \tag{3.61}$$

$$F_{SRj} = c_{Rj} \cdot \left(-\beta + \frac{l_R \cdot \dot{\psi}}{v_{CoG}} \right) \quad . \tag{3.62}$$

However, the linear approximation is only valid for lateral accelerations below $4m/s^2$, [53]. For growing lateral accelerations, that means with increasing tire side slip angles and wheel load shift, the linear approximation

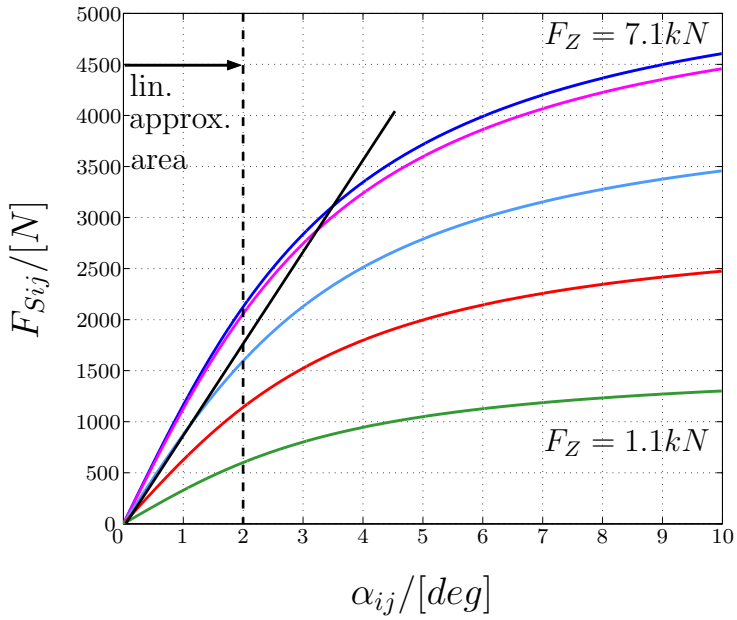

Figure 3.11: Non-linear characteristic line for lateral wheel force

deviates more and more from the real lateral wheel force characteristic (Fig. 3.11). The cornering stiffnesses c_{ij} describe the slope of the straight line in Fig. 3.11. That means, they represent the proportionality factor for the linear relationship expressed in Eqn. (3.60). It is obvious that for higher lateral accelerations the cornering stiffnesses are reduced. Section 3.4.2 explains a methodology which approximates the time-varying reduction of cornering stiffnesses according to the driving situation.

3.3.7 Final State Space Equations of the Non-Linear Two Track Model

The longitudinal and lateral wheel forces determined in Sections 3.3.5 and 3.3.6 are transformed into the center of gravity coordinate system now. The forces F_{Xij} and F_{Yij} in Eqns. (3.45) to (3.47) therefore are replaced by the longitudinal and lateral wheel forces F_{Lij} and F_{Sij}. These are the forces acting on the tires and causing the vehicle motion. For the transformation of the forces, Eqns. (3.25) to (3.28) are employed again. With the transformed wheel forces F_{Lij} and with F_{Sij} according to Eqns. (3.61) and (3.62), with the approximation of F_{WX} (Eqn. (3.53)) and the neglect of less important forces, the equations for the vehicle model can be set up now.
Goal of this section is the derivation of a non-linear two track model. To reduce the complexity, several approximations were carried out. For example, as mentioned before, the rolling resistance was not considered due to

its small influence. This yields the following state space equations for the non-linear two track model:

$$\begin{aligned}
\dot{v}_{CoG} &= \frac{1}{m_{CoG}} \cdot \Big\{ (F_{LFL} + F_{LFR}) \cos(\delta_W - \beta) \\
&\quad -(c_{FL} + c_{FR}) \cdot \left(\delta_W - \beta - \frac{l_F \, \dot{\psi}}{v_{CoG}} \right) \cdot \sin(\delta_W - \beta) \\
&\quad + \left(F_{LRL} + F_{LRR} - c_{WX} \cdot v_{CoG}^2 \right) \cdot \cos\beta \\
&\quad +(c_{RL} + c_{RR}) \cdot \left(-\beta + \frac{l_R \, \dot{\psi}}{v_{CoG}} \right) \cdot \sin\beta \Big\} \quad , \qquad (3.63)
\end{aligned}$$

$$\begin{aligned}
\dot{\beta} &= \frac{1}{m_{CoG} v_{CoG}} \cdot \Big\{ (F_{LFL} + F_{LFR}) \sin(\delta_W - \beta) \\
&\quad +(c_{FL} + c_{FR}) \cdot \left(\delta_W - \beta - \frac{l_F \, \dot{\psi}}{v_{CoG}} \right) \cdot \cos(\delta_W - \beta) \\
&\quad +(c_{RL} + c_{RR}) \cdot \left(-\beta + \frac{l_R \, \dot{\psi}}{v_{CoG}} \right) \cdot \cos\beta \\
&\quad -(F_{LRL} + F_{LRR} - c_{WX} \cdot v_{CoG}^2) \sin\beta \Big\} - \dot{\psi} \quad , \qquad (3.64)
\end{aligned}$$

$$\begin{aligned}
\ddot{\psi} &= \frac{1}{J_Z} \cdot \Big\{ (l_F - n_{LF} \cos\delta_W) \cdot (F_{LFL} + F_{LFR}) \cdot \sin\delta_W \\
&\quad +(l_F - n_{LF} \cos\delta_W) \cdot (c_{FL} + c_{FR}) \cdot \left(\delta_W - \beta - \frac{l_F \cdot \dot{\psi}}{v_{CoG}} \right) \cdot \cos\delta_W \\
&\quad +\frac{b_F}{2} \cdot (F_{LFR} - F_{LFL}) \cos\delta_W + \frac{b_R}{2} \cdot (F_{LRR} - F_{LRL}) \\
&\quad -\frac{b_F}{2} \cdot (c_{FR} - c_{FL}) \cdot \left(\delta_W - \beta - \frac{l_F \cdot \dot{\psi}}{v_{CoG}} \right) \cdot \sin\delta_W \\
&\quad -(l_R + n_{LR}) \cdot (c_{RL} + c_{RR}) \cdot \left(-\beta + \frac{l_R \, \dot{\psi}}{v_{CoG}} \right) \Big\} \quad . \qquad (3.65)
\end{aligned}$$

With these three differential equations, the dynamics of a vehicle can be described by a state space model

$$\dot{\underline{x}} = \underline{f}(\underline{x}, \underline{u}) \tag{3.66}$$

with three state variables

$$\underline{x} = \left[\begin{array}{ccc} v_{CoG} & \beta & \dot{\psi} \end{array} \right]^T \quad .$$

The non-linear vector function $\underline{f}$ is defined by the differential equations (3.63), (3.64) and (3.65).
Keeping the number of inputs small was a main aspect of the considerations in Section 3.3. The final state space model gets by with only five input variables

$$\underline{u} = \left[\begin{array}{ccccc} F_{LFL} & F_{LFR} & F_{LRL} & F_{LRR} & \delta_W \end{array} \right]^T \quad .$$

Two of the state variables are measurable: the center of gravity velocity v_{CoG} and the yaw rate $\dot{\psi}$. This yields the output equation

$$\underline{y} = \left[\begin{array}{cc} v_{CoG} & \dot{\psi} \end{array} \right]^T = \underline{C} \cdot \underline{x} = \left[\begin{array}{ccc} 1 & 0 & 0 \\ 0 & 0 & 1 \end{array} \right] \cdot \underline{x} \quad . \tag{3.67}$$

This model is the basis for the non-linear vehicle body side slip angle observers designed in Section 5.4 and for the extended Kalman-Bucy-Filter of Section 5.4.7.

3.4 Adaptation of Time-varying Parameters

To handle the trade-off between simpleness and accuracy of the vehicle model, two important parameters of the model are adapted: the wheel force reduction factors k_{redij} and the cornering stiffnesses c_{ij}. The cornering stiffnesses are approximated with a non-linear approximation equation.

3.4.1 Wheel Force Reduction Factor

According to Eqn. (3.20) the maximum force F_{fric} which can be transmitted to the ground is limited by the friction coefficient μ. The wheel adhesion limit describes the limit, where the wheel is not rolling any more and starts sliding. The calculated wheel forces are adapted now to meet the adhesion condition. If longitudinal and lateral forces are acting simultaneously, the

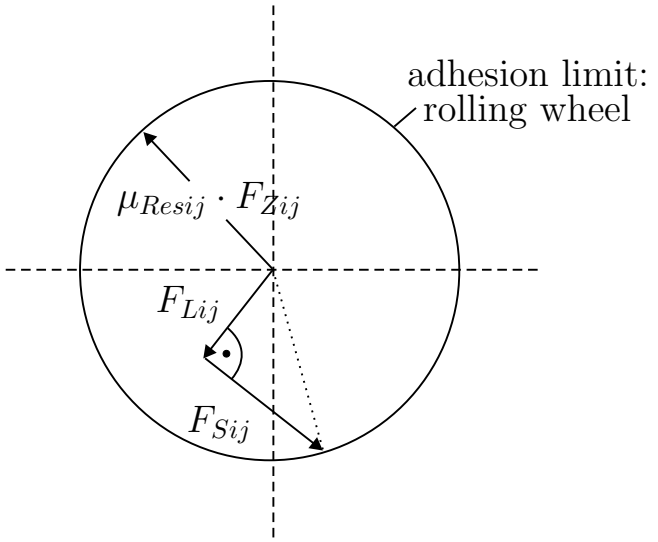

Figure 3.12: The KAMM-circle

geometric sum of the forces must be inside the KAMM-circle (see Fig. 3.12) and meet the adhesion condition

$$\sqrt{F_{Lij}^2 + F_{Sij}^2} \leq \mu_{Resij} \cdot F_{Zij} \quad . \tag{3.68}$$

In extreme driving situations the friction forces may be calculated too large. In order to consider that fact, a wheel force reduction factor k_{red} is introduced which reduces the longitudinal and lateral wheel forces F_{Lij} and F_{Sij}, if the relation (3.68) is not fulfilled any more

$$k_{redij} = \frac{\mu_{Resij} \cdot F_{Zij}}{\sqrt{F_{Lij}^2 + F_{Sij}^2}} \quad . \tag{3.69}$$

If both F_{Lij} and F_{Sij} are zero when rolling straightforward, the adhesion condition (3.68) holds. Then, k_{redij} is set to one to avoid singularities of Eqn. (3.69). The wheel force reduction factor ensures that the geometric sum of the forces lies within the borders of the KAMM-circle. It has to be adapted in every calculation step of the vehicle model in order to guarantee, that the maximum force transmission to the ground is not exceeded. However, if the wheel is sliding over the ground, the force transmission will still be calculated too high, as a sliding wheel is almost not at all capable to transmit forces to the ground. That means, that the wheel force reduction factor is a means to come closer to reality. In sliding situations, though, the calculated wheel forces are still too large.
Fig. 3.13 shows the lateral wheel force F_{SFL} of a test drive, where the vehicle is understeering. That means, the adhesion contact to the ground

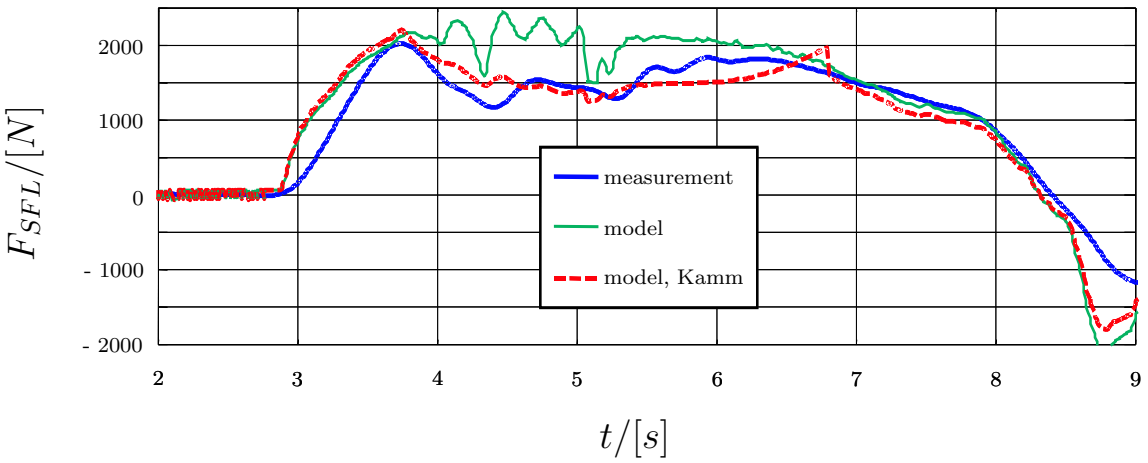

Figure 3.13: Modeled side forces with and without considering the KAMM-Circle

on the front axle gets lost. Fig. 3.13 shows that the modeled lateral wheel force without regarding the KAMM-Circle is too high. Considering the relation (3.68) and employing the wheel force reduction factor according to Eqn. (3.69), the measured reference is approximated more accurately in the highly dynamical phase of the drive between $t = 4s$ and $t = 5.5s$. This gain of lateral wheel force accuracy influences the quality of the employed vehicle models.

3.4.2 Adaptation of the Cornering Stiffnesses

In order to keep the complexity of the non-linear two track model small, the linear relationship $F_S(\alpha)$ from Eqn. (3.60) remains. However, the time-varying cornering stiffnesses are adapted using a non-linear approximation equation of the lateral wheel forces as well as the TSSAs determined by means of Eqns. (3.13) and (3.14).

Approximation of the Non-Linear Lateral Wheel Force Characteristics

Several elementary functions such as $f(\alpha) = \sqrt{\alpha}$ or rational functions have been analyzed to meet the shape of the $F_S(\alpha)$-curve of Fig. 3.11. However, the arctan(x)-function coupled with a factor including varying wheel loads best fits the reference data set, [35]

$$F_S(\alpha, F_Z, \underline{\xi}) = k_{red} \cdot \left(1 - \frac{F_Z}{\xi_1}\right) F_Z \arctan(\xi_2 \cdot \alpha) \quad . \tag{3.70}$$

The wheel force reduction factor k_{red} is added to consider the limited friction on low μ road surfaces. The lateral wheel force does not build up instantly. [80] models the setup of the lateral wheel force with a first order dynamical behavior. As it is short compared to the vehicle behavior, the time constant is neglected here.
Eqn. (3.70) depends on a two element parameter vector $\underline{\xi} = (\xi_1, \quad \xi_2)^T$. Fig. 3.14 shows four characteristic maps of a tire. The circles are measurement points of the map. The parameter for the five curves is the wheel load, starting at the bottom with $F_Z = 1.1kN$ and ending on top with $F_Z = 7.1kN$. Changes of ξ_1 and ξ_2 in Eqn. (3.70) describe different tire characteristics. In Fig. 3.14(a) the "best fit" of the approximation (solid) with respect to the reference (circles) is plotted. However, the vector $\underline{\xi}$ can be varied to model different tire characteristics:
In Fig. 3.14(b), ξ_1 was increased and ξ_2 was decreased simultaneously. For large TSSAs, the force transmission is increased compared to the reference, whereas for small α it is rather small. This is typical for a tire which has a reduced tendency for understeer at high lateral accelerations, [64].
The characteristic map of the tire in Fig. 3.14(c) represents a tire with a strong understeer tendency at high lateral accelerations. This behavior results for decreasing ξ_1 and increasing ξ_2 compared to the "best-fit values".
In Fig. 3.14(d), a tire is characterized which in general is not capable to transmit forces as well as the "best-fit tire". This behavior can be achieved by decreasing ξ_1.
The examples show how tires with different self-steering behavior can be described by variations of $\underline{\xi}$.

Optimization of ξ_1 and ξ_2 for Best-Fit

In order to achieve "best-fits" of the curves using Eqn. (3.70), the parameter vector $\underline{\xi}$ must be optimized. The goal is to determine the parameter vector $\underline{\xi}$, so that the quadratic error between approximated and real characteristic map is minimized. As the parameters in function (3.70) are non-linear, standard least squares (LS-) methods cannot be applied. Therefore, a non-linear quality function must be minimized with non-linear optimization techniques. First, the deviation between approximation F_S and reference F_{ref} is defined

$$F_r(\underline{\xi}) = F_{ref,r} - F_{S,r}(\alpha_r, F_{Z,r}, \underline{\xi}) \qquad . \tag{3.71}$$

Using Eqn. (3.70) provides

$$F_r(\underline{\xi}) = F_{ref,r} - k_{red} \cdot \left(1 - \frac{F_{Z,r}}{\xi_1}\right) F_{Z,r} \arctan(\xi_2 \alpha_r) \qquad . \tag{3.72}$$

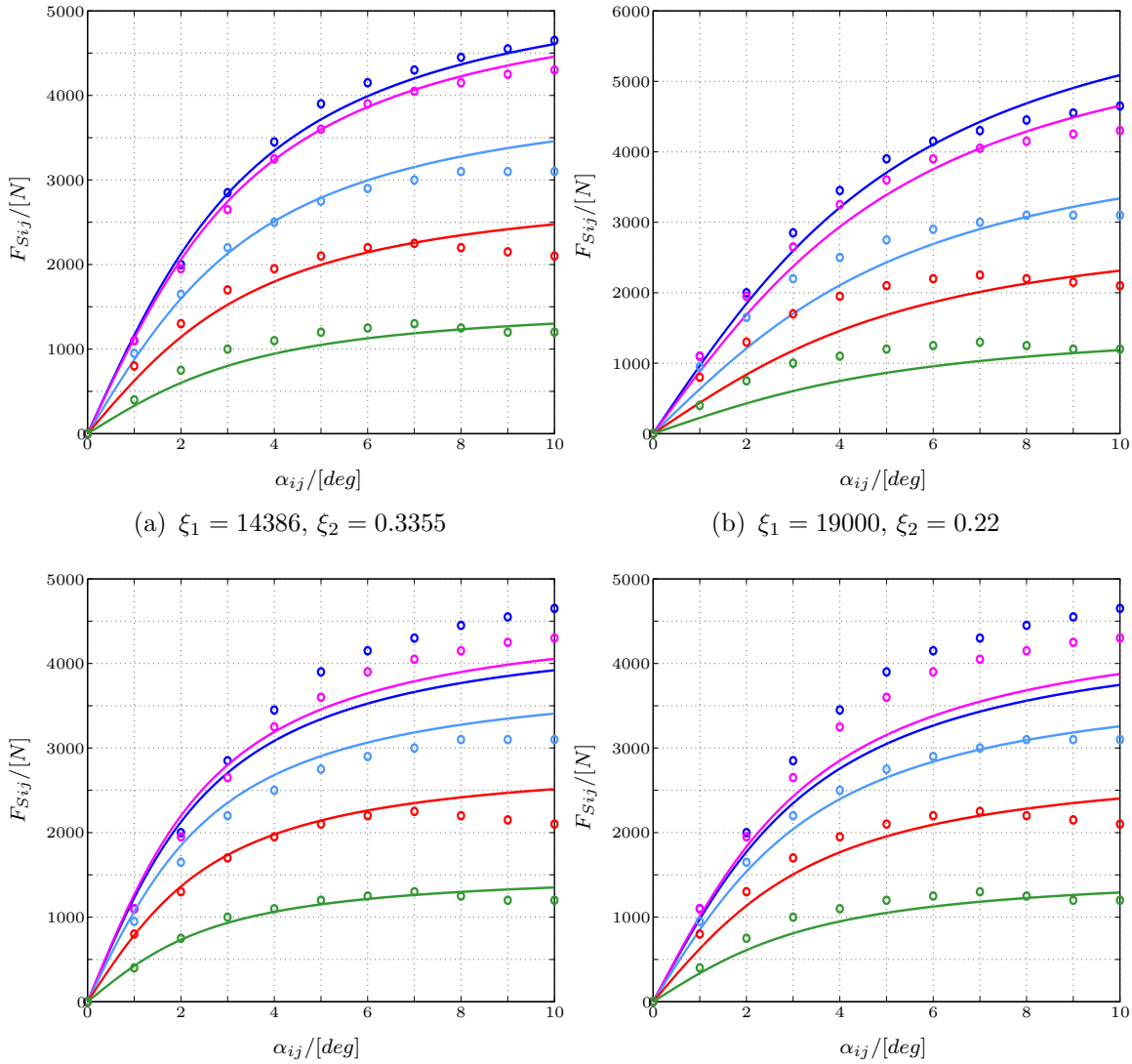

(a) $\xi_1 = 14386$, $\xi_2 = 0.3355$

(b) $\xi_1 = 19000$, $\xi_2 = 0.22$

(c) $\xi_1 = 12000$, $\xi_2 = 0.45$

(d) $\xi_1 = 12000$, $\xi_2 = 0.35$

Figure 3.14: Different tire characteristics when varying the tire parameters

$F_{S,r}$ represents the approximation for data point r $(r = 1, \ldots, N)$. $F_{ref,r}$ describes the $r-th$ value of the characteristic map of the tire to be approximated.
Next, a quality function is set up which sums up the quadratic errors in Eqn. (3.72). The optimization goal is to minimize the quality function

$$\min_{\underline{\xi}} \left\{ \sum_{r=1}^{N} \left[F_{ref,r} - F_{S,r}(\alpha_r, F_{Z,r}, \underline{\xi}) \right]^2 \right\} \quad . \tag{3.73}$$

with respect to the parameter vector $\underline{\xi}$. For the optimization, k_{red} is 1.
The Levenberg-Marquardt-Optimization, a numerical method of gra-

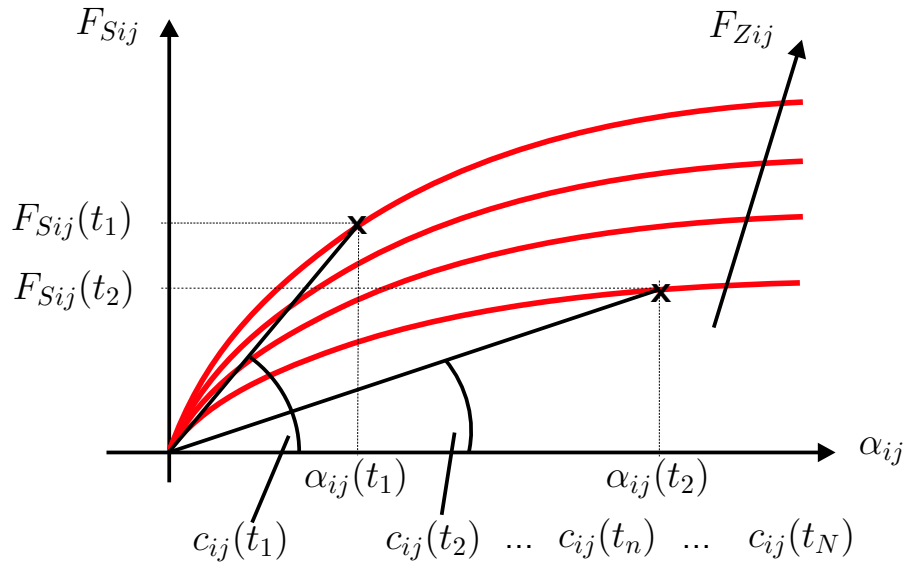

Figure 3.15: Adaptation of cornering stiffness

dient descent, was applied here to determine $\underline{\xi}$. The algorithm converges quickly and for the reference tire map of Fig. 3.14 yields $\xi_1 = 14386$ and $\xi_2 = 0.3355$.

Adaptation of the Cornering Stiffnesses

As the lateral wheel forces are the basis to describe the vehicle dynamics in curves, the non-linear and time-varying characteristics $F_S(t) = c(t) \cdot \alpha(t)$ must be approximated. To reduce the complexity of the adaptive non-linear state space model the cornering stiffnesses are adapted to the non-linear tire force characteristic in every simulation step (see Fig. 3.15)

$$c_{ij}(t) = \frac{F_{Sij}(t)}{\alpha_{ij}(t)} \quad , \tag{3.74}$$

with the F_{Sij} calculated by means of Eqn. (3.70).
[9] adapts the cornering stiffnesses with a recursive least-squares estimation (RLS-) algorithm. The method described in [4] estimates the current cornering stiffness using GPS velocity based measurements. The lateral wheel forces F_{Sij} crucial for both methods are determined from the lateral accelerations without explicitly considering wheel load changes. The approach described above is a parametric non-linear approximation equation, where the wheel load changes are included. The parameters can be adapted to a specific tire type easily.
Fig. 3.16 gives an overview over the cornering stiffness adaptation system. The changing vertical wheel force F_S as well as the TSSA α are flowing into

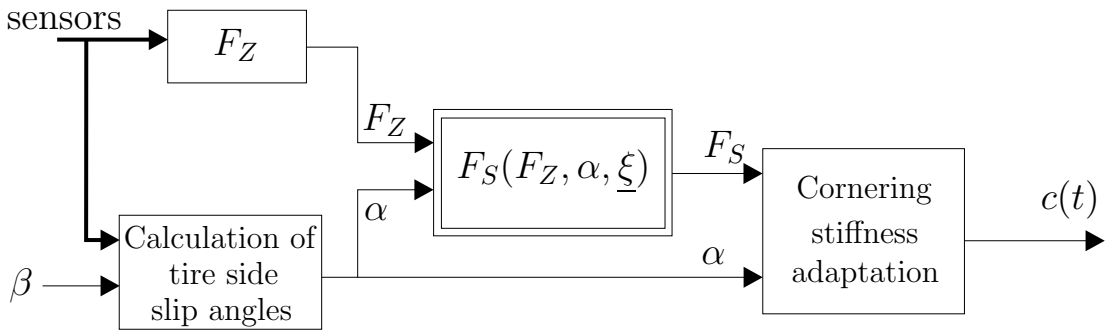

Figure 3.16: Overview of cornering stiffness adaptation

the non-linear approximation block represented by Eqn. (3.70). Here, the lateral wheel forces F_{Sij} on each individual wheel are calculated in every sampling step according to the tire characteristic map specified by the parameter vector $\underline{\xi}$. Using the tire side slip angle determined by means of existing sensor information and the estimated vehicle body side slip angle β from the last calculation step, the cornering stiffnesses can be adapted. Fig. 3.17 shows the time-varying cornering stiffnesses of a left clothoide drive. The cornering stiffnesses of the left track are dropping between $t = 2s$ and $t = 6s$ from about $50000N/rad$ (linear approximation value) to less than $10000N/rad$. This effect is caused by the increased side slip angle and even more by the wheel load shift to the outer (=right) track. In this driving situation the vehicle was understeering , therefore the cornering stiffness of the (loaded) front right wheel also decreases significantly. At the end of the drive, when the vehicle drives straight again the cornering stiffnesses return to their initial values. Fig. 3.17 points out that the decrease of lateral wheel force caused by the drop of the cornering stiffnesses influences the lateral vehicle dynamics significantly. That is the reason, why the $c_{ij}(t)$ have to be time-varying parameters for the vehicle model.

The final equation for the lateral wheel forces can now be expressed based on Eqns. (3.61) and (3.62) by considering the time-varying cornering stiffness $c_{ij}(t)$:

$$F_{SFj} = c_{Fj}(t) \cdot \left(\delta_W - \beta - \frac{l_F \cdot \dot{\psi}}{v_{CoG}} \right) \quad , \tag{3.75}$$

$$F_{SRj} = c_{Rj}(t) \cdot \left(-\beta + \frac{l_R \cdot \dot{\psi}}{v_{CoG}} \right) \quad . \tag{3.76}$$

In Eqns. (3.63) - (3.65) of the non-linear two track model the cornering

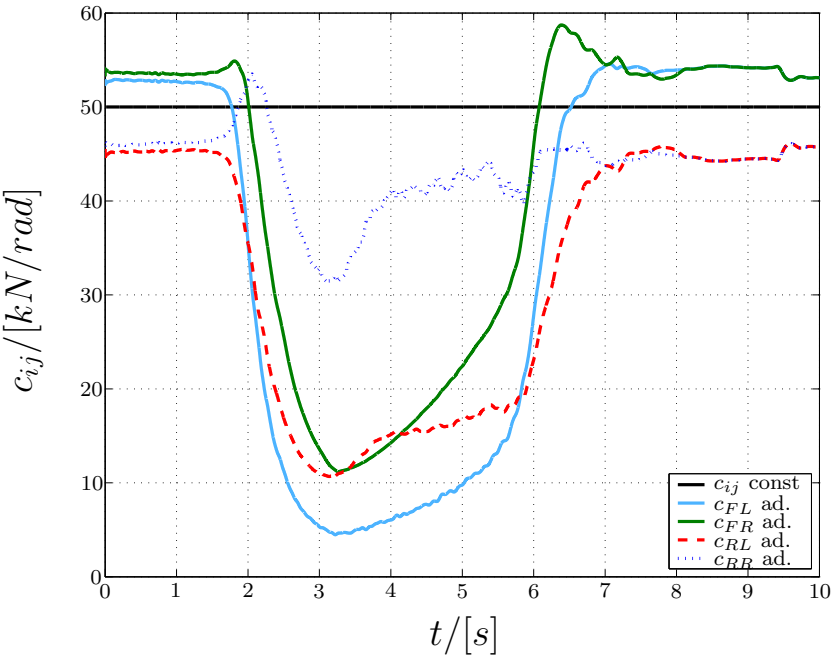

Figure 3.17: Adapted cornering stiffnesses over time for a clothoide drive

stiffnesses are adapted yielding an *adaptive* non-linear two track vehicle model.

3.5 Linear Single Track Model

Starting from the adaptive non-linear two track model the linear single track model is derived in this section. The linear single track model is also known as the "bicycle model". Several simplifications are made which limit its range of application:

- The wheels of one axle are merged to one resultant wheel. Therewith, b_F and b_R are zero. That means, wheel load changes are not considered.
- Assuming that the vehicle body side slip angle β and the wheel turn angle are small, the approximations $\sin\beta \approx \beta$, $\cos\beta \approx 1$, $\sin\delta_W \approx \delta_W$ and $\cos\delta_W \approx 1$ are applied.
- The lateral wheel forces affect in the middle of the wheel ground contact area. The casters n_{LF} and n_{LR} are zero.
- The center of gravity velocity is regarded as a constant parameter. That means: $\dot{v}_{CoG} \approx 0$. Neglecting additionally the wind force, no

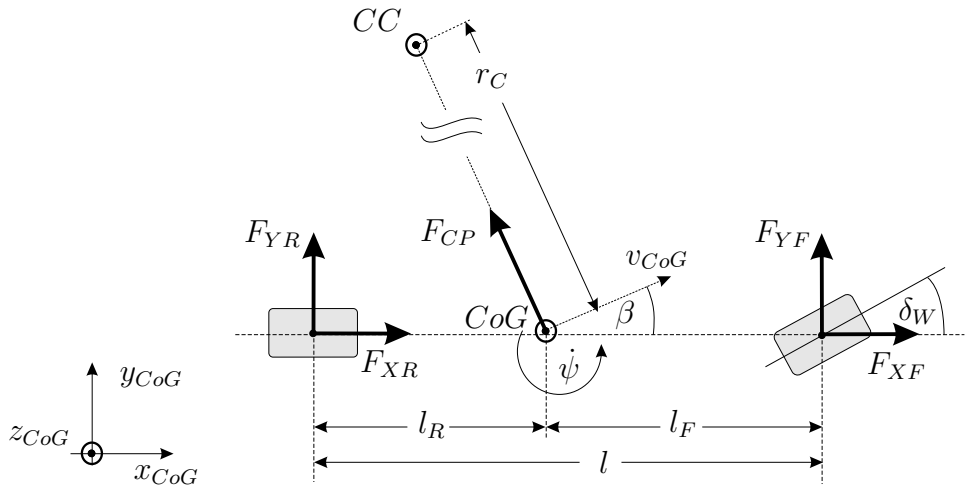

Figure 3.18: Linear single track model

forces are acting in longitudinal direction: $F_{XR} = F_{XF} = 0$. That is why the linear single track model consists only of two equations.

To describe the vehicle dynamics, the lateral force balance and the torque balance about the yaw axis are set up (see Fig. 3.18). The force balance in lateral direction is

$$m_{CoG}\dot{v}_{CoG}\sin\beta = F_{YF} + F_{YR} + F_{CP}\cos\beta \quad . \tag{3.77}$$

The wind forces F_{WX} and F_{WY} as well as the rolling resistance force F_R are neglected.
Applying the mentioned trigonometrical approximations and replacing F_{CP} (Eqn. (3.39)) provides

$$0 = F_{YF} + F_{YR} - m_{CoG} \cdot v_{CoG} \cdot (\dot{\beta} + \dot{\psi}) \quad . \tag{3.78}$$

Again, the wheel forces F_{SR} and F_{SF} must be transformed into the center of gravity coordinate system:

$$F_{YR} = F_{SR} \quad , \tag{3.79}$$

$$F_{YF} = F_{LF} \cdot \sin\delta_W + F_{SF} \cdot \cos\delta_W \approx F_{LF} \cdot \delta_W + F_{SF} \quad . \tag{3.80}$$

The lateral wheel forces are replaced with Eqns. (3.61) and (3.62). The cornering stiffnesses of the front axle c_F and of the rear axle c_R are constant. Neglecting the term $F_{LF} \cdot \delta_W$ yields

$$m_{CoG}\cdot v_{CoG}\cdot(\dot{\beta}+\dot{\psi}) = c_F\cdot\left(\delta_W - \beta - \frac{l_F\,\dot{\psi}}{v_{CoG}}\right)+c_R\cdot\left(-\beta + \frac{l_R\,\dot{\psi}}{v_{CoG}}\right) . \tag{3.81}$$

Isolating $\dot{\beta}$ leads to

$$\dot{\beta} = -\frac{c_F + c_R}{m_{CoG}\, v_{CoG}} \cdot \beta + \left(\frac{c_R l_R - c_F l_F}{m_{CoG}\, v_{CoG}^2} - 1 \right) \cdot \dot{\psi} + \frac{c_F}{m_{CoG}\, v_{CoG}} \cdot \delta_W . \quad (3.82)$$

The second differential equation for $\dot{\psi}$ is derived by means of the torque balance about the z_{CoG}-axis (see also Fig. 3.18)

$$J_Z \cdot \ddot{\psi} = l_F \cdot F_{YF} - l_R \cdot F_{YR} \quad . \quad (3.83)$$

Here, the wheel forces are also replaced with Eqns. (3.79) and (3.80). Again $F_{LF} \cdot \delta_W$ is not considered and $\ddot{\psi}$ is isolated providing

$$\ddot{\psi} = \frac{c_R l_R - c_F l_F}{J_Z} \cdot \beta - \frac{c_F l_F^2 + c_R l_R^2}{J_Z v_{CoG}} \cdot \dot{\psi} + \frac{c_F l_F}{J_Z} \cdot \delta_W \quad . \quad (3.84)$$

In order to set up a state space model, the vehicle body side slip angle β and the yaw rate $\dot{\psi}$ are defined as the state space vector

$$\underline{x} = \begin{bmatrix} \beta \\ \dot{\psi} \end{bmatrix} \quad .$$

The time derivative of $\underline{x}$ is described by the two differential equations (3.82) and (3.84) which yields the vector differential equation

$$\dot{\underline{x}} = \begin{bmatrix} -\frac{c_F + c_R}{m_{CoG}\, v_{CoG}} & \frac{c_R l_R - c_F l_F}{m_{CoG}\, v_{CoG}^2} - 1 \\ \frac{c_R l_R - c_F l_F}{J_Z} & -\frac{c_F l_F^2 + c_R l_R^2}{J_Z v_{CoG}} \end{bmatrix} \cdot \underline{x} + \begin{bmatrix} \frac{c_F}{m_{CoG}\, v_{CoG}} \\ \frac{c_F l_F}{J_Z} \end{bmatrix} \cdot \delta_W \quad . \quad (3.85)$$

Eqn. (3.85) represents a linear state space model

$$\dot{\underline{x}} = \underline{A}(v_{CoG}) \cdot \underline{x} + \underline{B}(v_{CoG}) \cdot u$$

with

$$\underline{A}(v_{CoG}) = \begin{bmatrix} -\frac{c_F + c_R}{m_{CoG}\, v_{CoG}} & \frac{c_R l_R - c_F l_F}{m_{CoG}\, v_{CoG}^2} - 1 \\ \frac{c_R l_R - c_F l_F}{J_Z} & -\frac{c_F l_F^2 + c_R l_R^2}{J_Z v_{CoG}} \end{bmatrix} \text{ and } \underline{B}(v_{CoG}) = \begin{bmatrix} \frac{c_F}{m_{CoG}\, v_{CoG}} \\ \frac{c_F l_F}{J_Z} \end{bmatrix}.$$

The wheel turn angle δ_W is the only input variable and β and $\dot{\psi}$ are the two state space variables. The velocity v_{CoG} is a time-varying parameter. The only measurable output variable is the yaw rate. The output equation is therefore

$$y = \dot{\psi} = \underbrace{\begin{bmatrix} 0 & 1 \end{bmatrix}}_{\underline{C}} \cdot \begin{bmatrix} \beta \\ \dot{\psi} \end{bmatrix} = \underline{C} \cdot \underline{x} \quad . \quad (3.86)$$

The linear single track model will be needed as a reference model to detect critical driving situations in Chapter 4.

3.6 Validation of the Vehicle Models

The vehicle models are the basis for the reconstruction of the vehicle motion. Section 5.4 presents approaches for the model based determination of the vehicle body side slip angle. The quality of these model based approaches significantly depends on the accuracy of the underlying vehicle models. Therefore, this section validates the adaptive non-linear two track and the linear single track vehicle model. Measured input quantities are applied to the models. The modeled state variables are simulated and afterwards compared to the measured reference. The in- and output quantities $\underline{u}$ and $\underline{y}$ are measured, the state variables $\underline{x}$ are usually unknown. The model is simulated with the very same input values than the process. Additionally, it depends on the initial state $\underline{x}_0$ of the state variables. As the process state variables and their initial values are unknown, process and simulation start with different values $\underline{x}_0$ and $\underline{x}_{s,0}$. Therefore, even if the model described the process exactly, the state variables of the model and the process would deviate.
For the validation, though, measurement values for the state variables are existing. The initial value of these reference measurements can be chosen for the model as well. Then, the vehicle model and the real vehicle dynamics start in the very same state and the modeled and measured signals can be compared in order to assess the model quality.

3.6.1 Test Drives

Three test drives described here are exciting the dynamics of the vehicle. Sinusodial changes of the steering angle cause a *slalom drive* of the car. The test drive was carried out at medium velocity. The test drive therefore is a mixture of exciting the lateral and longitudinal vehicle dynamics. Secondly, a *clothoide with high dynamics* excites the lateral dynamics up to the stability limit of the car. The last test drive is a *straightforward drive* to analyze the simulation quality of the longitudinal vehicle dynamics.

Slalom Drive

Fig. 3.19 shows the wheel turn angle δ_W, the velocity v_{CoG}, vehicle body side slip angle β and the yaw rate $\dot{\psi}$. As the wheel turn angle and the vehicle body side slip angle range between $-1°$ and $+2°$, the simplifications of the linear single track model should not be too severe. Therefore, this test drive appears to be adequate to validate the single track model.

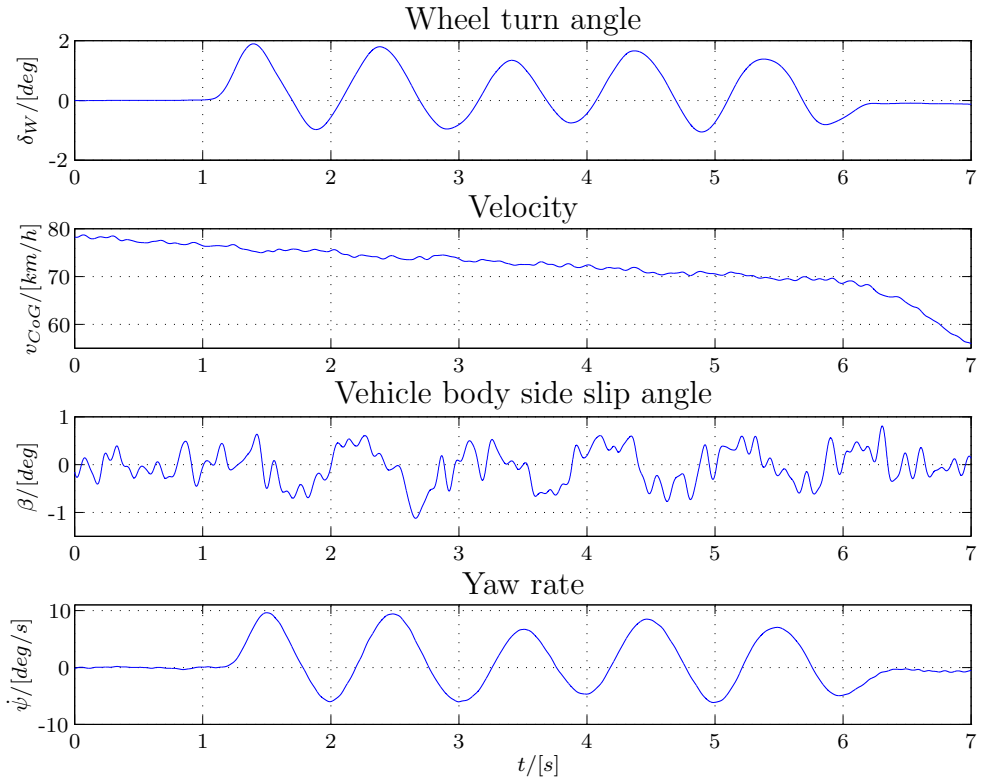

Figure 3.19: Measured signals of the slalom drive

Clothoide with High Dynamics

A clothoide driving maneuver is a test drive, where the curvature increases linearly with the traveled distance, [53]. For small velocities, this is equivalent to equally increasing the steering wheel angle until a steady final value. For the high dynamical clothoide, the wheel turn angle is increased until its maximum value within only $1.5s$. With a certain delay, the vehicle body side slip angle increases up to as much as 15° (Fig. 3.20). The wheels of the inner track almost lose road contact. The rough trajectory of the test drive can be seen in Fig. 3.21 for clarification. This test drive describes a driving situation right at the stability limit and therefore is appropriate to test, whether the vehicle models are sufficiently accurate for accident detection and reconstruction.

3.6.2 Simulation of the Linear Single Track Model

Describing the lateral vehicle dynamics with the linear single track model requires several simplifications (see Section 3.5). Among others, small values for the wheel turn angle δ_W and for β are pre-assumed.
First, the linear single track model is analyzed by means of the slalom drive described in Section 3.6.1. Fig. 3.22 compares the simulated and the

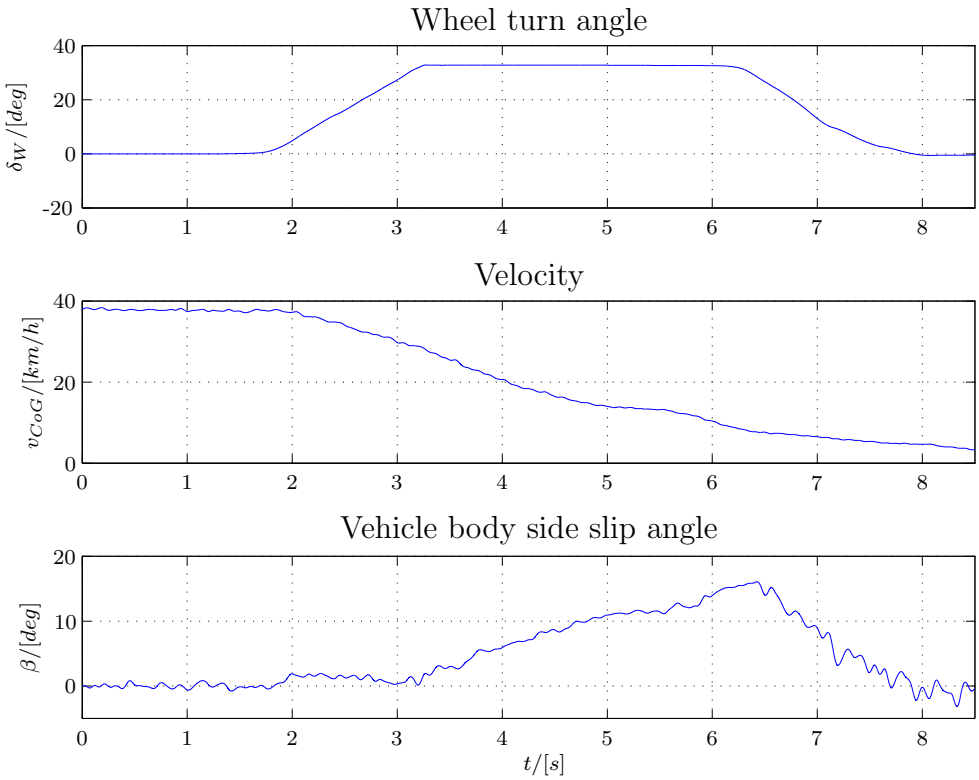

Figure 3.20: Measured signals for the clothoide drive with high dynamics

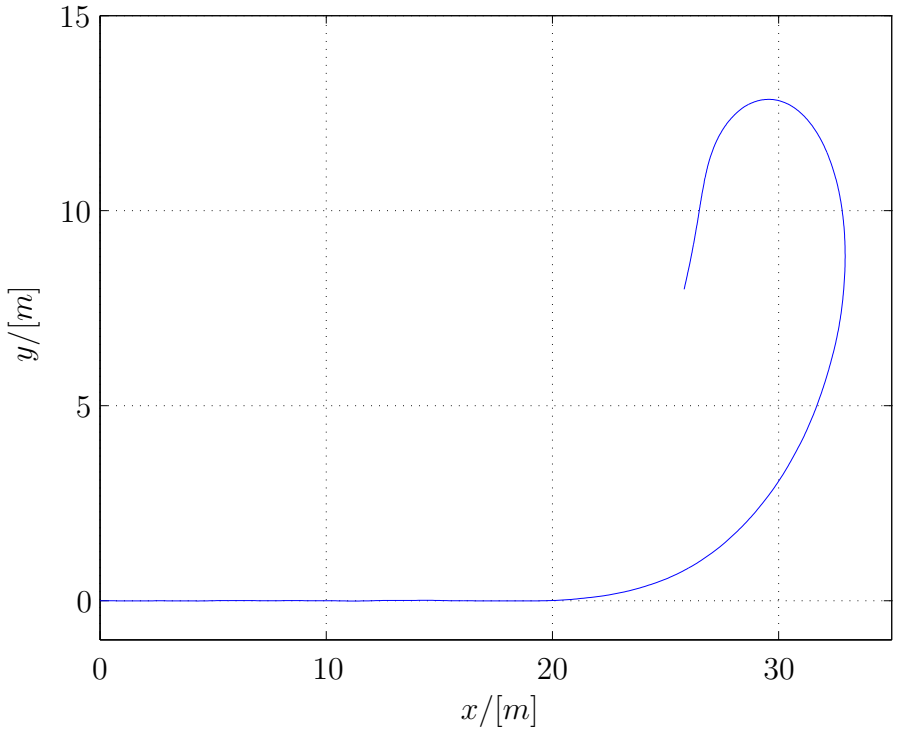

Figure 3.21: Trajectory of a clothoide drive with high dynamics

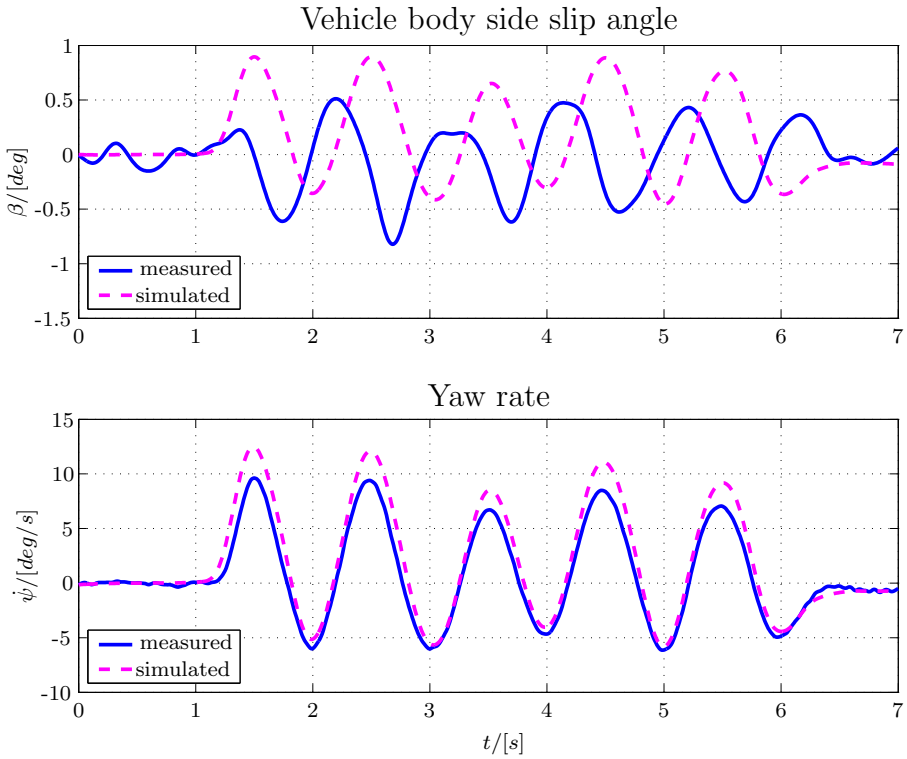

Figure 3.22: Simulation of the slalom drive with the linear single track model

measured signals for the state variables β and $\dot{\psi}$. The measured signal of the vehicle body side slip angle was filtered with a third order BUTTERWORTH Low-pass Filter (cut-off frequency: $f_C = 2.5$ Hz). On principal, the modeled yaw rate signal (bottom) and its measured reference are similar. The model provides maxima, which are about 25% too large. The side slip angle simulations (top) are significantly worse. Here, the modeled and measured signals deviate abundantly clear. The basic characteristics of the signal are different. There is an offset and a phase delay between modeled and measured signal. The maxima and minima of side slip angle and yaw rate show noticeable correlation. All in all, the simulated vehicle body side slip angle matches the reference unsatisfactory even though δ_W and β are small.

The deviations are even more obvious for the second test drive employed here, the clothoide drive with high dynamics (Fig. 3.23). Initially, the simulated yaw rate increases too fast and slightly decreases after circa $t = 3.2s$, while the real value is still growing. The deviations for β are even more severe. The vehicle body side slip angle builds up too fast. Especially at the beginning of the test drive, the results are unacceptable.

The simulation results of both test drives show that the linear single track model cannot describe the lateral dynamics with sufficient accuracy. The

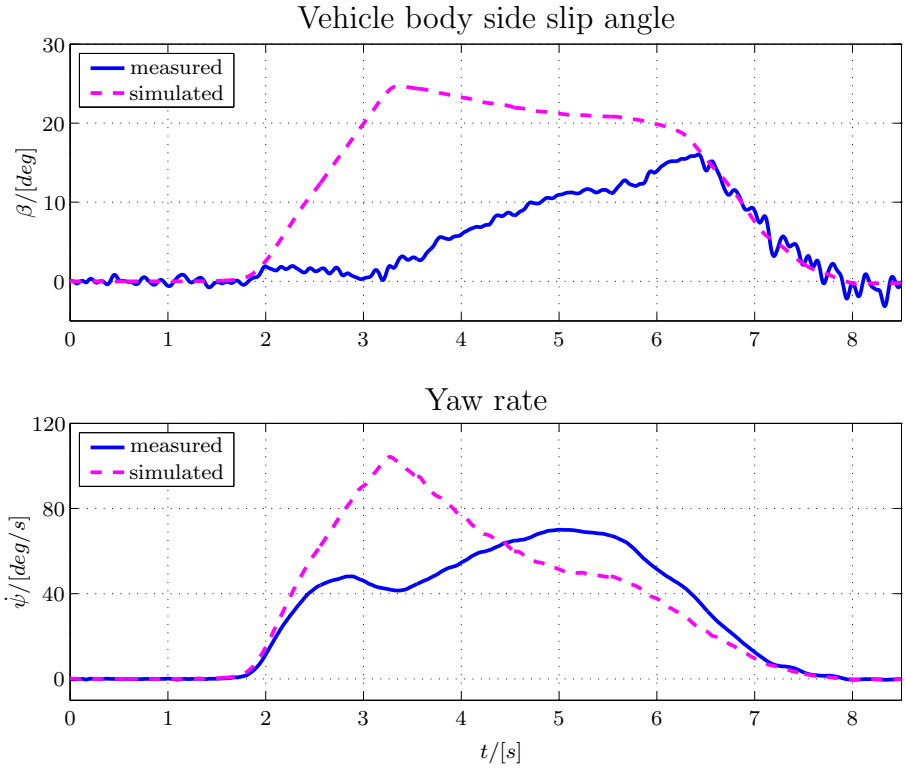

Figure 3.23: Simulation of the linear single track model for a high dynamical clothoide drive

detection and reconstruction of pre-crash situations or the design of a state space observer require a model which is much more accurate.

3.6.3 Simulation of the Non-Linear Two Track Model

Constant Cornering Stiffnesses

Initially, the non-linear two track model is simulated with the clothoide of high dynamics. First, the cornering stiffnesses are kept constant. Fig. 3.24 shows the simulation results. Similar to the bicycle model, the modeled yaw rate $\dot{\psi}$ increases too fast and reaches too high values. The side slip angle also increases too fast, converges against the reference value at the end, though. The velocity is also too large.
As the cornering stiffnesses were kept constant, a linear relation between the tire side slip angle α and the lateral wheel force F_S was presumed (Eqn. (3.60)). This assumption is only valid for small wheel load changes and little values of α. However, this measurement drive was carried out at the stability limit of the car. Therefore, the linear relationship surely is not fulfilled any more. In the following, the effects of cornering stiffness adaptation are analyzed.

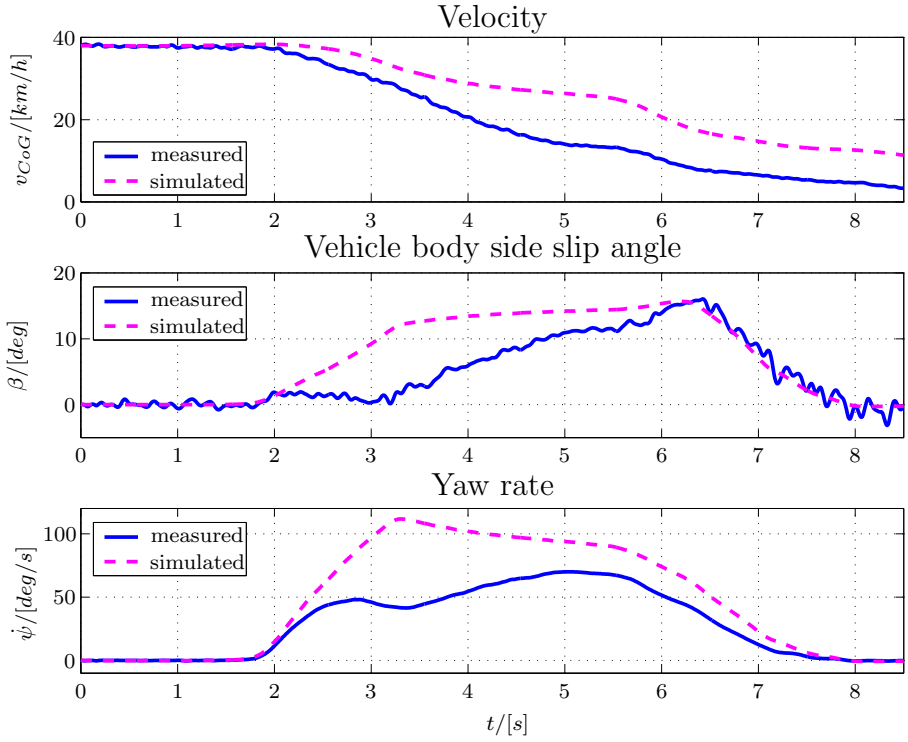

Figure 3.24: Simulation of the non-linear two track model with constant cornering stiffnesses for the clothoide drive with high dynamics

Adapted Cornering Stiffnesses

The adaptation of the cornering stiffnesses requires the calculation of the tire side slip angles α_{ij} and the current vertical wheel forces F_{Zij}. The vertical wheel force approximation was already validated in Section 3.3.4. Knowing the vertical wheel forces F_{Zij} and the α_{ij}, the lateral wheel forces are approximated with Eqn. (3.70). Finally, the cornering stiffnesses are adapted according to Eqn. (3.74). Fig. 3.25 shows that the theoretical side forces are more than 500% too large when using constant cornering stiffnesses. Adapting the cornering stiffnesses provides much better approximations for the lateral wheel forces of the front axle. Using these improvements, the simulation accuracy of the adapted non-linear state space model is much better. Fig. 3.26 shows the three state variables with and without parameter adaptation and with the measured reference.
Adapting the cornering stiffnesses yields very much better results, especially for the vehicle body side slip angle and the yaw rate. The simulated velocity is improved as well, however still too large. All in all, the adapted non-linear state space model is accurate enough to describe the lateral dynamics up to the stability limit of the vehicle.

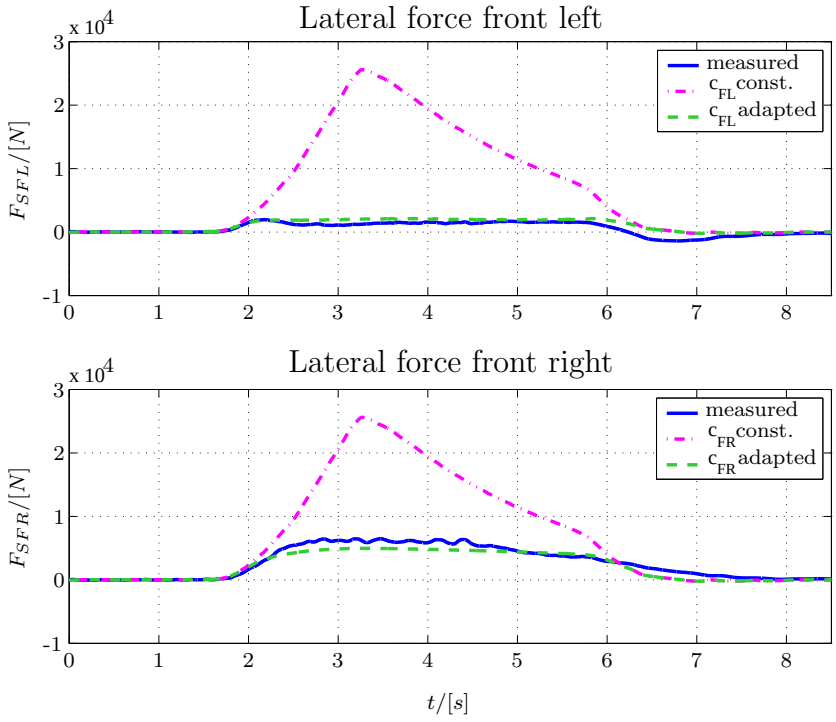

Figure 3.25: Comparison of side forces with and without adaptation of the cornering stiffnesses with the measured reference for the clothoide with high dynamics

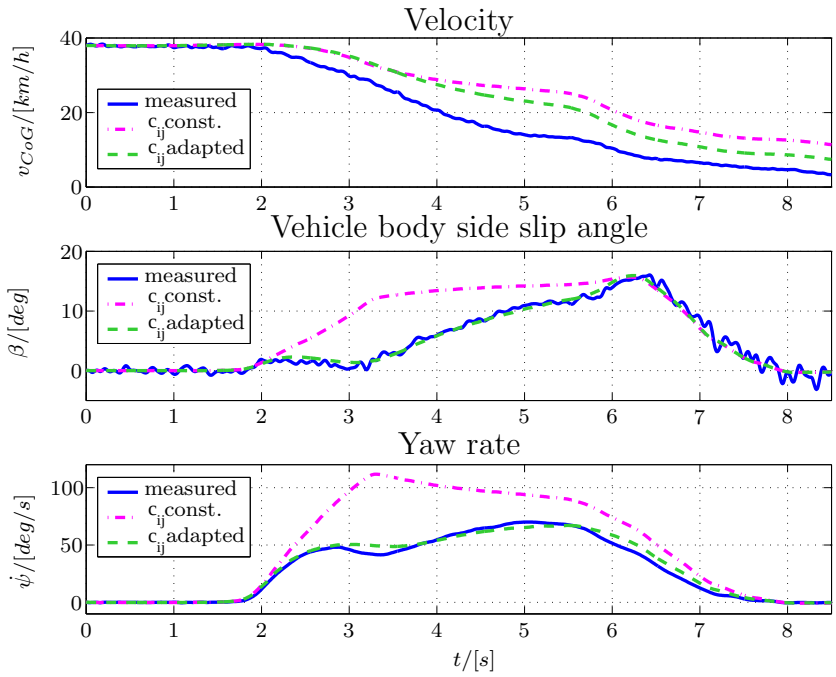

Figure 3.26: Effect of cornering stiffness adaptation on the simulation accuracy for a clothoide of high dynamics

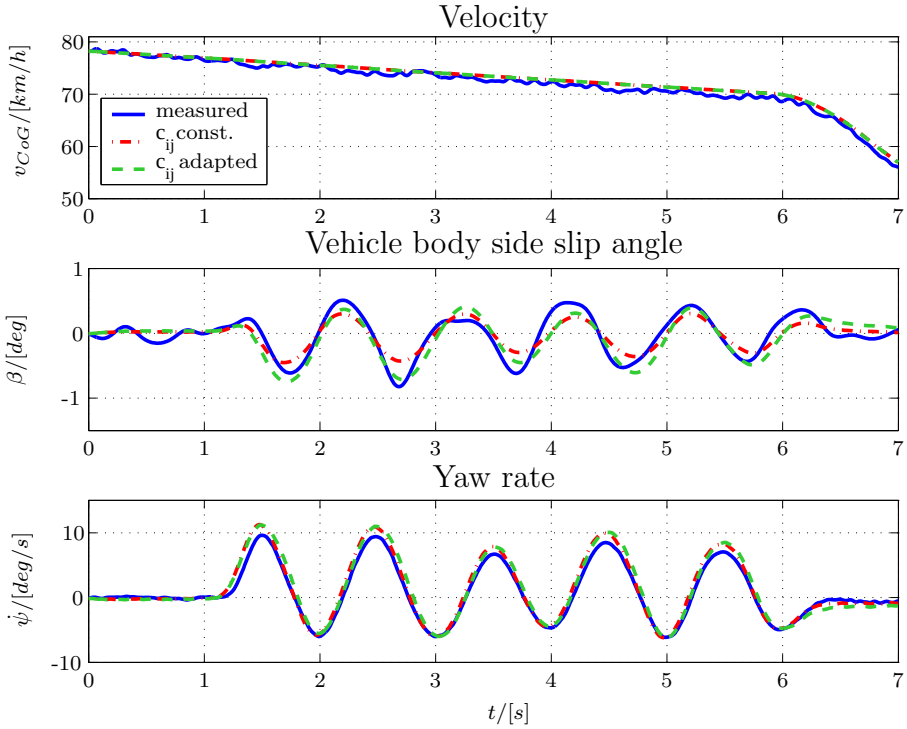

Figure 3.27: Simulation of the non-linear two track model with constant and with adapted cornering stiffnesses for a slalom drive

Simulation of a Slalom Drive

Fig. 3.27 shows the results of the simulation of the slalom drive with and without adaptation of the cornering stiffnesses. The velocity and the yaw rate are practically not influenced by parameter adaptation. That is why the respective curves are covering each other. Only the amplitude of the vehicle body side slip angle approaches the one of the measured reference. The improvements are slight, though, as during the slalom drive only small wheel turn angles were applied. That means, the tire side slip angles were moderate as well. Therefore, the tire behavior remains linear and the adaptation is not necessary any more.

Simulation of a Straightforward Drive

The straightforward drive was chosen to validate the longitudinal dynamics of the vehicle model. Fig. 3.28 shows that the vehicle was accelerated up to 50 km/h. Afterwards, the car brakes down again to almost standstill. The driver was not steering at all. Therefore, the vehicle body side slip angle and the yaw rate are almost zero. The figure shows, that the vehicle model describes the longitudinal dynamics (i.e. the velocity v_{CoG}) very accurately. The modeled and the measured velocities can hardly be distinguished. The

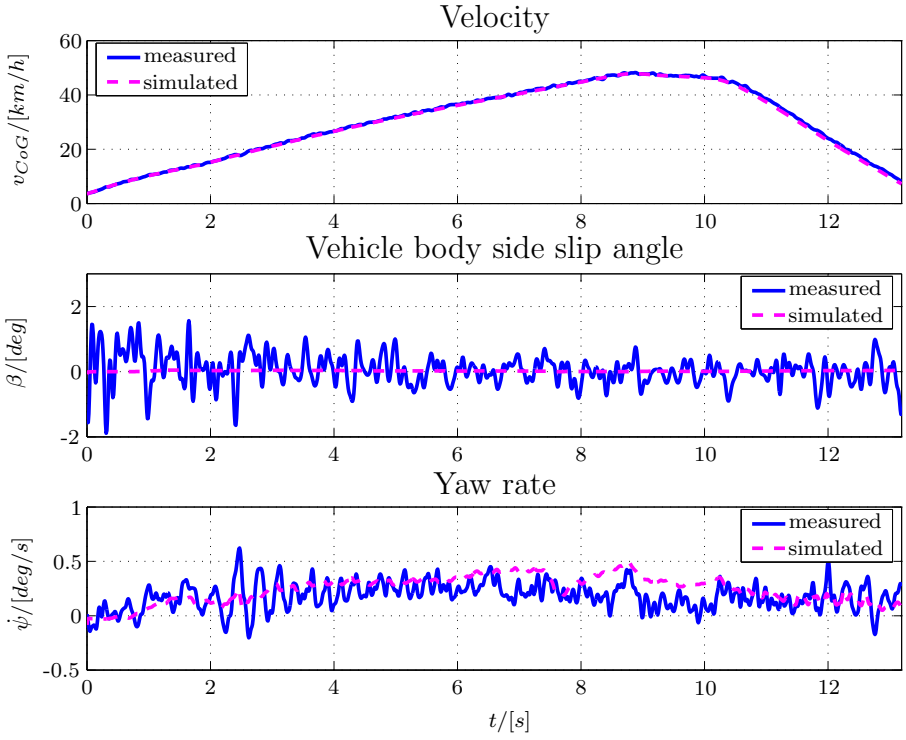

Figure 3.28: Simulation of the non-linear two track model for a straightforward drive

yaw rate and the vehicle body side slip angle as measures for the lateral dynamics are also correctly calculated. That means, that also for straightforward drives with small lateral excitation the vehicle model provides very good results.

3.7 Conclusion

In Chapter 3 a wheel force model was presented which calculates the longitudinal and lateral wheel forces on basis of the slip. Thereby, a friction model of BURCKHARDT was employed as a compromise between complexity and approximation accuracy. The tire side slip angles are calculated on basis of a linear model.
Afterwards, the motions of the vehicle body were regarded. For accident reconstruction purposes, though, the vehicle motion in plane is most important. Therefore, the focus of this chapter was the derivation of a non-linear two track state space model. As a basic condition, the model should be kept as simple as possible. Therefore, the input variables were limited to the longitudinal wheel forces and the wheel turn angle. To gain satisfactory accuracy, several time-varying parameters must be adapted. The most important parameters are the cornering stiffnesses. With a non-linear ap-

proximation equation considering varying wheel loads, the cornering stiffnesses are adapted in every calculation cycle of the model. The state space model therefore is non-linear *and* adaptive.
In a next step, the adaptive non-linear two track model was simplified to the well known linear single track (or "bicycle") model.
Both the bicycle model and the (adaptive) non-linear two track model were validated with several test drives. The presented simulation results show that the linear single track model is not capable to describe the lateral vehicle dynamics with sufficient accuracy. For test drives close to the stability limit, both state variables of the model are significantly too high compared to the measured reference. State space observers or other approaches to reconstruct the vehicle motion in an instable pre-crash situation require a very exact vehicle model. The linear model is not sufficiently accurate for these purposes.
Compared to the linear single track model, the non-linear two track model provides a much more accurate vehicle description, particularly of the lateral dynamics. Regarding all four wheels allows to consider load changes. Linearizations are not necessary here. Adaptation of the cornering stiffnesses is a crucial improvement for the model performance. All in all, the adaptive non-linear model is more complex. However, the vehicle dynamics can be described up to the stability limit which is the basis for reconstructing the pre-crash phase of a road traffic accident.

4 Detection and Classification of Pre-Accident Situations

A model based event data recorder records data continuously and saves it in a circular buffer. After a certain time, when the storage capacity of the memory is reached, the memory management starts writing at the beginning of the buffer again. That means, it overwrites the data already stored in the memory.
The time before an accident is crucial for accident reconstruction. Knowing the vehicle and driver behavior provides information about the cause of the accident. Therefore, a major task of an EDR is to guarantee that the crucial information of the pre-accident phase is stored in a memory. To define the beginning of the time period which must not be overwritten any more, a robust accident detection mechanism has to be developed.
Existing event data recorders use the longitudinal acceleration signal a_X. If it exceeds a certain predefined threshold (for instance $a_X > 2g$, [19]), the system suspends overwriting existing data.
The system presented here additionally regards laterally critical driving situations (oversteer, understeer, sliding, etc.) occurring before the crash event. This is advantageous because the system not only detects but also classifies a driving situation. Therefore, the behavior of car and driver in the pre-crash phase can be assessed. Secondly, accidents resulting from a laterally critical driving situation are of special interest for reconstruction. Such accidents mainly occur on country roads, they are characterized by a significantly increased fatality rate, the victims are often young drivers, [57], [59]. Furthermore, there are often no witnesses, as single car accidents are over proportional for this accident type. For these accidents, it is advantageous to use model based detection strategies. Then, if a few seconds before the freezing signal are stored in the memory additionally, the complete critical pre-accident phase crucial for accident reconstruction is recorded as well. Conventional systems detecting an accident by means of the longitudinal acceleration need much more memory to capture the whole pre-accident phase, because the trigger signal is usually generated at a later point of time.

Before a detection and classification methodology can be presented, the term "critical driving situation" must be defined. First of all, "critical situation" in this chapter means *laterally* critical situations. The longitudinal dynamics is of less importance in this context, as the freezing problematic can be solved by applying intelligent acceleration thresholds. Therefore, in this chapter not the braking performance but only the vehicle reaction on steering inputs is regarded. A widespread approach defines a laterally critical situation, if the vehicle behavior deviates significantly from the driver's driving experience (see for instance [55], [68], [75], [76] and others). A driver is capable to manage and control the lateral vehicle behavior without problems, if the vehicle reacts proportional to the driver's steering desire. The driver applies a certain steering angle and anticipates that the vehicle will react with a certain yaw rate, that means with a specific cornering behavior. If the vehicle reaction is too weak or too strong, the driving situation deviates from the driver's desire and anticipation. The situation might become uncontrollable for the driver and lead to an accident. The "proportional" vehicle behavior is described by the linear single track model (see Section 3.5), as 85% of all drivers drive their car within a lateral acceleration band of $\pm 0.3g$, [77]. Even standard microprocessors can calculate this linear reference model in real-time. Real-time operation is a crucial basic condition for the model based detection of accidents by means of event data recorders. Comparing the real vehicle behavior measured by sensors with linear reference models is the underlying idea for the detection methodologies presented in this chapter.

Modern vehicle control systems (known as ESP, VDC, DSC, etc.) additionally assess the reliability of the employed sensors to detect sensor failures, [9], [16]. However, in this chapter, sensor failures are not explicitly considered. In fact, four different methods basing on different sensor configurations are presented to detect and categorize critical driving situations. According to the respective driving situation, different methods detect a critical situation earlier or later and more or less reliably. In order to increase robustness, a "two-of-four" strategy is implemented: if two out of these four methods detect an accident situation then the freezing of data in an EDR is triggered. As mentioned, freezing thereby means that a certain amount of seconds *before* the calculated trigger event, data must not be overwritten any more. The "two-of-four" strategy reduces false triggering caused by single sensor errors.

The model based accident detection system automatically recognizes, if a potentially critical driving situation was defused by the driver. Then, the vehicle state will sooner or later converge to the linear vehicle behavior again. If no accident has occurred, the system deletes the triggering event

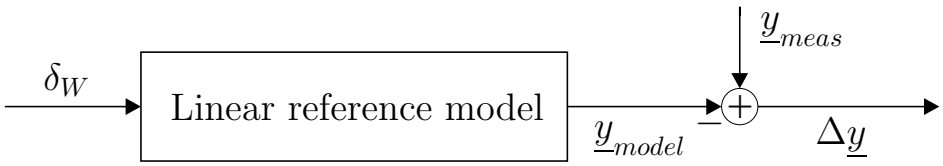

Figure 4.1: Classification of driving situations by assessing the deviation from a linear reference model

and the data acquisition continues as if nothing had happened.
In Section 4.1 the discrete stability index (DSI) will be introduced to categorize the driving situation. Afterwards, in Sections 4.1.1 - 4.1.4 the four detection methods are explained. Section 4.1.5 compares these methods. An extension of the discrete stability index approach is presented in Section 4.2 yielding the definition of the continuous stability index (CSI). Afterwards, the methods are fused and the integration in the event data recorder is described in Section 4.3.

4.1 Discrete Stability Index to Assess Driving Situation

All the detection methods described in Chapter 4 contain the wheel turn angle as an input variable. Based on the wheel turn angle straightforward driving is distinguished from cornering. The measured signals $\underline{y}_{meas}$ are afterwards compared to a quantity $\underline{y}_{model}$ calculated with equations basing on a linear reference (see Fig. 4.1). The deviation $\Delta\underline{y}$ between measured and modeled quantities can be used to categorize the driving situation. In the following, six driving situations describing different driving behavior are distinguished by means of threshold evaluation. The thresholds are fixed for dry road conditions, as most of the available measurement data sets were recorded on such surface. Furthermore, the underlying considerations assume constant self-steering properties of the test cars. Evaluating the thresholds, a discrete number is assigned to each of these driving situations, the so called discrete stability index (Table 4.1).

Stable straightforward A stable straightforward drive is characterized by a very small absolute value $|\delta_W|$ of the wheel turn angle causing model quantities $\underline{y}_{model}$ similar to the measured values $\underline{y}_{meas}$. Then, the discrete stability index becomes "1".

Driving situation	Discrete Stability Index
Stable straightforward	1
Stable cornering	2
Instable straightforward	3
Understeer	4
Oversteer	5
Breakout	6

Table 4.1: Assessment of driving situations with the discrete stability index

Stable cornering If the absolute value $|\delta_W|$ of the wheel turn angle ranges above a certain threshold (i.e. indicates cornering) and additionally the measured output quantities range within a tolerance band around the modeled output quantities, then the driving situation is assessed "stable cornering". The discrete stability index is "2".

Instable straightforward In this driving situation, the measured quantities $\underline{y}_{meas}$ do not range within a tolerance band around the modeled quantities $\underline{y}_{model}$, although the steering wheel angle is small indicating straightforward driving. In this case, the discrete stability index "3" is assigned. Braking situations on μ-split road surface are typical for this behavior. Here, the adhesion coefficients of left and right track are different. Braking on such ground results in a yaw motion caused by different braking forces, although the wheel turn angle is zero.

Understeer Understeer describes a driving situation where the measured vehicle reaction to a steering input δ_W is not as strong as expected by the driver. A car is understeering, if the adhesion limit at the front axle is exceeded. Caused by high lateral accelerations, the required side force F_S (Eqn. (3.70)) cannot be transmitted to the ground any more. The vehicle "shifts" out of the curve (Fig. 4.2(a)). Understeer behavior can be described as follows:

$$|y_{model}| \geq |y_{meas}| \quad . \tag{4.1}$$

Discrete stability index "4" is assigned to understeer behavior.

Oversteer If the measured vehicle reaction exceeds the driver's expectation, then the vehicle oversteers. Oversteer is caused by loss of adhesion on

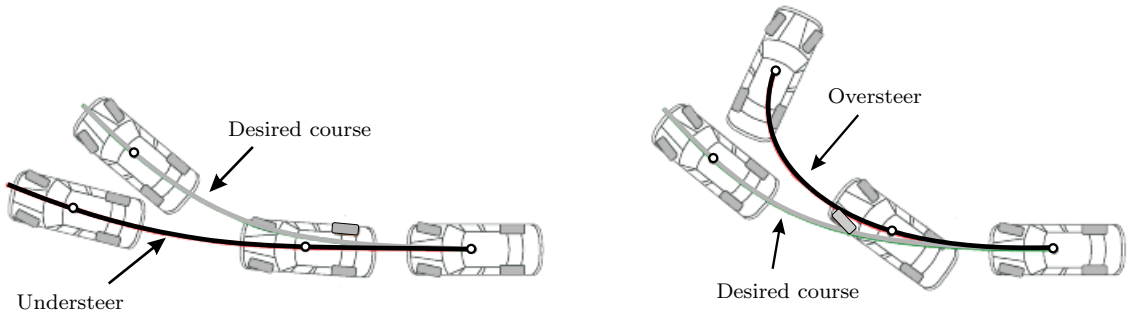

(a) Understeer (b) Oversteer

Figure 4.2: Comparison of desired curve drive with understeer and oversteer

the rear axle. The lateral force F_S on the rear axle cannot be transmitted to the ground any more. The rear end of the car slips away (Fig. 4.2(b)). This critical situation is usually more severe than understeer and can be described by

$$|y_{model}| \leq |y_{meas}| \quad . \tag{4.2}$$

For oversteer behavior, "DSI=5" was chosen.

Breakout Vehicle breakout is a more severe driving situation than the ones described before. In this situation, the vehicle reaction is hardly controllable for the driver and may even behave opposite to the driver's anticipation. In such situations, the measured quantities can have opposite algebraic sign than the results gained from the reference model. The car can often only be stabilized by counter-steering. Breakout is characterized by a discrete stability index "6".

4.1.1 Yaw Gain Method

Theoretical Background

The range of experience of average drivers can be described with the linear single track model (Section 3.5). The modeled system output $\underline{y}_{model}$ is the yaw rate $\dot{\psi}_{model}$, Eqn. (3.86). The difference between the measured and the modeled yaw rate signal

$$\Delta\dot{\psi} = \dot{\psi}_{meas} - \dot{\psi}_{model} \tag{4.3}$$

is evaluated and represents the basis of the yaw gain method. The basic problem is the proper definition of thresholds for $\Delta\dot{\psi}$. The most practical

method is to evaluate test drives of average drivers. [68] has carried out a variety of tests on dry, icy and snowy road surface with five test persons. One of the results is that constant threshold values can be utilized as a criterion independent from lateral accelerations or from the vehicle velocity. As the amount of test drives available for this thesis was limited, this fact could not be checked with an own measurement campaign. However, assuming that the construction of modern vehicles and its tires do not provide completely different vehicle behavior than described in [68], the following thresholds $\Delta\dot{\psi}_u$ and $\Delta\dot{\psi}_l$ for the yaw rate deviation $\Delta\dot{\psi}$ can be defined:

- Yaw reaction stronger than expected by the driver:
  $\Delta\dot{\psi} > 0,\ \Delta\dot{\psi}_u = 0,05\frac{rad}{s}$
- Yaw reaction smaller than expected by the driver:
  $\Delta\dot{\psi} < 0,\ \Delta\dot{\psi}_l = 0,05\frac{rad}{s}$

These thresholds define, at which yaw rate difference the driver senses the situation as critical. The two quantities $\Delta\dot{\psi}_u$ and $\Delta\dot{\psi}_l$ define the maximum and minimum yaw rate value of the tolerance band around the model yaw rate:

$$\dot{\psi}_{max}(t) = \dot{\psi}_{model}(t) + \Delta\dot{\psi}_u \quad , \tag{4.4}$$

$$\dot{\psi}_{min}(t) = \dot{\psi}_{model}(t) - \Delta\dot{\psi}_l \quad . \tag{4.5}$$

If the measured yaw rate exceeds the tolerance band, a critical situation is assumed. This means, for instance for a left curve with $|\delta_W| > \delta_{W,th} = 0.5°$: if the measured yaw rate $\dot{\psi}_{meas}$ is larger than $\dot{\psi}_{max}$, the vehicle is oversteering (DSI=5). If $\dot{\psi}_{meas}$ falls below $\dot{\psi}_{min}$, the vehicle understeers (DSI=4). For a breakout in a right curve (DSI=6), the driver steers to the left to re-stabilize the car. Then, the car is in a curve ($|\delta_W| > \delta_{W,th}$), the measured yaw rate exceeds the tolerance band and additionally has opposite direction compared to the model yaw rate.
The relations to categorize the driving situations can be found in Table 4.2.

Assessment of a Measurement Drive

After describing the yaw gain method by simulations, the method shall be validated with measurements. The measurements were conducted with a Ford Scorpio (see Appendix D.1) or with an Opel Vita (Appendix D.2). Fig. 4.3(a) shows the course of the drive for better understanding. It is a J-Turn maneuver where the vehicle rear breaks out on low μ suface. The

δ_W	$\dot{\psi}_{model}$	$\dot{\psi}_{meas}$	DSI
Straightforward			
$\lvert\delta_W\rvert < \delta_{W,th}$	$\dot{\psi}_{model} \approx 0$	$\dot{\psi}_{min} < \dot{\psi}_{meas} < \dot{\psi}_{max}$	1
		$\left(\dot{\psi}_{meas} \geq \dot{\psi}_{max}\right) \vee \left(\dot{\psi}_{meas} \leq \dot{\psi}_{min}\right)$	3
Left curve			
$\delta_W \geq \delta_{W,th}$	$\dot{\psi}_{model} \geq 0$	$\dot{\psi}_{min} < \dot{\psi}_{meas} < \dot{\psi}_{max}$	2
		$\left(\dot{\psi}_{meas} \leq \dot{\psi}_{min}\right) \wedge \left(\dot{\psi}_{meas} \geq 0\right)$	4
		$\dot{\psi}_{meas} \geq \dot{\psi}_{max}$	5
		$\left(\dot{\psi}_{meas} \leq \dot{\psi}_{min}\right) \wedge \left(\dot{\psi}_{meas} < 0\right)$	6
Right curve			
$\delta_W \leq -\delta_{W,th}$	$\dot{\psi}_{model} < 0$	$\dot{\psi}_{min} < \dot{\psi}_{meas} < \dot{\psi}_{max}$	2
		$\left(\dot{\psi}_{meas} \geq \dot{\psi}_{max}\right) \wedge \left(\dot{\psi}_{meas} < 0\right)$	4
		$\dot{\psi}_{meas} \leq \dot{\psi}_{min}$	5
		$\left(\dot{\psi}_{meas} \geq \dot{\psi}_{max}\right) \wedge \left(\dot{\psi}_{meas} \geq 0\right)$	6

Table 4.2: Algorithm for assessment of driving situations with the yaw gain method

drive starts on asphalt which changes to cobblestone after approximately five seconds. After $t = 9.3s$, the algorithm detects understeer (DSI=4, Fig. 4.3(d)). After approximately $t = 11s$, oversteer occurs (DSI=5), which becomes even more critical after approximately $t = 12.3s$. Finally, the rear axle of the car breaks out, DSI=6. Figures 4.3(b) and 4.3(c) show that the steering desire of the driver (negative wheel turn angle) causes an increasing yaw rate of *opposite* algebraic sign in the last phase of the drive.
Figure 4.3(d) proves that the assessment algorithm of the yaw gain method works properly.

4.1.2 Method of Characteristic Speed

Determination of the Stability Criterion

The characteristic speed method is a mathematical detection method. It describes the vehicle behavior from the viewpoint of system theory: the stability behavior of the linear single track model is analyzed by means of the HURWITZ-criterion, [51]. The dynamic matrix of the linear single track

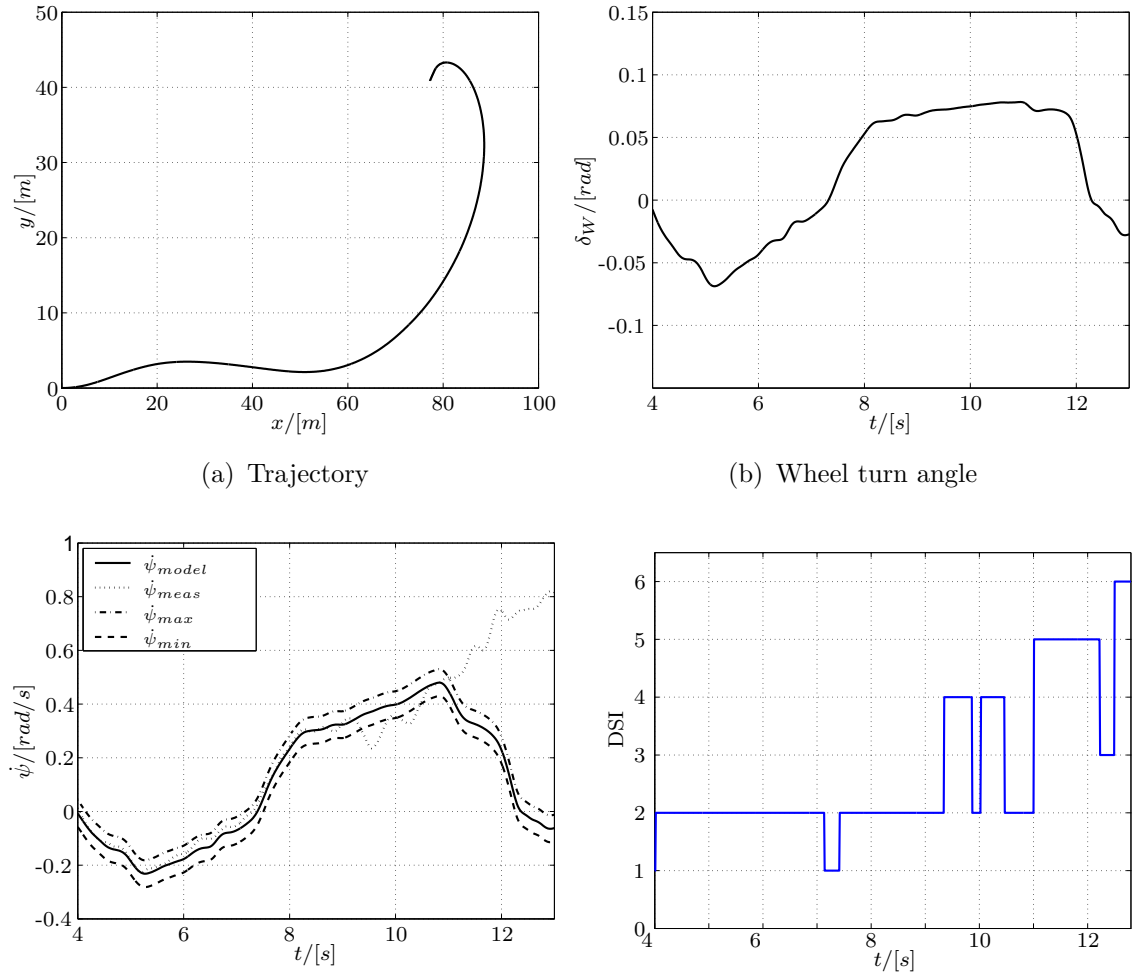

(a) Trajectory

(b) Wheel turn angle

(c) Yaw rate tolerance band

(d) DSI according to yaw gain method

Figure 4.3: Assessment of an instable curve drive with the yaw gain method

model is

$$\underline{A} = \begin{bmatrix} -\frac{c_F+c_R}{m_{CoG}\,v_{CoG}} & \frac{c_R l_R - c_F l_F}{m_{CoG}\,v_{CoG}^2} - 1 \\ \frac{c_R l_R - c_F l_F}{J_Z} & -\frac{c_F l_F^2 + c_R l_R^2}{J_Z v_{CoG}} \end{bmatrix} \quad . \tag{4.6}$$

Stability analysis of the system comprises the setup of the characteristic equation, [24],

$$\det(s\underline{I} - \underline{A}) = 0 \quad . \tag{4.7}$$

Inserting Eqn. (4.6) yields

$$\begin{vmatrix} s + \frac{c_F+c_R}{m_{CoG}\,v_{CoG}} & 1 - \frac{c_R l_R - c_F l_F}{m_{CoG}\,v_{CoG}^2} \\ -\frac{c_R l_R - c_F l_F}{J_Z} & s + \frac{c_F l_F^2 + c_R l_R^2}{J_Z v_{CoG}} \end{vmatrix} = 0 \quad . \tag{4.8}$$

After some mathematical conversions, a polynomial of second order results:

$$s^2 + a_1 s + a_2 = 0 \qquad , \tag{4.9}$$

with

$$a_1 = \frac{m_{CoG}(c_F l_F^2 + c_R l_R^2) + J_Z(c_F + c_R)}{J_Z m_{CoG} v_{CoG}} \tag{4.10}$$

and

$$a_2 = \frac{c_F c_R (l_F + l_R)^2 - m_{CoG} v_{CoG}^2 (c_F l_F - c_R l_R)}{J_Z m_{CoG} v_{CoG}^2} \qquad . \tag{4.11}$$

According to the HURWITZ-criterion, a second order linear system is stable, if all the coefficients of its characteristic equation are positive. The coefficient a_1 is always positive, as the cornering stiffnesses are positive: $c_F > 0$ and $c_R > 0$. Therefore, the parameter a_2 must be analyzed to set up the stability criterion:

$$\begin{aligned} a_2 &= \frac{c_F c_R (l_F + l_R)^2 - m_{CoG} v_{CoG}^2 (c_F l_F - c_R l_R)}{J_Z m_{CoG} v_{CoG}^2} \\ &= \frac{c_F c_R (l_F + l_R)^2}{J_Z m_{CoG} v_{CoG}^2} \left(1 + v_{CoG}^2 \frac{m_{CoG}(c_R l_R - c_F l_F)}{c_F c_R (l_F + l_R)^2} \right) \qquad . \end{aligned} \tag{4.12}$$

With the abbreviation

$$v_{ch}^2 = \frac{c_F c_R (l_F + l_R)^2}{m_{CoG}(c_R l_R - c_F l_F)} = \frac{c_F (l_F + l_R)^2}{m_{CoG}(l_R - l_F \frac{c_F}{c_R})} \qquad , \tag{4.13}$$

the term (4.12) is simplified:

$$a_2 = \frac{c_F c_R (l_F + l_R)^2}{J_Z m_{CoG} v_{CoG}^2} \left(1 + \frac{v_{CoG}^2}{v_{ch}^2} \right) \qquad . \tag{4.14}$$

v_{ch} is called the "characteristic speed" and defined according to Eqn. (4.13), [82]. For non-linear vehicle behavior, it cannot be interpreted physically as a "conventional" vehicle velocity.
Coming back to the stability analysis: the vehicle is stable, if the coefficient a_2 is positive. Regarding Eqn. (4.14) leads to the stability condition

$$1 + \frac{v_{CoG}^2}{v_{ch}^2} > 0 \qquad . \tag{4.15}$$

The square of the characteristic speed v_{ch}^2 plays an important role. According to Eqn. (4.13) it can be positive or negative. Therefore, two cases must be distinguished:

Case 1: $v_{ch}^2 > 0$

For positive square of the characteristic speed v_{ch}^2, the coefficient a_2 of the characteristic equation is positive. This fulfills the stability criterion for the vehicle model, i.e. the vehicle is stable for all vehicle velocities. The square of the characteristic speed (Eqn. (4.13)) is positive, if the condition

$$c_R l_R > c_F l_F \tag{4.16}$$

is fulfilled. In normal driving situations Eqn. (4.16) is valid for vehicles with understeer tendency, [33], [53].

Case 2: $v_{ch}^2 < 0$

The stability criterion for negative square of the characteristic velocity is valid only for specific velocities. Considering the negative algebraic sign, Eqn. (4.15) can be converted:

$$v_{CoG}^2 < |v_{ch}^2| \quad . \tag{4.17}$$

The vehicle is stable as long as Eqn. (4.17) is fulfilled. If the square of the characteristic speed falls below the squared velocity v_{CoG}^2, the vehicle becomes unstable. The square of the characteristic speed is negative, if $c_R l_R < c_F l_F$. The vehicle behavior is called "oversteer" in this case, [33], [53].
Regarding $c_R l_R < c_F l_F$ allows to draw parallels to the yaw gain method. The yaw gain method states that the vehicle oversteers, if the yaw rate $\dot{\psi}_{meas}$ exceeds the tolerance band due to the breakout of the vehicle rear. The breakout is caused by a reduced lateral wheel force F_{YR} on the rear axle. The reduction of the wheel force can be explained with a reduction of the cornering stiffness c_R. Eqn. (4.13) shows that a reduction of c_R causes a decrease of v_{ch}^2. If $|v_{ch}^2|$ falls below v_{CoG}^2, the stability condition (4.17) is

δ_W	v_{CoG}^2	$\dot{\psi}_{meas}$	DSI
$\lvert\delta_W\rvert < \delta_{W,th}$	$v_{CoG}^2 > 0$	$\lvert\dot{\psi}_{meas}\rvert < \dot{\psi}_{th}$	1
		$\lvert\dot{\psi}_{meas}\rvert \geq \dot{\psi}_{th}$	3

Table 4.3: Algorithm for assessment of the driving situation using the method of characteristic speed, part I

not fulfilled any more. The vehicle becomes unstable.
Knowing the vehicle velocity v_{CoG} and the square of the characteristic speed v_{ch}^2, an algorithm for detection and assessment of critical driving situations is set up by using Eqn. (4.17). According to [53] an alternative equation for constant curve drives can be set up using only measurable signals:

$$v_{ch}^2(t) = -\frac{v_{CoG}^2(t)}{1 - \frac{\delta_W(t) v_{CoG}(t)}{\dot{\psi}_{meas}(t) l}} \quad . \tag{4.18}$$

The velocity v_{CoG} can be approximated with the wheel speed signals. The wheel turn angle δ_W is calculated from the measured steering wheel angle δ_S. For the yaw rate $\dot{\psi}_{meas}$, a sensor signal exists as well. Hence, Eqn. (4.18) is taken to calculate the characteristic speed and to analyze the stability with the criterion from Eqn. (4.17).

Algorithm for Detection and Assessment

Like before, in this section the discrete stability index is used for categorizing the driving situation. The principle of assessment is the same as described before: if the yaw reaction of the vehicle is stronger than expected, then the driving situation is rated as critical. The respective algorithms can be seen in Tables 4.3 and 4.4. The first part of the algorithm in Table 4.3 describes straightforward driving (wheel turn angle limited: $|\delta_W| < \delta_{W,th}$). The threshold value for $\delta_{W,th}$ is 0.5°. For cornering, the second part of the algorithm is displayed in Table 4.4. Cornering is detected, if the absolute value of the steering angle $|\delta_W|$ exceeds the specified threshold $\delta_{W,th}$.
The square of the characteristic speed v_{ch}^2 can be positive or negative. The current driving situation is assessed by analyzing the algebraic sign of v_{ch}^2 and by comparing v_{ch}^2 and v_{CoG}^2. Furthermore, a factor k is introduced, which was gained from measurements. Evaluating these measurements, the factor was fixed to $k = 3$.

δ_W	v_{CoG}^2	v_{ch}^2	$\lvert v_{ch}^2 \rvert$	DSI
$\lvert\delta_W\rvert \geq \delta_{W,th}$	$v_{CoG}^2 > 0$	$v_{ch}^2 \geq 0$	$\lvert v_{ch}^2 \rvert \leq k v_{CoG}^2$	4
			$\lvert v_{ch}^2 \rvert > k v_{CoG}^2$	2
$\lvert\delta_W\rvert \geq \delta_{W,th}$	$v_{CoG}^2 > 0$	$v_{ch}^2 < 0$	$\lvert v_{ch}^2 \rvert > k v_{CoG}^2$	2
			$v_{CoG}^2 < \lvert v_{ch}^2 \rvert \leq k v_{CoG}^2$	5
			$\lvert v_{ch}^2 \rvert \leq v_{CoG}^2$	6

Table 4.4: Algorithm for assessment of the driving situation using the method of characteristic speed, part II

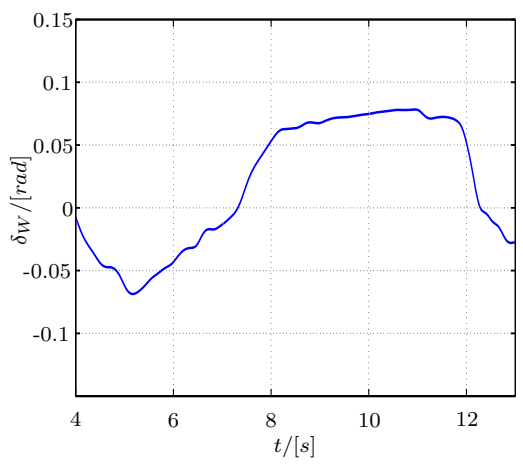

(a) Wheel turn angle

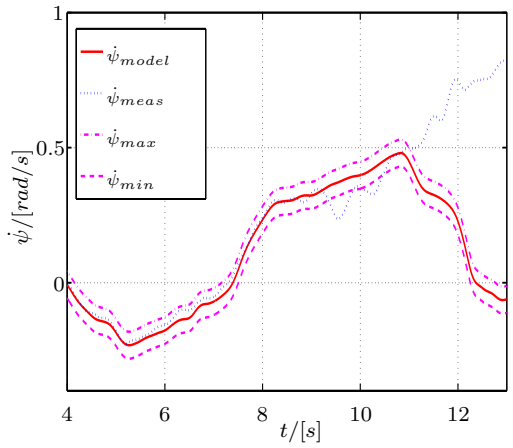

(b) Yaw rate tolerance band

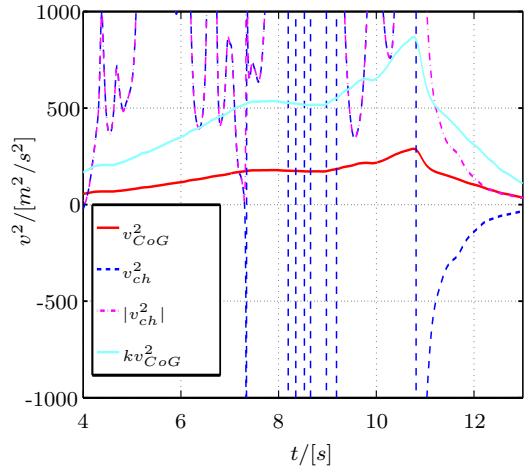

(c) Velocities

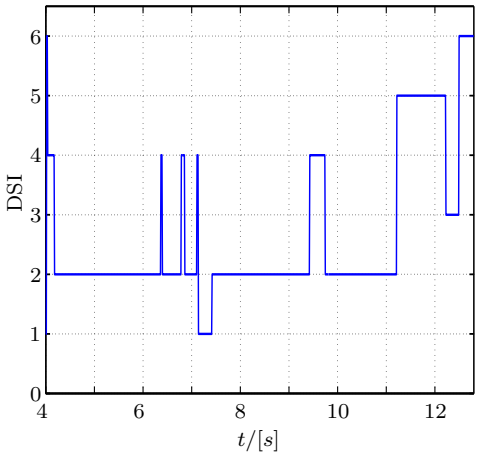

(d) DSI according to v_{ch}^2

Figure 4.4: Assessment of an instable curve drive with the characteristic speed method

Assessment with Measurements

A measurement drive already used in Section 4.1.1 is taken for validation here, too. Fig. 4.4(a) shows the driver's steering input. The vehicle yaw reaction can be seen in 4.4(b). For clarification, Fig. 4.4(c) displays the vehicle velocity and the time-varying characteristic speed of the test drive. After $t = 9s$ v_{ch}^2 is permanently negative and its absolute value falls below $k \cdot v_{CoG}^2$ for $t > 11s$. The real yaw rate remains positive after $t = 11s$, whereas the driver starts counter-steering. The situation is rated "oversteer" (DSI=5, Fig. 4.4(d)) and after $t = 12.5s$ "breakout" (DSI=6), as $|v_{ch}^2|$ falls below v_{CoG}^2 then.
The characteristic speed method is capable to assess the driving behavior correctly. The results confirm the subjective feeling of the driver during the maneuvers.

4.1.3 Curve Radius Method

The principle of the curve radius method (CRM) is rather pragmatic and can be compared to the yaw gain method. The currently measured curve radius is compared to the curve radius determined by means of the vehicle model in Eqns. (3.85) and (3.86). Large deviations between measured and modeled curve radius indicate laterally critical driving situations. Note that in this method the curve radius is determined from the wheel speeds and not by using the gyroscope. In combination with the other methods, this provides physical redundancy to improve the detection.

Determination of Model Curve Radius

The model curve radius r_{model} is determined with the linear single track model and Eqn. (3.39):

$$r_{model} = \frac{v_{CoG}}{\dot{\beta} + \dot{\psi}} \quad . \tag{4.19}$$

The linear single track model uses constant cornering stiffnesses c_F and c_R. Therefore, the lateral forces F_{SF} and F_{SR} can be much larger as realistic and the forces keeping a car in a curve are modeled larger than physically reasonable (see Section 3.4.2). Therefore, the curve radius behavior of the real vehicle deviates from the modeled one.

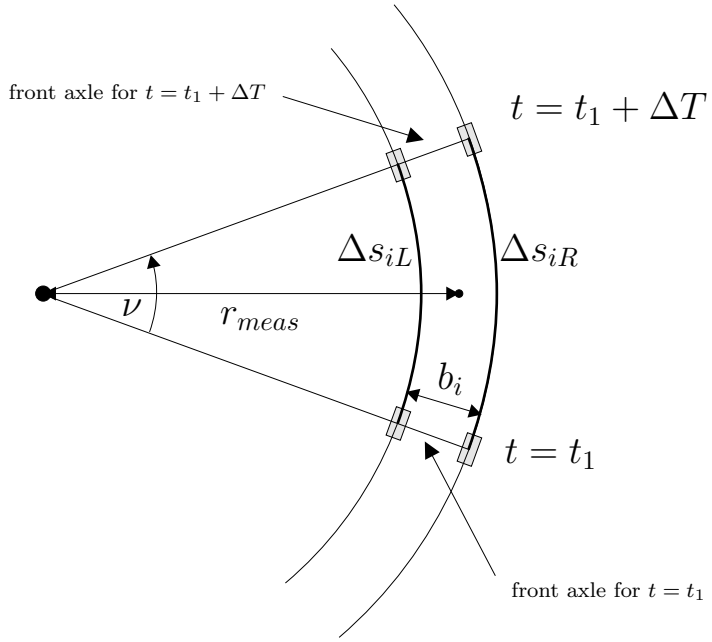

Figure 4.5: Determination of current curve radius r_{meas}

Determination of Current Curve Radius

In order to compare the modeled and the measured curve radius the distances traveled by a wheel of the left Δs_{iL} and the right track Δs_{iR} are compared. Fig. 4.5 shows a left curve. The term b_i represents the track (i is a wildcard for F-front, R-rear). For a left curve, the distances are calculated using the curve angle ν and the current ($\hat{=}$measured) curve radius

$$\Delta s_{iL} = \left(r_{meas} - \frac{b_i}{2} \right) \nu \quad \text{and} \quad \Delta s_{iR} = \left(r_{meas} + \frac{b_i}{2} \right) \nu \quad . \tag{4.20}$$

The ratio of Δs_{iL} and Δs_{iR} eliminates ν and yields

$$\frac{\Delta s_{iL}}{\Delta s_{iR}} = \frac{r_{meas} - \dfrac{b_i}{2}}{r_{meas} + \dfrac{b_i}{2}} \quad . \tag{4.21}$$

The current curve radius r_{meas} becomes

$$r_{meas} = \frac{b_i}{2} \left(\frac{\Delta s_{iL} + \Delta s_{iR}}{\Delta s_{iR} - \Delta s_{iL}} \right) \quad . \tag{4.22}$$

For a right curve, the equations are derived respectively.
The distance increments Δs_{ij} can be determined by integrating the velocities: $v_{Wij}(t) \cdot \Delta T$. ΔT is one integration time step fixed to $40ms$. To reduce

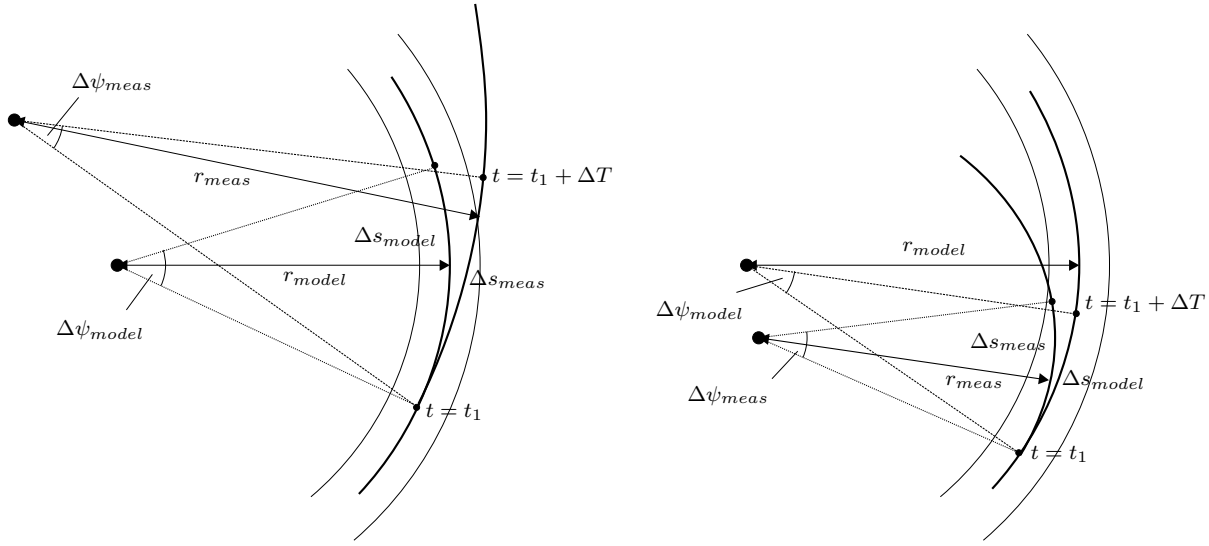

(a) Radius behavior "Understeer" (b) Radius behavior "Oversteer"

Figure 4.6: Curve radii in critical driving situations

the computational effort, v_{CoG} in Eqn. (4.19) is approximated by averaging the equivalent rotational wheel speeds of both wheels of the rear axle:

$$v_{CoG} \approx \frac{1}{2}\left(v_{RiL} + v_{RiR}\right) \quad . \tag{4.23}$$

The modeled curve radius can be negative or positive. The algebraic sign depends on the direction of the curve. For a left curve it is defined positive, for a right curve it is negative in accordance with the definition of the yaw angle. The algebraic sign is an important means for the assessment criterion.

Current Curve Radius in Critical Situations

After the derivation of the measured and the modeled curve radius, the characteristics of the current curve radius in critical driving situations is explained. Like in the sections before, understeer, neutral steer and oversteer situations are regarded in the following.

Curve Radius in Extreme Understeer Situations

Fig. 4.6(a) shows that in a critical situation the curve radius of an understeering vehicle is larger than the curve radius calculated by the reference model. The vehicle "shifts" out of the curve.
This behavior can additionally be expressed by means of the yaw rate $\dot{\psi}_{meas}$. For an understeering vehicle, the absolute value of the measured

yaw rate $|\dot{\psi}_{meas}|$ is smaller than the modeled one $|\dot{\psi}_{model}|$. The absolute values of the yaw rate signals therefore correspond to the respective curve radii.

Curve Radius for Oversteering Vehicle

Oversteering vehicles drive smaller curve radii than calculated by the vehicle model. The vehicle reacts stronger to the steering input δ_W as desired by the driver. Figure 4.6(b) expresses this behavior.
The "overreaction" of the car can be explained with a higher yaw rate $\dot{\psi}_{meas}$. The reduced curve radius of an oversteering vehicle causes a larger angle $\Delta\psi_{meas}$ in the same time increment. That means, the real yaw rate is larger than the modeled yaw rate. Therefore, this measurement also shows a significant analogy of yaw rate and curve radius r_{meas}. One advantage of determining the curve radius with the wheel speeds will be shown in Section 4.1.5.

Algorithm of the Curve Radius Method

In the previous section, the relation between the modeled and the measured curve radius r_{model} and r_{meas} was analyzed in critical driving situations: for oversteer, the curve radius is smaller whereas for understeer it is larger than the model radius r_{model} calculated with the single track model. Thus, the following stability criterion can be set up: If the vehicle is in a stable driving situation, the measured curve radius r_{meas} deviates only little from the model radius. If the driving situation becomes critical, the radius difference becomes more significant. The proper operativeness of the detection algorithm was checked by means of a variety of simulations and measurements. The algorithm structure can be found in Table 4.5. Table 4.5 shows that for the detection the inverse curve radii were used, because for straightforward driving the curve radius is infinite, whereas the inverse radius is zero. For better understanding, Fig. 4.7 contains the tolerance band of the inverse curve radii and the respective thresholds. Like before, a critical driving situation is detected, if the measured inverse curve radius leaves the tolerance band limited by the upper border $\frac{1}{r_{model}} + \Delta p_1$ and the lower border $\frac{1}{r_{model}} - \Delta n_1$. The numerical values for Δp_1 and Δn_1 were determined by means of experiments and set to $\Delta p_1 = \Delta n_1 = 0,008m^{-1}$. The additional thresholds Δp_2 and Δn_2 are needed to distinguish between "understeer" (DSI=4) and "breakout" (DSI=6). These values were also determined with test drives and fixed to $\Delta p_2 = \Delta n_2 = 0.015m^{-1}$.

$\frac{1}{r_{model}}$	$\frac{1}{r_{meas}}$	DSI
	Straightforward: $\lvert\delta_W\rvert < \delta_{W,th}$	
$\left\lvert\frac{1}{r_{model}}\right\rvert < \infty$	$\frac{1}{r_{model}} - \Delta n_1 < \frac{1}{r_{meas}} < \frac{1}{r_{model}} + \Delta p_1$	1
	$(\frac{1}{r_{meas}} \geq \frac{1}{r_{model}} + \Delta p_1) \ \vee \ (\frac{1}{r_{meas}} \leq \frac{1}{r_{model}} - \Delta n_1)$	3
	Left curve: $\lvert\delta_W\rvert \geq \delta_{W,th}$	
$\frac{1}{r_{model}} \geq 0$	$\frac{1}{r_{model}} - \Delta n_1 < \frac{1}{r_{meas}} < \frac{1}{r_{model}} + \Delta p_1$	2
	$(\frac{1}{r_{meas}} \leq \frac{1}{r_{model}} - \Delta n_1) \ \wedge \ (\frac{1}{r_{meas}} \geq -\Delta n_2)$	4
	$\frac{1}{r_{meas}} \geq \frac{1}{r_{model}} + \Delta p_1$	5
	$(\frac{1}{r_{meas}} \leq \frac{1}{r_{model}} - \Delta n_1) \ \wedge \ (\frac{1}{r_{meas}} \leq -\Delta n_2)$	6
	Right curve: $\lvert\delta_W\rvert \geq \delta_{W,th}$	
$\frac{1}{r_{model}} < 0$	$\frac{1}{r_{model}} - \Delta n_1 < \frac{1}{r_{meas}} < \frac{1}{r_{model}} + \Delta p_1$	2
	$(\frac{1}{r_{meas}} \geq \frac{1}{r_{model}} + \Delta p_1) \ \wedge \ (\frac{1}{r_{meas}} < \Delta p_2)$	4
	$\frac{1}{r_{meas}} \leq \frac{1}{r_{model}} - \Delta n_1$	5
	$(\frac{1}{r_{meas}} \geq \frac{1}{r_{model}} + \Delta p_1) \ \wedge \ (\frac{1}{r_{meas}} \geq \Delta p_2)$	6

Table 4.5: Algorithm for assessment of the driving situation by means of the CRM

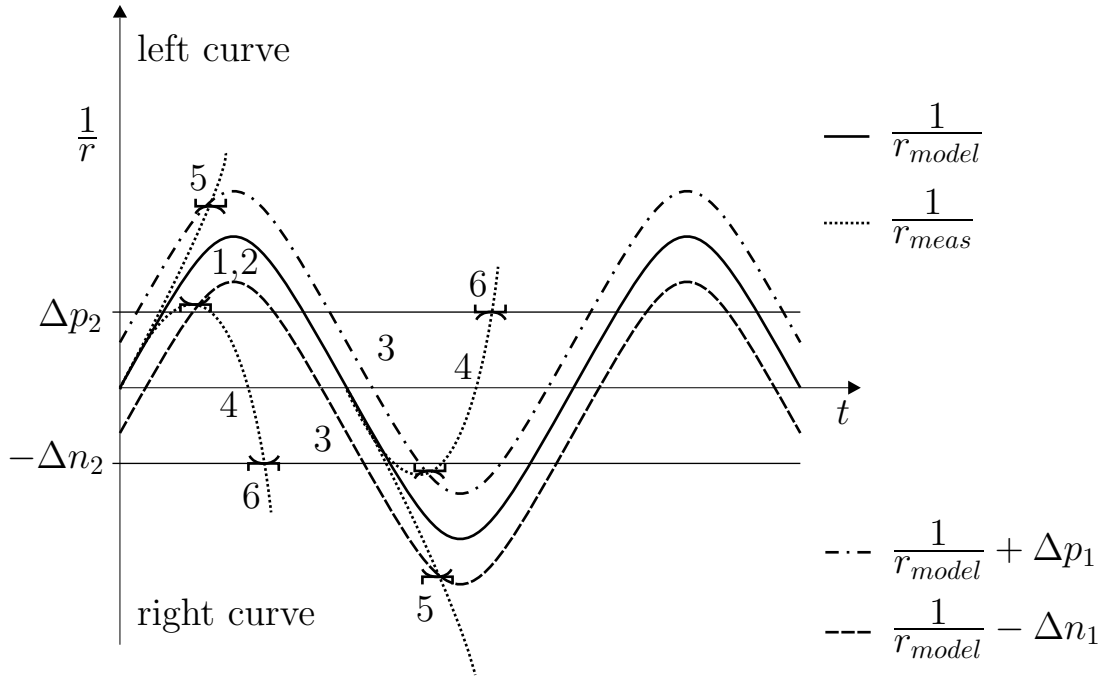

Figure 4.7: Tolerance band of inverse radii

To assess its accuracy and quality for real-world applications, the curve radius method was tested with a data set recorded during a test drive with the Ford Scorpio (see Appendix D.1). It is the same data set as the one presented in the sections before. The results are displayed in Fig. 4.8. However, the reaction of this method displayed in Fig. 4.8(c) between $t = 9s$ and $t = 11s$ is much stronger than with the two other methods. The reason for this behavior and its advantage will be discussed in Section 4.1.5 when comparing all the detection methods. Apart from this, the CRM yields almost the same results like the other two methods. Thus, the method provides reasonable results for the simulations and for the test drives in accordance with the subjective feeling of the test driver.

4.1.4 Self-Steer Gradient Method

The self-steer gradient method (SSGM) is related to the characteristic velocity method. It bases on the physical effect that the self-steer behavior of the vehicle supervenes the steering desire of the driver. After explaining the underlying theory, the implementation of the method will be presented and a measurement drive will be assessed with the discrete stability index.

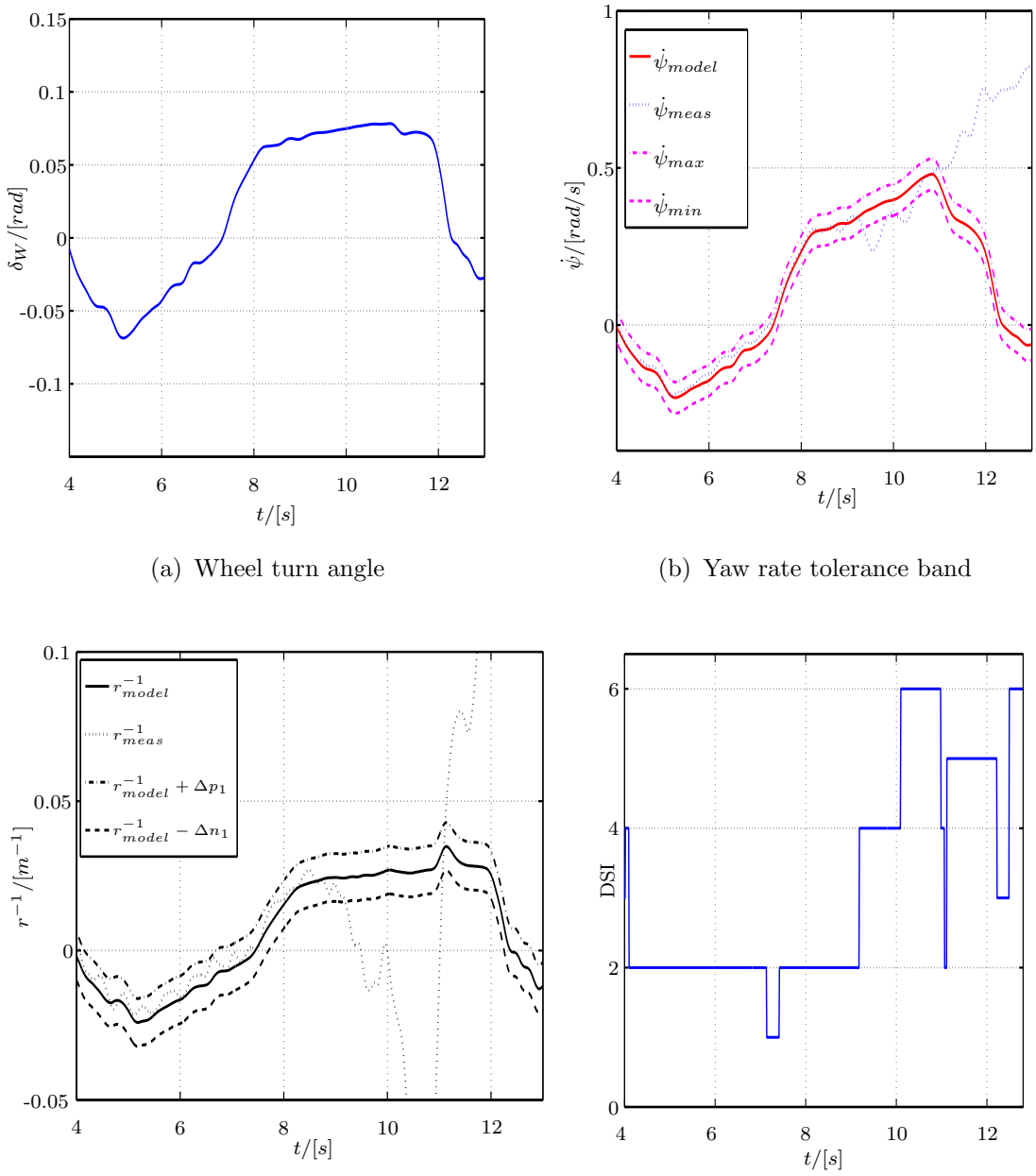

(a) Wheel turn angle

(b) Yaw rate tolerance band

(c) Tolerance band of inverse curve radii

(d) SI according to the CRM

Figure 4.8: J-Turn maneuver and detection of critical situation with the curve radius method

Underlying Theory

To understand the cornering behavior of a vehicle it is convenient to discuss the cornering behavior at low speeds. Fig. 4.9 shows the single track model and the vehicle geometry for a low speed turn. In this situation, the wheels roll without lateral slip. Centrifugal forces are neglected. The velocity vectors of the front wheel v_F and of the rear wheel v_R lie exactly in the wheel plane. The turn center is the intersection of the curve radii of

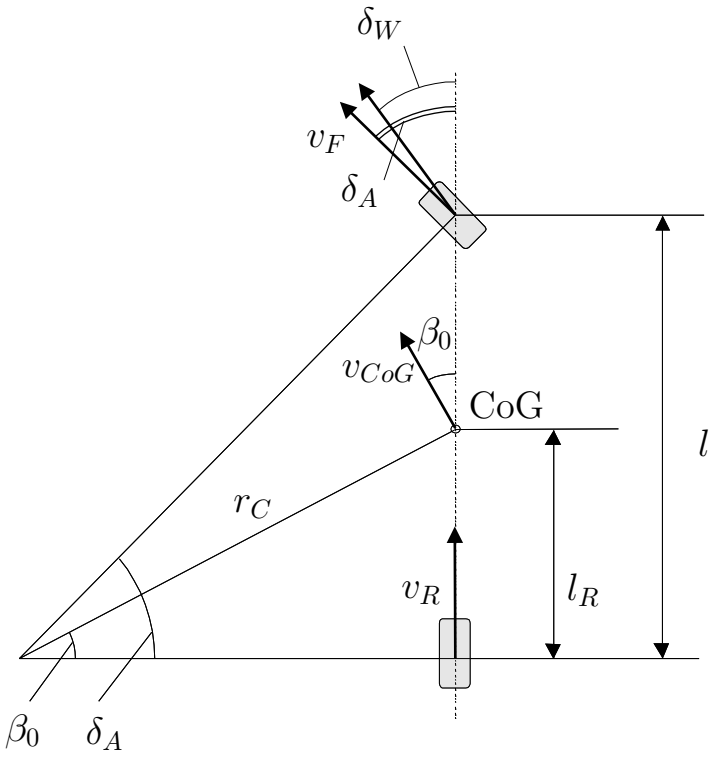

Figure 4.9: Geometry of the linear single track vehicle for low speed turn

front and rear wheel. Both of these radii are perpendicular to the respective wheel velocity. The ideal turn angle δ_A only depends on the curve radius r_C and on the geometric parameters l and l_R:

$$\tan \delta_A = \frac{l}{\sqrt{r_C^2 - l_R^2}} \quad . \tag{4.24}$$

Assuming small angles of δ_A and $r_C \gg l_R$, Eqn. (4.24) is

$$\delta_A = \frac{l}{r_C} \quad . \tag{4.25}$$

δ_A is called "ACKERMANN-angle" and the geometric relations of Fig. 4.9 "ACKERMANN-steering", [26], [79], [82]. Using Eqn. (3.38) for slow and stationary cornering ($\dot{\beta} \approx 0$) the ACKERMANN-angle can also be written as

$$\delta_A = \frac{l \cdot \dot{\psi}}{v_{CoG}} \quad . \tag{4.26}$$

For higher velocities, the centrifugal force increases and the lateral slip cannot be neglected any more. Then, the wheel turn angle δ_W and the

ACKERMANN-angle are not equal any more (see Fig. 4.9), due to the tire side slip angles α_F and α_R:

$$\delta_W = \delta_A + \alpha_F - \alpha_R \quad . \tag{4.27}$$

The additional angle $(\alpha_F - \alpha_R)$ is caused by the self-steer behavior of the vehicle which describes the steering properties of a car independent from the steering influence of the driver. The self-steer behavior can also be described with the self-steer gradient (SSG) :

$$SSG = \frac{1}{i_S} \cdot \frac{\partial \delta_S}{\partial a_Y} - \frac{\partial \delta_A}{\partial a_Y} \quad . \tag{4.28}$$

For a stationary circle and linear vehicle behavior, the differentials in Eqn. (4.28) can be replaced by quotients. Isolating the steering wheel angle δ_S yields

$$\delta_S \approx i_S \cdot \delta_A + i_S \cdot SSG \cdot a_Y \quad , \tag{4.29}$$

where i_S describes the steering transmission factor. Without differentials, Eqn. (4.28) becomes

$$SSG = \frac{\frac{\delta_S}{i_S} - \delta_A}{a_Y} \quad . \tag{4.30}$$

In order to increase the robustness of the detection algorithm, the lateral acceleration in the denominator of Eqn. (4.30) is replaced by its algebraic sign: $a_Y \rightarrow \text{sign}(a_Y)$. Especially for straightforward driving with little accelerations the self-steer gradient values would become very large and would cause false detections due to noise. This was verified with test measurements. Simplifying the denominator leads to the employed *modified* self-steer gradient

$$SSG_m = \frac{\frac{\delta_S}{i_S} - \delta_A}{\text{sign}(a_Y)} = \frac{\frac{\delta_S}{i_S} - \frac{l \cdot \dot{\psi}}{v_{CoG}}}{\text{sign}(a_Y)} \quad . \tag{4.31}$$

The ACKERMANN-angle is a measure for the self-steer behavior of a car: for small centrifugal forces, δ_S/i_S and δ_A are approximately equal. The modified SSG is around zero. With growing lateral accelerations, the desired wheel turn angle δ_S/i_S deviates from δ_A, because Eqn. (4.25) is not fulfilled

any more. Again there is a deviation between the "model" Ackermann-angle and the real angle measured with $l \cdot \dot{\psi}/v_{CoG}$. For understeer, the term $l \cdot \dot{\psi}/v_{CoG}$ is smaller than δ_S/i_S. SSG_m is bigger than zero. On the other hand, for oversteer the yaw reaction of the car is too large. The nominator of Eqn. (4.31) is negative and so is SSG_m. The idea of detecting critical situations with the self-steer gradient is obvious: if SSG_m exceeds a threshold, the vehicle understeers, the DSI is 4. In case that SSG_m falls below the oversteer threshold, the DSI is 5.
Before the implementation of the method is described, a physical consideration points out the similarity to the other methods. According to [82] for a stationary and linear circle drive the self-steer gradient can also be described by means of the constant cornering stiffnesses c_F and c_R:

$$SSG = \frac{m_{CoG}(c_R \cdot l_R - c_F \cdot l_F)}{l \cdot c_F \cdot c_R} \quad . \tag{4.32}$$

For small lateral accelerations (dry road: $a_Y < 4m/s^2$), the self-steer gradient is constant depending on the properties of the tires (c_F, c_R) and on the geometric measures of the vehicle and its mass. Neutral steer ($SSG = 0$) requires

$$c_R \cdot l_R = c_F \cdot l_F \quad . \tag{4.33}$$

Accordingly, understeer is described by $SSG > 0$ and

$$c_R \cdot l_R > c_F \cdot l_F \quad , \tag{4.34}$$

and finally oversteer by $SSG < 0$ and

$$c_R \cdot l_R < c_F \cdot l_F \quad . \tag{4.35}$$

As the cornering stiffnesses cannot be measured with commercial-off-the-shelf sensor equipment, a measurable approximation must be found. Eqn. (4.31) represents such an approximation. Although several simplifications are made, the next sections will show that the self-steer gradient method can also be used as a detection and classification method for critical driving situations.

Implementation of the Method

In accordance with the other detection methods thresholds have to be defined for SSG_m to distinguish between the different driving states. The thresholds were chosen by evaluating a variety of test drives with two different vehicles and on basis of existing detection methods (mainly the yaw

δ_W	SSG_m	DSI
Straightforward		
$\lvert\delta_W\rvert < \delta_{W,th}$	$(SSG_m < SSG_{u1}) \wedge (SSG_m > SSG_{l1})$	1
	$(SSG_m \geq SSG_{u1}) \vee (SSG_m \leq SSG_{l1})$	3
Left/right curve		
$\lvert\delta_W\rvert \geq \delta_{W,th}$	$(SSG_m < SSG_{u1}) \wedge (SSG_m > SSG_{l1})$	2
	$(SSG_m < SSG_{u2}) \wedge (SSG_m \geq SSG_{u1})$	4
	$(SSG_m > SSG_{l2}) \wedge (SSG_m \leq SSG_{l1})$	5
	$(SSG_m \geq SSG_{u2}) \vee (SSG_m \leq SSG_{l2})$	6

Table 4.6: Algorithm for assessment of the driving situation using the self-steer gradient method

gain method of Section 4.1.1). Table 4.6 shows the criteria to distinguish between the six states of the discrete stability index. The tolerance band for SSG_m around zero is limited by $SSG_{u1} = 0.025$ rad and $SSG_{l1} = -0.025$ rad.
Small values of the modified self-steer gradient indicate stable straightforward drive (DSI=1) or a stable curve (DSI=2), if additionally the steering wheel angle $|\delta_W|$ exceeds the "curve-threshold" of $\delta_{W,th} = 0.5°$.
If the calculated SSG_m lies outside the tolerance band, although δ_W indicates straightforward driving, then the algorithm detects DSI=3, instable straightforward drive.
For the states DSI=4, 5, 6, the wheel turn angle indicates cornering. For understeer (DSI=4), SSG_m lies between SSG_{u1} and SSG_{u2}, a second threshold at 0.2 rad. If SSG_m ranges between SSG_{l1} and $SSG_{l2} = -0.2$ rad, the situation is oversteer (DSI=5). For breakout (DSI=6), the wide tolerance band limited by SSG_{l2} and SSG_{u2} is exceeded.

Assessment with Measurement Drive

The self-steer gradient method was validated with instable test drives on different road surfaces. Fig. 4.10 shows the results of a J-Turn test drive on cobblestone. At a velocity $v_{CoG} \approx 50km/h$ the vehicle turns into a left curve. After a short understeer peak at $t \approx 9.5s$, where the car was changing from asphalt to cobblestone, the car oversteers after $t = 11s$. The self-steer gradient crosses the first threshold SSG_{l1} and the DSI changes to "5". At $t = 12.2s$, the driver counter-steers and for a short time the

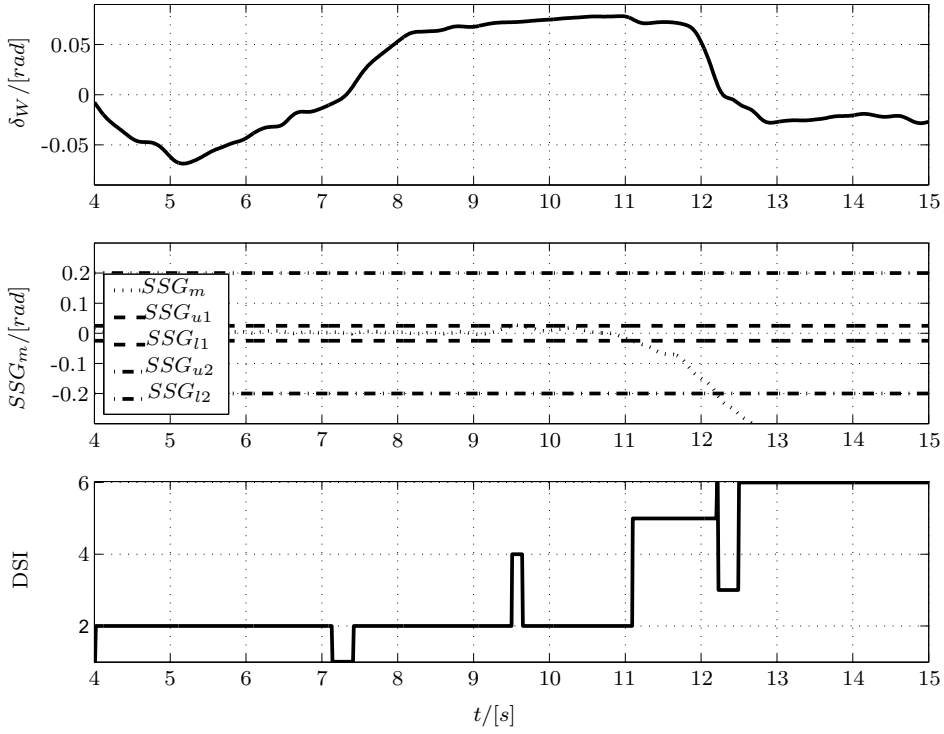

Figure 4.10: Steering wheel angle, self-steer gradient with tolerance band and respective stability index

steering wheel is straight. In this period, the algorithm detects instable straightforward driving. The DSI is "3" in this phase. Finally, the vehicle rear breaks out. The self-steering gradient falls below the lower border SSG_{l2} and the stability index becomes "6". The stability index values confirm the driver's feeling during the test drive.

4.1.5 Comparison of the Methods

In the last sections four different methods for the detection and assessment of critical driving situations were presented: the yaw gain method (YGM), the characteristic speed method (CSM), the curve radius method (CRM) and the self-steering gradient method (SSGM). All of these methods are based on a linear reference model representing the range of experience of average drivers. The four methods are related to each other. All of the methods somehow detect the fading capability of the car to transmit the lateral forces to the ground. The sensor combination of the individual methods varies, though. That means, the physical redundancy of the different sensor combinations allows to enhance robustness of accident detection and assessment.

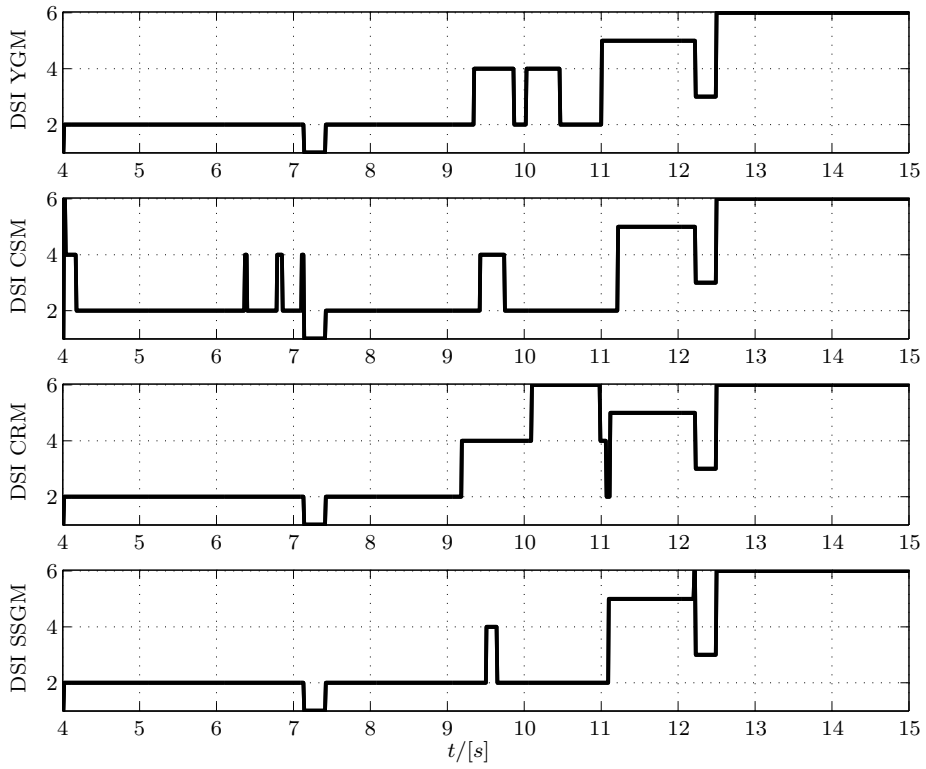

Figure 4.11: Comparison of different detection methods for a critical J-Turn drive

The detection methods are tested with several test drives. Out of these test drives, Fig. 4.11 shows a representative measurement. The results were already presented in the last sections for the individual methods. Now, they are compared to show similarities and to point out differences of the methods. The basic shape of the discrete stability indices in Fig. 4.11 looks similar for all methods. A major deviation represents only the curve radius method between $t = 10s$ and $t = 11s$. The car was moving on cobblestone. The wheel load shifts dramatically to the outer track. Therefore, the left wheels were relieved. This effect causes increasing drive slip on the rear left wheel. The velocity of this wheel gets higher and Δs_{RL} increases according to Eqn. (4.22). The curve radius method detects clockwise cornering ($r_{meas} < 0$: the inner wheel appears to "overtake" the outer wheel), whereas the real curve calculated by the model indicates counter clockwise driving. In such situations, the curve radius method detects a "breakout". In fact, the increase of drive slip is a sign that the wheel force transmission to the ground gets lost on the rear track, the vehicle is approaching an oversteer situation. The increased slip effect was observed on asphalt as well. However, it is not so dramatic on this ground. That means, the curve radius method is capable to detect oversteer very early, especially on low μ road surface. Fig. 4.12 shows a clothoide drive. Until $t = 8s$ the four

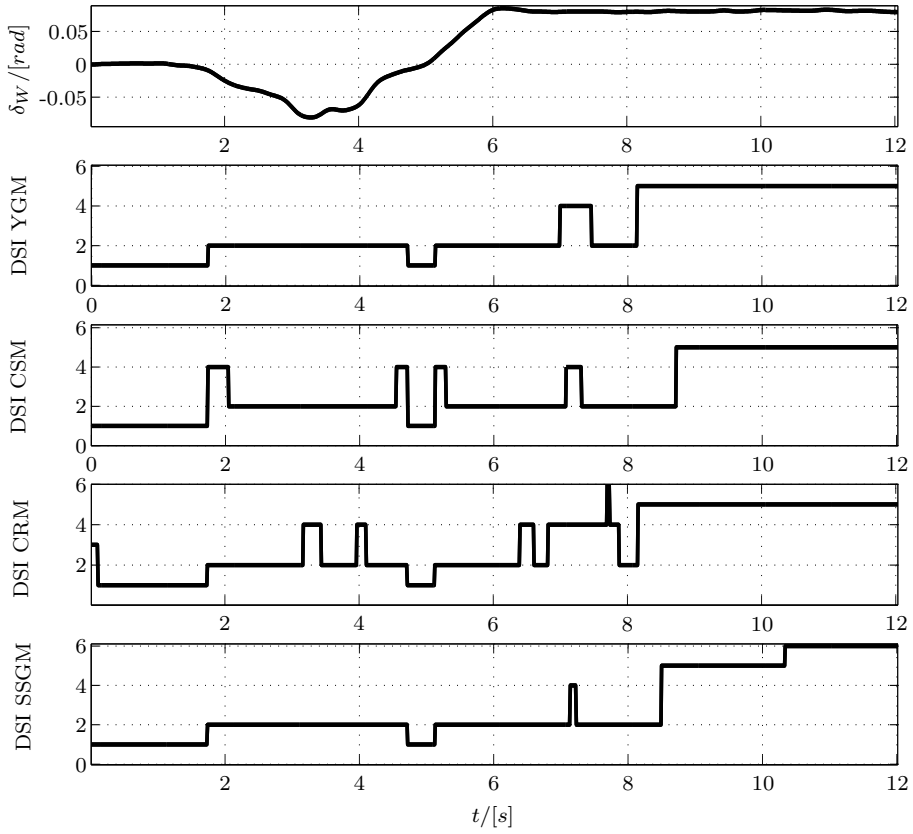

Figure 4.12: Comparison of different detection methods for a clothoide

methods more or less detect the same situation: a stable curve with a tendency to understeer. For $t > 8s$ the laterally critical situation can be seen. After an oversteer period for $t > 8.5s$ the DSI of the SSGM changes to 6 at $t = 10.5s$. In this driving situation, the velocity was decreasing significantly. Regarding Eqn. (4.31) for the modified self-steer gradient explains the early detection of DSI=6: the wheel turn angle is kept constant for $t > 6s$ and the yaw rate increases only slightly. The significant drop of the velocity causes a decreasing negative value for the self-steer gradient. The self-steer gradient method is therefore capable to detect critical situations, where the driver tries to stabilize the car by braking. The driver reduces speed and the negative value of SSG_m further decreases indicating an instable driving situation.

This section has shown that the different methods basically assess a critical driving situation coherently for the conducted test drives. However, these results should be confirmed by conducting further test drives like double lane changes, μ-split braking or sinusodial steering excitation with growing frequency. With the methods presented, in certain driving situations one method can be faster or less reliable. Fusing all of the presented methods by means of the "two-of-four-method" (Section 4.3) provides a more robust detection of critical driving situations.

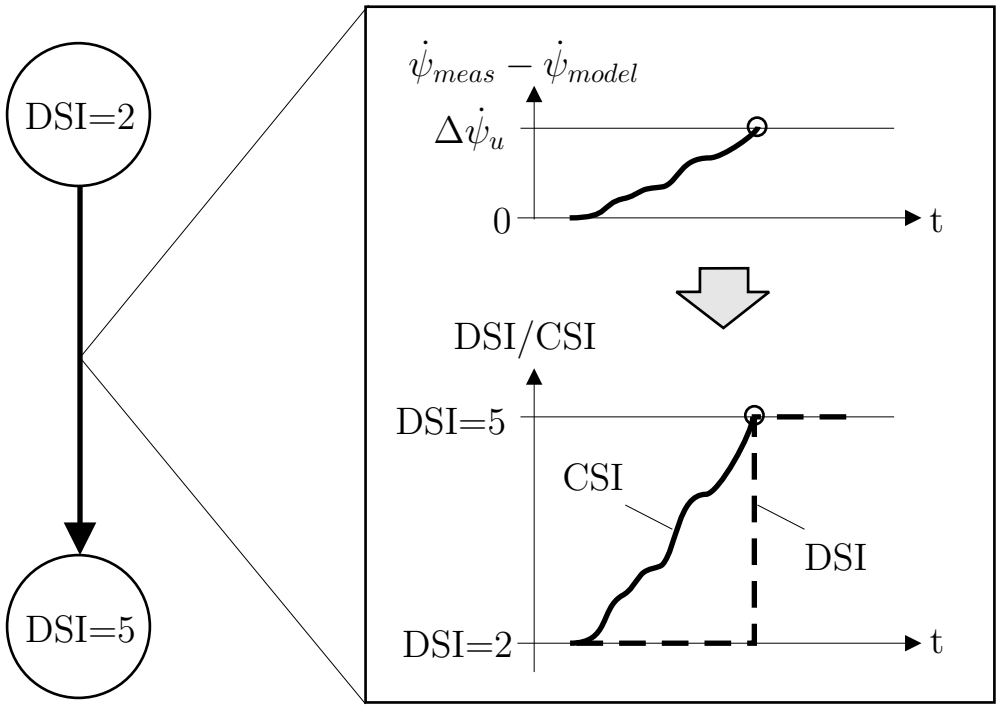

Figure 4.13: Growing difference between measured and modeled yaw rate makes the CSI grow accordingly

4.2 Continuous Stability Index

4.2.1 Motivation

The methods presented in Sections 4.1.1 to 4.1.4 classify the driving situation in six discrete states using a *discrete* stability index. The comparison of the methods in Section 4.1.5 has shown that the methods basically work and provide similar results.
Anyhow, classifying the driving state with discrete thresholds causes deviations of the results gained from the individual methods. If the specified threshold is not exceeded by one method whereas another method lies right on the "other side" of the threshold, then the difference is very significant, if for instance one method detects "stable curve drive" (DSI=2), the other one "oversteer" (DSI=5). That means, the DSI provides only a rough classification of the current driving state.
This drawback will be reduced by introducing a *continuous* stability index . The CSI is derived from the discrete stability index. Fig. 4.13 shows the step from the discrete to the continuous stability index by means of the yaw gain method. If the yaw rate difference $\dot{\psi}_{meas} - \dot{\psi}_{model}$ between measurement and model grows over time and approaches $\Delta\dot{\psi}_u$, the continuous stability index grows accordingly and causes a smooth transition

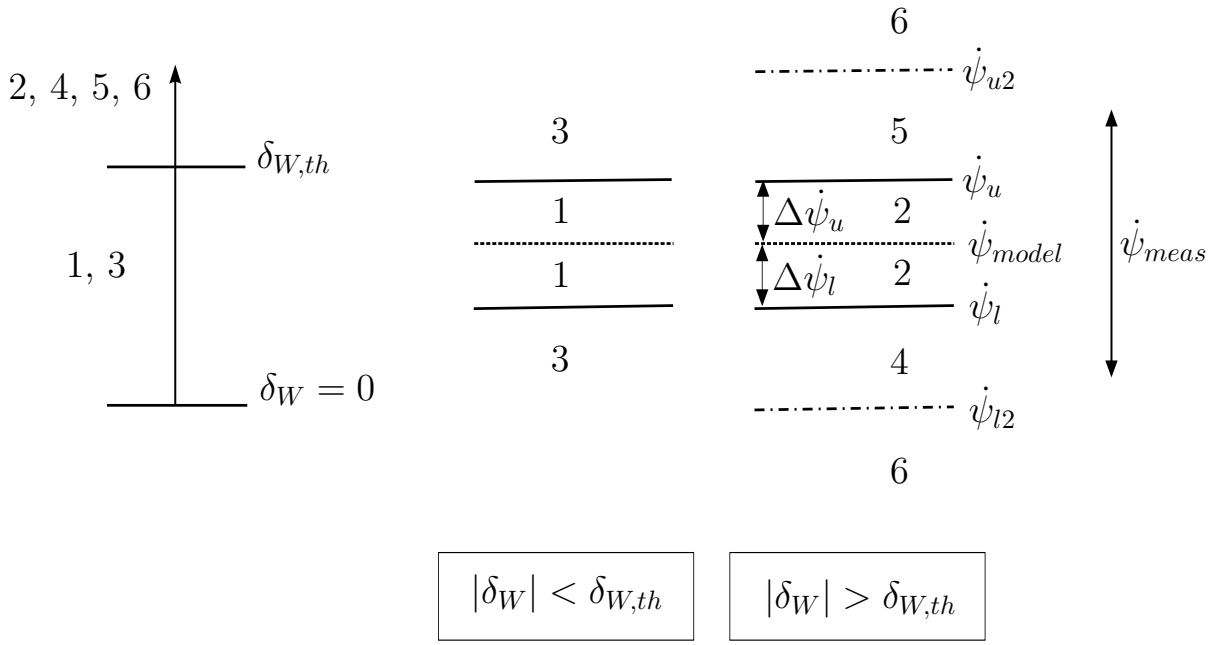

Figure 4.14: Stability index and thresholds of the yaw gain method

from DSI=2 to DSI=5. The DSI would jump up at once. As the DSI is a very demonstrative method to classify the driving state, it is convenient to derive the CSI from the discrete stability index.

4.2.2 Yaw Gain Method

Fig. 4.14 shows the possible transitions of the DSI-values: on the left side the wheel turn angle tolerance band can be seen. If the wheel turn angle $|\delta_W|$ lies below the threshold $\delta_{W,th}$, a yaw rate threshold decides, whether the straightforward drive is stable or unstable (middle of Fig. 4.14). For cornering ($|\delta_W| > \delta_{W,th}$) individual thresholds $\Delta\dot{\psi}_u, \Delta\dot{\psi}_l, ...$ describe the transitions to adjacent discrete states (right of Fig. 4.14).
Generally, for the CSI values the transitions from adjacent DSI values must be expressed continuously. This is carried out by evaluating the thresholds $\Delta\dot{\psi}_u, \Delta\dot{\psi}_l$, etc. . As an example, the transition from a stable curve drive to oversteer is explained by means of the third row in Table 4.7. Starting with DSI=2 (left column of the table), a main condition decides, whether the transition to DSI=4 or DSI=5 (right column of the table) must occur. In the example, the measured yaw rate shall be larger than the modeled one: $|\dot{\psi}_{meas}| > |\dot{\psi}_{model}|$. Then, the third column of Table 4.7 contains the calculation formula for the CSI. If the deviation between modeled and measured yaw rate grows, the term $|\dot{\psi}_{meas} - \dot{\psi}_{model}|/\Delta\dot{\psi}_u$ gets bigger until finally it reaches its maximum value 1, when the deviation exceeds $\Delta\dot{\psi}_u$

Start: DSI	Main condition	Calculation of CSI	Limit CSI→x
1		$1 + \left(\underbrace{\frac{\lvert\delta_W\rvert}{\delta_{W,th}}}_{max=1} \cdot 1 + \underbrace{\frac{\left\lvert\dot{\psi}_{meas} - \dot{\psi}_{model}\right\rvert}{\Delta\dot{\psi}_l}}_{max=1} \cdot 2 \right)$	x=2 or x=3
2	$\lvert\dot{\psi}_{meas}\rvert < \lvert\dot{\psi}_{model}\rvert$	$2 + \underbrace{\frac{\left\lvert\dot{\psi}_{meas} - \dot{\psi}_{model}\right\rvert}{\Delta\dot{\psi}_l}}_{max=1} \cdot 2$	x=4
	$\lvert\dot{\psi}_{meas}\rvert > \lvert\dot{\psi}_{model}\rvert$	$2 + \underbrace{\frac{\left\lvert\dot{\psi}_{meas} - \dot{\psi}_{model}\right\rvert}{\Delta\dot{\psi}_u}}_{max=1} \cdot 3$	x=5
3	$\dot{\psi}_{meas} < \dot{\psi}_l$	$3 + \underbrace{\frac{\lvert\delta_W\rvert}{\delta_{W,th}}}_{max=1} \cdot 1$	x=4
	$\dot{\psi}_{meas} > \dot{\psi}_u$	$3 + \underbrace{\frac{\lvert\delta_W\rvert}{\delta_{W,th}}}_{max=1} \cdot 2$	x=5
4	left curve	$4 + \underbrace{\frac{\left\lvert\dot{\psi}_{meas} - \dot{\psi}_l\right\rvert}{\dot{\psi}_{l2} - \dot{\psi}_l}}_{max=1} \cdot 2$	x=6
	right curve	$4 + \underbrace{\frac{\left\lvert\dot{\psi}_{meas} - \dot{\psi}_u\right\rvert}{\dot{\psi}_{u2} - \dot{\psi}_u}}_{max=1} \cdot 2$	x=6
5	left curve	$5 + \underbrace{\frac{\left\lvert\dot{\psi}_{meas} - \dot{\psi}_u\right\rvert}{\dot{\psi}_{u2} - \dot{\psi}_u}}_{max=1} \cdot 1$	x=6
	right curve	$5 + \underbrace{\frac{\left\lvert\dot{\psi}_{meas} - \dot{\psi}_l\right\rvert}{\dot{\psi}_{l2} - \dot{\psi}_l}}_{max=1} \cdot 1$	x=6
6		no changes	

Table 4.7: Yaw gain method: continuous stability index

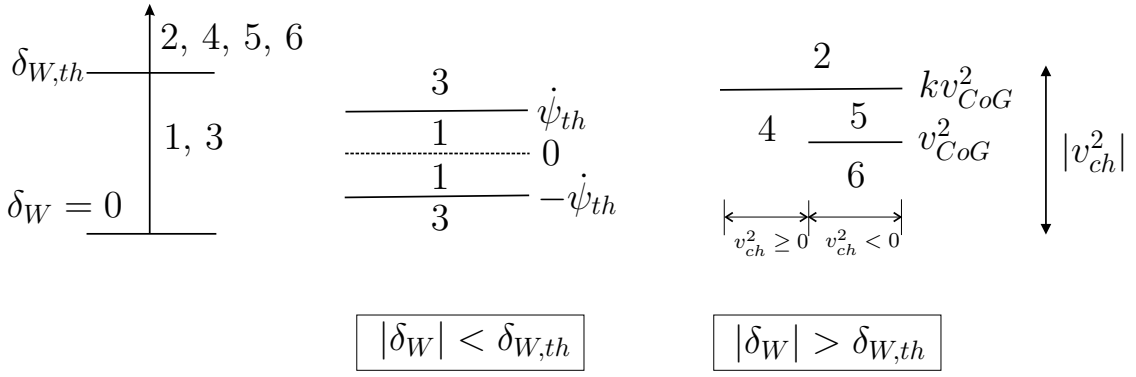

Figure 4.15: Stability index and thresholds of the characteristic speed method

(see also Fig. 4.13). Then, the algorithm "jumps" to the discrete stability index 5 (row 8 in Table 4.7) and the transition to the discrete state "6" must be evaluated. If the measured yaw rate returns to the tolerance band around the model yaw rate, a main condition causes a jump back to the third column of Table 4.7 starting with DSI=2 again.
For the other DSI, the check of a main condition (column 2 in Table 4.7) clarifies which transition equation is chosen to calculate the CSI for the respective transition shown in Fig. 4.14. The equations in the table prove that the stability index can have all real values between 1 and 6.

4.2.3 Characteristic Speed Method

The algorithm for the continuous stability index according to the characteristic speed also bases on the discrete stability index. Table 4.8 describes the transition of one discrete stability index (left column) to the next one (right column) by means of an appropriate calculation method for the CSI. Fig. 4.15 illustrates the different discrete stability indices based on δ_W, $\dot{\psi}$ and v_{ch}. According to Fig. 4.15, for example a stability index of 5 results, if the wheel turn angle exceeds the cornering threshold and the absolute value of the characteristic speed additionally ranges between v_{CoG}^2 and $k \cdot v_{CoG}^2$. One of the "adjacent states" for DSI=5 is for example DSI=6. That means, the more $|v_{ch}^2|$ approaches v_{CoG}^2, the larger the continuous stability index becomes until it finally converges against DSI=6. The equation for the calculation of the CSI between 5 and 6 is presented in Table 4.8.
Table 4.8 shows the transitions between the discrete stability indices by means of the CSI. Starting with DSI=1, depending on the wheel turn angle a transition towards a stable curve drive (DSI=2) or an instable straightforward situation (DSI=3) occurs.

Start: DSI	Main condition	Calculation of CSI	Limit: CSI→x
1		$1 + \left(\underbrace{\frac{\lvert\delta_W\rvert}{\delta_{W,th}}}_{max=1} \cdot 1 + \underbrace{\frac{\left\lvert\dot{\psi}_{meas}\right\rvert}{\dot{\psi}_{th}}}_{max=1} \cdot 2 \right)$	x=2 or x=3
2	$v_{ch}^2 \geq 0$	$2 + \left(1 - \underbrace{\frac{\left\lvert\lvert v_{ch}^2\rvert - k v_{CoG}^2\right\rvert}{v_{Ch,t}}}_{max=1} \right) \cdot 2$	x=4
	$v_{ch}^2 < 0$	$2 + \left(1 - \underbrace{\frac{\left\lvert\lvert v_{ch}^2\rvert - k v_{CoG}^2\right\rvert}{v_{Ch,t}}}_{max=1} \right) \cdot 3$	x=5
3		$3 + \underbrace{\frac{\lvert\delta_W\rvert}{\delta_{W,th}}}_{max=1} \cdot 1$	x=4
		$3 + \underbrace{\frac{\lvert\delta_W\rvert}{\delta_{W,th}}}_{max=1} \cdot 2$	x=5
4		$4 + \left(\underbrace{\frac{\left\lvert\lvert v_{ch}^2\rvert - k v_{CoG}^2\right\rvert}{k v_{CoG}^2}}_{max=1} \right) \cdot 1$	x=5
5		$5 + \left(\underbrace{\frac{\left\lvert\lvert v_{ch}^2\rvert - k v_{CoG}^2\right\rvert}{\left\lvert v_{CoG}^2 - k v_{CoG}^2\right\rvert}}_{max=1} \right) \cdot 1$	x=6
6		no changes	

Table 4.8: Characteristic speed method: continuous stability index

Start: DSI	Main condition	Calculation of CSI	Limit: CSI→x
1		$1+\left(\underbrace{\frac{\lvert\delta_W\rvert}{\delta_{W,th}}}_{max=1}\cdot 1+\underbrace{\frac{\left\lvert\frac{1}{r_{meas}}-\frac{1}{r_{model}}\right\rvert}{\Delta p_1}}_{max=1}\cdot 2\right)$	x=2 or x=3
2	$\frac{1}{r_{meas}}<\frac{1}{r_{model}}$	$2+\underbrace{\frac{\left\lvert\frac{1}{r_{meas}}-\frac{1}{r_{model}}\right\rvert}{\Delta n_1}}_{max=1}\cdot 2$	x=4
	$\frac{1}{r_{meas}}\geq\frac{1}{r_{model}}$	$2+\underbrace{\frac{\left\lvert\frac{1}{r_{meas}}-\frac{1}{r_{model}}\right\rvert}{\Delta p_1}}_{max=1}\cdot 3$	x=5
3	$\frac{1}{r_{meas}}\leq\frac{1}{r_{model}}-\Delta n_1$	$3+\underbrace{\frac{\lvert\delta_W\rvert}{\delta_{W,th}}}_{max=1}\cdot 1$	x=4
	$\frac{1}{r_{meas}}\geq\frac{1}{r_{model}}+\Delta p_1$	$3+\underbrace{\frac{\lvert\delta_W\rvert}{\delta_{W,th}}}_{max=1}\cdot 2$	x=5
4	$\frac{1}{r_{model}}\geq 0$	$4+\underbrace{\frac{\overbrace{\left\lvert\frac{1}{r_{meas}}-\frac{1}{r_{model}}+\Delta n_1\right\rvert}^{(*)}}{\left\lvert-\Delta n_2-\frac{1}{r_{model}}+\Delta n_1\right\rvert}}_{max=1}\cdot 2$	x=6
5	$\frac{1}{r_{model}}\geq 0$	$5+\underbrace{\frac{\left\lvert\frac{1}{r_{meas}}-\frac{1}{r_{model}}-\Delta p_1\right\rvert}{\left\lvert\Delta p_2-\frac{1}{r_{model}}-\Delta p_1\right\rvert}}_{max=1}\cdot 1$	x=6
6		no changes	

Table 4.9: Curve radius method: CSI (equations for left curve only)

If the car is driving in a stable curve (DSI=2), as a main condition the square of the characteristic speed v_{ch}^2 must be considered: if v_{ch}^2 is positive, the vehicle understeers and consequently a transition from DSI=2 to DSI=4 must occur. For oversteer, the state changes to DSI=5. In this case, if $|v_{ch}^2|$ approaches $k \cdot v_{CoG}^2$ (see Fig. 4.15), the fraction in brackets of Table 4.8 is zero and the CSI converges against DSI=5. The division by $v_{Ch,t} = 2050$ is required to achieve a smooth transition between stable curve drive and oversteer or understeer. It represents a vehicle parameter gained from a variety of test drives.
The other calculation equations can be reconstructed by means of Fig. 4.15.

4.2.4 Curve Radius Method

Fig. 4.7 shows the wheel turn angle and the tolerance band of the inverse curve radius. For a left curve with $1/r_{meas} > 0$ the following considerations are underlying: if the inverse curve radius falls below the "inner tolerance band" the vehicle understeers. Right at the border the measured curve radius is $1/r_{model} - \Delta n_1$. According to Table 4.9, the CSI in this case is 4, because the fraction $(*)$ is 0. Approaching the outer tolerance band $-\Delta n_2$ linearly increases the CSI value to its limit CSI=6 (see Table 4.9), because the fraction $(*)$ in the respective equation of the table becomes 1. The equation guarantees that the CSI covers every real value between 4 and 6. The main condition in Table 4.9 decides, whether the equations for a left or a right curve must be applied. In the table, only the equations for a left curve are displayed for space reasons. For DSI=2 and DSI=3 the main condition is also used to distinguish between transitions to DSI=4 (understeer) and DSI=5 (oversteer).
Processing an algorithm with the conditions specified in Table 4.9 guarantees that the stability index is a real number between 1 and 6. CSI=6 cannot be exceeded.
For a right curve, the equations are accordingly.

4.2.5 Self-steer Gradient Method

The conversion from the discrete to the continuous stability index is simpler for the self-steer gradient method than for the other methods, because the thresholds are symmetrical around 0 (see Fig. 4.16). The following example illustrates the calculation of the CSI by means of Table 4.10: if the wheel turn angle is larger than the cornering threshold $\delta_{W,th}$ and if additionally the SSG_m passes the SSG_{u1} threshold, the CSI becomes 4 (see Table 4.10).

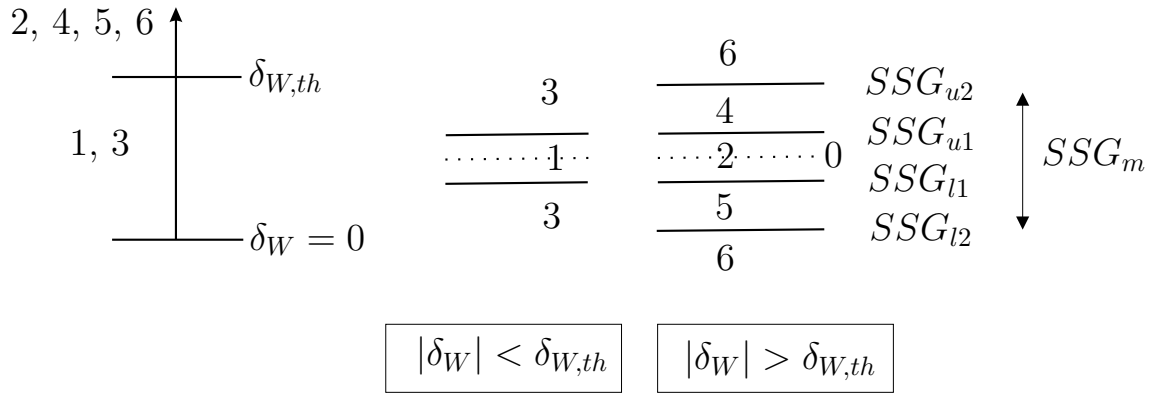

Figure 4.16: Tolerance band of the self-steer gradient method

Starting from DSI=4, the CSI increases to DSI=6, if SSG_m approaches SSG_{u2}. The fraction $(**)$ then linearly reaches its maximum value 1. The position of SSG_m between SSG_{u1} and SSG_{u2} in Fig. 4.16 determines the value of the CSI.
The transition from DSI=5 to DSI=6 is symmetrical to $SSG_m = 0$. The main condition in the second column of Table 4.10 decides, whether the states "2" and "3" change to DSI=4 (understeer) or DSI=5 (oversteer).
Compared to the other methods, the calculation of the continuous stability index of the self-steer gradient method is much simpler. This is one of the main advantages for implementing the method.

4.2.6 Implementation of the CSI-method

The motivation to introduce a continuous stability index in the last sections was to bring the results of the individual methods in line. The choice of fixed limits for the discrete stability index can cause significant deviations, if an inconvenient combination of sensor signals occurs.
The Tables 4.7 to 4.10 have shown that the CSI is a real number in the range of $1 \leq \text{CSI} \leq 6$. Compared to the DSI, the classification of a driving situation with linguistic terms like "understeer" or "oversteer" gets lost. For example, if one method yields a CSI of 5.2 it is unclear, if this is caused by an understeer or oversteer drive (see Fig. 4.17). Either the DSI or the evaluation of the main condition in Tables 4.7 - 4.10 is necessary to decide, if the left (DSI=4 $\rightarrow$ 6) or the right transition (DSI=5 $\rightarrow$ 6) is responsible for CSI=5.2. Only with knowledge about the currently active edge in the DSI-graph shown in Fig. 4.17 a classification with the CSI is possible.
Accepting that the classification characteristic gets more complex for the CSI, the advantage is obvious: the larger the CSI-value is, the more a

Start: DSI	Main condition	Calculation of CSI	Limit: SI→x
1		$1+\left(\underbrace{\frac{\lvert\delta_W\rvert}{\delta_{W,th}}}_{max=1}\cdot 1+\underbrace{\frac{\lvert SSG_m\rvert}{SSG_{u1}}}_{max=1}\cdot 2\right)$	x=2 or x=3
2	$SSG_m \geq 0$	$2+\underbrace{\left\lvert\frac{SSG_m}{SSG_{u1}}\right\rvert}_{max=1}\cdot 2$	x=4
	$SSG_m < 0$	$2+\underbrace{\left\lvert\frac{SSG_m}{SSG_{l1}}\right\rvert}_{max=1}\cdot 3$	x=5
3	$SSG_m \geq SSG_{u1}$	$3+\underbrace{\frac{\lvert\delta_W\rvert}{\delta_{W,th}}}_{max=1}\cdot 1$	x=4
	$SSG_m \leq SSG_{l1}$	$3+\underbrace{\frac{\lvert\delta_W\rvert}{\delta_{W,th}}}_{max=1}\cdot 2$	x=5
4		$4+\underbrace{\frac{\overbrace{SSG_m-SSG_{u1}}^{(**)}}{SSG_{u2}-SSG_{u1}}}_{max=1}\cdot 2$	x=6
5		$5+\underbrace{\frac{SSG_m-SSG_{l1}}{SSG_{l2}-SSG_{l1}}}_{max=1}\cdot 1$	x=6
6		no changes	

Table 4.10: Self-steer gradient method: continuous stability index

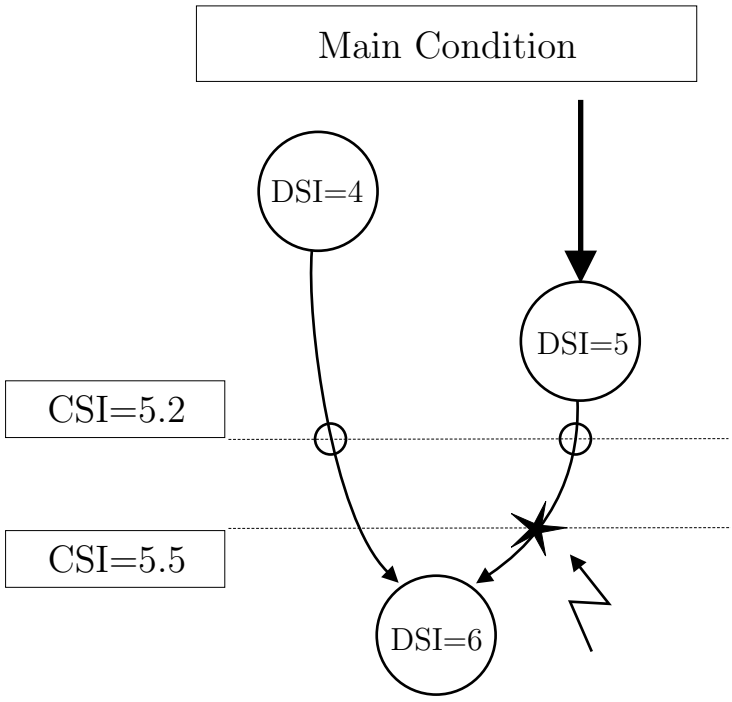

Figure 4.17: Different possible transitions in the DSI-graph cause uncertainties in the CSI method

drive situation deviates from the (linear) driver's desire. That means, for average drivers the increase of the CSI-value is a measure for a critical drive situation.

Fig. 4.18 shows the discrete and real stability indices gained from the four different methods for a test drive. The figure shows that for this combination of measurement signals the DSI values of the different methods significantly deviate. The characteristic speed method for example does not correctly detect the understeer drive between $t = 5s$ and $t = 11s$ and the oversteer situation for $t > 14s$. Comparing the four methods shows that the correlation between the CSI values is bigger than between the DSI. Only the peak for the CS-method between $t = 2.5s$ and $t = 4s$ is false. One peculiarity of the curve radius method can be seen as well. It is the only method where the DSI and CSI drop out between $t = 12s$ and $t = 14s$ is missing. The drops are caused by the steering behavior of the driver in this situation. As the CRM does not process the wheel turn angle, it does not "recognize" the CSI drop.

For this test drive of an inconvenient signal combination the results can be improved. Tests with a variety of measurements confirm the tendency that the CSI increases the robustness of the detection process.

As mentioned above, the CSI describes the "deviation from a linear reference". In Sections 4.2.7 and 4.2.8 the physical behavior of the car is compared with the continuous stability index.

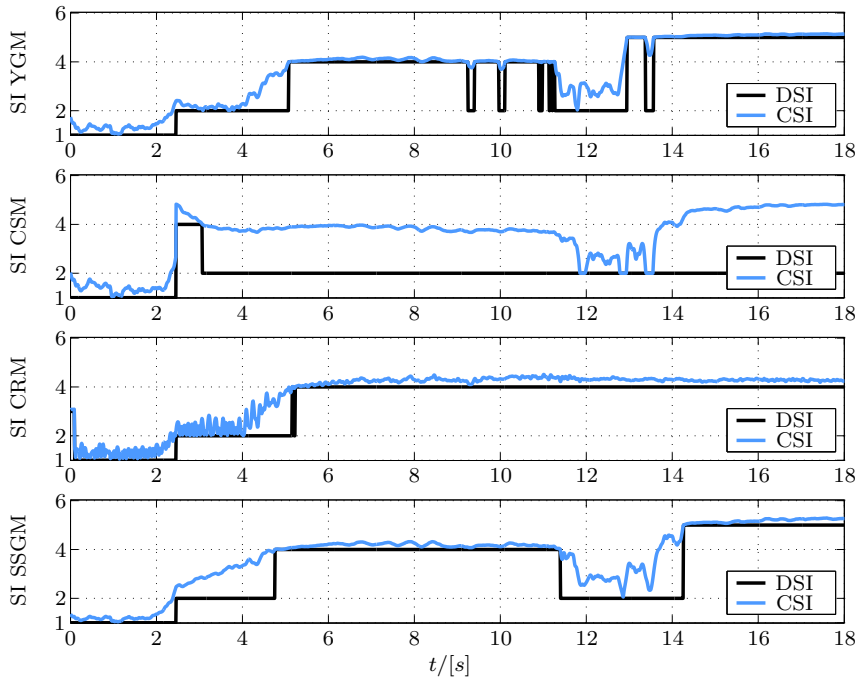

Figure 4.18: Discrete and continuous stability indices for a clothoide drive

4.2.7 Comparing CSI and Cornering Stiffness

In critical situations, the lateral vehicle dynamics becomes non-linear. Section 3.4.2 shows that this is mainly caused by the non-linear lateral wheel force characteristic causing a decrease of the cornering stiffnesses. The relation between the DSI and the cornering stiffnesses is illustrated in Figs. 4.19(a) and 4.19(b). The lateral wheel forces were measured with a multi-axes wheel torque sensor (see Section 6.3), the tire side slip angle with an optical reference sensor (Table D.2 in Appendix D.3). Employing Eqn. (3.74) provides a measured reference value for the cornering stiffness. The underlying test drive of Fig. 4.19(a) was a stationary circle drive on dry asphalt with lateral accelerations of approximately $4m/s^2$. According to [53] this is the upper border of linear vehicle behavior for dry roads. The CSI values range between 2.3 and 3.5 indicating stable driving. The measured cornering stiffness at the inner rear wheel remains constant at about $35500N/rad$. Fig. 4.19(b) is a faster stationary circle drive with lateral accelerations of averagely $6m/s^2$. Here, the driving behavior deviates significantly from the linear reference model. Accordingly, the CSI values exceed CSI=4. The cornering stiffness value falls below $20000N/rad$.
Comparing Figs. 4.19(a) and 4.19(b) shows that the reduction of cornering stiffness is tightly related to an increase of the stability index. If the wheel force reserve and so the cornering stiffness decreases the vehicle responses

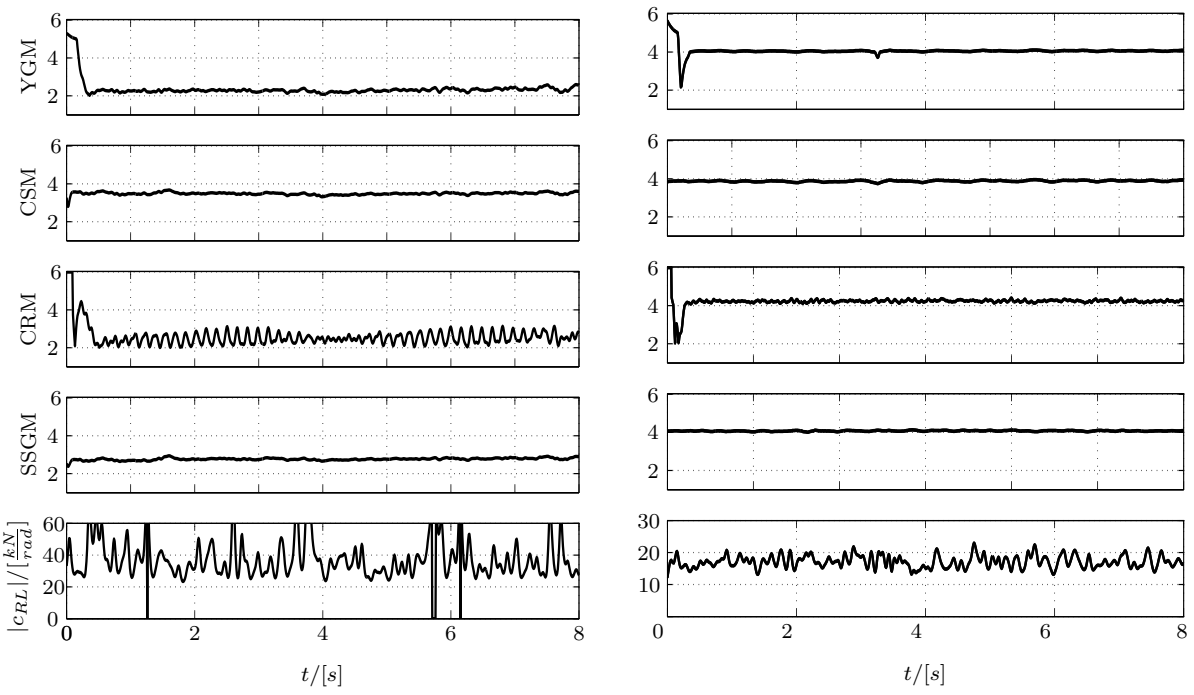

(a) small lateral acceleration

(b) medium lateral acceleration

Figure 4.19: Continuous stability indices and cornering stiffness for a stationary circle

to the driver inputs are no more proportional. The vehicle behavior deviates from the driver's desire. That is the reason for the increasing continuous stability index.
The CSI method is capable to describe the physical vehicle behavior of the conducted test drives correctly.

4.2.8 Comparing CSI and Side Slip Angle

In this section, the CSI of the self-steer gradient method is compared to the vehicle body side slip angle. According to [27] the VBSSA is a measure for the controllability of cars. Large absolute values or increased vehicle body side slip rates are sensed as very inconvenient by the driver. This means that large VBSSA values should correspond to large CSI values.
Fig. 4.20 shows a transient curve drive with slow increase of the steering angle. The vehicle body side slip angle was measured with an optical reference sensor. The increase of δ_W causes a yaw rate $\dot{\psi} = 1rad/s$ and a lateral acceleration up to $a_Y = 7.5m/s^2$. The vehicle body side slip angle grows constantly up to a very large value of $\beta = 13°$. The self-steering gradient method instantly detects an understeer tendency which changes to an in-

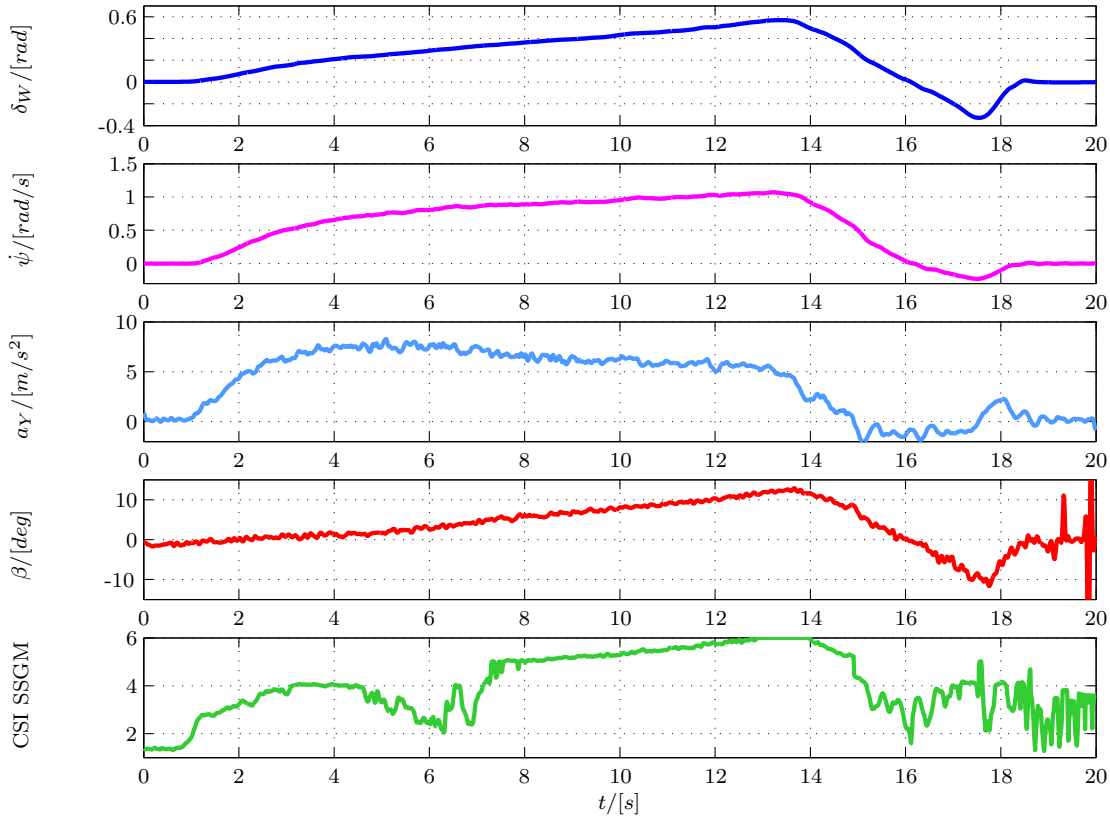

Figure 4.20: Comparison of CSI and measured vehicle body side slip angle β of a transient circle with decreasing curve radius

stable drive at $t > 8s$. The driver is counter-steering at $t = 16s$ causing the decrease of CSI. At $t = 19s$ the vehicle stands still. The CSI correctly detects instable driving situations with increased β-values. For highly dynamical curve drives, the increase of β lags. The CSI is then capable to detect the critical situation before the VBSSA builds up.

4.3 Trigger Signal for Event Data Recorder

In order to not overwrite the data recorded in an EDR, a trigger signal for "freezing" must be generated.
The continuous stability index is a means to detect laterally critical driving situations. A real number between $1 \leq \text{CSI} \leq 6$ is generated providing information about the driving state by means of four different methods. Tests with a variety of measurement data gained from two test cars with different drivers have shown that a critical situation can be defined by a CSI exceeding 5.5.

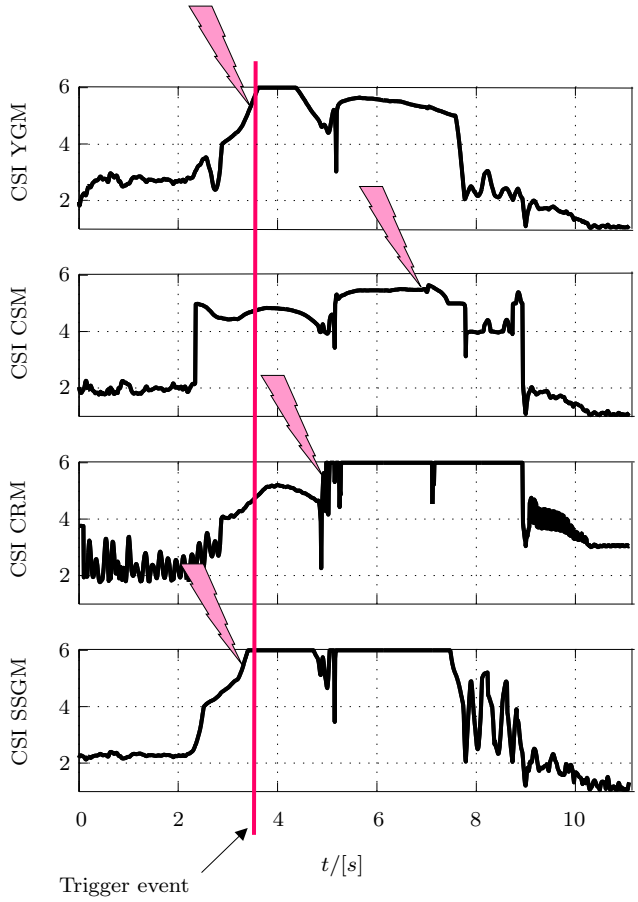

Figure 4.21: Continuous stability index and trigger signal for event data recorder

The reliability and robustness can be increased by employing the "two-of-four method": only if at least two of the four methods have got a CSI > 5.5, then the trigger signal for the event data recorder is generated. To avoid false triggering by sensor drop outs, additionally each CSI signal must exceed the detection threshold for more than five sampling steps, i.e. for more than $50ms$.
Fig. 4.21 shows the real stability indices of an unstable J-Turn measurement drive. The arrows mark the points in time, when the respective method's CSI exceeds the detection threshold. In this test drive, the yaw gain method (YGM) first "detects" the critical situation after $t = 3.3s$ followed by the self-steer gradient method (SSGM) at $t = 3.51s$. Both methods have got a CSI > 5.5 for more than $50ms$. As two of the four methods are permanently above DSI=5.5, the trigger event signal for the EDR is generated. The curve radius method (CRM) and the characteristic speed method (CSM) exceed DSI=5.5 at $t = 4.9s$ and at $t = 7s$. Therefore, they do not contribute to the triggering process in this test drive.

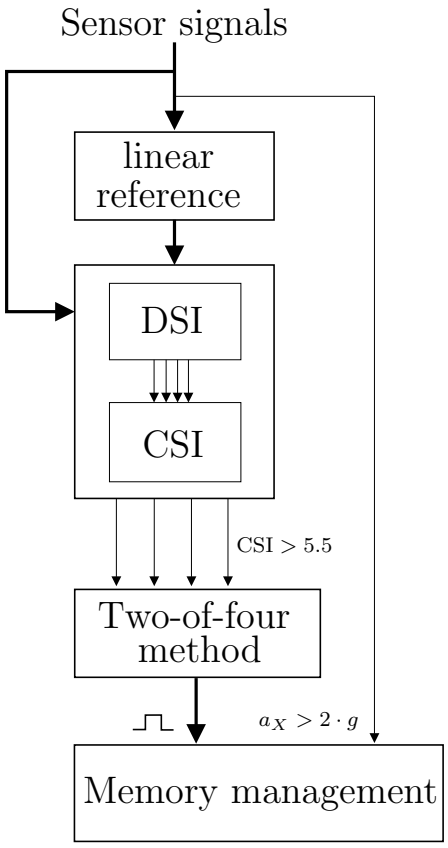

Figure 4.22: Triggering concept based on the stability index

4.4 Conclusion

Chapter 4 deals with the detection and classification of laterally critical driving situations to "freeze" the data in an event data recorder. Existing concepts for triggering EDRs do not consider the vehicle dynamics. They evaluate only the longitudinal acceleration. If the longitudinal acceleration exceeds a certain threshold, then the data in the EDR is "frozen".
The methodology presented in this chapter is an extension of this triggering strategy (see Fig. 4.22). It considers accidents with critical vehicle dynamics behavior before the crash.
For the definition of a critical driving situation, the deviation from a linear reference model is evaluated. The underlying idea is that the average driver's steering behavior and the responding vehicle reaction can be described with a linear model. If the real vehicle dynamics deviates too much from the linear field of experience of the driver, then the situation is rated as laterally critical.
Four different methods were presented in this chapter which evaluate the deviation from the linear model. An integer value called *discrete stability index* categorizes the driving situation in six states: a stable or an

unstable straightforward drive, a stable curve, an under- or an oversteer situation and finally a breakout situation. The employed thresholds result from a measurement campaign carried out by [68]. This assumes, however, that newer vehicle constructions and tire design do not affect the thresholds. Furthermore, the thresholds were determined for dry road conditions. Changes of the thresholds on low μ roads are imaginable. Thirdly, if the self-steer properties of a car varies with increasing velocity, this might not be considered by the thresholds. The DSI method was validated with measurements and approved the driver's sense during most of the test drives.

However, due to the fix thresholds of the DSI method, the individual stability indices of the four methods can deviate for inconvenient sensor signal combinations. The introduction of a *continuous stability index* reduces this problem. The CSI of the four detection methods correlate more than the DSI. However, a classification of driving states with the CSI methodology is complicated.

The CSI method was validated with measurements of two different vehicles. Some of the parameters and thresholds employed must be adapted to the respective test car. The results were compared with measurements of the cornering stiffness and the vehicle body side slip angle. They were consistent proving that the physics of lateral vehicle motion is correctly described by the CSI method.

To trigger the memory management (Fig. 4.22) not to overwrite recorded data in an EDR any more, a *two-of-four method* was employed. If at least two of the four presented methods output a CSI > 5.5 for more than $50ms$, then a trigger signal for the EDR is generated.

The methodology to detect and classify pre-accident situations enhances the known strategies to freeze EDR data. Apart from detecting accident situations, the results can also be used to reconstruct accidents by analyzing the vehicle dynamics in the pre-crash phase (see also steering performance assessment in Section 5.9).

The methods should be tuned with more test drives and varying cars on different friction characteristics.

5 Reconstruction of Road Traffic Accidents

According to [15], a road traffic accident is *a violent disruption of the intended motion sequence combined with damage and personal injury.*
Reconstruction of road traffic accidents is necessary for increasing the traffic security. Apart from this idealistic approach, of course the materialistic aspect must be clarified as well: the liability question.
To obtain as much information as possible about the accident situation, two main goals of accident reconstruction can be defined:

1. Motions of persons and vehicles directly or indirectly involved into the accident situation must be reconstructed from the beginning of the pre-accident phase over the actual accident event until the standstill position of the accident participants.

2. Driver, vehicle and environmental causes must be investigated concerning their influence on the reconstructed vehicle motion.

Of course, the complete accident cannot be reconstructed only by means of the data acquired and calculated by the event data recorder presented in Chapter 2. An accident reconstruction expert is still required. His work can be *supported* by EDR data, but he cannot be *completely replaced.*
Even the first demand of accident reconstruction cannot be met. With the specified sensor equipment of the employed system it is impossible to gain information about other vehicles involved in the accident scene.
Fig. 5.1 gives an overview over accident reconstruction based on EDR data. The information acquired can be used to reconstruct vehicle, driver and environmental influences. For the *vehicle* motion, the trajectory and particularly its heading and center of gravity location must be reconstructed. The fuzzy system presented in Sections 5.1 - 5.3 in combination with the vehicle body side slip angle observers of Section 5.4 guarantee complete trajectory reconstruction.
The vehicle dynamics behavior of the car can be reconstructed with the discrete stability index presented in Chapter 4. Driving situations like over-

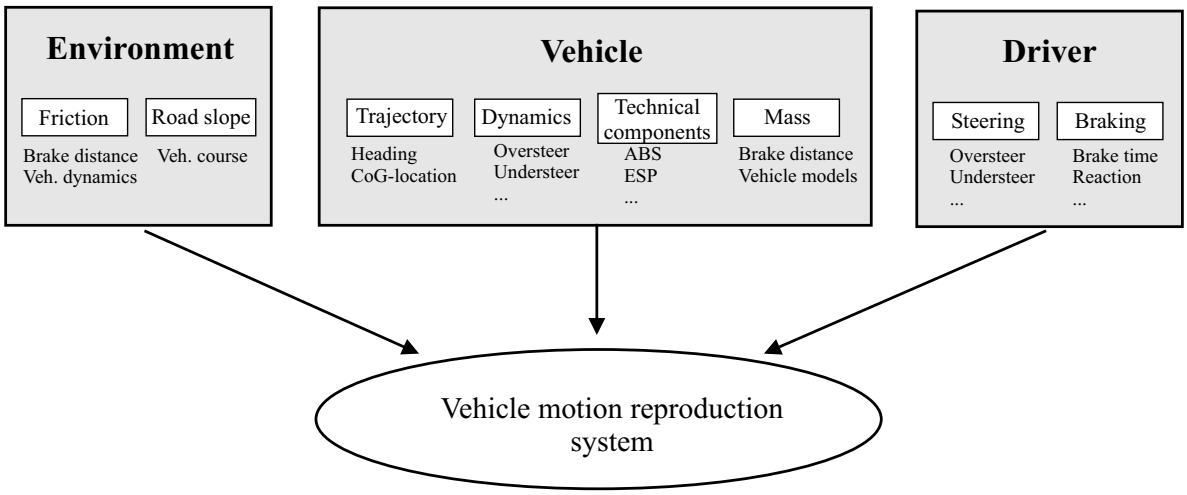

Figure 5.1: Goals of accident reconstruction with EDR data

steer, understeer and so on are distinguished to clarify the pre-accident vehicle behavior.

The vehicle model accuracy and the braking distance significantly depend on the vehicle mass. Among other parameters, the vehicle mass is certainly the one which has the greatest significance for accident reconstruction. Therefore, in Section 5.5 the vehicle mass is determined by means of a recursive least squares algorithm applied in certain driving situations.

Modern vehicles contain a variety of electronic control systems. Knowledge about the proper functionality of these systems is an important issue of accident reconstruction. Therefore, an algorithm to detect ABS-cycles by processing only the wheel speed sensor signals is presented in Section 5.6.

The *environment* significantly affects the vehicle and driver behavior. The illumination of the accident scene, the temperature, the road condition, the view are influencing not only the braking behavior and vehicle motion. Without external sensors, it is almost impossible to gain information about the environment. Without human knowledge and statements of witnesses, complete accident reconstruction is unthinkable. Nevertheless, in Section 5.7 the friction coefficient is estimated in hard braking and acceleration situations to get more knowledge about the road surface. In combination with ABS-cycle detection, in most cases those situations can be detected, where the friction of the road surface is maximal. Only then, the road condition can be assessed. The road gradient is determined in Section 5.8 with a linear observer. For complete vehicle motion reproduction and to get an idea of the vehicle environment, the road gradient is a useful quantity.

Finally, the *driver* behavior must of course be considered. Driver application of indicators, lights and so on have to be evaluated as well as the

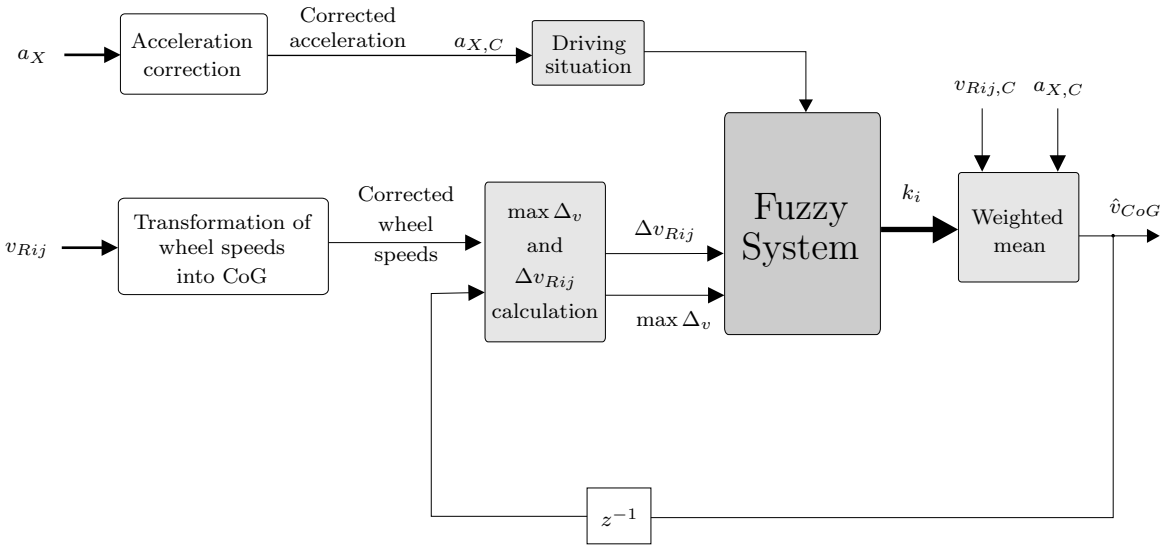

Figure 5.2: Structure of the fuzzy estimator with data pre-processing

driver's braking and steering performance. Reactions to e.g. understeer and oversteer behavior can be evaluated using the stability index method of Chapter 4. As complete driver assessment increases the boundaries of this thesis, the driver performance is limited to a theoretical approach analyzing the driver's steering behavior in critical driving situations (Section 5.9).

5.1 Fuzzy Velocity Estimator

Fig. 5.2 shows the complete fuzzy velocity estimation system. In a first step, the wheel speed and acceleration signals are preprocessed. On basis of the corrected signals, appropriate inputs into the fuzzy system are generated and the driving situation is categorized. The fuzzy system outputs weighting factors for the individual wheel speed signals and for the acceleration signal and calculates the velocity estimate $\hat{v}_{CoG}$ with a weighted mean equation.

5.1.1 Sensor Data Preprocessing

Wheel speeds The wheel speed sensors are providing false values when the vehicle is cornering: the outer wheels are traveling a longer distance in curves than the inner. The inner wheel speeds are too small, whereas the outer ones are too high. Therefore, the wheel speeds have to be transformed

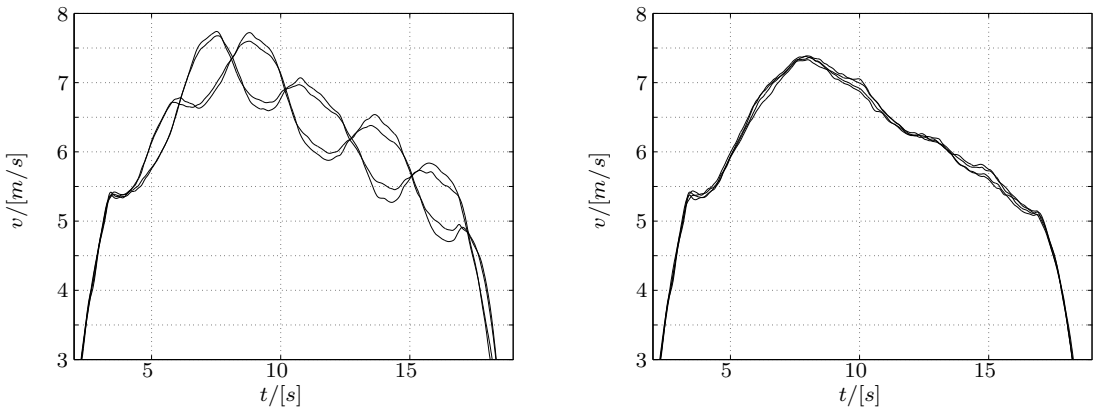

(a) Wheel speeds v_{Rij} before transformation into CoG

(b) Wheel speeds $v_{Rij,C}$ after transformation into CoG

Figure 5.3: Wheel speeds during a sinusodial drive

into the center of gravity to eliminate these systematic errors:

$$\begin{aligned} v_{RFL,C} &= \left(v_{RFL} + \dot{\psi}\left(\frac{b_F}{2} - l_F \sin\beta\right)\right)\cos(\delta_W - \beta) \quad , \\ v_{RFR,C} &= \left(v_{RFR} - \dot{\psi}\left(\frac{b_F}{2} + l_F \sin\beta\right)\right)\cos(\delta_W - \beta) \quad , \\ v_{RRL,C} &= \left(v_{RRL} + \dot{\psi}\left(\frac{b_R}{2} + l_R \sin\beta\right)\right)\cos\beta \quad , \\ v_{RRR,C} &= \left(v_{RRR} - \dot{\psi}\left(\frac{b_R}{2} - l_R \sin\beta\right)\right)\cos\beta \quad . \end{aligned} \tag{5.1}$$

Fig. 5.3(a) shows the individual wheel speeds of a slalom drive before and after the transformation into the center of gravity. The original velocity differences caused by the individual curve radii are almost eliminated in Fig. 5.3(b).

Acceleration signal The acceleration signal is unreliable due to offsets of the acceleration sensor. As the acceleration must be integrated in order to achieve the velocity, these offset errors cumulate. Additional errors of the acceleration sensor are caused by false orientation. False orientation occurs, when the sensor is not mounted exactly in the vehicle's longitudinal axis or when the longitudinal axis deviates significantly from the velocity vector. This happens in driving situations with large vehicle body side slip angle values β, for big pitch angles χ (panic braking) or for significant road slopes χ_{Road}, [30]. All these influences are considered in the following correction

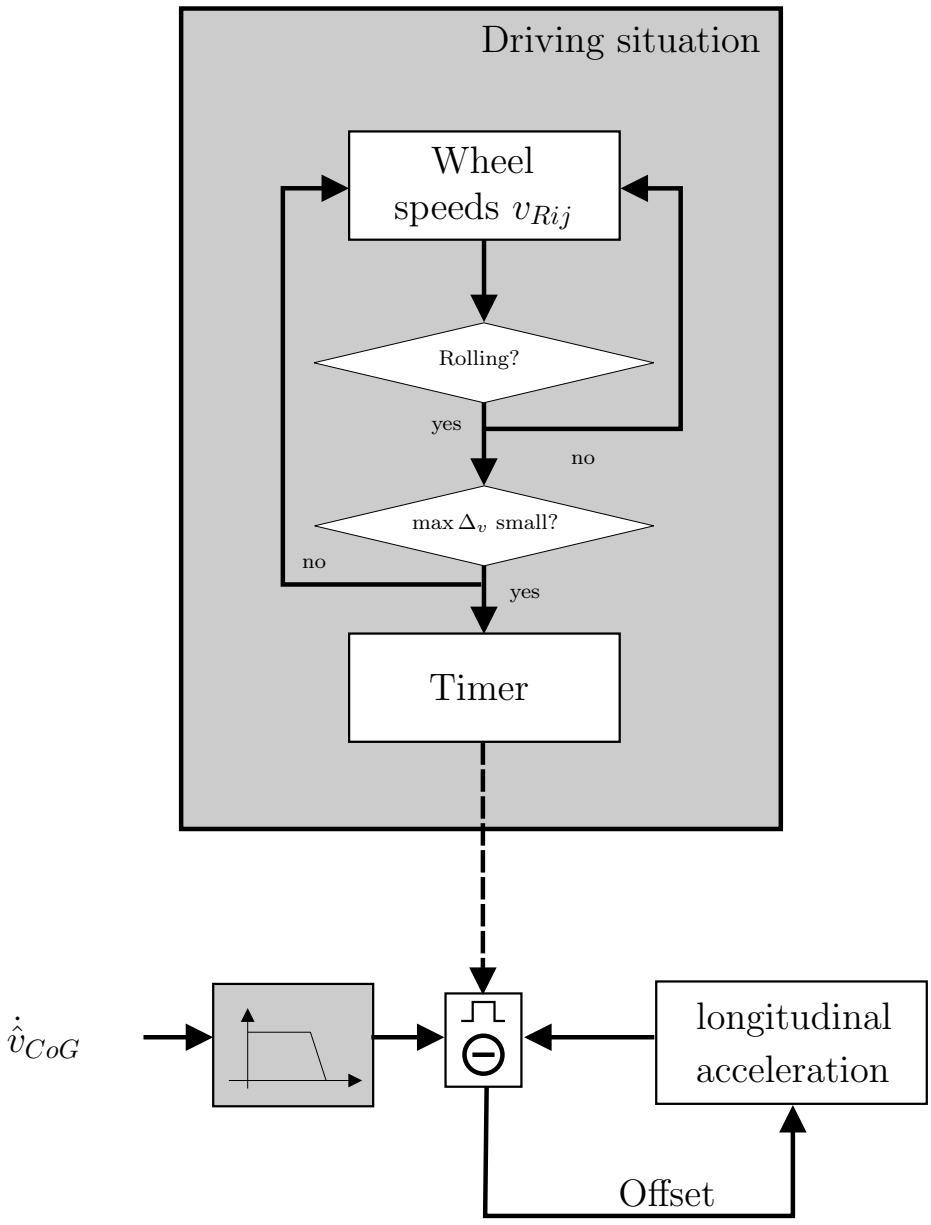

Figure 5.4: Process of offset elimination of the acceleration sensor

equation:

$$a_{X,C} \approx a_X - \underbrace{g \sin(\chi - \chi_{Road})}_{\text{gravitational effects}} + a_Y \cdot \beta - a_{X,0} \quad . \tag{5.2}$$

Note that the definitions of the angles χ_{Road} and χ are important: the pitch angle χ is positive in braking situations, whereas the road slope is positive for uphill driving (see Appendix B.3).
In order to reduce the error of the acceleration sensor signal, an offset reduction algorithm was set up. Fig. 5.4 shows the procedure to reduce the sensor errors explained in Eqn. (5.2). The signal $\dot{\hat{v}}_{CoG}$ gained from the fuzzy

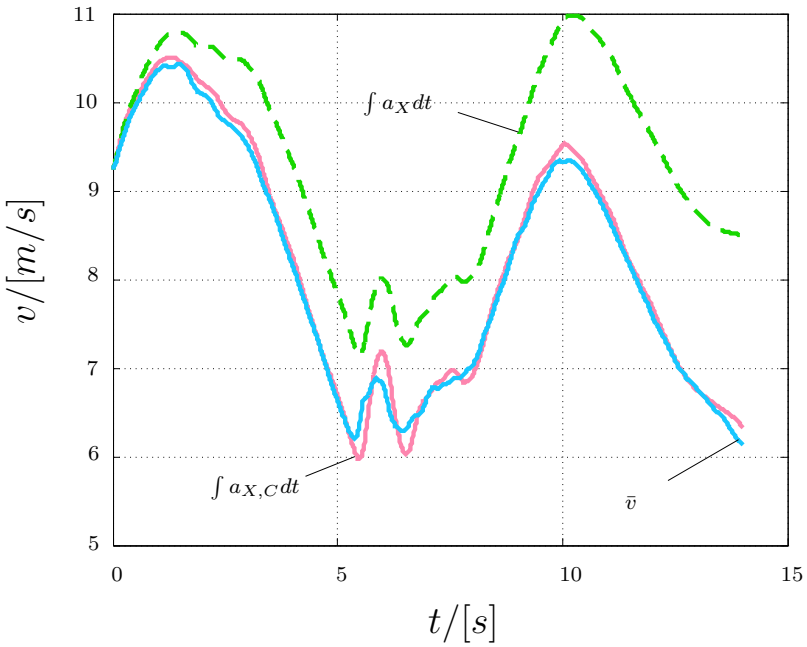

Figure 5.5: Effect of offset elimination on integrated acceleration signal

estimate of the last simulation step is used as a reference. To reduce noise caused by the derivation of $\hat{v}_{CoG}$, a third order BUTTERWORTH-filter with a cut-off frequency $f_C = 200Hz$ is applied.
If the maximum velocity difference is small and the acceleration close to zero, then the state "rolling" is detected and $\max \Delta_v$ is small. To avoid sensor errors, this state must not change for $t = 20ms$. In case these conditions are fulfilled, the difference to the value of $\dot{\hat{v}}_{CoG}$ represents the offset which is subtracted from the measured acceleration signal.
Fig. 5.5 shows the positive effects of the offset elimination strategy. The integrated acceleration is too large without offset elimination. Employing offset elimination, the integrated acceleration ranges close to the averaged wheel speed $\bar{v}$.

5.1.2 Fuzzy System

In this section, the data fusion of the four wheel speed signals and the longitudinal acceleration sensor signal is implemented with a fuzzy estimator. The rule base of the fuzzy estimator contains the heuristic knowledge about the individual sensor signal errors during different driving situations. Based on the sensor errors, weighting factors are generated by the fuzzy estimator. The four weighting factors $k_1, \ldots, k_4$ for the wheel speed sensor signals and that for the acceleration signal k_5 are employed to determine the estimation value $\hat{v}_{CoG}$ for the center of gravity velocity

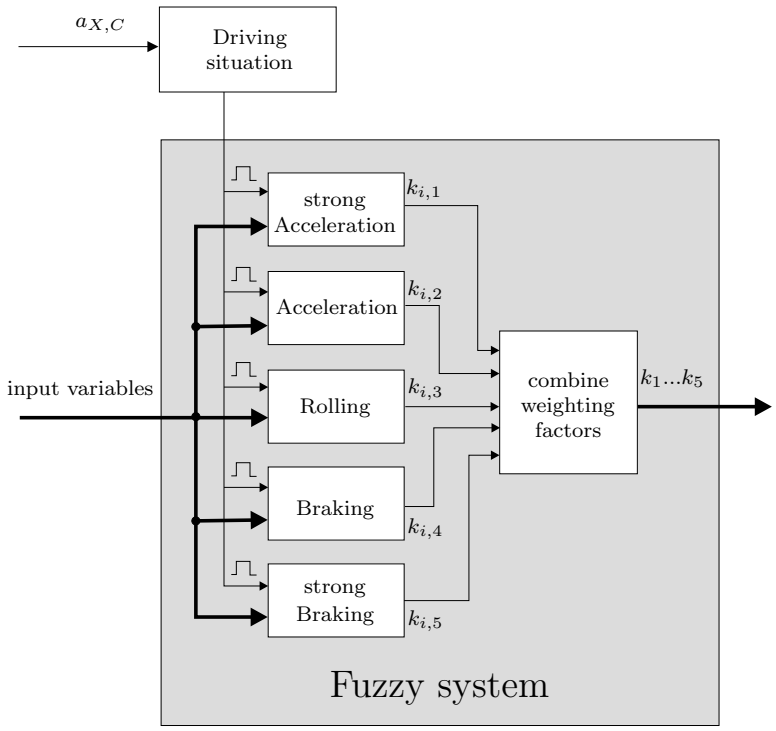

Figure 5.6: Partitioned fuzzy estimator

$$\hat{v}_{CoG}(k) = \frac{\sum_{i=1}^{4} k_i \cdot v_{Ri,C}(k) + k_5 \left[\hat{v}_{CoG}(k-1) + T_S \cdot a_{X,C}(k)\right]}{\sum_{i=1}^{5} k_i} \quad . \tag{5.3}$$

Eqn. (5.3) is a weighted mean of all sensor signals. The $v_{Ri,C}$ in Eqn. (5.3) are the $v_{Rij,C}$ from Eqns. (5.1). The goal of the fuzzy estimator is to determine the weighting factors k_i in Eqn. (5.3) appropriately.

Sub-Models

In order to reduce the number of active rules in the rule base of the fuzzy estimator, the fuzzy system is partitioned into five sub-models, see Fig. 5.6. The corrected longitudinal acceleration signal $a_{X,C}$ is taken to distinguish between the five driving conditions "strong Acceleration", "Acceleration", "Rolling", "Braking" and "strong Braking". Each of these sub-systems contains a reduced rule base suited for the respective driving situation. The input signals of all five sub-systems are identical and will be presented next.

Input Signals

Apart from the corrected longitudinal acceleration $a_{X,C}$ only signals containing information about the sensor signal reliability are suitable as inputs into the fuzzy estimator.
In addition to the above five signals, the difference between the corrected wheel speeds $v_{Rij,C}$ and the last estimated vehicle velocity value $\hat{v}_{CoG}$ is considered:

$$\Delta v_{Rij} = v_{Rij,C}(k) - \hat{v}_{CoG}(k-1) \quad . \tag{5.4}$$

Large deviations Δv_R of a specific wheel speed indicate slip at this wheel. Under such conditions, the wheel speed signal of the respective wheel is inaccurate. Therefore, the respective weighting factor is reduced by the fuzzy estimator. The difference Δv_R is correlated to the slip. However, the absolute value of Δv_R is usually larger than the slip and less sensitive to noise and errors.
The maximum deviation $\max \Delta_v$ of the corrected wheel speeds $v_{Rij,C}$ is taken to assess the quality of a signal

$$\max \Delta_v = \left| \hat{v}_{CoG} - \max_{ij} \{v_{Rij,C}\} \right| + \left| \hat{v}_{CoG} - \min_{ij} \{v_{Rij,C}\} \right| \quad . \tag{5.5}$$

For values of $\max \Delta_v$ around zero, the vehicle velocity can be determined by just averaging the four corrected wheel speeds $v_{Rij,C}$. In this case, the fuzzy estimator is not used at all.
If $\max \Delta_v$ is "small", as shown in the lower left corner of Fig. 5.7, the wheel speed signal deviations may no longer be neglected. In this case, the fuzzy estimator generates individual weighting factors for the wheel speeds and the acceleration signal.
"Small" values of $\max \Delta_v$ indicate that two conditions are fulfilled: firstly, the measured velocity signal from the wheel speed sensors is close to the previously estimated value $\hat{v}_{CoG}$. If the estimated value $\hat{v}_{CoG}$ drifts away, this is detected by $\max \Delta_v$ exceeding a certain threshold, see Fig. 5.8(a). Secondly, if both the maximum and the minimum wheel speed are very close to $\hat{v}_{CoG}$, the individual wheel speeds do not deviate significantly from each other. Then, the wheel speed signals are considered reliable and the fuzzy estimator generates a high weight for them.
"Big" values of $\max \Delta_v$ indicate sensor errors or disturbances (see Fig. 5.8(b)), for instance spinning wheels or ABS-braking. The fuzzy estimator then reduces the wheel speed signal weights accordingly.

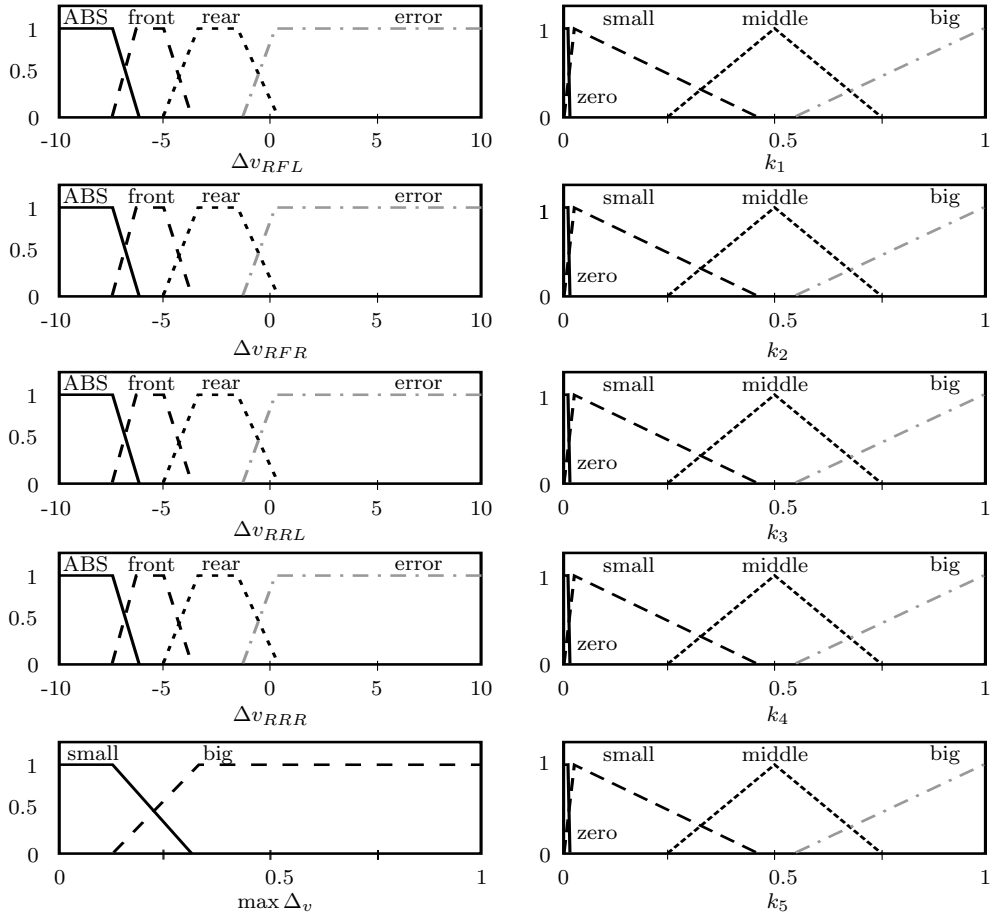

Figure 5.7: Membership functions of sub-system "strong Braking"

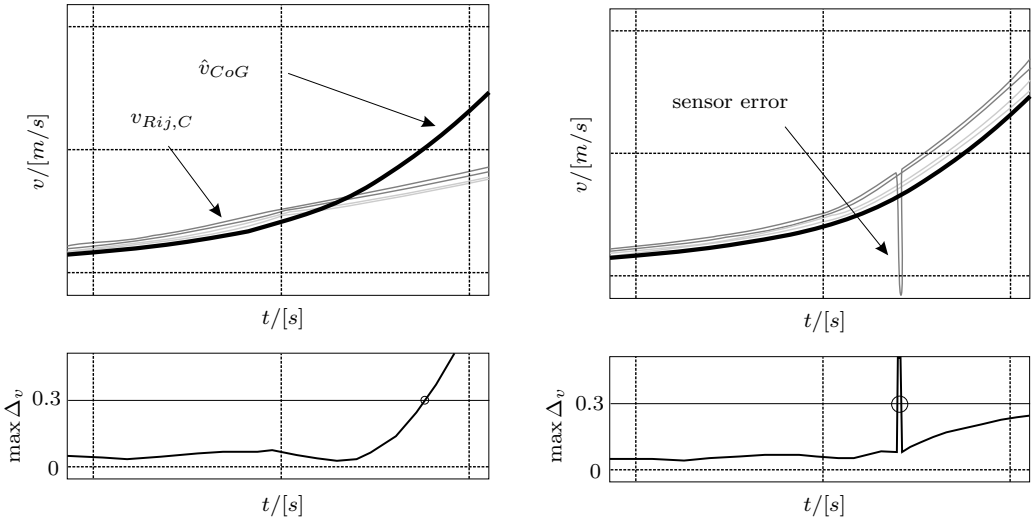

(a) Detection of instabilities of the fuzzy estimator

(b) Detection of a sensor error

Figure 5.8: Detection of errors using $\max \Delta_v$

Output Signals

The fuzzy system generates weighting factors in correlation to the accuracy of the wheel speed signals and the acceleration signal. According to its input signals $a_{X,C}$, $\max \Delta_v$ and Δv_{Rij} the rule base of the fuzzy estimator generates a signal reliability "zero", "small", "middle" or "'big". The membership functions can be seen in the right column of Fig. 5.7. The defuzzified, crisp output values k_i, $i = 1, \ldots, 5$, are weighting factors in the range of [0...1]. The k_i are processed by Eqn. (5.3) to generate the estimated value $\hat{v}_{CoG}$ for the center of gravity velocity.

Rule Base

All rules in the rule base contain the AND operator only. The MAMDANI-implication ([41]) is employed and all the membership functions used in the system are trapezoid to reduce processing complexity.
Due to a sensor-specific drift, the acceleration sensor signal is unreliable. Therefore, its weight should be kept small whenever possible. The time periods, during which the acceleration signal is integrated to gain the vehicle speed should be as short as possible. To meet this constraint, the weight of at least one wheel speed signal generated from the rule base is non-zero. This will normally prevent the estimated vehicle velocity from drifting away when solely using the integrated acceleration. When the vehicle velocity still drifts away in some cases, $\max \Delta_v$ and Δv_{Rij} are analyzed to detect this effect (see Fig. 5.8(a)).
For the sub-system "strong Braking" ($a_{X,C} < -3m/s^2$) the membership functions are displayed in Fig. 5.7. Table 5.1 provides an idea of the rule base structure.
Braking with a deceleration below $-3m/s^2$ causes large slip values on the wheels. Therefore, a small weighting factor is assigned to the wheel speed signals here. Generally, the braking force on the front wheels is higher than that on the rear wheels. This increases the probability of ABS-cycles on the front axle. Accordingly, the front wheel speed signals are used only if the rear wheel speed signals are erroneous. In such situations, the acceleration sensor provides the best signal. The integrated acceleration signal is then weighted highest.
For the other four sub-systems, the rule base is composed of similar rules (see Appendix C.1). However, these rules are adapted specifically to the respective driving situation.

Δv_{RFL}	Δv_{RFR}	Δv_{RRL}	Δv_{RRR}	max Δ_v	k FL	k FR	k RL	k RR	k v(a)
-	-	-	-	small	zero	zero	small	small	big
-	-	rear	rear	big	zero	zero	small	small	middle
-	-	not rear	rear	big	zero	zero	zero	big	middle
-	-	rear	not rear	big	zero	zero	big	zero	middle
front	-	not rear	not rear	big	small	zero	zero	zero	big
-	front	not rear	not rear	big	zero	small	zero	zero	big
ABS	ABS	front	front	big	zero	zero	small	small	big

Table 5.1: Rule base for the v-Fuzzy subsystem "strong Braking"

5.1.3 Results of Vehicle Velocity Estimator

A test drive with hard braking is used to validate the vehicle velocity estimation. The results can be seen in Fig. 5.9. After accelerating up to a vehicle speed of $v_{CoG} = 11m/s$, a panic braking to vehicle standstill was conducted. At the bottom of Fig. 5.9, the current driving conditions can be seen, compare Fig. 5.6. The dashed line for the integrated acceleration shows that the vehicle velocity would drift away even when derived from the *corrected* acceleration signal $a_{X,C}$. Therefore, the time windows during which the acceleration signal is integrated are kept as short as possible. In the first phase of Fig. 5.9 ("bad ABS-sensors"), the wheel speed sensors are below their activation threshold. Due to their measuring principle, inductive ABS sensors are only activated above a certain wheel speed. Below the activation threshold, the signal is unreliable. The vehicle velocity is derived solely by integrating the acceleration signal $a_{X,C}$. The middle part of Fig. 5.9 shows the difference velocities Δv_{Rij}. In the second phase ("strong Acceleration"), the corrected wheel speeds are all above the estimated vehicle velocity $\hat{v}_{CoG}$ due to drive slip. Between $t = 5.2s$ and $t = 5.6s$, the vehicle is in "Rolling" condition. Almost no slip occurs and the velocity differences are close to zero. In the last phase ("strong Braking"), the velocity differences Δv_{Rij} are significantly below 0 due to a large brake slip. ABS-cycles at the front wheels cause velocity drops of $v_{RFL,C}$ and $v_{RFR,C}$. The front wheel speed signals are rated as "ABS" or "erroneous". Thus, the weights for these signals are zero. At the very end of the measurement, the wheel speed signals fall below the activation threshold of the ABS sensors. The velocity is again determined only by integration of $a_{X,C}$.
Fig. 5.10 zooms into the start of the strong braking phase of the test drive described above. At the beginning, after approximately $t = 10.6s$, the fuzzy estimator detects large deviations Δv_{Rij} of the front wheel speeds and

rates the front wheel speed sensor signals as erroneous. The estimated vehicle velocity $\hat{v}_{CoG}$ is then approximately equal to the velocity of the rear wheels. After approximately $t = 10.75s$, the driving condition changes from "Rolling" to "Braking/strong Braking". Now, all the wheel speed signals are rated as unreliable due to slip. In this driving situation the integrated acceleration signal is the main signal for estimating the vehicle velocity. The estimated vehicle velocity in Fig. 5.10 is almost permanently slightly above the highest wheel velocity. ABS control cycles from the wheel speeds are completely suppressed.

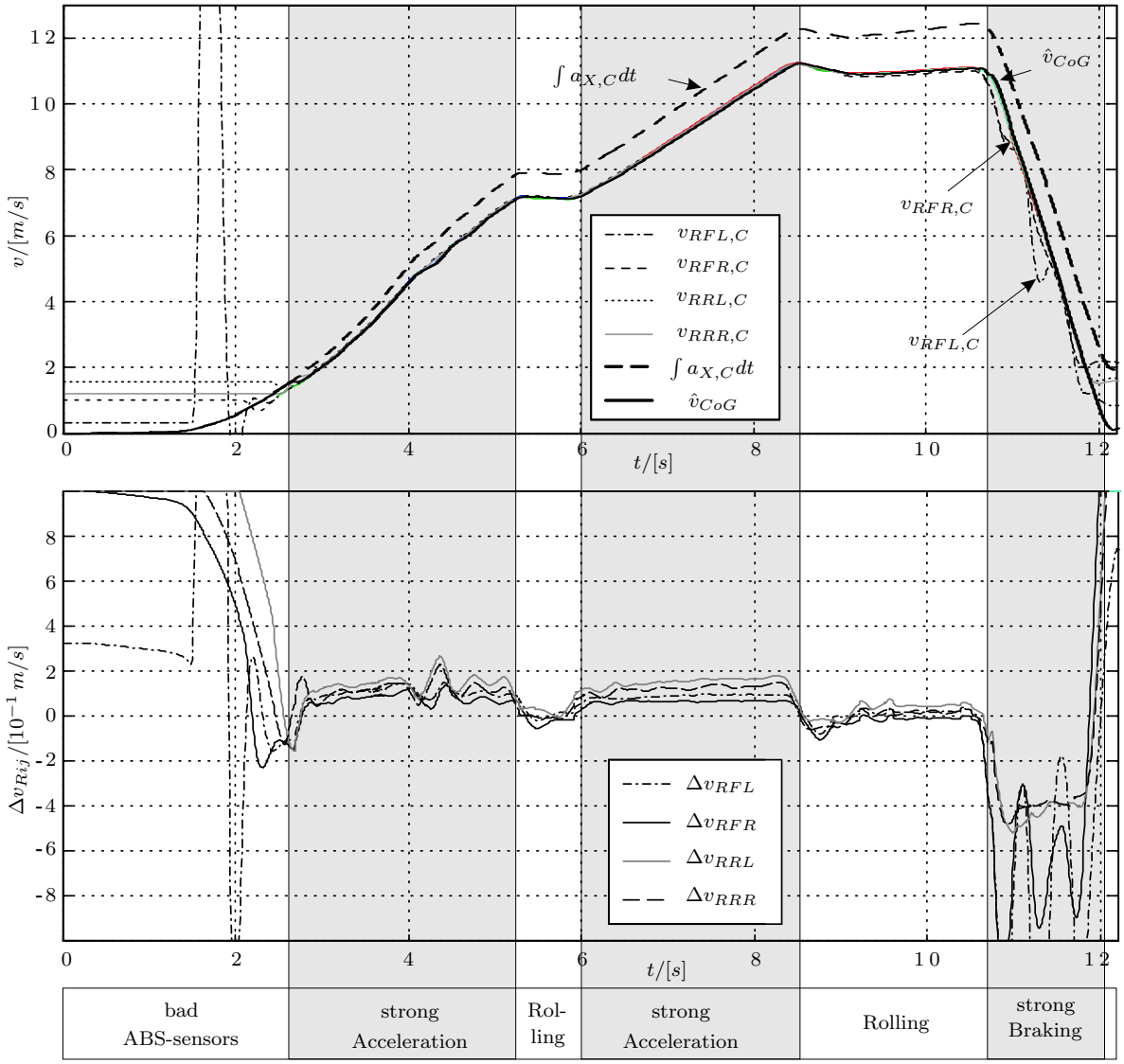

Figure 5.9: Velocities (top) and Δv_{Rij} (bottom) during an ABS test drive

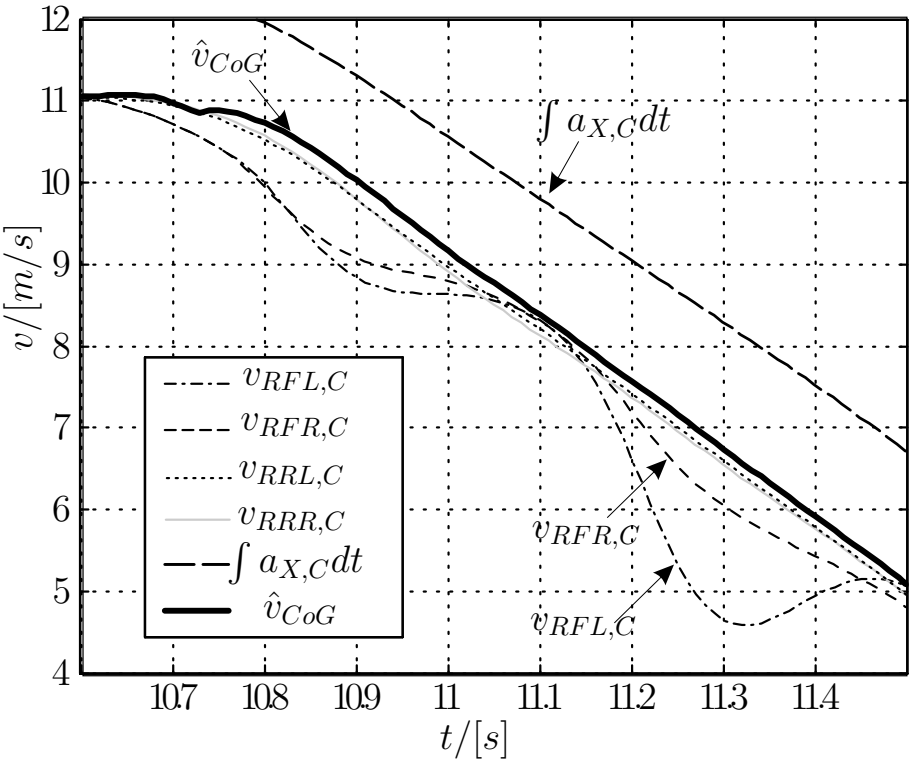

Figure 5.10: Initial phase of an ABS braking test drive

5.2 Fuzzy Yaw Rate Estimator

Accurate yaw rate signals $\dot{\psi}$ are crucial for vehicle dynamics control systems. Usually the yaw rate is measured with a gyroscope sensor. One main disadvantage of available gyroscopes is their offset drift caused by temperature changes. In order to increase the accuracy of the yaw rate signal, signals from different sensors are fused for yaw rate calculation. Their weights are determined according to the driving situation. For this procedure, a fuzzy estimator similar to the one presented in Section 5.1 is used. After describing the setup of the fuzzy yaw rate estimator, its quality and robustness shall be validated in Section 5.3 by means of trajectory reconstruction.

5.2.1 Sensor Data Preprocessing

The gyroscope signal is preprocessed before using it for yaw rate calculation. The idea is to eliminate the time-varying gyroscope offset according to the driving situation. The gyroscope signal value is certainly zero if the vehicle is standing still or when driving exactly straightforward. The goal therefore is to determine these driving situations: standstill and straight-

forward driving. After turning the ignition key to start the vehicle, the gyroscope's yaw rate signal is reset to zero. At traffic lights or during other standstill situations, the wheel speed signals and the acceleration signals are taken as a means to detect standstill in order to eliminate the gyroscope signal offset. A more sophisticated approach is chosen to detect straightforward driving. Assuming equal slip values $s_{Res,ij}$ and equal tire radii $r_{stat,ij}$ at each wheel the rotational wheel speeds ω_{Rij} can be used as a means to detect straightforward driving. Ideally, all rotational wheel speeds should be equal then. However, due to noise, radius deviations, different tire pressures and other influences, the rotational velocities will slightly deviate even when driving straightforward. Taking the maximum deviation $\max \Delta_\omega$ of the rotational equivalent wheel velocities, ω_{Rij} though, provides a sufficiently accurate criterion to detect straightforward driving:

$$\max \Delta_\omega = \max_{ij}\{\omega_{Rij}\} - \min_{ij}\{\omega_{Rij}\} \tag{5.6}$$

If $\max \Delta_\omega$ ranges below a certain threshold ε, the signal value from the gyroscope sensor $\dot{\psi}_S$ can be set to zero:

$$\max \Delta_\omega < \varepsilon \quad \Rightarrow \quad \dot{\psi}_S \stackrel{!}{=} 0 \tag{5.7}$$

The standstill detection presented above and the criterion for straightforward driving (Eqns. (5.6) and (5.7)) improve the gyroscope sensor signal already. However, sufficient accuracy for the yaw rate signal can only be achieved when fusing the gyroscope sensor signal with yaw rate signals calculated from the wheel speeds. This will be shown in the following sections.

5.2.2 Yaw Rate Calculation Using the Wheel Speeds

In curves, the wheels of outer and inner vehicle track run with different velocities. The outer wheels travel a larger distance than the inner wheels. By using a simple triangular approximation, the velocity difference can be used to calculate the yaw rates of front and rear axle:

$$\dot{\psi}_F = \frac{(\omega_{RFR} - \omega_{RFL}) \cdot r_{stat}}{b_F \cdot \cos \delta_W} \quad , \tag{5.8}$$

$$\dot{\psi}_R = \frac{(\omega_{RRR} - \omega_{RRL}) \cdot r_{stat}}{b_R} \quad . \tag{5.9}$$

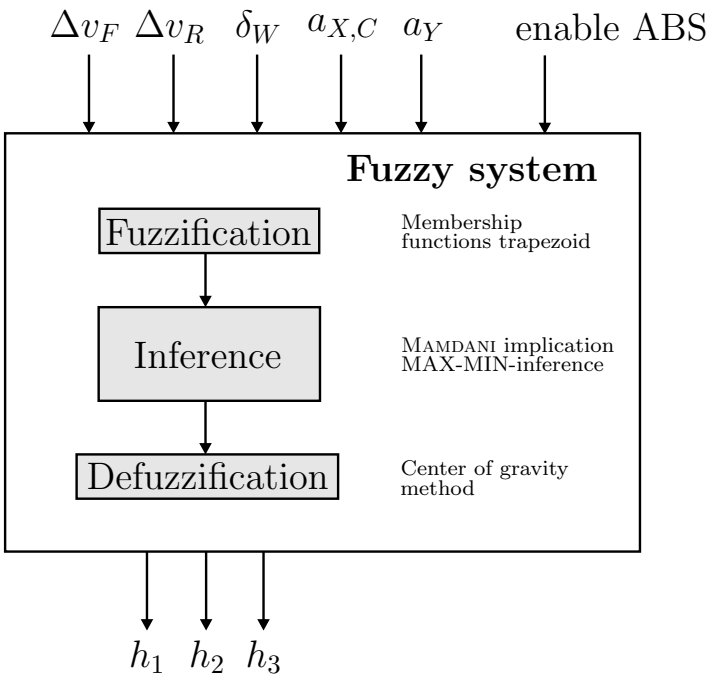

Figure 5.11: Overview over employed fuzzy system, [36]

Eqns. (5.8) and (5.9) assume the same tire radius r_{stat} on all wheels. The parameters b_F and b_R are again the track of front and rear axle. Considering the third yaw rate signal $\dot{\psi}_S$ coming from the gyroscope sensor, the fuzzy system generates weighting factors h_i, $i = 1, \ldots, 3$, before merging the respective individual sensor signals.

5.2.3 Fuzzy System

Fig. 5.11 shows the setup of the fuzzy system. The inputs will be explained in this section. Additionally, a status flag "enable ABS" is used. This flag indicates whether or not the ABS sensor signals can be used for yaw rate calculation. Due to the inductive working principle of today's ABS wheel speed sensors, the velocity is not reliable below a certain velocity threshold. In this case, only the yaw rate sensor's signal $\dot{\psi}_S$ is used for the yaw rate estimate $\dot{\psi}_{Fuz}$.
The inference method used in the fuzzy system is the MAMDANI-implication. This means that the logical value of the conclusion is always smaller than the one of the assumption. The linguistic inputs are logically connected with the AND operator. The rule base of the system can be found in Appendix C.2.
For defuzzification, the center of gravity method was chosen. It represents the standard method and it is capable of smoothing the output.

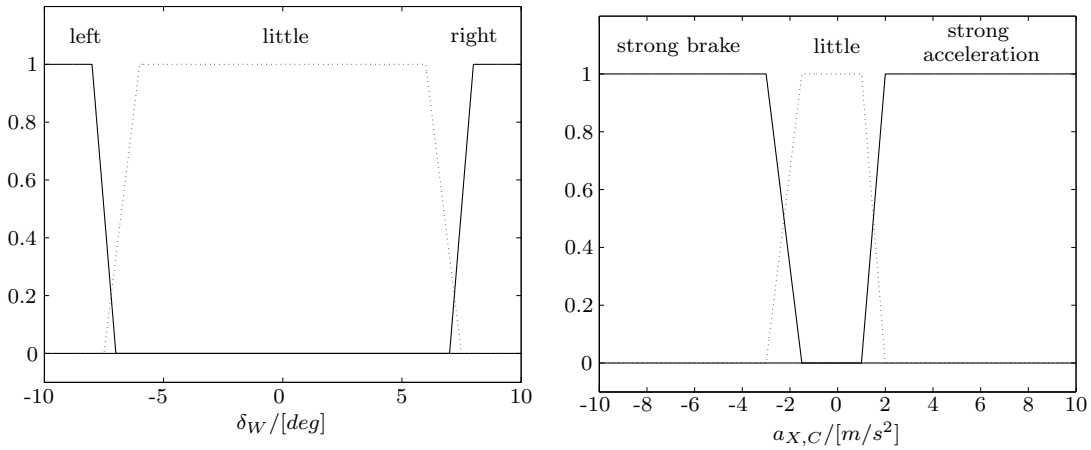

(a) Membership functions of δ_W (b) Membership functions of $a_{X,C}$

Figure 5.12: Membership functions of system inputs

Inputs

The estimator inputs should allow to consider the current driving situation. The rules generate weighting factors corresponding to the individual sensors' measurement errors.

Wheel Turn Angle δ_W The wheel turn angle indicates whether the curve radius is large or small. It also disturbs the velocity calculation at the front axle. As a consequence, the calculated yaw rate increases with growing steering angle, [68]. Furthermore, for small curve radii the yaw rate calculated from the wheel speeds of the rear track is weighted less. The membership functions of δ_W are displayed in Fig. 5.12(a).

Longitudinal Acceleration $a_{X,C}$ The longitudinal acceleration signal's membership functions are illustrated in Fig. 5.12(b). Accelerations $a_{X,C}$ other than little indicate large brake or drive slip, where the wheel speed signals are inaccurate. Therefore, in braking situations the front axle's wheel speeds are weighted small, whereas those for the rear axle are weighted medium. This is due to the braking force distribution. The braking force and the resulting braking slip are larger at the front axle.

Lateral Acceleration a_Y Along with the wheel turn angle δ_W, the lateral acceleration assesses the degree of curve driving. At very high lateral accelerations, the wheel load shifts to the outer wheels and causes large slip values at the inner wheels. Therefore, the inner wheel speeds are weighted less. The membership functions for a_Y are almost equal to the ones of $a_{X,C}$.

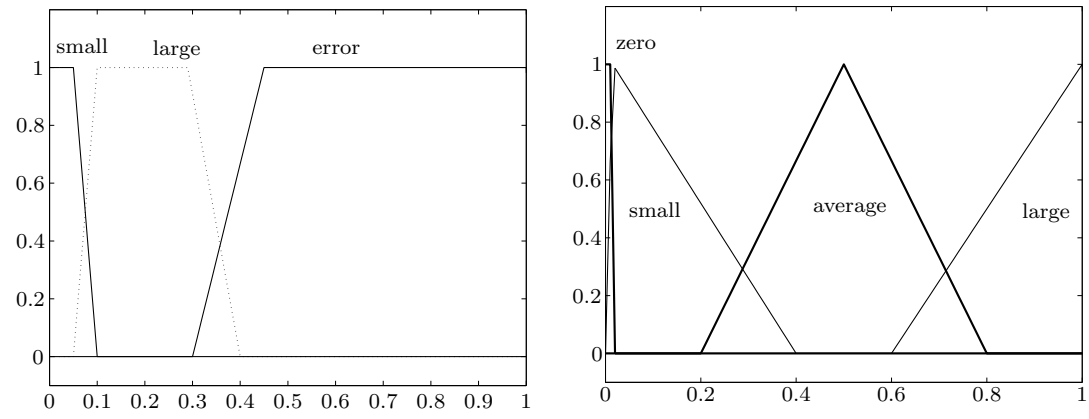

(a) Input Δv_F (in m/s) (b) Outputs h_i

Figure 5.13: Membership functions of fuzzy estimator

Wheel Speed Differences at Front and Rear Axle Δv_F and Δv_R
Δv_F and Δv_R describe the two axle's wheel speed differences. For the front axle, this yields

$$\Delta v_F = |\hat{v}_{CoG} - v_{RFR,C}| + |v_{RFR,C} - v_{RFL,C}| \quad . \tag{5.10}$$

For the rear axle, respectively

$$\Delta v_R = \underbrace{|\hat{v}_{CoG} - v_{RRR,C}|}_{\text{"condition 1"}} + \underbrace{|v_{RRR,C} - v_{RRL,C}|}_{\text{"condition 2"}} \quad . \tag{5.11}$$

Δv_R in Eqn. (5.11) is small, if two conditions are fulfilled: firstly, if the corrected velocity $v_{RRR,C}$ is close to the previously estimated vehicle velocity $\hat{v}_{CoG}$ ("condition 1"). Secondly, both corrected velocities $v_{RRL,C}$ and $v_{RRR,C}$ must be almost equal ("condition 2"). If both ABS sensors failed, then $v_{RRL,C}$ and $v_{RRR,C}$ would be equal. Without condition 1, the weight for the failing ABS sensors would be high. The estimation results would then be completely wrong. By means of condition 1 though, a large deviation from the vehicle velocity is detected and the sensors are not weighted at all. Condition 1 therefore ensures the stability of the fuzzy estimator. That means, if Δv_R is small, then the calculated yaw rate signal is reliable and the weight for the respective sensors is high.
Fig. 5.13(a) shows the membership functions for Δv_F. Those for Δv_R are similar.

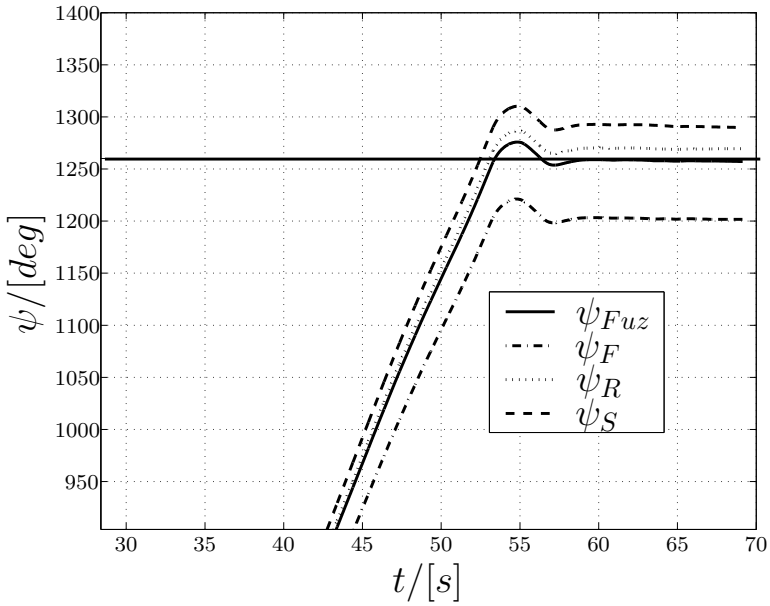

Figure 5.14: Reconstructed yaw angle of multiple drive through roundabout traffic

Outputs

The output variables of the fuzzy estimator are the three weighting factors, h_1 for the gyroscope, h_2 for the yaw rate at the front axle and h_3 for the yaw rate at the rear axle. The weight ranges between $[0, 1]$ and the membership functions are displayed in Fig. 5.13(b). If a signal is not reliable at all, then it is weighted "zero". If the reliability increases, the corresponding weight rises and the membership functions are "small", "average" and "large". The weighting factors are used to calculate a weighted mean of the sensor signals according to their reliability:

$$\dot{\psi}_{Fuz} = \frac{h_1 \cdot \dot{\psi}_S + h_2 \cdot \dot{\psi}_F + h_3 \cdot \dot{\psi}_R}{\sum_{i=1}^{3} h_i} \quad . \tag{5.12}$$

5.2.4 Measurement: Roundabout Traffic on Public Road

The test drive was carried out on a public road. The test vehicle initially parks along the road before driving for a distance of approximately 80 m. Then it enters a roundabout traffic. The vehicle drives three times through the roundabout traffic and finally leaves it in the opposite direction back to

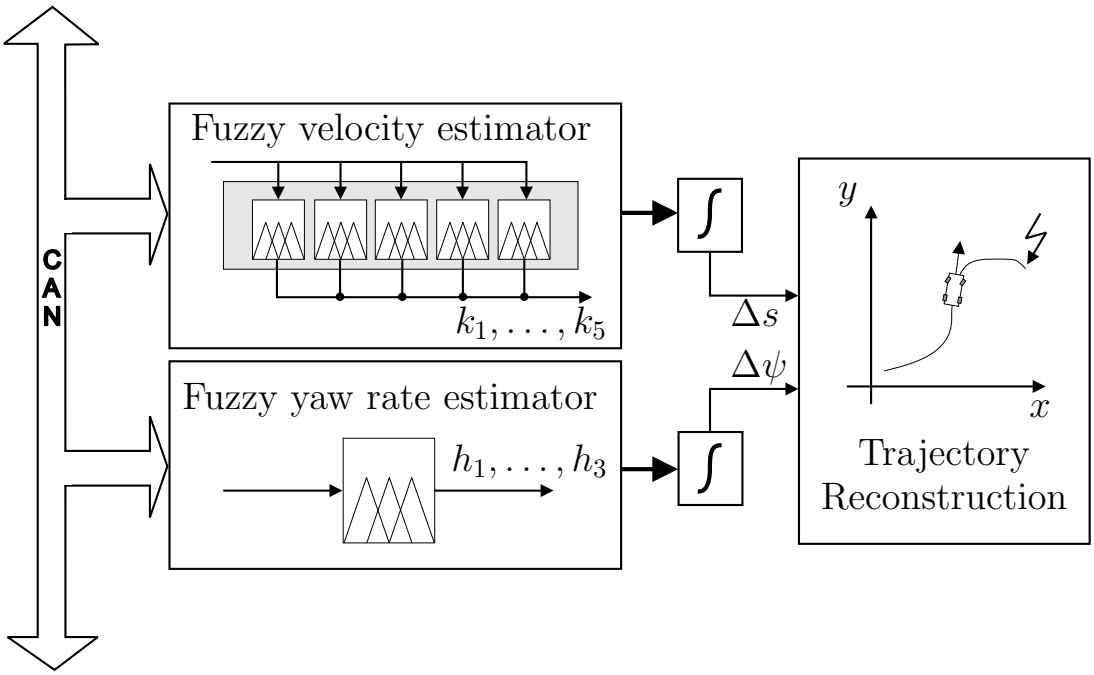

Figure 5.15: Trajectory reconstruction using the fuzzy velocity and yaw rate estimator

its initial location. Fig. 5.14 shows the results of the test drive during which the vehicle turns by a yaw angle of 1260 degrees. The straight horizontal line represents this final value. To validate the yaw rate estimation, the yaw rates from the sensors and from the fuzzy system were integrated to get the yaw angle. As expected, the fuzzy yaw angle ψ_{Fuz} approximates the true value best. The yaw angles from the gyroscope (ψ_S) and from the rear axle ψ_R are too large, whereas the one from the front axle ψ_F is too small in this test.

5.3 Trajectory Reconstruction

The reconstruction of the vehicle trajectory can be used as a means to validate the fuzzy velocity and the fuzzy yaw rate estimator. For this, the velocity calculated in Section 5.1 and the yaw rate determined in Section 5.2 are integrated and applied to the trajectory reconstruction block. A block diagram of it can be seen in Fig. 5.15.

In this section, the equations for the vehicle location are derived. Then the fuzzy systems are analyzed regarding their robustness. Apart from accident reconstruction, an accurate vehicle position is e.g. desired in vehicle navigation systems, should the satellite-based positioning not be available in specific situations.

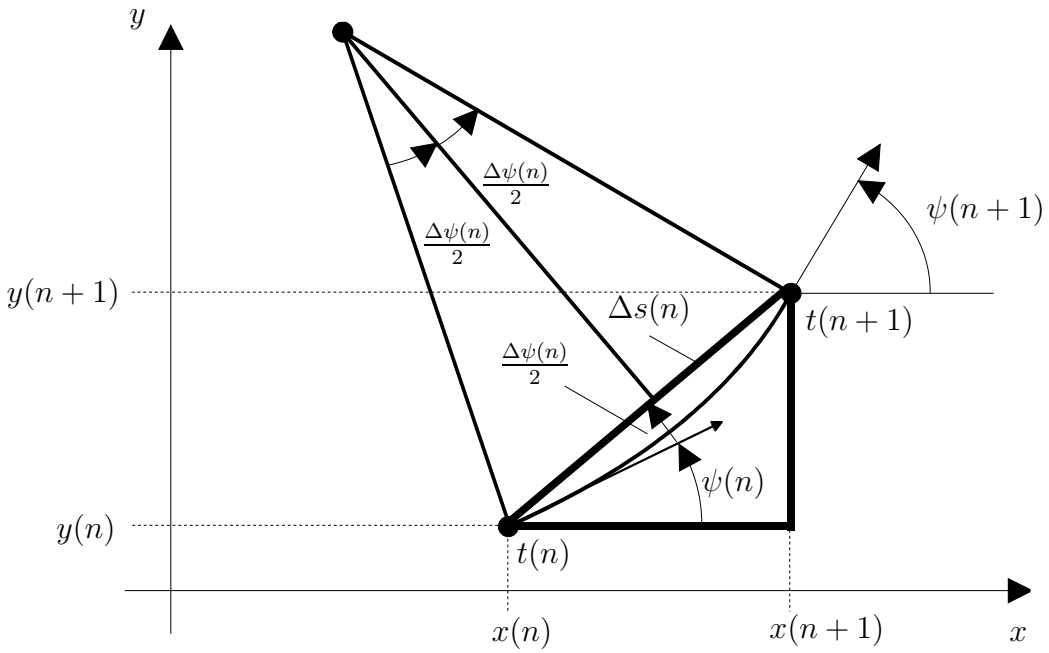

Figure 5.16: Determination of the vehicle trajectory by means of triangular approximation

5.3.1 Vehicle Location

The vehicle location is calculated recursively. Based on the old location and heading, the new location is determined by processing the distance increment $\Delta s(n)$ and the yaw angle increment $\Delta\psi(n)$. Fig. 5.16 shows a circular motion increment during one sampling period between $t = n \cdot T_S$ and $t = (n+1) \cdot T_S$. Based on the vehicle location $\underline{x}(n) = [x(n), \quad y(n)]^T$ the new location at time instant $(n+1) \cdot T_S$ is calculated. Using the triangular approximation in Fig. 5.16, the location equations for trajectory calculation are

$$x(n+1) = x(n) + \Delta s(n) \cdot \cos\left(\psi(n) + \frac{\Delta\psi(n)}{2}\right) \quad , \tag{5.13}$$

$$y(n+1) = y(n) + \Delta s(n) \cdot \sin\left(\psi(n) + \frac{\Delta\psi(n)}{2}\right) \quad . \tag{5.14}$$

The two variables Δs and $\Delta\psi$ are calculated using the vehicle velocity estimate $\hat{v}_{CoG}$ and the yaw rate estimate $\dot{\psi}_{Fuz}$:

$$\Delta s(n) = \hat{v}_{CoG}(n-1) \cdot T_S \quad , \tag{5.15}$$

$$\Delta\psi(n) = \dot{\psi}_{Fuz}(n-1) \cdot T_S \quad . \tag{5.16}$$

In order to get the absolute distance $s(n)$ and the absolute yaw angle $\psi(n)$, the distance and the time increments of Eqns. (5.15) and (5.16) are added,

$$s(n) = s(n-1) + \Delta s(n) \quad , \tag{5.17}$$

$$\psi(n) = \psi(n-1) + \Delta\psi(n) \qquad . \tag{5.18}$$

Eqns. (5.17) and (5.18) describe a time-discrete integration process. That means that errors made calculating the time increments Δs and $\Delta\psi$ accumulate over time. Therefore, it is crucial for trajectory reconstruction to determine Δs and $\Delta\psi$ and due to Eqns. (5.15) and (5.16) also $\hat{v}_{CoG}$ and $\dot{\psi}_{Fuz}$ very accurately. Thus, trajectory reconstruction is a good application to validate the fuzzy estimators presented in Sections 5.1 and 5.2.

5.3.2 Reconstructed Trajectories

During the test drive through the roundabout traffic (see Section 5.2.4), the vehicle trajectory was calculated. The angular differences between the measured and estimated yaw angles in Fig. 5.14 appear to be reasonably small. However, regarding the trajectories of the roundabout traffic drive in Fig. 5.17 calculated with Eqns. (5.13) and (5.14) shows that even such small deviations from the real vehicle heading result in a poor reconstruction quality. If only one of the three measured yaw angles is taken for reconstruction the resulting vehicle course is not sufficiently accurate. The gyroscope yaw angle ψ_S drifts away at the end of the measurement. The yaw angles from the wheel speeds ψ_F and ψ_R also yield large deviations from the real vehicle course. Only fuzzy estimation describes the vehicle motion accurately from the beginning to the end of the course. Only there, the vehicle returns to its initial location.

5.3.3 Robustness Analysis

Sensor errors are inevitable in real-world measurements. During the test drives, for instance, low battery load caused ABS sensor failures with significant drop outs in the wheel speed signal. In order to assess its robustness, the fuzzy system was tested with artificially injected sensor failures. The plots of Figs. 5.20 and 5.21 represent the results from the test drive. In Fig. 5.18, velocity drops were artificially inserted every 10 seconds at the front left wheel. That means that the calculated yaw rate from the front axle $\dot{\psi}_F$ was corrupted then. Fig. 5.18 also shows that the wheel speeds fail below $1m/s$ at the very beginning and at the end of the measurement.

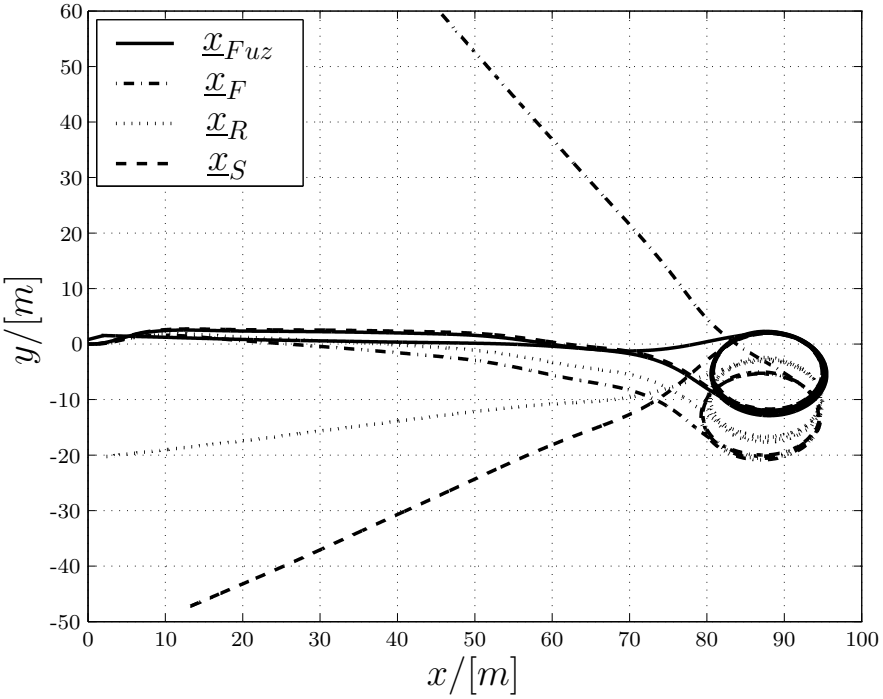

Figure 5.17: Vehicle trajectory reconstruction of multiple drive through a roundabout traffic

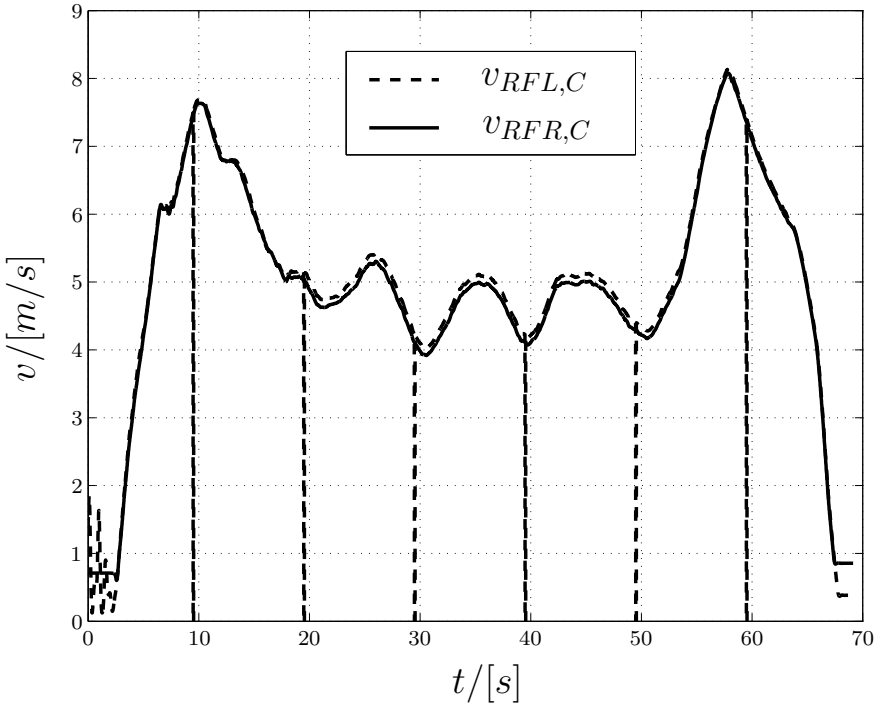

Figure 5.18: Artificially induced errors of ABS sensor (front left)

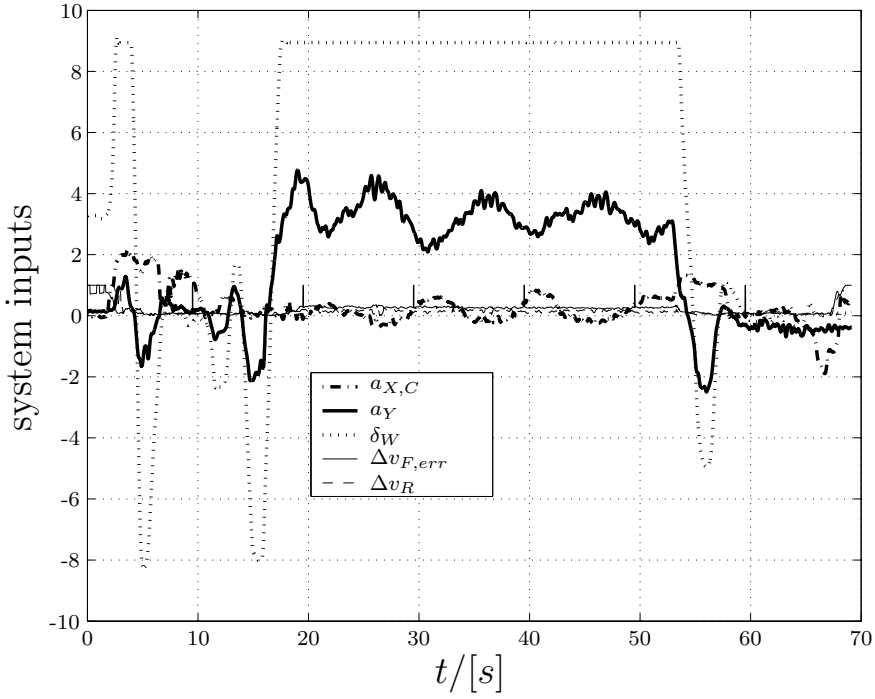

Figure 5.19: System inputs

Fig. 5.19 displays the system inputs into the fuzzy system. During the circular motion in the roundabout traffic (between $17s$ and $53s$), the wheel turn angle is high resulting in a high lateral acceleration. Close to the zero-axis, peaks in the $\Delta v_{F,err}$-signal can be recognized resulting from the sensor signals drops.
Fig. 5.20 depicts the various yaw rate signals and their weighting factors. At the beginning and at the end of the measurement, the weighting factors h_2 and h_3 for the wheel speed signals are zero and h_1 for the gyroscope signal is high. In such conditions, the wheel speed sensors are below their activation threshold. In the middle of the measurement at high lateral accelerations a_Y and for large wheel turn angles δ_W the rear axle's yaw rate signal $\dot{\psi}_R$ is only little weighted, whereas the other two yaw rates ($\dot{\psi}_S$ and $\dot{\psi}_F$) are rated as "medium reliable". During the wheel speed signal drops at $t \approx 9s, 19s, ...$ the weighting factor h_2 for the front axle drops to zero as well, whereas h_1 for the gyroscope signal increases. The sensor signal errors cause sharp yaw rate peaks (dashed) in the middle plot of Fig. 5.20. In curves the yaw rate from the rear axle is generally weighted small, so that the sensor signal drops do not influence h_3. In the phases before the circular motion ($3s < t < 17s$) and after the circular motion ($53s < t < 68s$) the car is driving almost straightforward. Here, the wheel speeds are generally preferred to the gyroscope. In these phases, the weights h_2 and h_3 are hig-

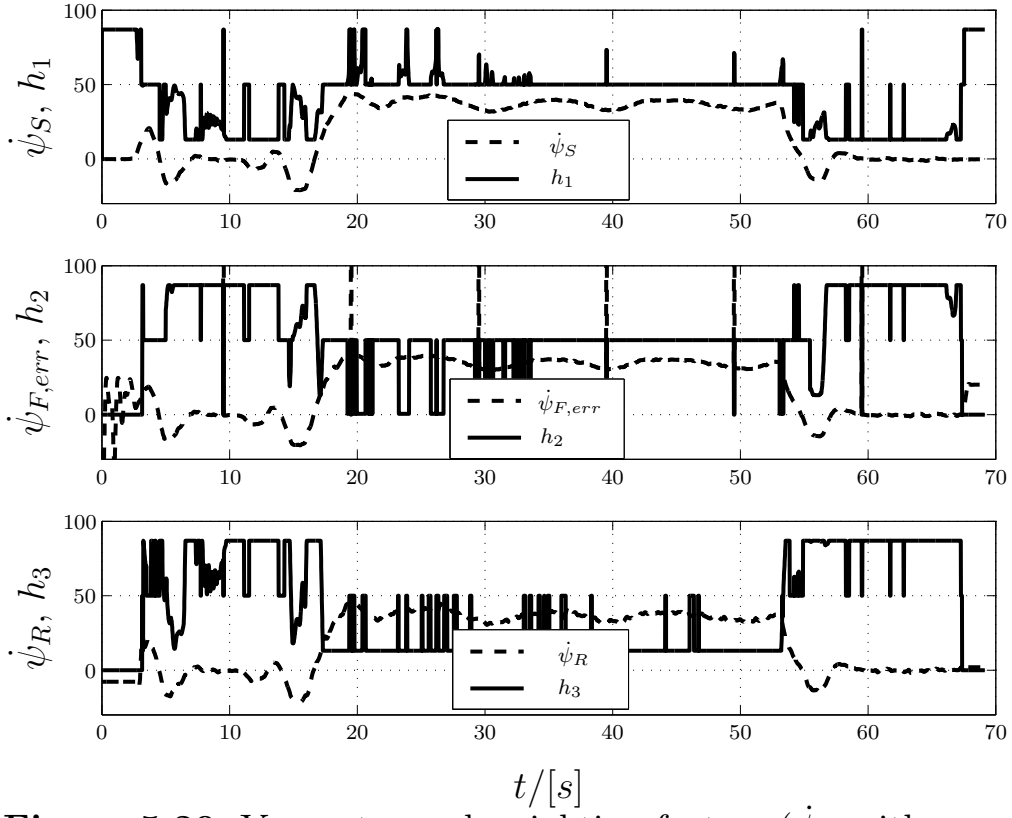

Figure 5.20: Yaw rates and weighting factors ($\dot{\psi}_F$ with errors)

her than h_1.
As mentioned above, the edges of the membership functions were chosen relatively steep. This causes fast switches between different driving conditions. Fig. 5.20 shows that the sharp velocity signal drops are very quickly detected and the estimation can therefore recover very fast.

Fig. 5.21 shows the results of the robustness test for the yaw angle estimation and for the trajectory calculation. In Fig. 5.21(a), steps in the calculated yaw angle signal can be recognized. Driving counter-clockwise through a roundabout traffic results in positive yaw angles. Sensor signal drops at the left wheel cause erroneous positive yaw rates in the ψ_F-signal at $t \approx 49s$ and $t \approx 59s$. This is because the velocity difference increases according to Eqn. (5.8). Fig. 5.21(a) shows that the fuzzy estimation completely ignores the false yaw rate signal. Comparing Figs. 5.14 and 5.21(a), the results for ψ_{Fuz} are almost equal with or without sensor signal drops.
The effect of sensor failures on the accuracy of the reconstructed trajectory is illustrated in Fig. 5.21(b). The dash-dotted course represents the trajectory $\underline{x}_{F,err}$ reconstructed using the front axle yaw rate $\psi_{F,err}$ only. The figure points out that the course is corrupted significantly. Even the circles of the roundabout traffic are no longer centrical. The signal the-

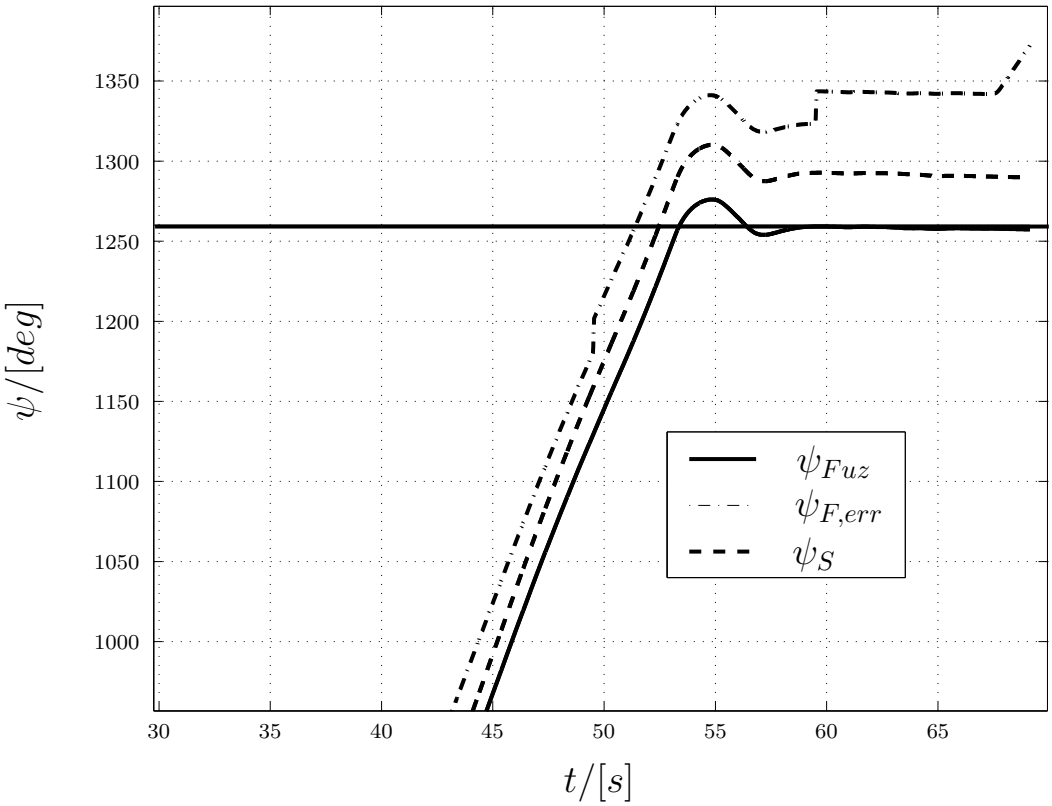

(a) Reconstructed yaw angle

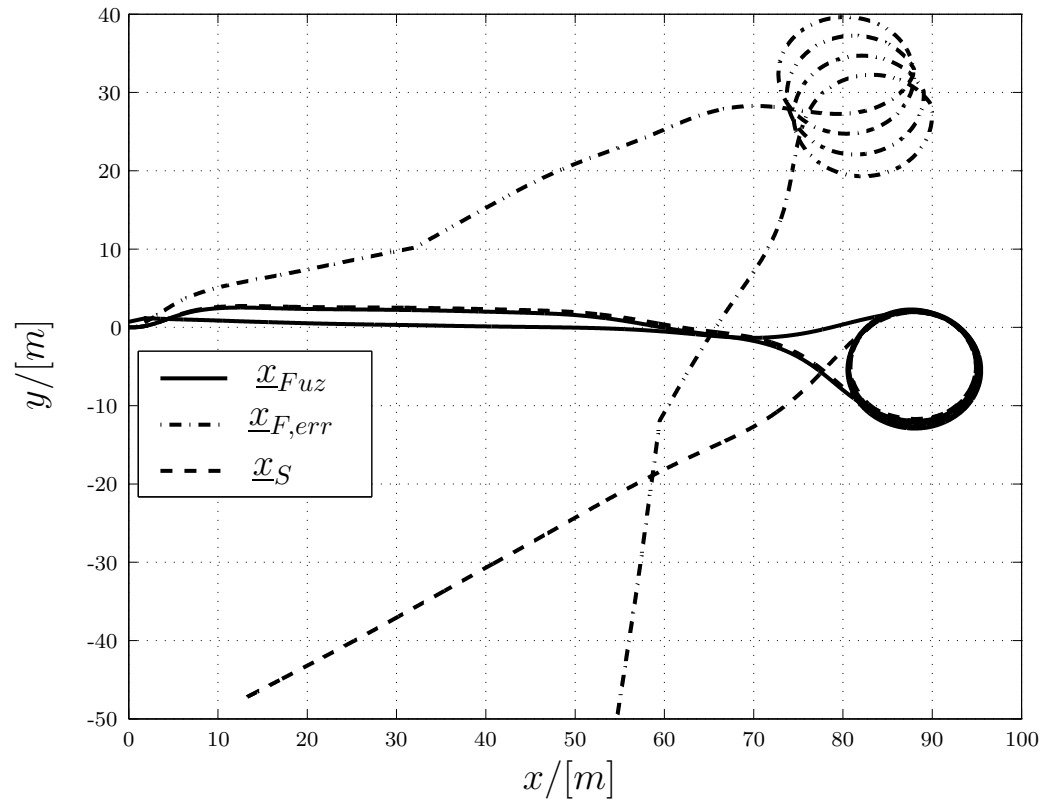

(b) Reconstructed trajectory

Figure 5.21: Results of a test drive with artificial errors

refore is absolutely inapplicable for trajectory reconstruction. Comparing Figs. 5.21(b) and 5.17 shows that the fuzzy system's trajectory is not at all affected by the sensor signal failures.

5.4 Vehicle Body Side Slip Angle Observer

The vehicle body side slip angle β is one of the most important variables in vehicle dynamics. It is defined as the angle between the vehicle's longitudinal axis $\underline{x}_{CoG}$ and the vector of the center of gravity velocity $\underline{v}_{CoG}$. Drivers perceive the vehicle body side slip angle or its gradient very sensitively and desire to keep these quantities small, [54]. Growing vehicle body side slip angles at high lateral accelerations are an indicator for an instable driving situation, [55], [27], see also Section 4.2.8. For complete vehicle motion reproduction, for example for accident reconstruction purposes, [15], the location of the center of gravity (i.e. the actual trajectory) *and* the course angle are required. The course angle is the sum of yaw angle and vehicle body side slip angle $(\psi + \beta)$.
The vehicle body side slip angle cannot be measured with commercial-off-the-shelf sensors. Instead, a very expensive optical sensor system is used for development purposes. Newer systems base on GPS data, [3], [66]. However, this method is also too expensive for series production.
Due to the importance of the vehicle body side slip angle especially for vehicle dynamics control systems, it has to be calculated from measurable sensor signals. [25] calculates the VBSSA from the ratio of the lateral and longitudinal vehicle velocity v_Y and v_X:

$$\beta = \frac{v_Y}{v_X} \quad , \tag{5.19}$$

where v_Y is calculated from estimates of the side forces. A similar approach is described in [31].
Another approach can be found in [39]. In stable driving situations, the VBSSA is calculated by means of a linear observer. However, the model is not adapted to measured outputs but runs "open loop". If the vehicle behavior becomes non-linear, an integration equation is applied:

$$\beta = \int \left(\frac{a_Y}{v_X} - \dot{\psi} \right) dt \quad . \tag{5.20}$$

The method has two major disadvantages. Firstly, running a model "open loop" can cause difficulties, if the unknown initial process state and the modeled one deviate. Furthermore, the integration method from Eqn. (5.20)

is problematic because of cumulated offsets of the acceleration and yaw rate sensor signals employed in this method.
To avoid these problems, a state space observer will be presented in this section. The feedback of the observer reduces modeling errors and is capable to handle the mentioned deviations of the initial values of model an process. However, a state space observer is only as good as its underlying model. For accident reconstruction and the description of unstable pre-accident situations, linear observer approaches are not applicable (see the model validation in Section 3.6).
That is the reason why this section presents a selection of *non-linear* observers. Only the non-linear two track model shown in Section 3.3.7 with the necessary adaptations in Section 3.4.2 is sufficiently accurate to gain satisfactory results.
In contrast to linear observer design there exists a variety of approaches for non-linear systems. The form of the non-linearity plays a crucial role for the choice of a suitable observer concept, [32]. Some of the observers presented in this section are limited to systems with a special structure. That is, why the adaptive non-linear two track model according to Section 3.3 must be restructured.
The observability of a system is a necessary and sufficient condition for observer design. The fundamentals of non-linear observability are described in Section 5.4.1. After proving the requirements for observer design, Section 5.4.2 presents a non-linear state space observer where the non-linear model is linearized around the currently estimated state vector. This observer uses all measurable information available in the system. The second part of Section 5.4.2 reduces the measurement vector to a scalar, where only the measured yaw rate supports the observer. In Section 5.4.3 the adaptive non-linear state space model is restructured. This enables the observer design of a new type of observer which adapts the estimation error of the non-linear observer to the dynamics of a linear reference model (Section 5.4.5). In Section 5.4.4 the linearization observer is also designed according to the restructured model. Section 5.4.6 compares the individual observer concepts. The extended Kalman-Bucy-Filter is capable to employ heuristic knowledge about model inaccuracies or sensor characteristics. Its design and validation results are presented in Section 5.4.7. Section 5.4.8 enhances the reconstruction of the vehicle motion using the knowledge about the vehicle body side slip angle. Finally, in Section 5.9 the driver's steering performance in a critical drive situation is assessed by means of a simple control approach.

5.4.1 Observability of State Space Models

Linear Observability

Starting with the observability of a linear state space model, the respective definition for non-linear models is presented afterwards.
The observability of a linear state space model

$$\begin{aligned} \underline{\dot{x}} &= \underline{A}\,\underline{x} + \underline{B}\,\underline{u} \quad , \\ \underline{y} &= \underline{C}\,\underline{x} + \underline{D}\,\underline{u} \end{aligned} \tag{5.21}$$

is defined as follows, [24]:

Definition 5.1 (Linear Observability)
A linear and time-invariant system (5.21) is observable, if its initial state $\underline{x}(t_0)$ can be calculated uniquely, when the input and output variables are known.

Knowing the initial state of a system, all the other state vectors $\underline{x}(t), t > t_0$ and thus the complete state trajectory can be reconstructed. [49] gives a necessary and sufficient condition for the observability of a linear system:

Theorem 5.2
A linear and time-invariant state space system with n state variables and q output variables defined by Eqn. (5.21) is observable, if the (nq, n)-observability matrix

$$\underline{Q}_B = \begin{bmatrix} \underline{C} \\ \underline{C}\,\underline{A} \\ \vdots \\ \underline{C}\,\underline{A}^{n-1} \end{bmatrix} \tag{5.22}$$

has maximum rank n. ◇

If $\underline{Q}_B$ has maximum rank, then the observer can be designed. Based on the considerations of this section, the observability term is expanded to non-linear systems in the next section.

Non-Linear Observability

The most common form of a non-linear dynamical system is

$$\begin{aligned} \underline{\dot{x}}(t) &= \underline{f}\big(\underline{x}(t), \underline{u}(t)\big) \quad , \\ \underline{y}(t) &= \underline{h}\big(\underline{x}(t), \underline{u}(t)\big) \quad , \end{aligned} \tag{5.23}$$

where the functions $\underline{f}$ and $\underline{h}$ can depend non-linearly from all state space and input quantities.
The definition of observability for non-linear systems is similar to Def. 5.1. According to [5], global and local observability must be distinguished.

Definition 5.3 (Global Observability)
A dynamical system according to (5.23) is called globally observable, if an arbitrary initial state $\underline{x}(t_0)$ can be reconstructed uniquely from the input quantities $\underline{u}$ and from the output quantities $\underline{y}$.

Definition 5.4 (Local Observability)
A dynamical system according to (5.23) is called locally observable in a point $\underline{x}_p$, if all initial states $\underline{x}(t_0)$ in a surrounding area of $\underline{x}_p$ can be reconstructed uniquely from the input quantities $\underline{u}$ and from the output quantities $\underline{y}$. If this is fulfilled for arbitrary points $\underline{x}_p$, then the system is called locally observable.

For analysis of the observability of non-linear systems, the state and input variables of the system are transformed to the output quantities by means of an observability transformation $\underline{q}_{obs}$ which is defined as

$$\underline{q}_{obs} := \underline{y}^{[n-1]} = \begin{bmatrix} \underline{y} \\ \dot{\underline{y}} \\ \vdots \\ \underline{y}^{(n-1)} \end{bmatrix} = \begin{bmatrix} \underline{h}(\underline{x},\underline{u}) \\ \frac{d}{dt}\underline{h}(\underline{x},\underline{u}) \\ \vdots \\ \frac{d^{n-1}}{dt^{n-1}}\underline{h}(\underline{x},\underline{u}) \end{bmatrix} \quad . \tag{5.24}$$

The first time derivative of the output variable is

$$\dot{\underline{y}} = \frac{\partial \underline{h}(\underline{x},\underline{u})}{\partial \underline{x}}\,\dot{\underline{x}} + \frac{\partial \underline{h}(\underline{x},\underline{u})}{\partial \underline{u}}\,\dot{\underline{u}} = \frac{\partial \underline{h}(\underline{x},\underline{u})}{\partial \underline{x}}\,\underline{f}(\underline{x},\underline{u}) + \frac{\partial \underline{h}(\underline{x},\underline{u})}{\partial \underline{u}}\,\dot{\underline{u}} \quad . \tag{5.25}$$

Accordingly, in all time derivatives of higher order, the derivatives of the state space variable $\dot{\underline{x}}$ are replaced by $\underline{f}(\underline{x},\underline{u})$. Then, $\underline{y}^{[n-1]}$ depends on the state variables and on the time derivatives of the input variables up to their maximum order $(n-1)$:

$$\underline{y}^{[n-1]} = \underline{q}_{obs}(\underline{x},\underline{u}^{[n-1]}) \quad . \tag{5.26}$$

If the inverse transformation

$$\underline{x} = \underline{q}_{obs}^{-1}(\underline{u}^{[n-1]},\underline{y}^{[n-1]}) \tag{5.27}$$

exists, then the state vector $\underline{x}$ can be determined from the in- and output quantities $\underline{u}$ and $\underline{y}$ and the system is globally observable, [5]. This yields the theorem for global observability.

Theorem 5.5
A dynamical system according to (5.23) is globally observable, if the observability transformation (5.26) is invertible. ◇

For a local examination in a point $\underline{x}_p$, the transformation is TAYLOR-expanded around $\underline{x}_p$ curtailing the TAYLOR-expansion after the linear term:

$$\underline{y}^{[n-1]} \approx \underline{q}_{obs}(\underline{x}_p, \underline{u}^{[n-1]}) + \left.\frac{\partial \underline{q}_{obs}}{\partial \underline{x}}\right|_{\underline{x}=\underline{x}_p} \cdot (\underline{x} - \underline{x}_p) \quad . \tag{5.28}$$

According to [5], $\underline{x}$ can be isolated in this set of equations, when the matrix

$$\left.\frac{\partial \underline{q}_{obs}}{\partial \underline{x}}\right|_{\underline{x}=\underline{x}_p} =: \underline{Q}_B(\underline{x}, \underline{u}^{[n-1]})\Big|_{\underline{x}=\underline{x}_p} \tag{5.29}$$

has full rank n.
In this case the system (5.23) is locally observable. Matrix $\underline{Q}_B$ is called observability matrix. Using $\underline{Q}_B$, a sufficient criterion for local observability can be defined:

Theorem 5.6
A dynamical system according to (5.23) is locally observable, if the (nq, n)-observability matrix $\underline{Q}_B$ according to Eqn. (5.29) has full rank n. ◇

After the observability definition of non-linear systems and the setup of the respective observability criteria, the different observer designs for non-linear systems are presented. Every time, the underlying model is changed or restructured, a new observability analysis must be carried out. The respective proofs of observability are provided in Appendix A.3.

5.4.2 Linearization Observer

Underlying theory

The linearization observer, [23], [81], can be used for observer design of arbitrary non-linear systems, assuming that they are locally observable. For a non-linear system of the common form

$$\begin{aligned} \dot{\underline{x}} &= \underline{f}(\underline{x}, \underline{u}) \quad , \\ \underline{y} &= \underline{h}(\underline{x}, \underline{u}) \quad , \end{aligned} \tag{5.30}$$

a non-linear observer is set up as follows:

$$\begin{aligned} \dot{\hat{\underline{x}}} &= \underline{f}(\hat{\underline{x}}, \underline{u}) + \underline{L}(\hat{\underline{x}}, \underline{u}) \cdot (\underline{y} - \hat{\underline{y}}) \quad , \\ \hat{\underline{y}} &= \underline{h}(\hat{\underline{x}}, \underline{u}) \quad . \end{aligned} \tag{5.31}$$

The observability proof of the underlying system can be found in Appendix A.3.1. The observer structure can be seen in Fig. 5.22. The estimation error $\underline{\tilde{x}}(t) = \underline{x}(t) - \underline{\hat{x}}(t)$ is described by the differential equation

$$\dot{\underline{\tilde{x}}} = \underline{f}(\underline{x}, \underline{u}) - \underline{f}(\underline{\hat{x}}, \underline{u}) - \underline{L}(\underline{\hat{x}}, \underline{u}) \cdot \big(\underline{h}(\underline{x}, \underline{u}) - \underline{h}(\underline{\hat{x}}, \underline{u})\big) \quad . \tag{5.32}$$

For determining an appropriate observer gain, this differential equation is linearized around the currently estimated state $\underline{\hat{x}}$ by TAYLOR-expanding $\underline{f}(\underline{x}, \underline{u})$ and $\underline{h}(\underline{x}, \underline{u})$ around $\underline{\hat{x}}$. The expansion is curtailed after the linear term

$$\underline{f}(\underline{x}, \underline{u}) \approx \underline{f}(\underline{\hat{x}}, \underline{u}) + \left.\frac{\partial \underline{f}(\underline{x}, \underline{u})}{\partial \underline{x}}\right|_{\underline{x}=\underline{\hat{x}}} \cdot (\underline{x} - \underline{\hat{x}}) \quad , \tag{5.33}$$

$$\underline{h}(\underline{x}, \underline{u}) \approx \underline{h}(\underline{\hat{x}}, \underline{u}) + \left.\frac{\partial \underline{h}(\underline{x}, \underline{u})}{\partial \underline{x}}\right|_{\underline{x}=\underline{\hat{x}}} \cdot (\underline{x} - \underline{\hat{x}}) \quad . \tag{5.34}$$

Insertion of Eqn. (5.33) and (5.34) in Eqn. (5.32) reads

$$\begin{aligned} \dot{\underline{\tilde{x}}} &= \underbrace{\left(\left.\frac{\partial \underline{f}(\underline{x}, \underline{u})}{\partial \underline{x}}\right|_{\underline{x}=\underline{\hat{x}}} - \underline{L}(\underline{\hat{x}}, \underline{u}) \cdot \left.\frac{\partial \underline{h}(\underline{x}, \underline{u})}{\partial \underline{x}}\right|_{\underline{x}=\underline{\hat{x}}} \right)}_{\underline{F}(\underline{\hat{x}}, \underline{u})} \cdot \underline{\tilde{x}} \\ &= \underline{F}(\underline{\hat{x}}, \underline{u}) \cdot \underline{\tilde{x}} \end{aligned} \quad . \tag{5.35}$$

The observer gain $\underline{L}$ and the matrix $\underline{F}$ depend on the input values $\underline{u}$ and on the estimated state variables $\underline{\hat{x}}$. Both of these quantities are known.
If the observer matrix $\underline{L}(\underline{\hat{x}}, \underline{u})$ can be chosen, so that the dynamic matrix $\underline{F}$ is constant *and* has fix eigenvalues, then the solution of the error differential equation is

$$\underline{\tilde{x}}(t) = \exp\left\{\underline{F} \cdot (t - t_0)\right\} \cdot \underline{\tilde{x}}(t_0) \quad . \tag{5.36}$$

In a sufficiently long time interval, the error $\underline{\tilde{x}}$ converges against zero for arbitrary initial estimation errors $\underline{\tilde{x}}(t_0) = \underline{x}(t_0) - \underline{\hat{x}}(t_0)$.
To determine the observer gain, it must fulfill the condition

$$\begin{aligned} \det(s\underline{I}_n - \underline{F}) &= \det\left(s\underline{I}_n - \left.\frac{\partial \underline{f}(\underline{x}, \underline{u})}{\partial \underline{x}}\right|_{\underline{x}=\underline{\hat{x}}} + \underline{L}(\underline{\hat{x}}, \underline{u}) \cdot \left.\frac{\partial \underline{h}(\underline{x}, \underline{u})}{\partial \underline{x}}\right|_{\underline{x}=\underline{\hat{x}}}\right) \\ &\stackrel{!}{=} \prod_{\nu=1}^{n} (s - \lambda_\nu) \quad . \end{aligned} \tag{5.37}$$

The elements of the matrix $\underline{L}(\underline{\hat{x}}, \underline{u})$ must be chosen appropriately.
In general, it is not possible to achieve fix poles *and* a constant dynamic

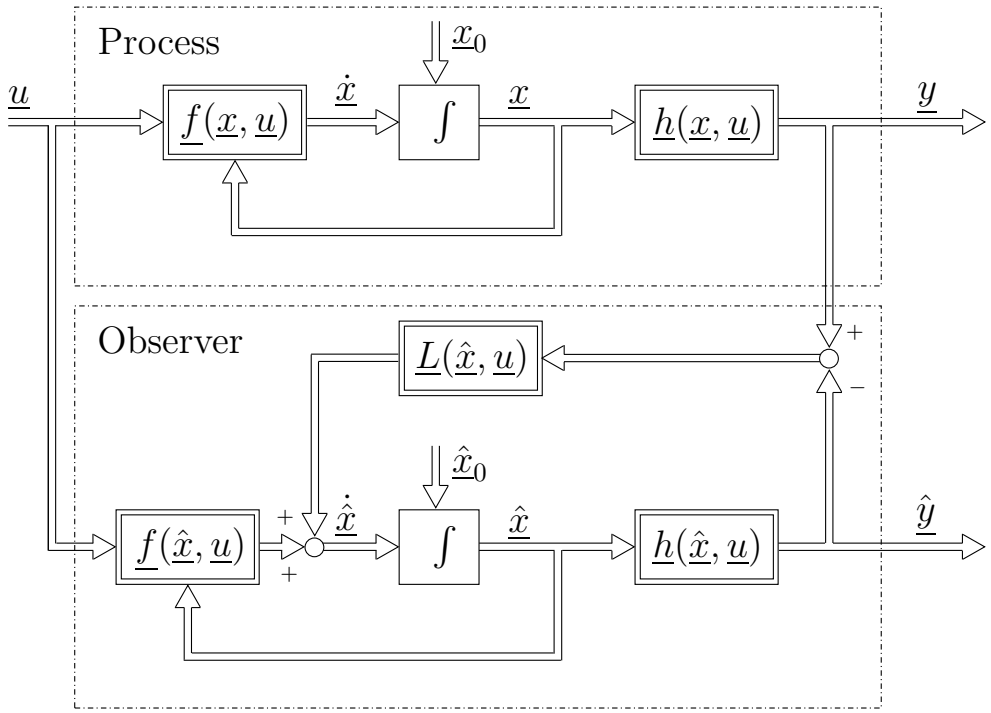

Figure 5.22: Structure of the linearization observer

matrix $\underline{F}$, [23]. A compromise between a simple structure of matrix $\underline{F}$ and fix eigenvalues is necessary. For the implementation, the stability of the observer and its sensitivity to noise and model inaccuracies must be analyzed by means of simulations.
One advantage of the linearization observer is that it can be applied to any non-linear and observable process.

Observer for Two Measurable Outputs

The non-linear two track model

$$\dot{\underline{x}} = \underline{f}(\underline{x},\underline{u}) \tag{5.38}$$

presented in Section 3.3 has three state variables

$$\underline{x} = \left[\; v_{CoG} \quad \beta \quad \dot{\psi} \;\right]^T$$

and five input variables

$$\underline{u} = \left[\; F_{LFL} \quad F_{LFR} \quad F_{LRL} \quad F_{LRR} \quad \delta_W \;\right]^T \quad .$$

The vector function $\underline{f}$ is described by Eqns. (3.63) to (3.65). Two of the three state variables are measured outputs, the center of gravity velocity

v_{CoG} and the yaw rate $\dot{\psi}$:

$$\underline{y} = \begin{bmatrix} v_{CoG} & \dot{\psi} \end{bmatrix}^T = \underline{C} \cdot \underline{x} = \begin{bmatrix} 1 & 0 & 0 \\ 0 & 0 & 1 \end{bmatrix} \cdot \underline{x} \quad . \tag{5.39}$$

For this system, due to $\underline{C} = \frac{\partial \underline{h}}{\partial \underline{x}}$, the error differential equation (5.35) provides the following dynamic matrix:

$$\begin{aligned} \underline{F}(\hat{\underline{x}}, \underline{u}) &= \left. \frac{\partial \underline{f}(\underline{x}, \underline{u})}{\partial \underline{x}} \right|_{\underline{x}=\hat{\underline{x}}} - \underline{L}(\hat{\underline{x}}, \underline{u}) \cdot \left. \frac{\partial \underline{h}(\underline{x})}{\partial \underline{x}} \right|_{\underline{x}=\hat{\underline{x}}} \\ &= \left. \begin{bmatrix} \frac{\partial \dot{v}_{CoG}}{\partial v_{CoG}} - l_{11} & \frac{\partial \dot{v}_{CoG}}{\partial \beta} & \frac{\partial \dot{v}_{CoG}}{\partial \dot{\psi}} - l_{12} \\ \frac{\partial \dot{\beta}}{\partial v_{CoG}} - l_{21} & \frac{\partial \dot{\beta}}{\partial \beta} & \frac{\partial \dot{\beta}}{\partial \dot{\psi}} - l_{22} \\ \frac{\partial \ddot{\psi}}{\partial v_{CoG}} - l_{31} & \frac{\partial \ddot{\psi}}{\partial \beta} & \frac{\partial \ddot{\psi}}{\partial \dot{\psi}} - l_{32} \end{bmatrix} \right|_{\underline{x}=\hat{\underline{x}}} \quad . \end{aligned} \tag{5.40}$$

The JACOBIAN-matrix $\frac{\partial \underline{f}(\underline{x},\underline{u})}{\partial \underline{x}}$ is calculated in Appendix A.1. Goal of the observer design is the appropriate choice of the elements of matrix $\underline{L}$ by means of Eqn. (5.37). For the poles $\lambda_1, \lambda_2, \lambda_3$ this yields

$$\det\left(\begin{bmatrix} \lambda_1 - \frac{\partial \dot{v}_{CoG}}{\partial v_{CoG}} + l_{11} & -\frac{\partial \dot{v}_{CoG}}{\partial \beta} & -\frac{\partial \dot{v}_{CoG}}{\partial \dot{\psi}} + l_{12} \\ -\frac{\partial \dot{\beta}}{\partial v_{CoG}} + l_{21} & \lambda_2 - \frac{\partial \dot{\beta}}{\partial \beta} & -\frac{\partial \dot{\beta}}{\partial \dot{\psi}} + l_{22} \\ -\frac{\partial \ddot{\psi}}{\partial v_{CoG}} + l_{31} & -\frac{\partial \ddot{\psi}}{\partial \beta} & \lambda_3 - \frac{\partial \ddot{\psi}}{\partial \dot{\psi}} + l_{32} \end{bmatrix} \right) \stackrel{!}{=} 0 \quad . \tag{5.41}$$

As already mentioned, the pole placement has two goals: firstly, the choice of fix eigenvalues and secondly a constant dynamic matrix $\underline{F}$. Eqn. (5.41) points out the dilemma: the six elements of matrix $\underline{L}$ are insufficient to place all three observer poles on the one hand, and to influence all nine elements of matrix $\underline{F}$ on the other hand. Therefore, a compromise must be found: if all the poles are fix, then $\underline{F}$ is very complex. Therefore, this section deals with the design of an observer with a simple dynamic matrix $\underline{F}$. At the end of this section, validations show the differences of these two approaches.
The dynamic matrix becomes as simple as possible, if the observer gain $\underline{L}$ is

$$\underline{L}(\hat{\underline{x}}, \underline{u}) = \begin{bmatrix} \frac{\partial \dot{v}_{CoG}}{\partial v_{CoG}} - \lambda_1 & \frac{\partial \dot{v}_{CoG}}{\partial \dot{\psi}} \\ \frac{\partial \dot{\beta}}{\partial v_{CoG}} & \frac{\partial \dot{\beta}}{\partial \dot{\psi}} \\ \frac{\partial \ddot{\psi}}{\partial v_{CoG}} & \frac{\partial \ddot{\psi}}{\partial \dot{\psi}} - \lambda_3 \end{bmatrix} \quad . \tag{5.42}$$

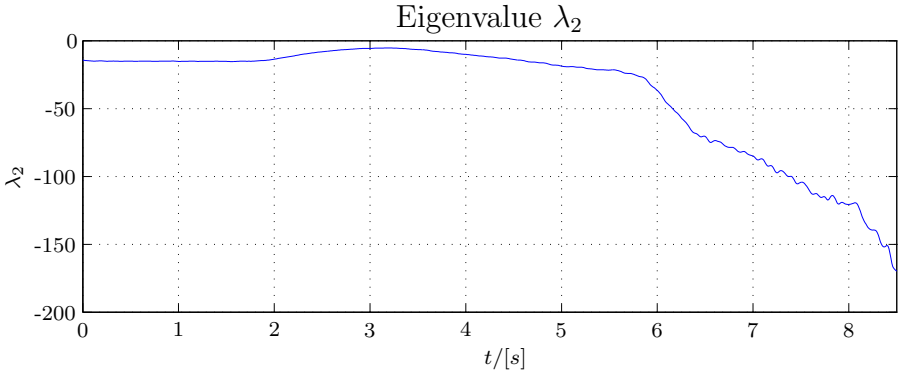

Figure 5.23: Time-varying positions of λ_2 for the clothoide with high dynamics

In this case, only two of the three poles are fix. According to Eqn. (5.41) the third one is

$$\begin{aligned}\lambda_2(t) = \left.\frac{\partial\dot{\beta}}{\partial\beta}\right|_{\underline{x}=\hat{\underline{x}}} = \frac{1}{m_{CoG}\hat{v}_{CoG}}\Big\{&(c_{FL}+c_{FR})(\delta_W-\hat{\beta}-\frac{l_F\hat{\dot{\psi}}}{\hat{v}_{CoG}})\sin(\delta_W-\hat{\beta})\\ &-(c_{FL}+c_{FR}+F_{LFL}+F_{LFR})\cos(\delta_W-\hat{\beta})\\ &-\big(c_{RL}+c_{RR}+F_{LRL}+F_{LRR}-c_{WX}\hat{v}_{CoG}^2\big)\cos\hat{\beta}\Big\}\\ &-(c_{RL}+c_{RR})(-\hat{\beta}+\frac{l_R\hat{\dot{\psi}}}{\hat{v}_{CoG}})\sin\hat{\beta} \quad . \end{aligned} \tag{5.43}$$

An analytical examination of the pole location is impossible, as Eqn. (5.43) contains eight time-varying parameters. Instead, the pole locations are simulated for the clothoide drive of high dynamics (see Section 3.6.1). This driving maneuver covers all driving situations starting from straightforward driving to a critical cornering situation.
Fig. 5.23 shows, that λ_2 remains in the open left half plane. That means that the observer designed with the observer gain (5.42) is stable, at least for all test drives conducted.
Fig. 5.24 compares the described observer with the observer where all three poles are fix. For the latter one, the observer gain and the dynamic matrix are very complex and therefore not listed here. At the beginning, the signals are almost congruent. After approximately $t = 6s$, the observer with three fix poles deviates significantly and finally it becomes unstable. Although the pole λ_2 of the other observer is time-varying, the results are much better, because the dynamic matrix is much simpler. However, between

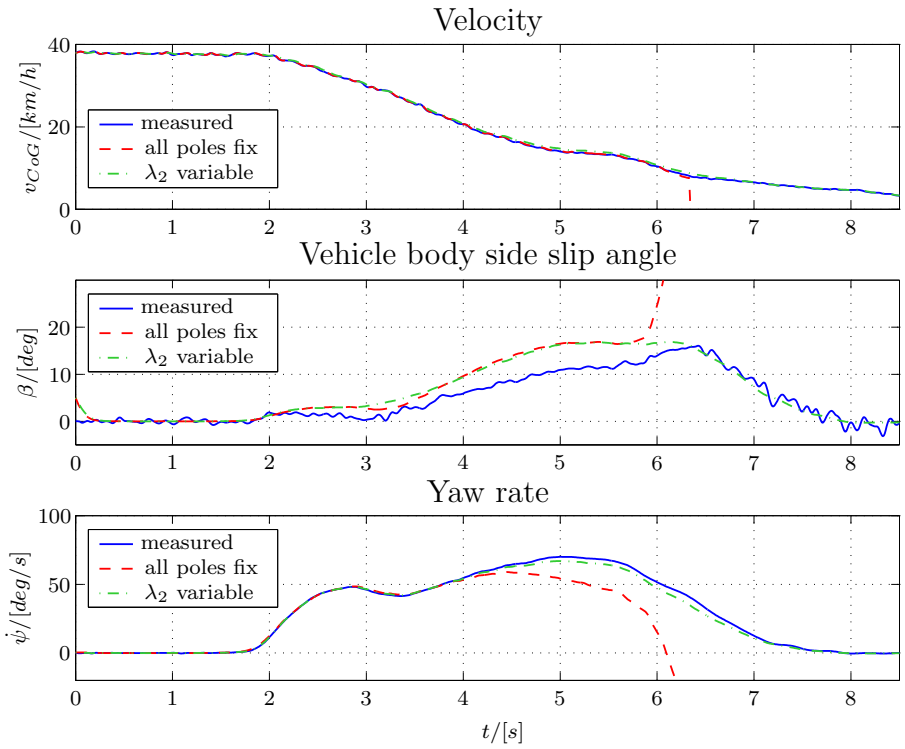

Figure 5.24: Results of the linearization observer with two measured output variables with and without time-varying poles (test drive: highly dynamical clothoide)

$t = 2.5s$ and $t = 6.5s$ the observed VBSSA is too high. Section 3.6.3 states that the velocity is modeled less accurately. These inaccuracies increase with growing side forces causing a significant deviation between measured and modeled velocity (see Fig. 3.26). The linearization observer adapts the modeled velocity to the measured one. This adaptation fudges the estimation result of the vehicle body side slip angle mainly because of inaccuracies of the first differential equation of the model. To avoid this problem, in the next step only the yaw rate is regarded as an output variable. Then, the observer adapts solely the yaw rate to the measured value. Therefore, there is no velocity adaptation any more and the model inaccuracy is ignored.

Observer for One Measurable Output Variable

If only the yaw rate is a system output, the system becomes

$$\underline{\dot{x}} = \underline{f}(\underline{x}, \underline{u}) = \begin{bmatrix} \dot{v}_{CoG} \\ \dot{\beta} \\ \ddot{\psi} \end{bmatrix}, \quad \underline{y} = \underline{C} \cdot \underline{x} \quad \text{with} \quad \underline{C} = \begin{bmatrix} 0 & 0 & 1 \end{bmatrix} \quad . \tag{5.44}$$

The non-linear function $\underline{f}(\underline{x}, \underline{u})$ is defined by Eqns. (3.63) - (3.65). The observability of this model must be proven separately. This is carried out in Appendix A.3.2.
As the system (5.44) contains only one output variable, the observer gain is a column vector with three elements:

$$\underline{L}(\underline{\hat{x}}, \underline{u}) := \begin{bmatrix} l_1 \\ l_2 \\ l_3 \end{bmatrix} \quad . \tag{5.45}$$

The characteristic equation for observer design then reads

$$\det\left(\begin{bmatrix} \lambda_1 - \frac{\partial \dot{v}_{CoG}}{\partial v_{CoG}} & -\frac{\partial \dot{v}_{CoG}}{\partial \beta} & -\frac{\partial \dot{v}_{CoG}}{\partial \dot{\psi}} + l_1 \\ -\frac{\partial \dot{\beta}}{\partial v_{CoG}} & \lambda_2 - \frac{\partial \dot{\beta}}{\partial \beta} & -\frac{\partial \dot{\beta}}{\partial \dot{\psi}} + l_2 \\ -\frac{\partial \ddot{\psi}}{\partial v_{CoG}} & -\frac{\partial \ddot{\psi}}{\partial \beta} & \lambda_3 - \frac{\partial \ddot{\psi}}{\partial \dot{\psi}} + l_3 \end{bmatrix}\right) \stackrel{!}{=} 0 \quad . \tag{5.46}$$

For this observer, a simple dynamic matrix $\underline{F}$ is preferred to fixing all eigenvalues. Again, the observer with all eigenvalues fixed has a very complex observer gain and therefore becomes instable.
A simple structure for $\underline{F}$ can be achieved when choosing

$$\underline{L}(\underline{\hat{x}}, \underline{u}) = \begin{bmatrix} \frac{\partial \dot{v}_{CoG}}{\partial \dot{\psi}} \\ \frac{\partial \dot{\beta}}{\partial \dot{\psi}} \\ \frac{\partial \ddot{\psi}}{\partial \dot{\psi}} - \lambda_3 \end{bmatrix} \quad . \tag{5.47}$$

In this case λ_3 is chosen -80 and the other two time-varying poles are

$$\lambda_{1/2} = \frac{1}{2}\left\{a_{11} + a_{22} \pm \sqrt{a_{11}^2 - 2a_{11}a_{22} + a_{22}^2 + 4a_{12}a_{21}}\right\} \quad ,$$

with the partial derivatives

$$a_{11} = \frac{\partial \dot{v}_{CoG}}{\partial v_{CoG}}\,, \quad a_{12} = \frac{\partial \dot{v}_{CoG}}{\partial \beta}\,, \quad a_{21} = \frac{\partial \dot{\beta}}{\partial v_{CoG}} \quad \text{and} \quad a_{22} = \frac{\partial \dot{\beta}}{\partial \beta}$$

listed in Appendix A.1. Again the stability of the observer must be ensured. Therefore, the time-varying poles λ_1 and λ_2 were analyzed with several test drives. For the most representative one, the highly dynamical clothoide, Fig. 5.25 shows the result of the simulation. Both real eigenvalues are permanently negative, i.e. in the open left half plane. This means, using the available test drives the observer gain (5.47) provides a stable state observer for the system (5.44).

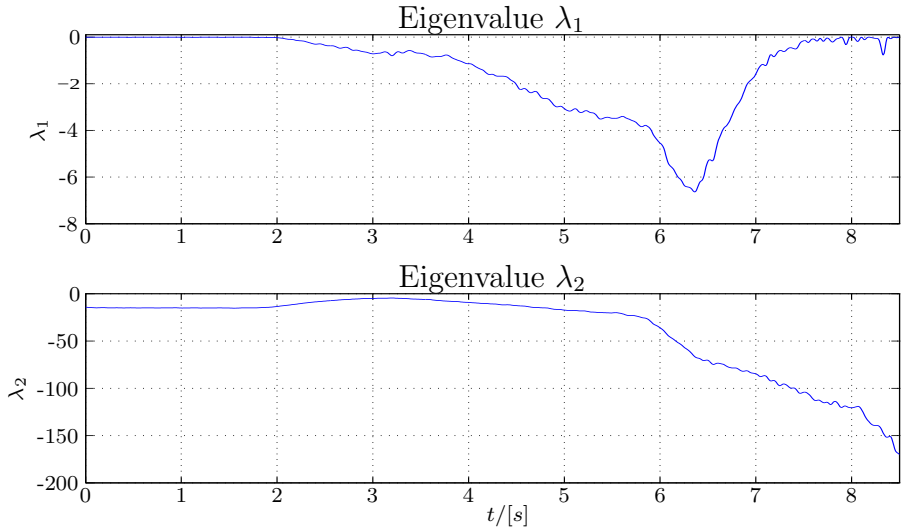

Figure 5.25: Time-varying eigenvalues λ_1 and λ_2 for the clothoide of high dynamics

After knowing its stability, the observer can be validated with test drives. The observer with two time-varying poles is compared to the one designed before with only one time-varying pole. Fig. 5.26 shows, that the observer does not adapt the model velocity to the measured velocity any more, as the velocity is no longer regarded as an output variable. Therefore, the estimated vehicle body side slip angle for the system with only one output variable is much more accurate then the one with two outputs. The measured and the modeled yaw rate for the observer with one output variable are congruent.
Choosing only one output variable provides much better observation results than considering the velocity as a second output as well. The observer presented in this section is capable to estimate the vehicle body side slip angle up to the stability limit.
However, for straightforward driving, it is desirable to have the velocity as an output variable as well. In this driving situation, the velocity should be more reliable than the yaw rate signal, e.g. due to offsets. Switching between an observer with one or two output variables would improve the observer results for driving situations with little side forces. The switching logic contains thresholds for the yaw rate and the yaw acceleration which are evaluated to select the system to be employed. However, the "sharp" switching certainly does not represent an optimal solution for an appropriate determination of the vehicle body side slip angle. Therefore, in Section 5.4.7 an extended Kalman-Bucy-Filter will provide a better solution to decide, how much weight the velocity gets as an output variable. There, situation dependent covariance matrices improve the methodology.

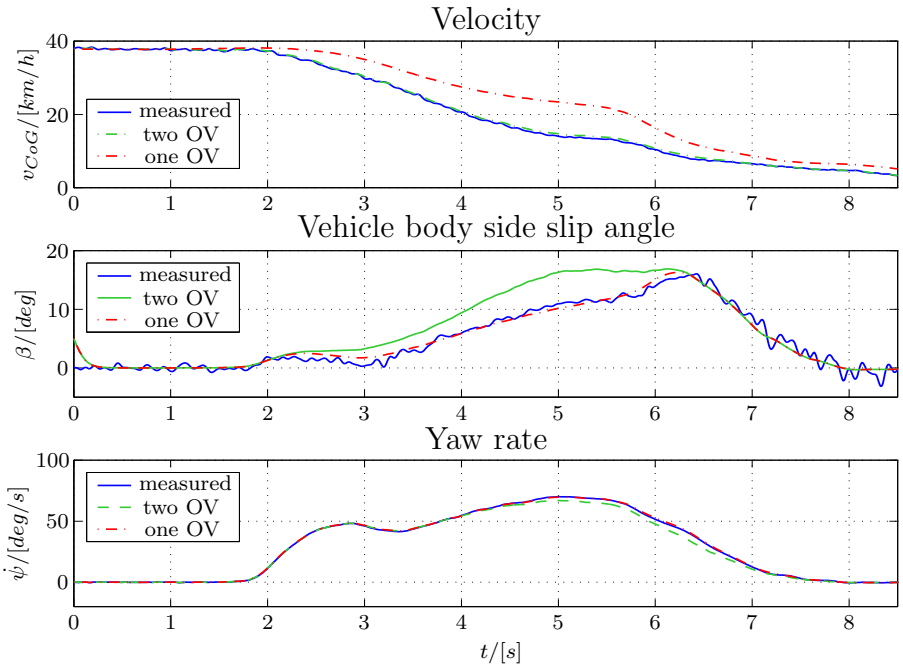

Figure 5.26: Comparison of the observers for the system with two and with one output variable (OV) (test drive: highly dynamical clothoide)

5.4.3 Restructuring of the State Space Model

As mentioned, the design of non-linear observers significantly depends on the structure of the underlying process model. For the observer design described later in Sections 5.4.4 and 5.4.5 and for other observers in canonical form, though, it is necessary to have a system structure of the form

$$\begin{aligned} \underline{\dot{x}} &= \underline{A}(\underline{y},\underline{u}) \cdot \underline{x} + \underline{b}(\underline{y},\underline{u}) \quad , \\ \underline{y} &= \underline{C}\,\underline{x} \quad . \end{aligned} \tag{5.48}$$

The state vector contains n state variables and p input variables. The output vector has the dimension q.
Therefore, the goal is to restructure the adaptive non-linear state space model to the form (5.48). Additionally, the system order decreases from $n = 3$ to $n = 2$. This reduces the complexity of the resultant state space model.

Linearization of the Side Slip Angle

The non-linear model is restructured so that the vehicle body side slip angle β has linear influence. Therefore, the three state equations are linearized with respect to the VBSSA. Eqn. (3.65) is already linear in β so that only the Eqns. (3.63) for v_{CoG} and (3.64) for β must be linearized.

Assuming side slip angles less than 10°, the sine and cosine approximations

$$\cos\beta \approx 1,\ \sin\beta \approx \beta$$

are applied. Using these approximations, two more transformations are carried out:

$$\begin{aligned}\cos(\delta_W - \beta) &= \cos\delta_W \cos\beta + \sin\delta_W \sin\beta \approx \cos\delta_W + \beta \sin\delta_W \quad , \\ \sin(\delta_W - \beta) &= \sin\delta_W \cos\beta - \cos\delta_W \sin\beta \approx \sin\delta_W - \beta\cos\delta_W \quad .\end{aligned}$$

Neglecting quadratic terms of β simplifies equations (3.63) and (3.64):

$$\begin{aligned}\dot{v}_{CoG} \;=\; & \beta \cdot \frac{1}{m_{CoG}} \cdot \Big\{ (F_{LFL} + F_{LFR}) \cdot \sin\delta_W + (c_{RL} + c_{RR}) \cdot \frac{l_R\,\dot{\psi}}{v_{CoG}} \\ & + (c_{FL} + c_{FR}) \left(\sin\delta_W + \cos\delta_W \ \left(\delta_W - \frac{l_F\,\dot{\psi}}{v_{CoG}} \right) \right) \Big\} \\ & + \frac{1}{m_{CoG}} \Big\{ (F_{LFL} + F_{LFR}) \cos\delta_W + \left(F_{LRL} + F_{LRR} - c_{WX} v_{CoG}^2 \right) \\ & - (c_{FL} + c_{FR}) \cdot \left(\delta_W - \frac{l_F\,\dot{\psi}}{v_{CoG}} \right) \cdot \sin\delta_W \Big\} \end{aligned} \tag{5.49}$$

and

$$\begin{aligned}\dot{\beta} \;=\; & \beta \cdot \frac{1}{m_{CoG} v_{CoG}} \Big\{ (c_{FL} + c_{FR}) \cdot \left[\sin\delta_W \cdot \left(\delta_W - \frac{l_F \cdot \dot{\psi}}{v_{CoG}} \right) - \cos\delta_W \right] \\ & - (c_{RL} + c_{RR}) - (F_{LFL} + F_{LFR}) \cdot \cos\delta_W \\ & - \left(F_{LRL} + F_{LRR} - c_{WX} v_{CoG}^2 \right) \Big\} \\ & + \frac{1}{m_{CoG} v_{CoG}} \cdot \Big\{ (c_{FL} + c_{FR}) \cdot \left(\delta_W - \frac{l_F \cdot \dot{\psi}}{v_{CoG}} \right) \cdot \cos\delta_W \\ & + (F_{LFL} + F_{LFR}) \cdot \sin\delta_W + (c_{RL} + c_{RR}) \cdot \frac{l_R \cdot \dot{\psi}}{v_{CoG}} \Big\} - \dot{\psi} \quad . \end{aligned} \tag{5.50}$$

The effects of the linearization of both differential equations is analyzed by means of simulations. For this, the differential function $f_1(\underline{x}, \underline{u}) =$

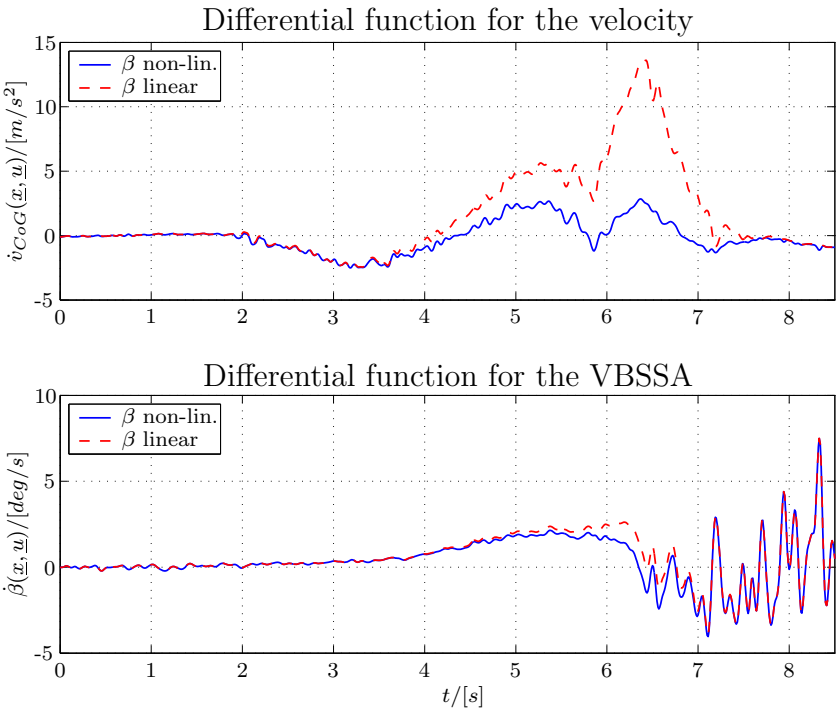

Figure 5.27: Effect of β-linearization on the accuracy of the simulation of the high dynamical clothoide

$\dot{v}_{CoG}(\underline{x},\underline{u})$ in its original version (Eqn. (3.63)) is compared with the linearized Eqn. (5.49). The same procedure is carried out for $f_2(\underline{x},\underline{u}) = \dot{\beta}(\underline{x},\underline{u})$. The simulation data set is again a clothoide drive of high dynamics. The measured state and input variables are applied for the simulation. Fig. 5.27 compares the linearized with the original differential function for v_{CoG} and β.
For the vehicle body side slip angle the linearized and the non-linear function are almost equal. For the velocity, there are significant deviations, though. To overcome this disadvantage, the velocity is regarded as an *input* instead of a *state* variable. Then, the differential equation for v_{CoG} is not needed any more.

Reduction of System Order

The reduced model contains only two differential equations. For the yaw rate, the original differential Eqn. (3.65) can be employed, as the vehicle body side slip angle has only linear influence. For the vehicle body side slip angle itself, the linearized Eqn. (5.50) is used:

$$\begin{aligned} \dot{\beta} &= a_{11}(\dot{\psi},\underline{u})\cdot\beta + a_{12}(\underline{u})\cdot\dot{\psi} + b_1(\underline{u}) \quad , \\ \ddot{\psi} &= a_{21}(\underline{u})\cdot\beta + a_{22}(\underline{u})\cdot\dot{\psi} + b_2(\underline{u}) \end{aligned} \tag{5.51}$$

with a_{11}, a_{12}, a_{21}, a_{22} and b_1 as well as b_2 being specified in Appendix A.2. The system has six input variables

$$\underline{u} = \left[\begin{array}{cccccc} F_{LFL} & F_{LFR} & F_{LRL} & F_{LRR} & \delta_W & v_{CoG} \end{array} \right]^T \quad .$$

The two state variables β and $\dot{\psi}$ build the state vector

$$\underline{x} = \left[\begin{array}{cc} \beta & \dot{\psi} \end{array} \right]^T \quad .$$

The only system output is the yaw rate $y = \dot{\psi}$.
The state space model (5.51) contains the vehicle body side slip angle as a linear quantity. Therefore, it fulfills the structural requirements for the observer design presented in Sections 5.4.4 and 5.4.5.
Simulations of the restructured model show that it is advantageous to use the modeled center of gravity velocity $\hat{v}_{CoG}$ instead of the measured one. The model accuracy can be significantly improved then. Fig. 5.28 shows the resulting structure of the observer. The observer gain $\underline{L}(\underline{\hat{x}}, \underline{u})$ is calculated based on the model (5.51) with two state variables and with linear influence of β. As the process model, though, the adaptive non-linear state space model with Eqns. (3.63) - (3.65) is used. It provides estimation values $\underline{\hat{x}}$ for all three state variables (velocity, vehicle body side slip angle and yaw rate). However, the observer only influences the side slip angle and the yaw rate directly. The velocity is only affected by the feedback of the corrected estimation values $\hat{\beta}$ and $\dot{\hat{\psi}}$. The observability of the restructured system is proven in Appendix A.3.3. After the proof of observability, the observer design can be carried out.

5.4.4 Linearization Observer for Restructured Model

For the restructured model (5.51)

$$\begin{array}{rcl} \dot{\underline{x}} & = & \underline{f}(\underline{x}, \underline{u}) = \underline{A}(y, \underline{u})\, \underline{x} + \underline{b}(y, \underline{u}) \quad , \\ y & = & \underline{C}\, \underline{x} \quad , \end{array}$$

a linearization observer is designed:

$$\begin{array}{rcl} \dot{\underline{\hat{x}}} & = & \underline{f}(\underline{\hat{x}}, \underline{u}) = \underline{A}(\hat{y}, \underline{u})\, \underline{\hat{x}} + \underline{b}(\hat{y}, \underline{u}) + \underline{L}(\underline{\hat{x}}, \underline{u}) \cdot (y - \hat{y}) \quad , \\ \hat{y} & = & \underline{C}\, \underline{\hat{x}} \quad . \end{array} \tag{5.52}$$

The output variable y is equal to x_2. It is replaced by its estimation value $y = \hat{x}_2$.

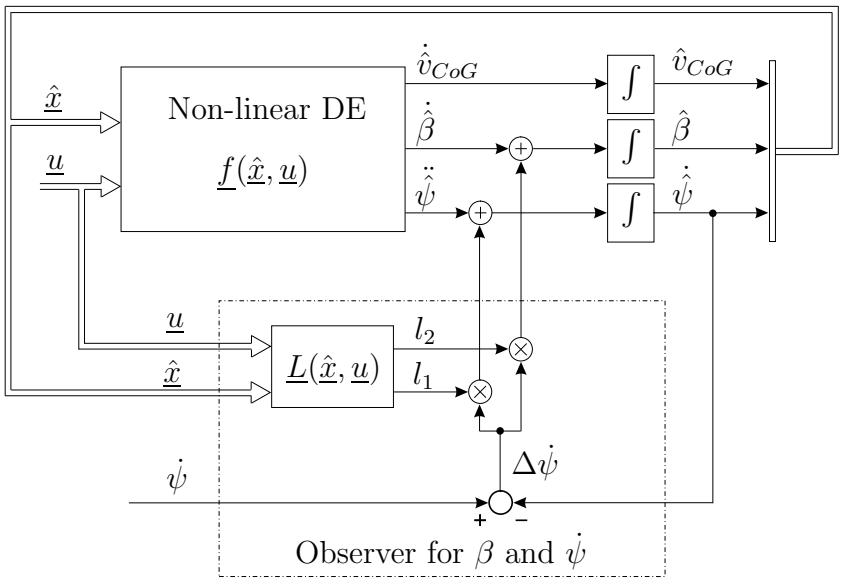

Figure 5.28: Structure of the observer for the restructured non-linear model

The dynamic matrix is set up like in Eqn. (5.35). For the system (5.51), the dynamic matrix $\underline{F}$ becomes

$$\underline{F}(\hat{\underline{x}}, \underline{u}) = \left.\frac{\partial \underline{f}(\underline{x}, \underline{u})}{\partial \underline{x}}\right|_{\underline{x}=\hat{\underline{x}}} - \underline{L}(\hat{\underline{x}}, \underline{u})\underline{C} = \begin{bmatrix} a_{11}(\hat{\dot{\psi}}, \underline{u}) & a_{12}^*(\hat{\beta}, \underline{u}) - l_1 \\ a_{21}(\underline{u}) & a_{22}(\underline{u}) - l_2 \end{bmatrix}. \tag{5.53}$$

The term a_{12}^* is

$$\begin{aligned} a_{12}^*(\beta, \underline{u}) &= \frac{\partial \dot{\beta}}{\partial \dot{\psi}} = \frac{\partial a_{11}(\dot{\psi}, \underline{u})}{\partial \dot{\psi}} \cdot \beta + a_{12}(\underline{u}) \\ &= -\frac{\beta \cdot (c_{FL} + c_{FR}) \cdot l_F \cdot \sin \delta_W}{m_{CoG} v_{CoG}^2} + a_{12}(\underline{u}). \end{aligned} \tag{5.54}$$

With the poles λ_1 and λ_2 the characteristic equation reads

$$\det\left(\begin{bmatrix} \lambda_1 & 0 \\ 0 & \lambda_2 \end{bmatrix} - \underline{F}\right) = \det\begin{pmatrix} \lambda_1 - a_{11} & -a_{12}^* + l_1 \\ -a_{21} & \lambda_2 - a_{22} + l_2 \end{pmatrix} \stackrel{!}{=} 0. \tag{5.55}$$

Like for the other linearization observers, the strategy is to prefer a simple dynamic matrix $\underline{F}$ to an observer where all eigenvalues are fix. Choosing

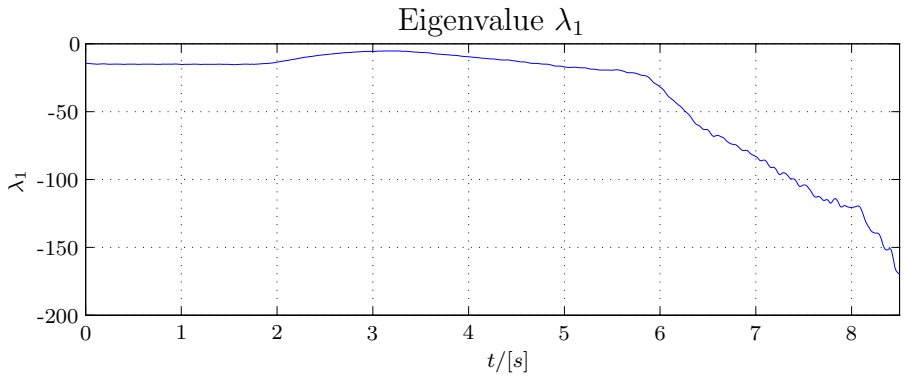

Figure 5.29: Behavior of time-varying pole for the linearization observer of the restructured system (drive: highly dynamical clothoide)

the observer gain

$$\underline{L} = \begin{bmatrix} a_{12}^{*}(\hat{\beta}, \underline{u}) \\ a_{22}(\underline{u}) - \lambda_2 \end{bmatrix} \tag{5.56}$$

provides a simple dynamic matrix

$$\underline{F}(\underline{\hat{x}}, \underline{u}) = \begin{bmatrix} a_{11}(\hat{\dot{\psi}}, \underline{u}) & 0 \\ a_{21}(\underline{u}) & \lambda_2 \end{bmatrix} \quad . \tag{5.57}$$

The pole λ_2 is fixed at -80. The other pole λ_1 is time-varying

$$\begin{aligned} \lambda_1(t) = a_{11}(\hat{\dot{\psi}}, \underline{u}) \;\; = \;\; & \frac{1}{m_{CoG} v_{CoG}} \cdot \Big\{ -(F_{LRL} + F_{LRR} - c_{WX} \cdot v_{CoG}^2) \\ & -(c_{RL} + c_{RR}) - (F_{LFL} + F_{LFR}) \cdot \cos \delta_W \\ & +(c_{FL} + c_{FR}) \cdot [\sin \delta_W \cdot (\delta_W - \frac{l_F \cdot \hat{\dot{\psi}}}{v_{CoG}}) - \cos \delta_W] \Big\}. \end{aligned}$$

To guarantee the stability of the observer, the time behavior of the eigenvalue λ_1 is simulated for the clothoide of high dynamics. Fig. 5.29 shows that the eigenvalue remains negative for the complete test drive. This result was confirmed by other test drives and shows that the observer is stable. Therefore, the observer gain (5.56) can be applied.
Fig. 5.30 compares the observer results of the observer design with the original model and the restructured model. The results for both observers are almost identical. Both observers approximate the measured reference very well. That means that the observer design with the restructured state space model is justifiable. Therefore, the observer design by means of a quality function can also be carried out in Section 5.4.5.

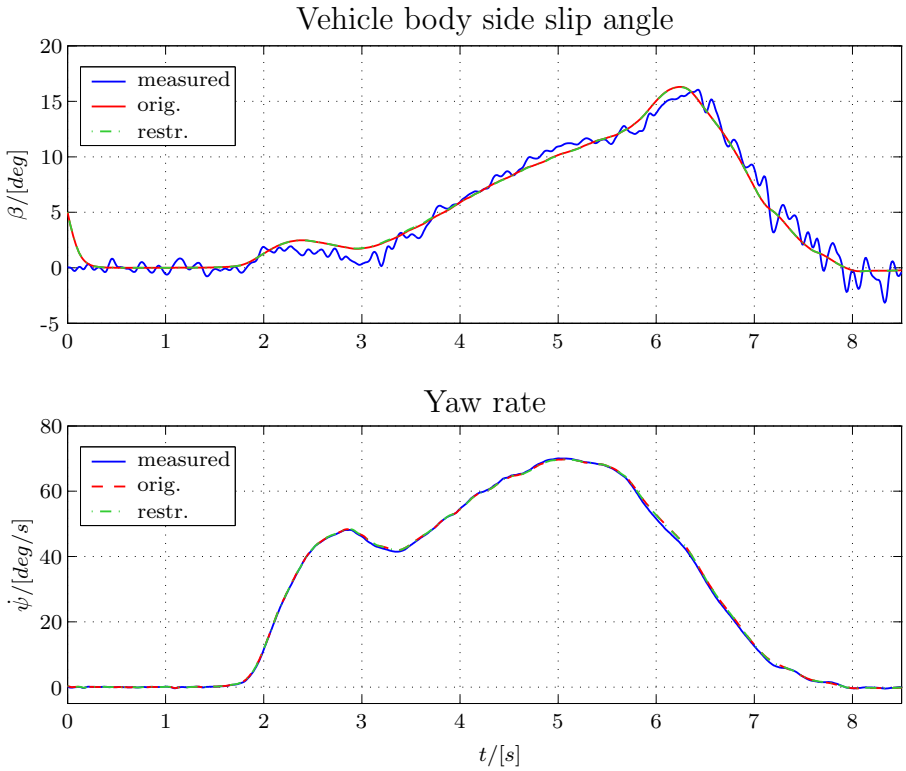

Figure 5.30: Comparison of the linearization observer for the original model and for the restructured two track model by means of a clothoide of high dynamics

5.4.5 Observer Design with Adaptation of a Quality Function for the Restructured Model

Observer Concept

In case that a system contains only *linear* non-measurable variables the observer by means of adaptation of a quality function (in the following called "AQF-observer") can be designed, [70]. The system equations are

$$\begin{aligned} \underline{\dot{x}} &= \underline{A}(\underline{y},\underline{u}) \cdot \underline{x} + \underline{b}(\underline{y},\underline{u}) \quad , \\ \underline{y} &= \underline{C}\,\underline{x} \quad . \end{aligned} \tag{5.58}$$

The dimension of the state vector is n. The system has p input quantities and q output quantities. Using a non-linear observer with the state equations

$$\begin{aligned} \underline{\dot{\hat{x}}} &= \underline{A}(\underline{y},\underline{u}) \cdot \underline{\hat{x}} + \underline{b}(\underline{y},\underline{u}) + \underline{L}(\underline{y},\underline{u}) \cdot (\underline{y} - \underline{\hat{y}}) \quad , \\ \underline{\hat{y}} &= \underline{C}\,\underline{\hat{x}} \end{aligned} \tag{5.59}$$

the estimation error differential equation is

$$\dot{\underline{\tilde{x}}} = \left[\underline{A}(\underline{y},\underline{u}) - \underline{L}(\underline{y},\underline{u})\underline{C}\right]\underline{\tilde{x}} \quad . \tag{5.60}$$

The design of the AQF-observer differs fundamentally from the linearization observers presented in Sections 5.4.2 and 5.4.4, which were designed by pole placement. The AQF-observer adapts the non-linear estimation error $\underline{\tilde{x}}$ according to Eqn. (5.60) to the estimation error of a linear reference model. The error $\underline{\tilde{x}}$ must converge to the error equilibrium point $\underline{\tilde{x}}_R$. Thereby, the area of convergence around $\underline{\tilde{x}}_R$ must be as large as possible.
The system (5.58) can be commonly described by

$$\begin{aligned} \dot{\underline{x}} &= \underline{f}(\underline{x},\underline{u}) \\ \underline{y} &= \underline{C}\,\underline{x} \end{aligned} \quad .$$

Linearizing the system around an equilibrium point $\underline{x}_R, \underline{u}_R$ yields a linear reference model. The equilibrium point is characterized by

$$\dot{\underline{x}}\,\big|_{\underline{x}_R,\underline{u}_R} = 0\,.$$

The linear reference model is given by

$$\begin{aligned} \dot{\underline{x}}_{lin} &= \underline{A}_0 \cdot \underline{x}_{lin} + \underline{B}_0 \cdot \underline{u}_{lin} \\ \underline{y}_{lin} &= \underline{C} \cdot \underline{x}_{lin} \end{aligned} \tag{5.61}$$

with

$$\underset{(n,n)}{A_0} = \left.\frac{\partial \underline{f}(\underline{x},\underline{u})}{\partial \underline{x}}\right|_{\underline{x}=\underline{x}_R,\,\underline{u}=\underline{u}_R}, \qquad \underset{(n,p)}{B_0} = \left.\frac{\partial \underline{f}(\underline{x},\underline{u})}{\partial \underline{u}}\right|_{\underline{x}=\underline{x}_R,\,\underline{u}=\underline{u}_R},$$

$$\underline{x}_{lin} = \underline{x} - \underline{x}_R, \quad \dot{\underline{x}}_{lin} = \dot{\underline{x}} - \dot{\underline{x}}_R = \dot{\underline{x}},$$

$$\underline{u}_{lin} = \underline{u} - \underline{u}_R \quad \text{and} \quad \underline{y}_{lin} = \underline{y} - \underline{y}_R\,.$$

For this system, a linear observer is designed:

$$\begin{aligned} \dot{\hat{\underline{x}}}_{lin} &= \underline{A}_0\,\hat{\underline{x}}_{lin} + \underline{B}_0\,\underline{u}_{lin} + \underline{L}_{lin} \cdot (\underline{y}_{lin} - \hat{\underline{y}}_{lin}) \\ \hat{\underline{y}}_{lin} &= \underline{C} \cdot \hat{\underline{x}}_{lin} \end{aligned} \quad . \tag{5.62}$$

The differential equation for the linear estimaton error $\underline{\tilde{x}}_{lin} = \underline{x}_{lin} - \hat{\underline{x}}_{lin}$ then reads:

$$\dot{\underline{\tilde{x}}}_{lin} = \left(\underline{A}_0 - \underline{L}_{lin}\underline{C}\right) \cdot \underline{\tilde{x}}_{lin} \tag{5.63}$$

with constant matrices $\underline{A}_0, \underline{L}_{lin}$ and $\underline{C}$. The coefficients of the *linear* $\underline{L}_{lin}$ are determined by pole placement:

$$\det(s\underline{I}_n - \underline{A}_0 + \underline{L}_{lin}\,\underline{C}) \stackrel{!}{=} \prod_{\nu=1}^{n}(s - \lambda_\nu) \quad . \tag{5.64}$$

The poles are placed in the open left half plane. Then, the error $\underline{\tilde{x}_{lin}}$ vanishes after sufficient time.
To adapt the dynamics of the non-linear estimation error (5.60) to the one of the linear reference system according to Eqn. (5.63), a stability criterion of the non-linear system theory is employed. The so called LJAPUNOV-method is explained in detail in [23] or [49]. The general idea is only briefly described here. After introducing the LJAPUNOV-method, it is applied to the estimation error $\underline{\tilde{x}}$.

Ljapunov-Method

The LJAPUNOV-method can be applied to non-linear systems of the form

$$\dot{\underline{x}} = \underline{f}(\underline{x}, \underline{u})$$

to analyze the stability of the equilibrium point $\underline{x}_R = \underline{0}$. Note that this equilibrium point $\underline{x}_R = \underline{0}$ is different from the one of the linear reference model specified by Eqn. (5.61). The equilibrium point is called globally asymptotically stable if the state vector $\underline{x}(t)$ converges to the equilibrium point $\underline{x}_R = \underline{0}$ from any arbitrary initial point $\underline{x}_0$ (see Fig. 5.31). If this is true only for a certain area around the equilibrium point the stability is called locally asymptotical. The LJAPUNOV-method provides a criterion to assess the characteristics of the stability:

Theorem 5.7
The equilibrium point $\underline{x}_R = \underline{0}$ of a dynamic system $\dot{\underline{x}} = \underline{f}(\underline{x}, \underline{u})$ is globally asymptotically stable, if a continuous function $V(\underline{x})$ exists which holds the conditions

$$\begin{aligned}
&(1) \quad V(\underline{x}) > 0 \;\forall\; \underline{x} \neq \underline{0} \quad , \\
&(2) \quad V(\underline{x}) = 0 \text{ for } \underline{x} = \underline{0} \ , \\
&(3) \quad \dot{V}(\underline{x}) < 0 \;\forall\; \underline{x} \neq \underline{0} \text{ and} \\
&(4) \quad \|\underline{x}\| \to \infty \quad \Rightarrow \quad V(\underline{x}) \to \infty \quad .
\end{aligned}$$

$V(\underline{x})$ is said to be positive definite, if it fulfills condition (1) and (2). $\dot{V}(\underline{x})$ is said to be negative definite, if condition (3) is fulfilled. $\diamond$

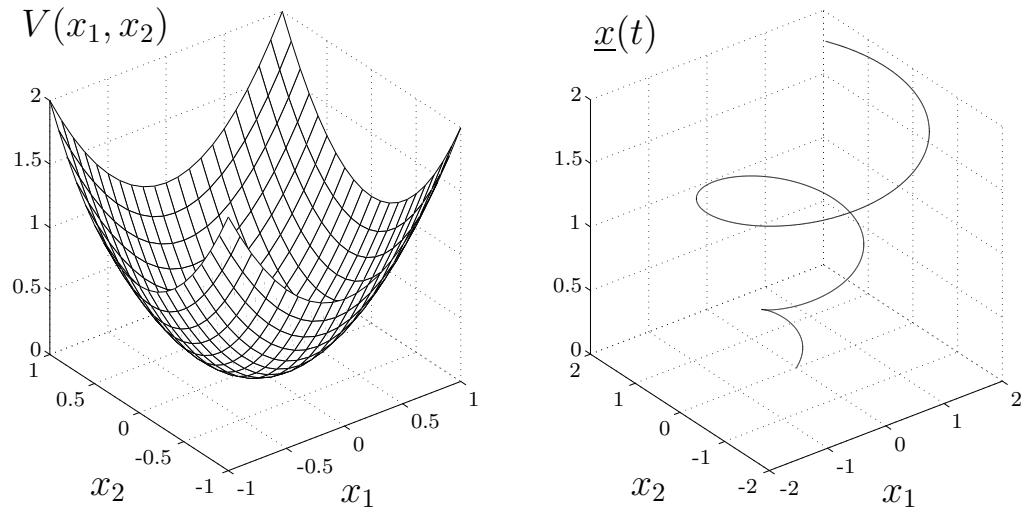

(a) LJAPUNOV-function $V(\underline{x})$ (b) Possible trajectory $\underline{x}(t)$

Figure 5.31: Quadratic, two-dimensional LJAPUNOV-function V($\underline{x}$)

This idea can be expanded to matrices. If function $V(\underline{x})$ has the special form

$$V(\underline{x}) = \underline{x}^T \cdot \underline{P}_L \cdot \underline{x} \quad ,$$

then matrix $\underline{P}_L$ is positive definite, in case $V(\underline{x})$ is positive definite. The definition for a negative definite matrix $\underline{P}_L$ is accordingly.

Adaptation of the Non-linear to the Linear Error Differential Equation

To adapt the dynamics of the non-linear estimation error (5.60) to the linear reference model (5.61) an appropriate LJAPUNOV-function *for the linear estimation error* $\underline{\tilde{x}}_{lin}$ is defined. It is called ideal LJAPUNOV-function and can be written as

$$V_{lin} = \underline{\tilde{x}}_{lin}^T \underline{P}_L \, \underline{\tilde{x}}_{lin} \quad , \tag{5.65}$$

with

$$\underline{P}_L = \sum_{i=1}^{n} \tilde{P}_{L,ii} \, \underline{\bar{w}}_i \, \underline{w}_i^T \quad .$$

The $\underline{w}_i$ are left-eigenvectors of the observer dynamic matrix $(\underline{A}_0 - \underline{L}_{lin} \, \underline{C})$ and $\underline{\bar{w}}_i$ is the complex conjugate of $\underline{w}_i$. The coefficients $\tilde{P}_{L,ii}$ are positive

weighting functions which can be set arbitrarily. Ideal LJAPUNOV-functions are positive definite for all $\underline{x}$, [23].
The time derivative of the LJAPUNOV-function is

$$\dot{V}_{lin} = -\underline{\tilde{x}}_{lin}^T \underline{R}_{L,lin} \underline{\tilde{x}}_{lin} \quad , \tag{5.66}$$

with

$$\underline{R}_{L,lin} = \left[\underline{C}^T \underline{L}_{lin}^T - \underline{A}_0^T\right] \underline{P}_L + \underline{P}_L \left[\underline{L}_{lin}\underline{C} - \underline{A}_0\right] \quad . \tag{5.67}$$

$\dot{V}_{lin}$ is negative definite and holds condition (3) in Theorem 5.7, if $\underline{R}_{L,lin}$ is positive definite. According to [23] $\underline{R}_{L,lin}$ is positive definite, if all eigenvalues $\lambda_i, i = 1, ..., n$ of the dynamic matrix $(\underline{A}_0 - \underline{L}_{lin} \cdot \underline{C})$ are in the open left half plane. As the design of the observer gain (5.64) fulfills this condition, $\dot{V}_{lin}$ decreases exponentially and the linear error $\underline{\tilde{x}}_{lin}$ converges against $\underline{\tilde{x}}_{lin,R} = \underline{0}$.
The ideal LJAPUNOV-function is set up *for the non-linear estimation error* $\underline{\tilde{x}}$ as well:

$$V = \underline{\tilde{x}}^T \underline{P}_L \underline{\tilde{x}} \quad \Rightarrow \quad \dot{V} = -\underline{\tilde{x}}^T \underline{R}_L \underline{\tilde{x}} \quad , \tag{5.68}$$

with

$$\underline{R}_L = \left[\underline{C}^T \underline{L}(\underline{y}, \underline{u})^T - \underline{A}(\underline{y}, \underline{u})^T\right] \underline{P}_L + \underline{P}_L \left[\underline{L}(\underline{y}, \underline{u})\underline{C} - \underline{A}(\underline{y}, \underline{u})\right] \quad . \tag{5.69}$$

The design of the linear observer according to Eqn. (5.64) makes the estimation error $\underline{\tilde{x}}_{lin}$ decrease fast. Therefore, $\dot{V}_{lin}$ also decreases quickly (Fig. 5.31). In order to adapt the *dynamics* of the non-linear estimation error $\underline{\tilde{x}}$ to the linear error $\underline{\tilde{x}}_{lin}$, $\dot{V}$ must be adapted to $\dot{V}_{lin}$ by minimizing the norm

$$N_{\underline{R}_L} = \left\| \underline{R}_{L,lin} - \underline{R}_L \right\| \quad , \tag{5.70}$$

with appropriate choice of the observer matrix $\underline{L}(\underline{y}, \underline{u})$ in Eqn. (5.69). The norm is the geometric sum of the deviations between the elements of matrix $\underline{R}_{L,lin} = \left(r_{L,ij}^{(lin)}\right)$ and those of $\underline{R}_L = (r_{L,ij})$:

$$N_{\underline{R}_L} = \sqrt{\sum_{i,j=1}^{n} \left(r_{L,ij}^{(lin)} - r_{L,ij}\right)^2} \quad .$$

Using Eqn. (5.69) yields:

$$\begin{aligned} \underline{R}_{L,lin} - \underline{R}_L \;=\; & \underline{R}_{L,lin} - \underline{C}^T \underline{L}(\underline{y}, \underline{u})^T \underline{P}_L + \underline{A}(\underline{y}, \underline{u})^T \underline{P}_L \\ & - \underline{P}_L \underline{L}(\underline{y}, \underline{u}) \underline{C} + \underline{P}_L \underline{A}(\underline{y}, \underline{u}). \end{aligned} \tag{5.71}$$

Isolating $\underline{L}$ in Eqn. (5.71) requires an extension of the commonly used matrix operations. The underlying theory shall not be explained in detail here. It can for instance be found in [70].

Observer Design for the Restructured Model

Starting point for the observer design is the underlying restructured model described by Eqns. (5.58). For this system, the observer differential equation is given by

$$\dot{\hat{\underline{x}}} = \underline{A}(\dot{\psi}, \underline{u}) \cdot \hat{\underline{x}} + \underline{b}(\underline{u}) + \underline{L}(\dot{\psi}, \underline{u}) \cdot (\dot{\psi} - \dot{\hat{\psi}}) \quad , \tag{5.72}$$

the error differential equation is

$$\dot{\tilde{\underline{x}}} = \left[\, \underline{A}(\dot{\psi}, \underline{u}) - \underline{L}(\dot{\psi}, \underline{u}) \, \underline{C} \, \right] \tilde{\underline{x}} = \begin{bmatrix} a_{11}(\dot{\psi}, \underline{u}) & a_{12}(\underline{u}) - l_1(\dot{\psi}, \underline{u}) \\ a_{21}(\underline{u}) & a_{22}(\underline{u}) - l_2(\dot{\psi}, \underline{u}) \end{bmatrix} \cdot \tilde{\underline{x}}. \tag{5.73}$$

For one equilibrium point of the system, where

$$\dot{\underline{x}} \, \big| \, _{\underline{x}=\underline{x}_R, \underline{u}=\underline{u}_R} = 0 \tag{5.74}$$

is fulfilled, the individual longitudinal wheel forces F_{Lij_R} are set to zero and δ_{W_R} as well as v_{CoG_R} are chosen arbitrarily. For $\delta_{W_R} = 1^\circ$ and $v_{CoG_R} = 10 m/s$ the equilibrium point can be calculated with Eqn. (5.72)

$$\underline{x}_R = \begin{bmatrix} \beta_R \\ \dot{\psi}_R \end{bmatrix} = \begin{bmatrix} 0,2374^\circ \\ 3,536 \frac{^\circ}{s} \end{bmatrix} \quad .$$

Linearizing the non-linear model around the calculated equilibrium point yields the linear reference model according to Eqn. (5.61). For the linear reference model, a LUENBERGER-Observer can be designed. Its observer gain $\underline{L}_{lin}$ is determined by pole placement. The observer poles are chosen left of the poles of the stable linear reference model. As the poles of the reference model are $\lambda_1 = -14,30$ and $\lambda_2 = -21,76$, the poles of the observer are fixed to $\lambda_{B_1} = -20$ and $\lambda_{B_2} = -120$. The free coefficients $\tilde{P}_{L,ii}$ of the ideal LJAPUNOV-function (5.65) are chosen $\tilde{P}_{L,11} = 2$ and $\tilde{P}_{L,22} = 1$. Finally, the observer gain of the non-linear system can be calculated:

$$\underline{L}(\dot{\psi}, \underline{u}) = \begin{bmatrix} 109,9 \\ 117,4 \end{bmatrix} + \begin{bmatrix} 1,404 & 0,3309 & 1 & 0 \\ -0,1038 & 1,033 & 0 & 1 \end{bmatrix} \cdot \begin{bmatrix} a_{11}(\dot{\psi}, \underline{u}) \\ a_{21}(\underline{u}) \\ a_{12}(\underline{u}) \\ a_{22}(\underline{u}) \end{bmatrix} . \tag{5.75}$$

The elements a_{11}, a_{12}, a_{21} and a_{22} are given in Appendix A.2 by Eqns. (A.10) - (A.13).

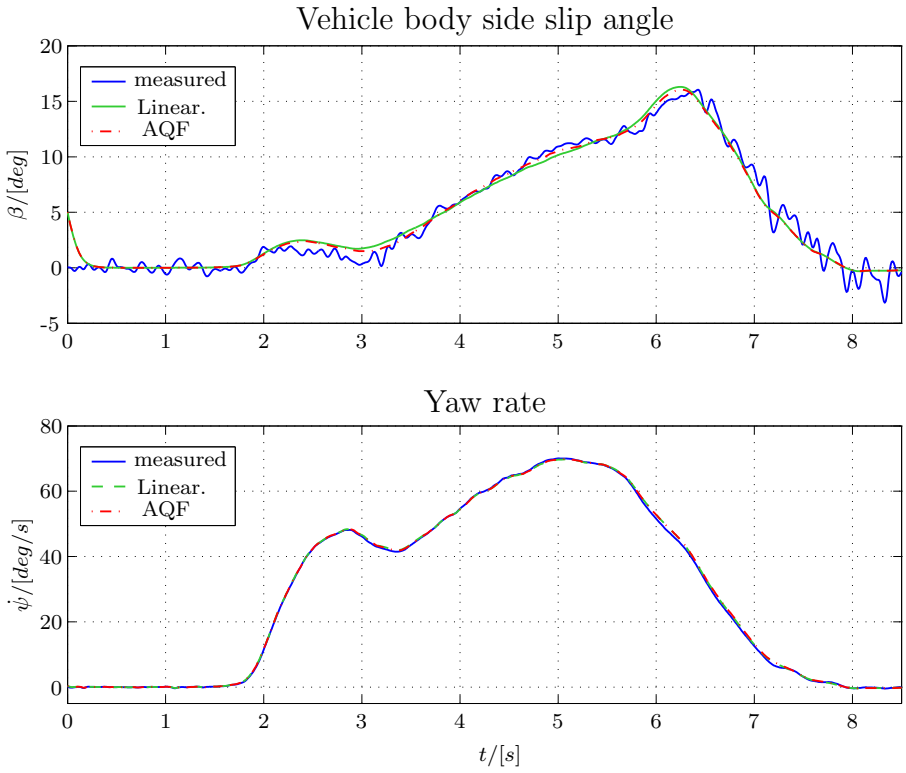

Figure 5.32: Comparison of linearization observer and observer with adaptation of a quality function (AQF) (test drive: clothoide of high dynamics)

Validation

Knowing the elements of the observer gain, the observer is designed and validated with three representative test drives. Fig. 5.32 compares the linearization observer and the observer with adaptation of a quality function (AQF). Both observers base on the restructured non-linear two track model. The yaw rate is the only measured output variable of this system. Both observers are capable to adapt the model to the measured yaw rate. The initial VBSSA values of the observers were chosen different from the process. After $t = 0.3s$, both observers converge against the measured reference. Between $t = 3s$ and $t = 3.5s$ and between $t = 6s$ and $t = 6.5s$ the AQF-observer is slightly more accurate than the linearization observer. To assess the quality of both observers, the average error over N measurement values

$$\Delta\beta = \frac{1}{N}\sum_{i=1}^{N}\sqrt{(\hat{\beta}(t_i) - \beta(t_i))^2} \tag{5.76}$$

is calculated. For the AQF-observer, the error is $\Delta\beta = 0,588°$, for the linearization observer it is slightly larger: $\Delta\beta = 0,667°$. The computational

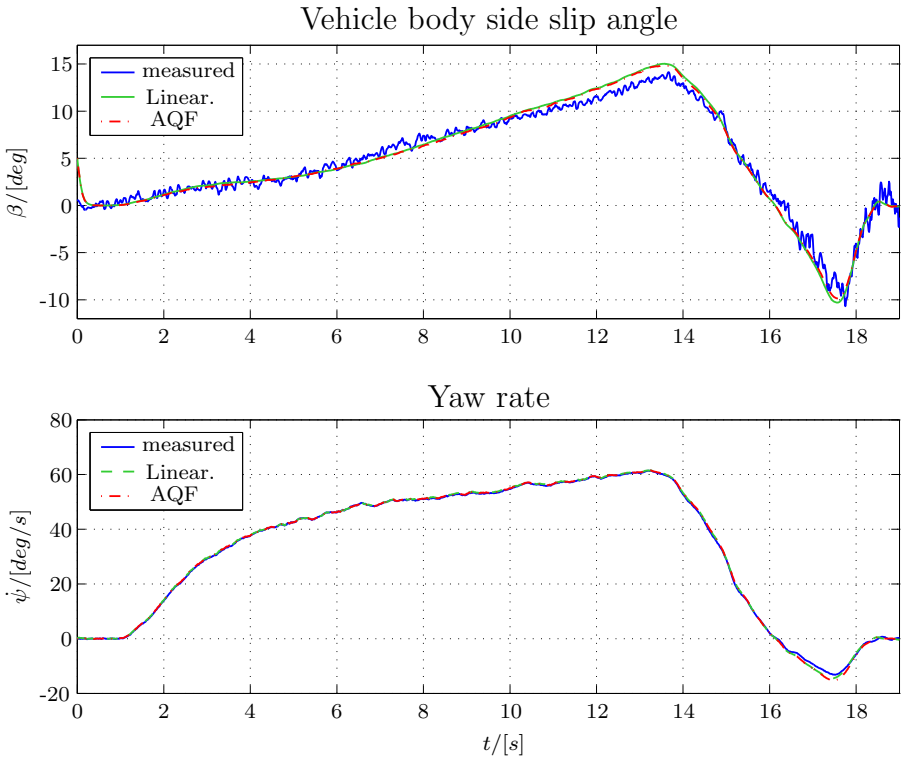

Figure 5.33: Comparison of linearization observer and observer with adaptation of a quality function (AQF) (test drive: transient circle)

complexity of the observers shall be compared as well. On an Athlon XP 2,4GHz personal computer with 512 MB RAM, the linearization observer takes $T_{Sim,L} = 43,7ms$ to simulate one second of a test drive. The AQF-observer is a little bit slower and takes $T_{Sim,AQF} = 49,7ms$. The AQF-observer is a little bit more accurate, but on the other hand a little bit slower. Therefore, the observers are tested with two more test drives.
Fig. 5.33 shows a test drive, where the driver drives straightforward and enters a curve afterwards. By increasing the steering angle, the curve radius gets smaller. That means, Fig. 5.33 describes a transient circle. Again both observers follow the measured reference very well. The average error (5.76) is $\Delta\beta = 0,603°$ for the AQF- and $\Delta\beta = 0,652°$ for the linearization observer.
The last test drive employed is a slalom drive shown in Fig. 5.34. Both observers follow the reference well and are almost equal. The linearization observer ($\Delta\beta = 0,123°$) is insignificantly more accurate than the AQF-observer ($\Delta\beta = 0,126°$).
It is hard to decide which of the observers is superior. The approximation quality and the computational complexity are almost equal, although the observer design strategies are completely different. Nevertheless, both observers are capable to estimate the vehicle body side slip angle up to the

stability limit of the vehicle.

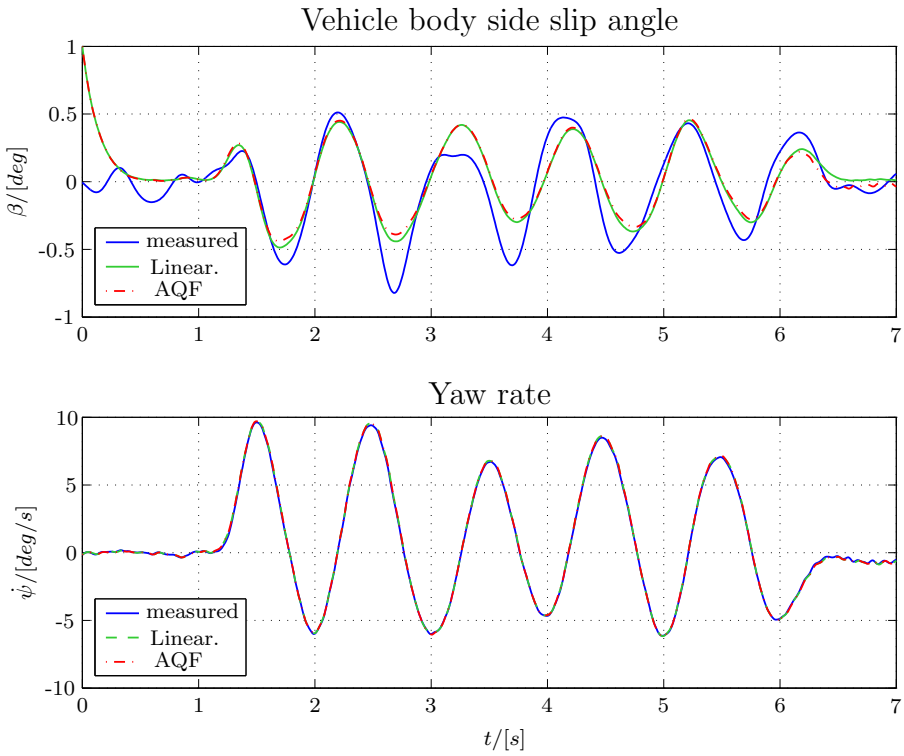

Figure 5.34: Comparison of linearization observer and observer with adaptation of a quality function (AQF) (test drive: slalom)

5.4.6 Comparison of the Observer Approaches

The goal of observer design in Sections 5.4.2 - 5.4.5 was the model based determination of the vehicle body side slip angle. The easiest way would be to apply a linear observer. For accident reconstruction purposes, though, the VBSSA shall be described up to the stability limit. Model validation of the linear single track model shows that the linear model and therefore also a linear observer is not sufficiently accurate to fulfill this requirement. Therefore, only non-linear observers were analyzed. Without changing the structure of the adaptive non-linear two track model from Section 3.3.7, only a *linearization observer* or an *extended* LUENBERGER-*observer* can be applied. The latter one was not presented in this thesis. The observer design is very complex. The results are not as good as those presented in this thesis and the computational complexity is large. The theory of the extended LUENBERGER-observer can be found in [6] or [81]. For highly dynamical drive situations, it provides good results, if the yaw rate is the only measured output. Otherwise, model inaccuracies for velocity calculation cause errors.

As the form of the non-linearity plays an important role for observer design, the adaptive non-linear two track model was restructured, so that the influence of the side slip angle is linear. Additionally, the model inaccuracy concerning the velocity must be eliminated by considering the modeled velocity as a system input. Then, a variety of other observers can be designed. One group of observers was not presented in this thesis: observers in canonical form. Here, a *high gain observer*, [5] and a *normal form observer*, [42] were analyzed. For both observers, the restructured vehicle model is transformed into a canonical form. Afterwards, an observer is designed in canonical coordinates and transformed back to initial coordinates at the end. Both the *high gain* and the *normal form observer* are not as accurate as the presented observers and tend to become unstable in certain driving situations.
The *linearization observer* for the restructured model and the *observer with adaptation of a quality function (AQF-observer)* both provide very accurate results. The linearization observer is designed with pole placement, whereas the AQF-observer adapts the dynamics of the non-linear estimation error to a linear reference model. The computational complexity and the accuracy of these observers is almost equal.
The presented vehicle body side slip angle observers were validated with a variety of test drives. For the test drives conducted the VBSSA can be approximated very accurately up to the stability limit with the observers presented in this thesis.

5.4.7 Extended Kalman-Bucy-Filter

In Section 5.4.2 the linearization observer was designed for one and two measured output signals. For normal test drives both observers show good results. In these cases, it is certainly better to use all available output signals. For highly dynamical driving situations, however, it is advantageous to use the yaw rate signal as the only measurable output (see Fig. 5.26).
In this section, an extended Kalman-Bucy-Filter (EKBF) is designed, to achieve both of these properties without the necessity to restructure the model and to design a new observer. The situation dependent choice of the filter's noise covariance matrices allows to determine appropriate weights for the vehicle model or the measured output signals. The idea is to detect drive situations, where the vehicle speed calculated by the model is unreliable due to model inaccuracies. In these drive situations, the respective element of the covariance matrix must be increased so that the filter does not consider it any more.
After describing the time-discrete Kalman-Filter, the time-continuous

KALMAN-BUCY-Filter (KBF) is described. Both filters can be designed for linear and time-varying processes. The extended KALMAN-BUCY-Filter is an extension to non-linear processes, where the system is linearized around the currently estimated state.
The derivation of the filter equations is lengthy and complex. For the linear filters it can be found for instance in [7], [8].

Kalman-Filter

In the following, the KALMAN-Filter and its working principle will be described. A linear and time-discrete system with the state vector $\underline{x}_k$, the output vector $\underline{y}_k$ which is disturbed by the vectorial noise processes $\underline{v}_k$ and $\underline{w}_k$ reads

$$\underline{x}_{k+1} = \underline{\Phi}(T_s) \cdot \underline{x}_k + \underline{H} \cdot \underline{u}_k + \underline{w}_k \quad , \tag{5.77}$$

$$\underline{y}_k = \underline{C} \cdot \underline{x}_k + \underline{v}_k \quad . \tag{5.78}$$

The matrix $\underline{\Phi}(T_s)$ is the time-discrete dynamic matrix derived from the continuous dynamic matrix $\underline{A}$ by

$$\underline{\Phi}(T_s) = \mathcal{L}^{-1}\{(s \cdot \underline{I} - \underline{A})^{-1}\} \Big|_{t=T_s} \quad , \tag{5.79}$$

where $\mathcal{L}^{-1}\{\cdot\}$ is the inverse LAPLACE-Transform of the term in brackets. Respectively, the time-discrete output matrix $\underline{H}$ can be calculated, [22]:

$$\underline{H} = \underline{A}^{-1} \cdot (\underline{\Phi}(T_s) - \underline{I}) \cdot \underline{B} \quad . \tag{5.80}$$

The vectorial noise processes thereby have got the following characteristics:

$$E\{\underline{w}_k\} = E\{\underline{v}_k\} = \underline{0} \quad \forall\, k \qquad \text{and} \qquad E\{\underline{w}_i \cdot \underline{v}_j^T\} = \underline{0} \quad \forall\, i, j \quad . \tag{5.81}$$

$E\{\cdot\}$ describes the expectation of a random variable, i.e. the random processes $\underline{v}_k$ and $\underline{w}_k$ have zero mean and are uncorrelated. The symmetric and positive definite covariance matrices are

$$E\{\underline{w}_i \cdot \underline{w}_j^T\} = \underline{Q}_i \cdot \delta_{ij} \quad \text{and} \tag{5.82}$$

$$E\{\underline{v}_i \cdot \underline{v}_j^T\} = \underline{R}_i \cdot \delta_{ij} \quad . \tag{5.83}$$

δ_{ij} is the KRONECKER-Symbol:

$$\delta_{ij} = \begin{cases} 1 & \text{, for } i = j \\ 0 & \text{, else} \end{cases} \quad .$$

The KALMAN-Filter calculates an estimation value $\underline{\hat{x}}_k$ for the state vector $\underline{x}_k$ by using the output vector $\underline{y}_k$ and the input vector $\underline{u}_k$. The estimation error $\underline{e}_k = \underline{x}_k - \underline{\hat{x}}_k$ has minimum variance.
The KALMAN-Filter for linear and time-discrete systems with the characteristics described by Eqns. (5.77) - (5.83) contains the following equations which are divided in a prediction and in a filter part:

Prediction equations:

$$\underline{\hat{x}}_{k+1|k} = \underline{\Phi}(T_s) \cdot \underline{\hat{x}}_{k|k} + \underline{H} \cdot \underline{u}_k \quad , \tag{5.84}$$

$$\underline{P}_{k+1|k} = \underline{\Phi}(T_s) \cdot \underline{P}_{k|k} \cdot \underline{\Phi}^T(T_s) + \underline{Q}_k \quad . \tag{5.85}$$

Filter equations:

$$\underline{K}_{k+1} = \underline{P}_{k+1|k} \cdot \underline{C}^T \cdot (\underline{C} \cdot \underline{P}_{k+1|k} \cdot \underline{C}^T + \underline{R}_{k+1})^{-1} \quad , \tag{5.86}$$

$$\underline{\hat{x}}_{k+1|k+1} = \underline{\hat{x}}_{k+1|k} + \underline{K}_{k+1} \cdot (\underline{y}_{k+1} - \underline{C} \cdot \underline{\hat{x}}_{k+1|k}) \quad , \tag{5.87}$$

$$\underline{P}_{k+1|k+1} = (\underline{I} - \underline{K}_{k+1} \cdot \underline{C}) \cdot \underline{P}_{k+1|k} \quad , \tag{5.88}$$

with the initial values

$$\underline{\hat{x}}_{0|0} = \underline{x}(t_0) \quad , \tag{5.89}$$

$$\underline{P}_{0|0} = \underline{P}(t_0) \quad . \tag{5.90}$$

In Eqns. (5.84) - (5.88) the matrix $\underline{P}$ is called the error covariance matrix, $\underline{K}$ the KALMAN matrix gain and $\underline{I}$ the identity matrix.
The filter works recursively: before the $(k+1)$-th measurement value $\underline{y}_{k+1}$ is available, in the *prediction step* the estimates for the cycle $k+1$ are calculated based on the results of cycle k. This is described by the notation $\underline{\hat{x}}_{k+1|k}$ and $\underline{P}_{k+1|k}$. After the new measurement value $\underline{y}_{k+1}$ is available, the results are corrected in the *filter step*. Accordingly, the notation is $\underline{\hat{x}}_{k+1|k+1}$ and $\underline{P}_{k+1|k+1}$.
Due to its dependence on $\underline{Q}_k$ the covariance matrix of the prediction step $\underline{P}_{k+1|k}$ is proportional to the system noise $\underline{w}_k$. The larger the variance of $\underline{w}_k$ becomes, the larger the covariance matrix and with it the KALMAN matrix gain $\underline{K}_{k+1}$ gets. Eqn. (5.87) shows that the filter then "trusts" the measurements $\underline{y}_{k+1}$ more and the predicted state variables $\underline{\hat{x}}_{k+1|k}$ less, respectively. The KALMAN matrix gain $\underline{K}_{k+1}$ is proportional to $\underline{R}_{k+1}^{-1}$ as well. If the output noise $\underline{v}_{k+1}$ has a high variance, the measurement weight is reduced. Furthermore, the variance of the filter step is always smaller

than the one of the prediction step

$$\underline{P}_{k+1|k+1} < \underline{P}_{k+1|k} \quad , \tag{5.91}$$

because the filter step contains one more measurement value.
For the state estimation of the linear system the KALMAN-Filter is an optimal minimum variance estimation algorithm. The coefficients of the covariance matrices $\underline{Q}$ and $\underline{R}$ are generally unknown, however. They must be chosen appropriately to achieve good estimation results. The elements of these matrices are weights for the model or the measurement values. If these coefficients are chosen arbitrarily, it cannot be guaranteed any more that the estimation is optimal concerning a minimum variance. This is the case only for the exact variances of the vectorial random processes. However, this pragmatic approach yields good results.
After describing the principle idea of the KALMAN-Filter, the equations for the KALMAN-BUCY-Filter and for the extended KALMAN-BUCY-Filter are set up.

Kalman-Bucy Filter (KBF)

A time-*continuous*, linear system disturbed by the vectorial noise processes $\underline{v}(t)$ and $\underline{w}(t)$ reads

$$\dot{\underline{x}}(t) = \underline{A} \cdot \underline{x}(t) + \underline{B} \cdot \underline{u}(t) + \underline{w}(t) \quad , \tag{5.92}$$

$$\underline{y}(t) = \underline{C} \cdot \underline{x}(t) + \underline{v}(t) \quad . \tag{5.93}$$

As for the time-discrete KALMAN-Filter, the following conditions hold:

$$E\{\underline{w}(t)\} = E\{\underline{v}(t)\} = \underline{0} \quad \forall\, t \quad , \quad E\{\underline{w}(t_i) \cdot \underline{v}^T(t_j)\} = \underline{0} \quad \forall\, t_i, t_j \tag{5.94}$$

$$E\{\underline{w}(t_i) \cdot \underline{w}^T(t_j)\} = \underline{Q}(t_i) \cdot \delta_{ij} \quad , \tag{5.95}$$

$$E\{\underline{v}(t_i) \cdot \underline{v}^T(t_j)\} = \underline{R}(t_i) \cdot \delta_{ij} \quad . \tag{5.96}$$

For this system, a KALMAN-BUCY-Filter is used. The theory of the KBF is described more detailed for instance in [7], [8], [67]. The filter equations are

$$\underline{K}(t) = \underline{P}(t) \cdot \underline{C}^T \cdot \underline{R}^{-1}(t) \quad , \tag{5.97}$$

$$\dot{\hat{\underline{x}}}(t) = \underline{A} \cdot \hat{\underline{x}}(t) + \underline{B} \cdot \underline{u}(t) + \underline{K}(t) \cdot \left[\underline{y}(t) - \underline{C} \cdot \hat{\underline{x}}(t)\right] \quad , \tag{5.98}$$

$$\dot{\underline{P}}(t) = \underline{A} \cdot \underline{P}(t) + \underline{P}(t) \cdot \underline{A}^T - \underline{P}(t) \cdot \underline{C}^T \cdot \underline{R}^{-1}(t) \cdot \underline{C} \cdot \underline{P} + \underline{Q}(t). \tag{5.99}$$

Eqn. (5.98) describes the structure of prediction by means of the linear state differential equation and correction by weighting the difference between measured system output $\underline{y}(t)$ and estimated system output $\underline{C} \cdot \hat{\underline{x}}(t)$. The recursive equation for the error covariance matrix $\underline{P}$ is replaced by a matrix RICATTI differential equation (5.99). The KALMAN-BUCY-Filter has the same characteristics like the KALMAN-Filter. Especially the KALMAN matrix gain (5.97) is still proportional to the system noise covariance matrix $\underline{Q}(t)$ and to the inverse measurement noise covariance matrix $\underline{R}^{-1}(t)$.

Extended Kalman-Bucy Filter (EKBF)

The underlying process of the employed filters is non-linear. The vehicle dynamics behavior can only be sufficiently described by means of the adaptive non-linear two track model (Section 3.3.7). Consequently, a *non-linear* KALMAN-BUCY-Filter must be employed known as the *extended* KALMAN-BUCY-Filter.
The time-continuous non-linear system

$$\dot{\underline{x}}(t) = \underline{f}(\underline{x}(t), \underline{u}(t)) + \underline{w}(t) \quad , \tag{5.100}$$

$$\underline{y}(t) = \underline{h}(\underline{x}(t)) + \underline{v}(t) \tag{5.101}$$

has the noise characteristics described by Eqns. (5.94) to (5.96). The EKBF designed for this system linearizes the system around the currently estimated state vector $\hat{\underline{x}}(t)$. The equations for the EKBF are similar to those of the KBF:

$$\underline{K}(t) = \underline{P}(t) \cdot \hat{\underline{C}}^T(t) \cdot \underline{R}^{-1}(t) \quad , \tag{5.102}$$

$$\dot{\hat{\underline{x}}}(t) = \underline{f}\left(\hat{\underline{x}}(t), \underline{u}(t)\right) + \underline{K}(t) \cdot \left[\underline{y}(t) - \underline{h}\left(\hat{\underline{x}}(t)\right)\right] \quad , \tag{5.103}$$

$$\begin{aligned} \dot{\underline{P}}(t) = {} & \hat{\underline{A}}(t) \cdot \underline{P}(t) + \underline{P}(t) \cdot \hat{\underline{A}}^T(t) \\ & - \underline{P}(t) \cdot \hat{\underline{C}}^T(t) \cdot \underline{R}^{-1}(t) \cdot \hat{\underline{C}}(t) \cdot \underline{P}(t) + \underline{Q}(t) \quad , \end{aligned} \tag{5.104}$$

with

$$\hat{\underline{A}}(t) = \left.\frac{\partial \underline{f}\,(\underline{x}, \underline{u})}{\partial \underline{x}}\right|_{\underline{x}=\hat{\underline{x}}(t), \underline{u}=\underline{u}(t)} \quad \text{and} \quad \hat{\underline{C}}(t) = \left.\frac{\partial \underline{h}\,(\underline{x})}{\partial \underline{x}}\right|_{\underline{x}(t)=\hat{\underline{x}}(t)} \quad . \tag{5.105}$$

Instead of Eqn. (5.98), now the non-linear Eqn. (5.103) is employed for the prediction. In the filter step, the non-linear output Eqn. (5.101) is used. In

a last step, the matrices $\underline{A}$ and $\underline{C}$ in Eqns. (5.97) and (5.99) are replaced by the JACOBIAN-matrices (5.105). The JACOBIANS are calculated in every simulation step for the currently estimated state $\underline{\hat{x}}(t)$. As they are time-varying, the computational complexity grows significantly.

Results

The KALMAN-Filter and the KALMAN-BUCY-Filter cannot be employed for VBSSA estimation. The linearization errors caused by linearizing around a fix equilibrium point are too large. The linear filters were only presented in this section to explain the principle of state estimation. To obtain sufficient accuracy, the linearization must occur in every calculation step. For the EKBF, the JACOBIAN-matrix $\underline{\hat{A}}$ must be calculated once and afterwards only $\underline{\hat{x}}(t)$ and $\underline{u}(t)$ must be inserted in every calculation step. As the output equation (3.67) is already linear, the time-varying calculation of $\underline{\hat{C}}$ is not required. The mathematical terms for Eqns. (5.103) - (5.105) were calculated with the software Maple. Due to their complexity, they are not given in this context.
To consider that the first differential equation of the adaptive non-linear two track model does not describe the driving behavior accurately enough (Fig. 5.26), the system and the observers had to be redesigned in Sections 5.4.2 and 5.4.3. The structure of the EKBF allows to consider the measurement or the model value more or less according to the choice of the elements of the noise covariance matrices $\underline{Q}$ and $\underline{R}$. By choosing these matrices for instance

$$\underline{Q}(t) = \begin{pmatrix} \mathbf{0.1} & 0 & 0 \\ 0 & 4 & 0 \\ 0 & 0 & 10 \end{pmatrix} \qquad \text{and}$$

$$\underline{R}(t) = \begin{pmatrix} \mathbf{1000} & 0 \\ 0 & 0.01 \end{pmatrix} \qquad ,$$

the element $(1,1)$ of matrix $\underline{Q}$ is very much smaller than the respective element of $\underline{R}$. As the element $(1,1)$ influences the weight of the velocity, this means that the system relies almost completely on the vehicle *model* velocity and does not consider the *measurement* any more. Then the estimated state is not adapted to the measured velocity any more. Therefore, the model inaccuracy can be considered without restructuring the system. The appropriate choice of $\underline{Q}$ and $\underline{R}$ is sufficient. Fig. 5.35 compares the

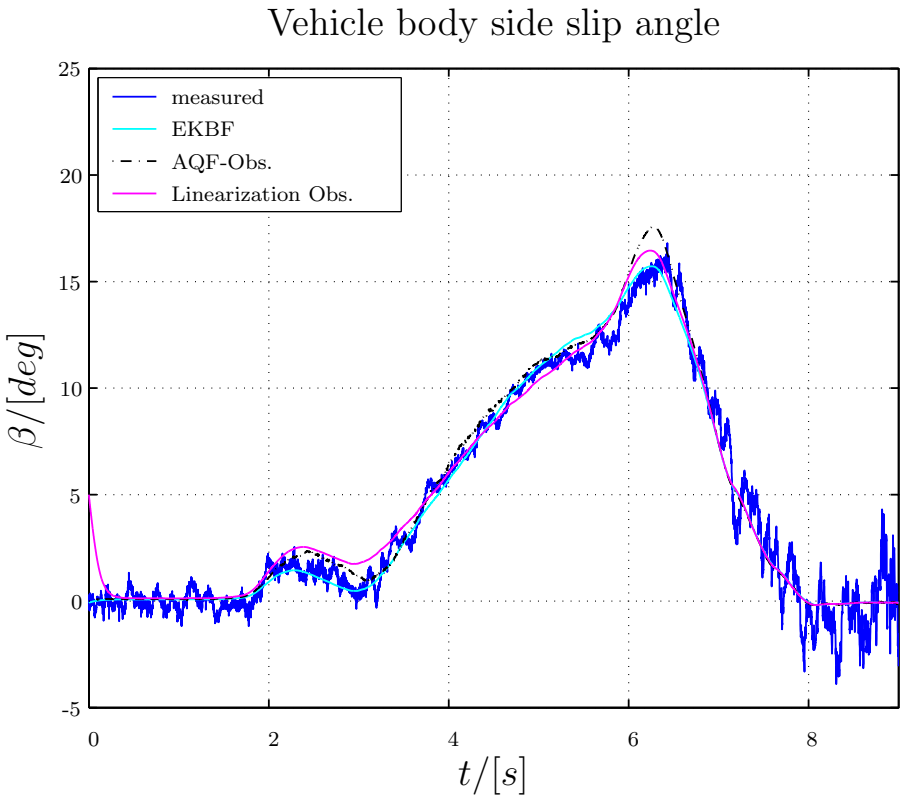

Figure 5.35: Comparison of estimation results of the non-linear state space observers and the extended KALMAN-BUCY-Filter

estimation results of the EKBF with those of the linearization observer designed in Section 5.4.2 and with the AQF-observer (Section 5.4.5). With the specified noise covariance matrices, for the test drives conducted the accuracy of the estimation can even be improved by using the EKBF.
A second estimation result with the same choice for $\underline{Q}$ and $\underline{R}$ can be seen in Fig. 5.36. Again, the EKBF estimates the vehicle body side slip angle very accurately. The error caused by the deviation between modeled and measured velocity shown in the top plot of Fig. 5.36 is eliminated by the appropriate choice of the upper left elements in matrix $\underline{Q}$ and $\underline{R}$.
The EKBF is even more complex than the non-linear observers. The computation time for one second is approximately three times as large as the one for the AQF- and for the linearization observer. On an Athlon 2.4GHz personal computer with 512 MBytes RAM, one second of the model was simulated with the observers and with the EKBF. The EKBF takes $T_{Sim} = 0.11s$ for the calculation whereas the non-linear observers only take approximately $T_{Sim} = 0.04-0.05s$. On the other hand, the big advantage of the extended KALMAN-BUCY-Filter is its flexibility. By changing the elements of the covariance matrices, different model effects can be considered or excluded according to the current drive situation.

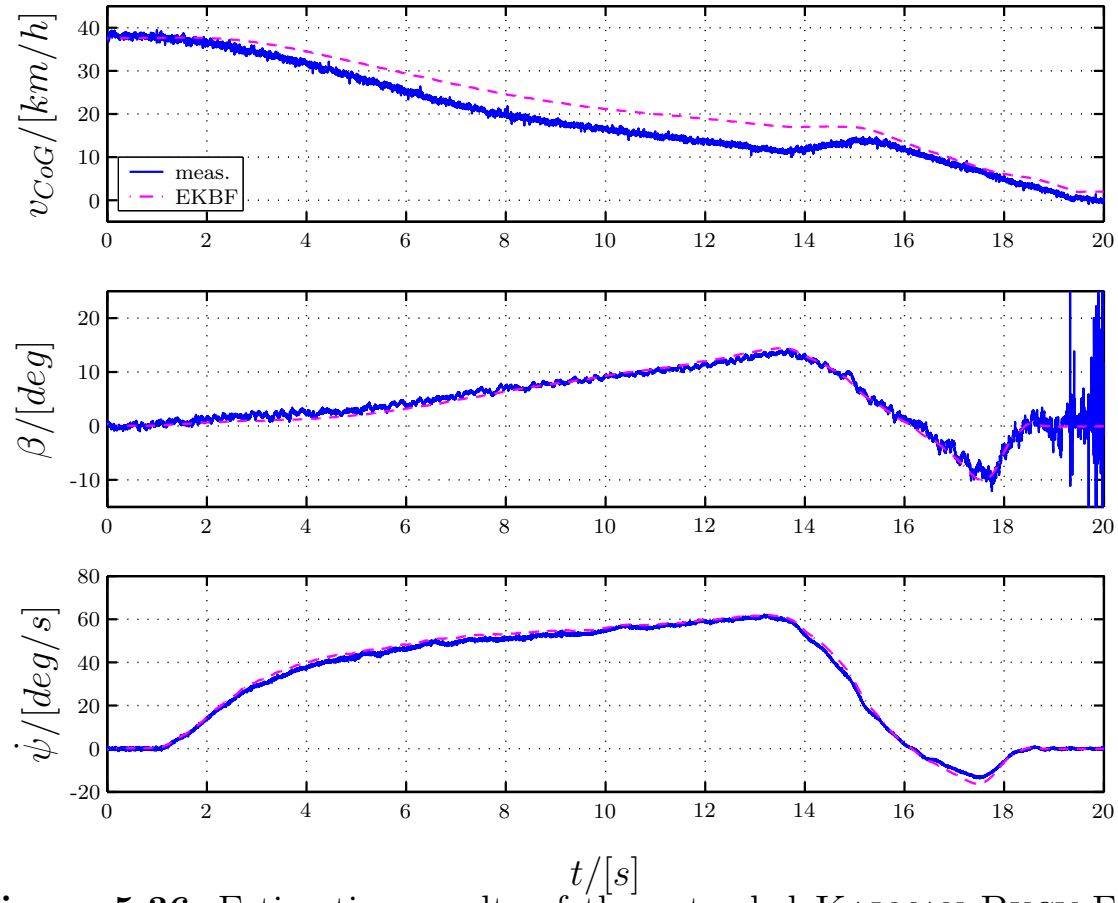

Figure 5.36: Estimation results of the extended KALMAN-BUCY-Filter (test drive: transient circle)

5.4.8 Complete Vehicle Motion Reconstruction

A main goal of accident reconstruction is the complete motion reproduction. In addition to the center of gravity location in an inertial coordinate system the heading of the vehicle must be considered. The course angle

$$\gamma = \psi + \beta \tag{5.106}$$

describes a vehicle's direction of traveling in an inertial coordinate system. That means, in addition to the yaw angle ψ the vehicle body side slip angle β must be known. The state space observers and the extended KALMAN-BUCY-Filter presented in Section 5.4 provide accurate VBSSA estimation values. Therefore, the vehicle motion can be completely reproduced.
Fig. 5.37 illustrates the center of gravity location including the heading. Reconstruction experts recognize that after entering the curve, the slip angle β constantly grows. This points to an unstable driving situation. Additionally, the distances between successive center of gravity locations decrease indicating deceleration of the vehicle. The vehicle body side slip angle of this test drive can be seen in the middle plot of Fig. 5.36.

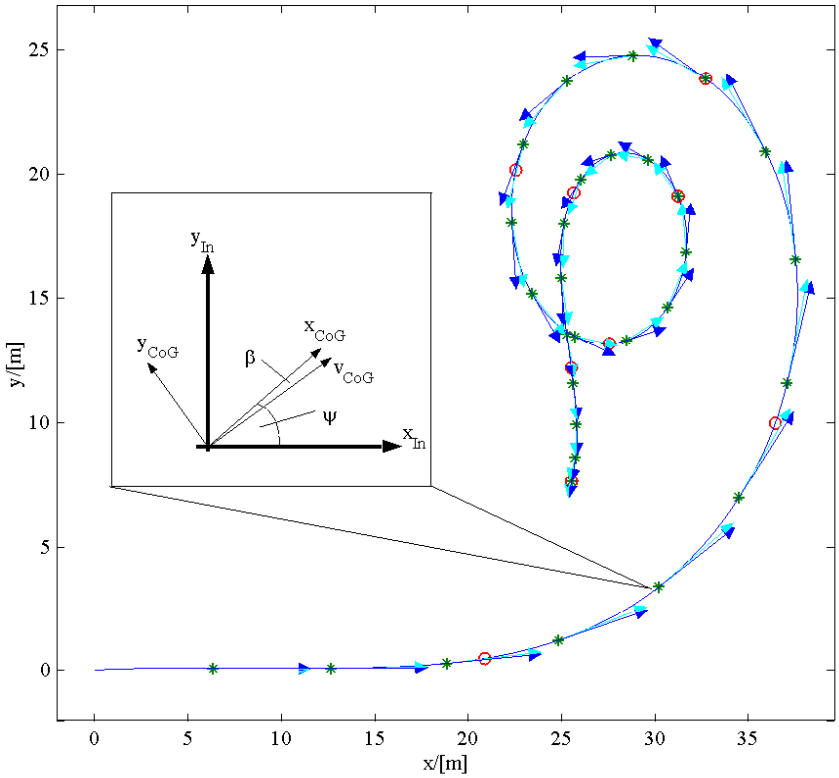

Figure 5.37: Complete vehicle motion of a transient circle drive

Fusing the fuzzy based trajectory reconstruction of Section 5.3 with vehicle body side slip angle estimation provides complete motion reproduction for accident reconstruction experts.
After knowing the center of gravity location and the vehicle heading, the vehicle motion can be "backtracked" after an accident. Starting from an initial position $(x_{In}(t_0),\ y_{In}(t_0))^T$ with a certain course angle $\gamma(t_0)$, the recorded trajectory and heading is calculated backward. The initial position can either be the position of vehicle standstill or any other point on the trajectory, for example the location of a crash with another car. Then, if both vehicles are equipped with an EDR, the location of the crash can be used as a joint origin for the later reconstruction process.

5.5 Mass Estimation

Variations of the vehicle mass influence for instance the accuracy of the vehicle models (see Chapter 3) and also the braking distance. Knowing the vehicle mass allows to draw conclusions whether a vehicle was overloaded or not.
The mass can be determined by evaluating the longitudinal force balance of a vehicle,see Fig. 5.38. The longitudinal drive or brake forces accelerate

or decelerate the vehicle depending on its mass:

$$\underbrace{\hat{m}_{CoG}}_{\frac{1}{\Theta}} \cdot \underbrace{a_{X,C}}_{y} = \underbrace{F_{XFL} + F_{XFR} + F_{XRL} + F_{XRR} - F_R - F_{WX}}_{u} \quad . \tag{5.107}$$

The rolling resistance force F_R can be approximated by Eqn. (3.52), the wind force with the commonly known quadratic approximation of Eqn. (3.53). The longitudinal forces F_{Xij} are determined from a drive and brake model or they are measured like here. The longitudinal acceleration $a_{X,C}$ is a measured signal.
The sum of the longitudinal forces is the input u into a recursive least squares (RLS-) estimator. For detailed information on the RLS-estimator see for instance [56]. The acceleration is the estimator output y. The vehicle mass is the inverse estimation parameter $\frac{1}{\Theta}$.
The *recursive* least squares estimator calculates a new estimation value $\Theta(k)$ by correcting a previously estimated parameter $\Theta(k-1)$. This ensures constant calculation time, in contrast to the "standard" least squares method, where the computation time grows with the number of acquired samples.
Some parameters are changing quickly over time. In this case, a forgetting factor $\lambda_F = (0, 1]$ is introduced which exponentially weights the history of the data set, [40]: $\lambda_F = 1$ considers all samples whereas small values for λ_F only consider the last acquired samples for calculation. That means, the smaller λ_F, the faster the algorithm adapts to parameter changes. On the other hand, the sensitivity to noise increases in this case.
As the vehicle mass is a parameter which is only changing little over time, a forgetting factor $\lambda_F = 1$ is required. A variety of systematic errors are fudging Eqn. (5.107). The most significant ones are gravitational effects caused by road slopes or pitching and rolling, for instance Eqn. (5.2). Secondly, influences of lateral forces affect the estimation accuracy. Therefore, a situation based long time estimation must be employed (Fig. 5.38). The mass estimation algorithm only starts, if the vehicle is driving straightforward. Like in Section 5.2 this is ensured by Eqn. (5.6).
Additionally, the car must be in a calm driving situation. Only then, gravitational influences due to pitching or other transient effects can be neglected. A calm driving situation is detected, if the average wheel acceleration is small:

$$|\dot{\bar{\omega}}_{ij}| = \frac{1}{4} \sum_{ij} |\dot{\omega}_{Rij}| < 1 m/s^2 \quad . \tag{5.108}$$

Gravitational errors caused by road slope are averaged, if the estimation is sufficiently long. Additionally, the results of several estimations carried

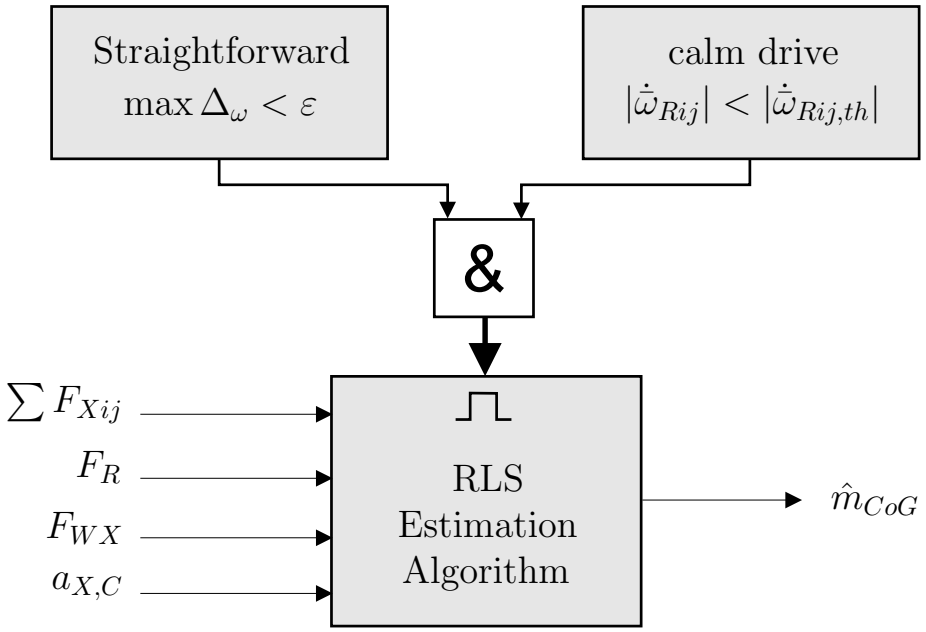

Figure 5.38: Situation based mass estimation

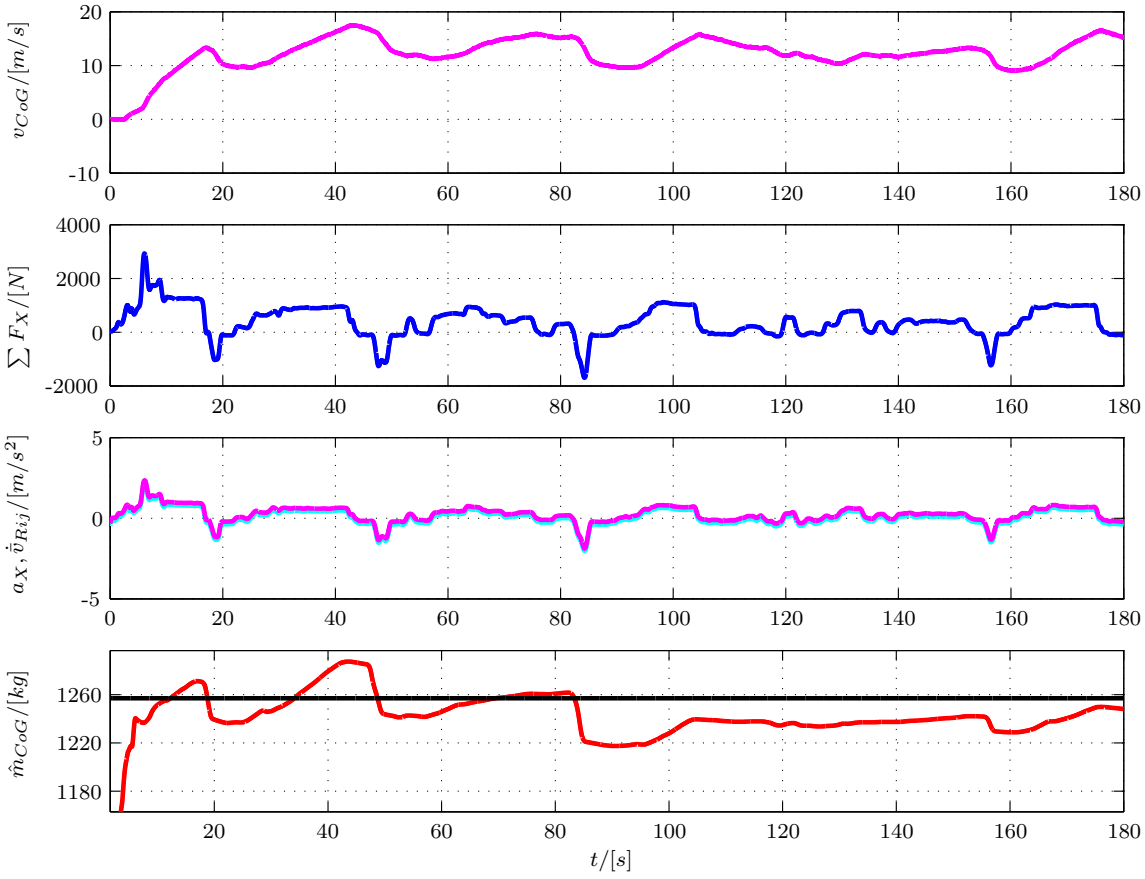

Figure 5.39: Mass estimation result of a long time measurement

out according to the procedure displayed in Fig. 5.38 should be averaged as well to increase the reliability of the estimation. That means that mass estimation is carried out continuously and not only in the pre-accident phase. The results of situation dependent mass estimation have to be stored in a separate memory which is not overwritten by new measurements.
With the presented algorithm, very good mass estimation results can be achieved. Fig. 5.39 shows a three minute record on a test course with little steering actions. The velocity of the test drive was about $35km/h$, the accelerations were little and the wheel accelerations and the measured acceleration of the sensor are almost equal. This indicates a very reliable driving situation. The estimated vehicle mass ranges in a band of $\pm 50kg$ around the real vehicle mass $m_{CoG} = 1257kg$. This is a maximum relative error of $\pm 4\%$.

5.6 ABS-cycle Detection

The estimation of the friction coefficient (see Section 5.7) is only reasonable, if the maximum friction is used, for example when braking. In order to be able to assess the type of the road surface (dry, icy, snow-covered and so on) the state "maximum braking" must be recognized. For vehicles equipped with ABS, a panic braking situation causes ABS control cycles. That is, if an ABS control cycle occurs, then usually the maximum friction is used. On the other hand, the operativeness of ABS shall be assessed in general to see if malfunction of the ABS system has influenced the investigated accident.
To solve these two questions, a three step algorithm will be presented which is capable to detect the characteristic ABS control cycle pattern.

5.6.1 Basic Approach of ABS-cycle Detection

An ABS-cycle pattern can be seen in Fig. 5.40. Fig. 5.40(a) shows a wheel speed signal of a real test run with a test car. The ABS-cycles are marked. Fig. 5.40(b) shows a cut-out of the wheel *acceleration* signal. It is the time-derivation of the first ABS-cycle of Fig. 5.40(a). The method must be capable to detect these patterns. The shape of the pattern is hardly changing. However, the amplitude and time duration of the pattern varies. Fig. 5.41 shows, that the algorithm of ABS-cycle detection contains three steps: after preprocessing, where for instance an actual braking situation is detected (step 1), a probable ABS-cycle is marked with a prediction approach (step 2, Section 5.6.2). To increase reliability and robustness of

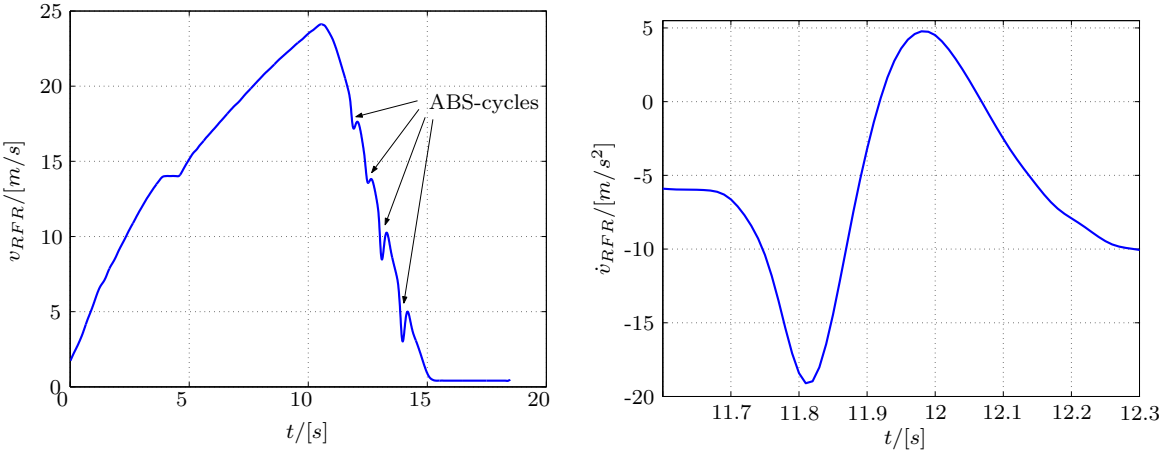

(a) wheel speed signal (b) cut-out of a wheel acceleration signal

Figure 5.40: Pattern of an ABS-cycle

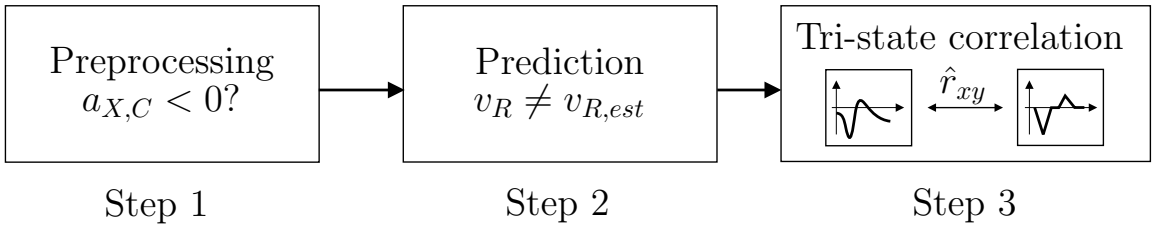

Figure 5.41: Three steps of ABS-cycle detection

the method, the result of the prediction is cross-checked with the tri-state correlation afterwards (step 3, Section 5.6.3).

5.6.2 Prediction

The prediction method employs the wheel *speed* measurements, in order to detect an ABS-cycle. Detecting the ABS-activity, the past two measurements of the wheel speed are utilized to extrapolate linearly a value of the current wheel speed (see Fig. 5.42). v_R denotes the measured wheel speed signal, whereas $v_{R,est}$ is calculated by means of

$$v_{R,est}(n) = 2 \cdot v_R(n-1) - v_R(n-2) \quad . \tag{5.109}$$

The estimated value $v_{R,est}(n)$ is compared with the currently measured value $v_R(n)$. The difference Δv_P between these two values is almost zero for normal signal behavior. An ABS-cycle, however, causes a prediction difference Δv_P, which exceeds specific limits (for an Opel Vita, see Eqn.

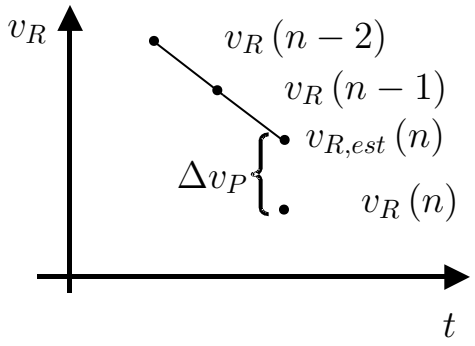

Figure 5.42: Sketch of extrapolated wheel speed signal

(5.110)) for the beginning and end of the ABS-cycle:

$$\Delta v_P = v_{R,est} - v_R \geq 0.08 \quad . \tag{5.110}$$

This approach detects ABS-cycles with a high probability. However, a signal drop out caused by sensor errors can be recognized wrongly as an ABS-cycle. Therefore, the wheel speed signals are preprocessed and the results of the detection are evaluated by another method, the so called "tri-state correlation".

5.6.3 Tri-state Correlation

The input signals into the ABS-cycle detection system are not zero-mean. Thus, the conventional correlation is replaced by a "tri-state correlation". In Eqn. (5.111) the calculation of the tri-state correlation of two signals x and y is presented:

$$\hat{r}_{xy}\,(k) = \frac{1}{N} \sum_{n=0}^{N-1-k} T\,(x^*\,(n)) \cdot T\,(y\,(n+k)) \quad . \tag{5.111}$$

The difference of the tri-state correlation to a polarity correlation, [43], [47], is an additional state "0". The states of the signals for the tri-state correlation are $+1$, 0, -1. The function $y(n+k)$ in Eqn. (5.111) is a test function shown in Fig. 5.43(a), whereas $x^*(n)$ is a "cut-out" of the wheel acceleration signal $\dot{v}$ displayed in Fig. 5.40(b). $T(\cdot)$ is a threshold function and maps the input signals to signals with the only values 0 and ± 1 according to thresholds specified in Eqn. (5.112). The thresholds are, however, depending on the ABS system installed in the car.

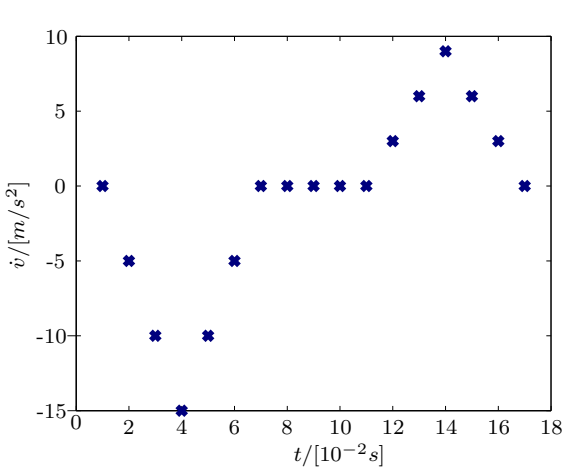

(a) Test signal for tri-state correlation

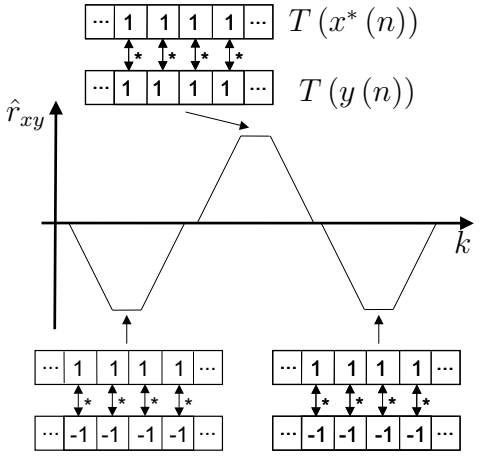

(b) Sequence of tri-state correlation coefficients of a single ABS-cycle pattern

Figure 5.43: Signals of the tri-state correlation method

$$T(x) = \begin{cases} 1 & , \quad \text{if} \quad x \geq 2 \\ 0 & , \quad \text{if} \quad -10 < x < 2 \\ -1 & , \quad \text{if} \quad -10 \geq x \end{cases} \tag{5.112}$$

The tri-state correlation can be carried out using the signal created by the threshold function. In Fig. 5.43(b) the result of a tri-state correlation of the test signal with an ABS acceleration pattern is sketched. This pattern is typical due to the structure of the signals. Because of the threshold function, the test signal possesses the values $|-1|-1|\cdots|-1|0|0|\cdots|0|1|1|\cdots|1|$. Applying the threshold function to the wheel acceleration signal yields a similar structure. Thus, if the test signal shown in Fig. 5.43(a) is "moving" over the measured wheel acceleration signal and matches an ABS-cycle, the structure of the signal shown in Fig. 5.43(b) is gained. The algorithm identifies this pattern to confirm or reject the probable ABS-cycle gained from the prediction. Tests show that this method is robust and reliable.

Since the tri-state correlation utilizes a 2-bit input signal, it is more suitable for microprocessor applications than a "conventional" correlation. Due to this advantage and the reliability of this approach, it is used for cross-checking the result of the prediction.
Fig. 5.44 shows the results of an ABS braking situation on very low μ road surface. The presented method detects all ABS-cycles above a velocity of $2m/s$. The method works well for different road surfaces. However, the threshold of the prediction method must be adapted to the respective car.

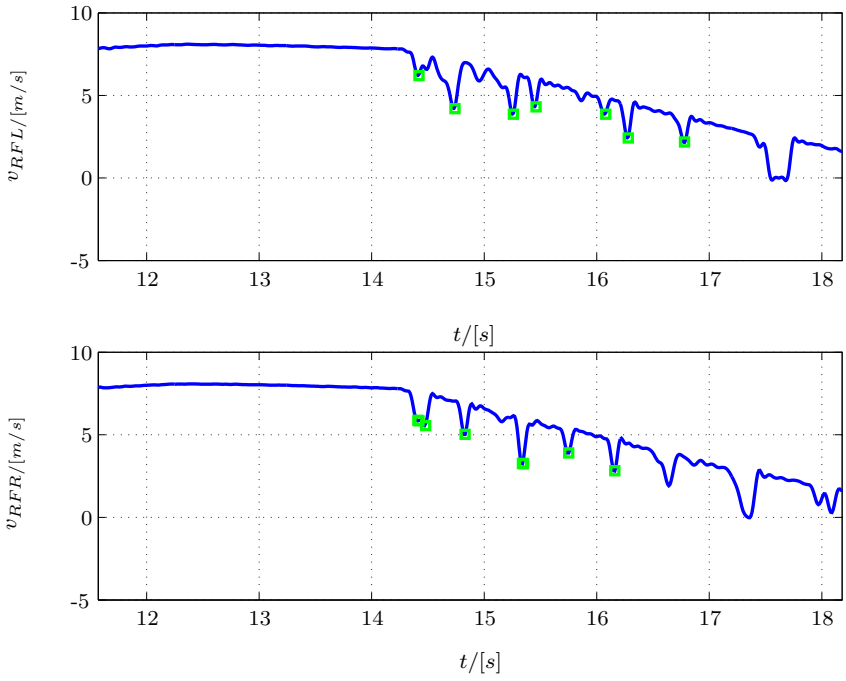

Figure 5.44: ABS-cycle detection for a very low μ braking maneuver with an Opel Vita

5.7 Estimation of the Friction Coefficient

In Section 3.1.5 the BURCKHARDT-method was presented for friction determination. The method approximates the $\mu(s)$-curve with an exponential approximation equation (Eqn. (3.17)). However, if there is no reliable slip signal, then the method fails. Additionally, real time processing is problematic with the non-linear BURCKHARDT-equation.
For accident reconstruction purposes, the *maximum* friction coefficient is desirable. Only then a statement about the road surface can be made and it can be assessed, whether the theoretical friction was utilized completely or not.
Before an accident occurs, usually full braking maneuvers are carried out. If the vehicle is equipped with ABS, the system controls the wheel slip in order to achieve high friction. However, if an old ABS-system is combined with modern tires, the control goal of the ABS system does not fit the maximum friction of the tires. When such cases are not considered, the ABS-cycle detection in Section 5.6 provides a possibility to detect full braking. Applying the RLS friction estimation only in these braking situations guarantees to estimate the maximum friction μ_{max} with a high probability. As real time processing is desirable, the friction coefficient is determined with a RLS algorithm. The underlying model is the torque balance on the

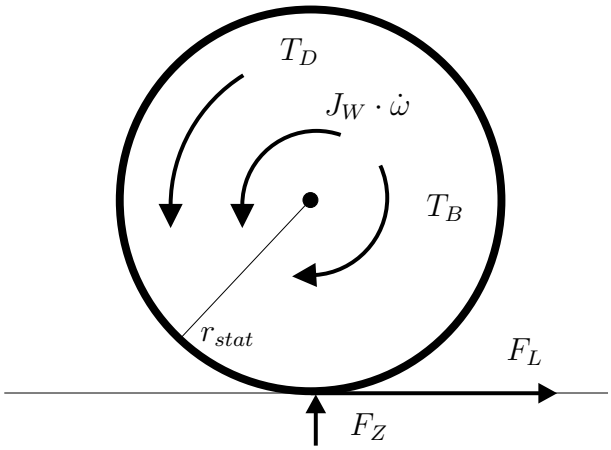

Figure 5.45: Side view of a wheel with torques and forces for μ-estimation

wheel shown in Fig. 5.45.
The definition of the friction coefficient

$$\mu = \frac{F_L}{F_Z} \tag{5.113}$$

shows that the longitudinal wheel force F_L must be calculated. The vertical wheel force F_Z can be efficiently approximated by Eqns. (3.59). Using Fig. 5.45 the torque balance around the wheel turn axis reads

$$F_L = \frac{J_W \cdot \dot{\omega} + T_B - T_D}{r_{stat}} \quad , \tag{5.114}$$

with J_W as the mass moment of inertia of the wheel and T_B and T_D as the brake and drive torque at the wheel. With Eqn. (5.113), the in- and output variables into the RLS-estimation algorithm can be defined:

$$\underbrace{\frac{J_W \cdot \dot{\omega} + T_B - T_D}{r_{stat}}}_{y} = \underbrace{\mu}_{\Theta} \cdot \underbrace{F_Z}_{u} \quad . \tag{5.115}$$

The friction coefficient is a parameter which can change very quickly, for example if a car brakes on asphalt initially and "slides" on ice afterwards. It is desirable, that the algorithm can "follow" the parameter change fast enough. Therefore, a compromise between good "tracking characteristics" and noise resistance must be found by influencing the forgetting factor. Tests with two cars on different road surfaces have shown that the forgetting factor λ_F should be in the range $0.95 \leq \lambda_F \leq 0.99$.
In order to validate the estimation method, various test drives on different road surfaces were conducted. The top plot of Fig. 5.46(a) shows that initially, the wheel speed signal is extremely large. The wheels were spinning

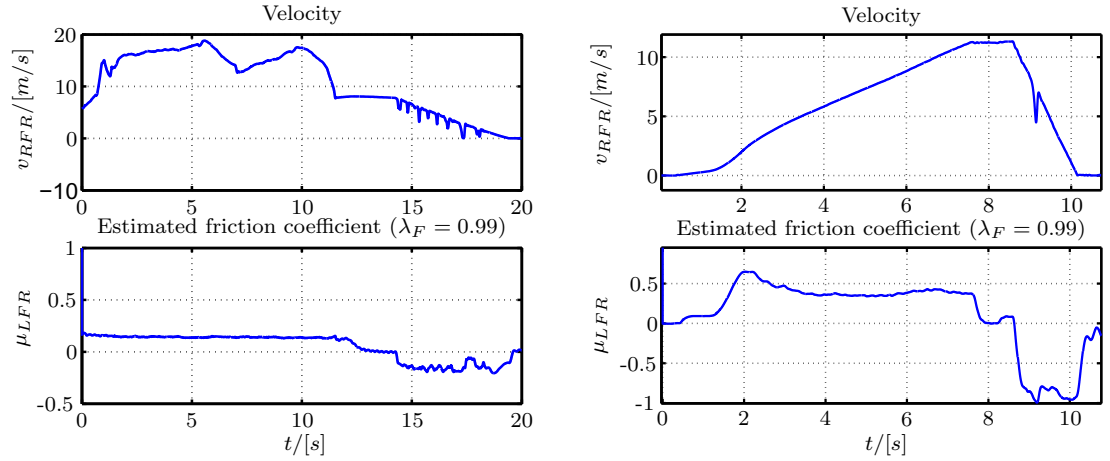

(a) Acceleration with spinning wheels and ABS braking on porcelain tiles (very low μ)

(b) Acceleration and ABS braking on dry asphalt ($\mu \approx 1$)

Figure 5.46: Test drives for μ-estimation

because the traction control system (TCS) was switched off. After approximately 11.5 s the car is rolling for 2.5 s before full braking is applied. The absolute value of the estimated friction coefficient is in the range of $\mu_{LFR} = 0.15$ during ABS-braking and spinning wheels acceleration. This value corresponds to the real value of the "low μ test course". During the rolling phase, the estimated friction coefficient is approximately 0, indicating that the theoretical friction is not used. The test drive makes clear, that the road surface can only be assessed during extreme driving situations.

Fig. 5.46(b) is an acceleration and ABS braking drive on dry asphalt. The top of the figure shows that the wheels were not spinning during the acceleration phase, although the TCS was switched off. The maximum friction was not used as can be seen in the estimated friction coefficient $\mu_{LFR} \approx 0.4 - 0.6$. During the rolling phase between 7.5 s and 8.5 s the estimated μ_{LFR} is around zero. Only in the ABS-braking phase, the maximum friction is used and the absolute value of the estimation corresponds to the theoretical value of $\mu_{LFR} \approx 1$.

For both measurements the forgetting factor is $\lambda_F = 0.99$. Still, the tracking capabilities of the RLS-algorithm are sufficient.

5.8 Road Gradient Observer

The employed method for road gradient determination is based on a linear Luenberger-observer, [50]. Instead of the longitudinal acceleration a_X, it employs the vehicle velocity v_{CoG} and its time derivative.

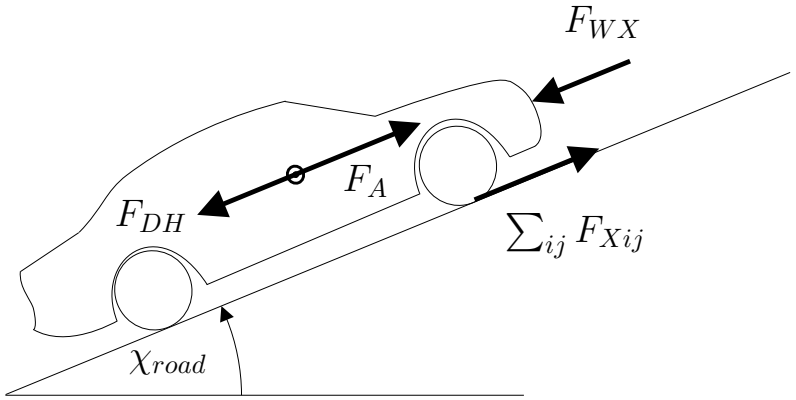

Figure 5.47: Sketch of longitudinal forces of an ascending car

Force Balance for Road Gradient Observation

The effect of the lateral dynamics on road gradient estimation is neglected here. The vehicle body side slip angle is assumed to be zero. This assumption is true for straightforward driving situations. Setting up the force balance of the forces displayed in Fig. 5.47 yields the nonlinear equation

$$\underbrace{m \cdot \dot{v}_{CoG}}_{F_A} = \sum_{ij} F_{Xij} - \underbrace{m \cdot g \cdot \sin \chi_{road}}_{F_{DH}} - \underbrace{c_{WX} \cdot v_{CoG}^2}_{F_{WX}} \quad . \tag{5.116}$$

Linearization of Equation (5.116)

To reduce the computational complexity, a *linear* observer is employed here, [34]. Therefore, Eqn. (5.116) is linearized. For the linearization, the following assumptions are made:

- the road gradient angle of public roads is limited to approx. $\pm$ 12°, [32], therefore: $\sin \chi_{road} \approx \chi_{road}$
- the forces $\sum F_{Xij}$ and F_{WX} are merged into a resultant force $F_{res} = \sum F_{Xij} - F_{WX}$. This is advantageous because the nonlinear term F_{WX} becomes part of the input. The remaining state space model therefore is linear.

As a consequence of these assumptions Eqn. (5.116) is simplified

$$m \cdot \dot{v}_{CoG} = F_{res} - m \cdot g \cdot \chi_{road} \quad , \tag{5.117}$$

where the F_{Xij} are measured or gained from a brake and drive model. v_{CoG} results from the fuzzy estimator in Section 5.1.

Linear State Space Equations

Eqn. (5.117) is now transformed into a state space model. The state vector $\underline{x}$ of the linear model contains the velocity v_{CoG} and the road gradient angle χ_{road}. The input $\underline{u}$ is the resultant force F_{res}, the only measured output y is the velocity v_{CoG}.

$$\underline{x} = \begin{bmatrix} v_{CoG} \\ \chi_{road} \end{bmatrix}, \underline{u} = \begin{bmatrix} F_{res} \\ 0 \end{bmatrix} \quad . \tag{5.118}$$

Then, the road gradient model reads

$$\underbrace{\begin{bmatrix} \dot{v}_{CoG} \\ \dot{\chi}_{road} \end{bmatrix}}_{\dot{\underline{x}}} = \underbrace{\begin{bmatrix} 0 & -g \\ 0 & 0 \end{bmatrix}}_{\underline{A}} \underbrace{\begin{bmatrix} v_{CoG} \\ \chi_{road} \end{bmatrix}}_{\underline{x}} + \underbrace{\begin{bmatrix} \frac{1}{m} & 0 \\ 0 & 0 \end{bmatrix}}_{\underline{B}} \underbrace{\begin{bmatrix} F_{res} \\ 0 \end{bmatrix}}_{\underline{u}} \quad , \tag{5.119}$$

$$\underbrace{v_{CoG}}_{y} = \underbrace{[1 \quad 0]}_{\underline{C}} \underbrace{\begin{bmatrix} v_{CoG} \\ \chi_{road} \end{bmatrix}}_{\underline{x}} \quad . \tag{5.120}$$

Observer design

The proof of observability for the system (5.119) and (5.120) is trivial. The linear observability matrix $\underline{Q}_B$ according to Eqn. (5.22) is quadratic. Therefore, it has maximum rank, if its determinant is non-zero:

$$\det\left(\underline{Q}_B\right) = \det\begin{bmatrix} 1 & 0 \\ 0 & -g \end{bmatrix} = -g \neq 0 \qquad . \tag{5.121}$$

The system is observable and a linear observer can be designed.
Since the system order is $n = 2$, the observer gain matrix $\underline{L}$ consists of two elements l_1 and l_2. In order to calculate these elements, the poles of the observed system must be placed appropriately. The characteristic polynomial of the closed-loop system is

$$\begin{aligned} \det\left(s\underline{I} - \underline{A} + \underline{L}\,\underline{C}\right) &= \det\left(\begin{bmatrix} s & 0 \\ 0 & s \end{bmatrix} - \begin{bmatrix} 0 & -g \\ 0 & 0 \end{bmatrix} + \begin{bmatrix} l_1 & 0 \\ l_2 & 0 \end{bmatrix}\right) \\ &= s^2 + l_1 \cdot s - g \cdot l_2 \quad . \end{aligned} \tag{5.122}$$

The eigenvalues are denoted as λ_1 and λ_2 and are chosen according to

$$s^2 + l_1 \cdot s - g \cdot l_2 \stackrel{!}{=} (s - \lambda_1)(s - \lambda_2) = s^2 - s \cdot (\lambda_1 + \lambda_2) + \lambda_1 \cdot \lambda_2. \quad (5.123)$$

For pole-placement, the coefficients of Eqn. (5.123) are compared. This yields the elements of the observer gain matrix $\underline{L}$:

$$l_1 = -\lambda_1 - \lambda_2 \ , \quad l_2 = \frac{-\lambda_1 \cdot \lambda_2}{g} \qquad . \quad (5.124)$$

Next, the eigenvalues λ_1 and λ_2 are determined. For this, a simulation model was implemented.
The following strategy for pole placement was employed to achieve suitable values of λ_1 and λ_2:

- the real part of the eigenvalues must be negative, otherwise the observer system becomes unstable.
- if the eigenvalues are too far left in the open left half plane, the observer becomes sensitive to noise
- if the eigenvalues are too close to the imaginary axis, the observer becomes too slow. It would not be able to follow the driving state of the vehicle properly (e.g. uphill and downhill driving).

Considering these constraints, and running a variety of simulations, the eigenvalues were fixed to

$$\begin{array}{rcll} \lambda_1 & = & -2 & \text{and} \\ \lambda_2 & = & -3 & . \end{array} \quad (5.125)$$

The height profile of a road calculated on basis of the estimated road gradient is displayed in Fig. 5.48. The test drive was carried out on a test course with a defined road gradient. Starting on a flat road, after $t = 2.5\,s$ the car enters an inclined plane with a gradient of 33 % ($\chi_{road} \approx 18°$). The car is moving on this inclined plane for approximately $10\,s$, returns to a flat road again and moves downhill at the end. The estimated road gradient of the first ramp is approximately 30 %. The deviation to the real road gradient is caused by the linear approximation which is not valid any more. At the end of the inclined plane the vehicle suddenly returns to a flat road. The pitch angle during this transition is responsible for the deviation of the maximum height ($\approx 10\,\%$). All in all, even for large road gradients, the linear observer provides very good results.

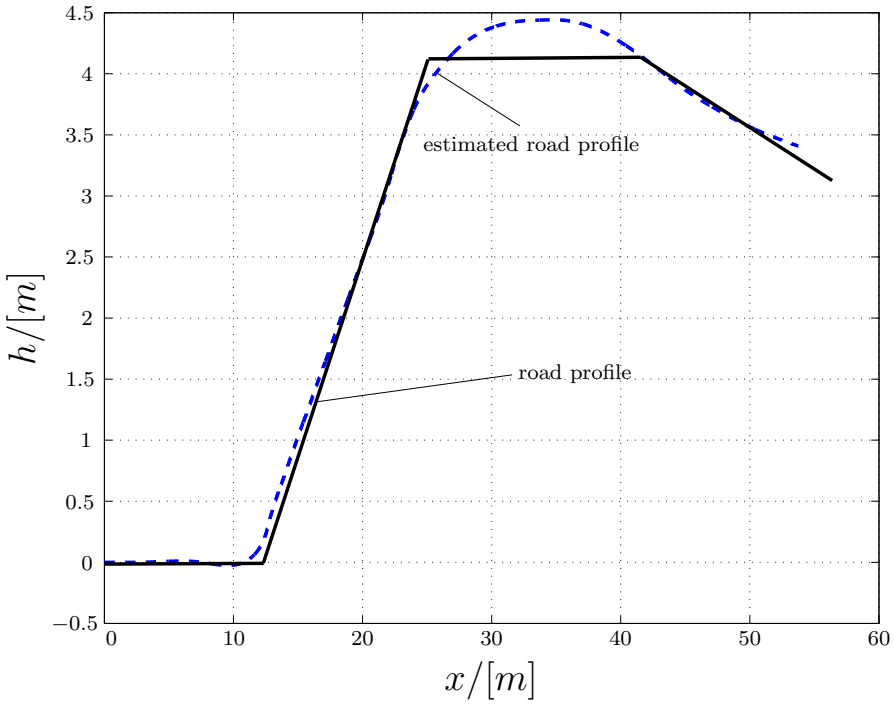

Figure 5.48: Road gradient of a test course with a defined gradient of 33%

5.9 Assessment of the Steering Behavior

In this section the steering behavior of the driver in critical situations shall be analyzed. Thereby it will be assessed whether the driver reacted appropriately in this situation. The vehicle trajectory is not regarded. The presented considerations can be regarded as a theoretical example, how model based approaches can be used for accident assessment. Fig. 5.49 shows the principle structure of the "assessment unit". After an accident has occurred, the recorded data from the EDR is applied to the adaptive non-linear two track model which estimates the side slip angle (Section 5.4). As the driver reacts very sensitively to increased side slip angles, the VBSSA is used to control the steering angle here. By exceeding two VBSSA thresholds the steering wheel angle is reduced proportionally. The first, lower, threshold is the so called "recognition threshold" β_1. Here, the driver recognizes an increased VBSSA. The second threshold is called the "risk threshold" β_2. Above this limit, the driving situation becomes unstable. Both thresholds were determined on basis of the discrete stability index values (see Section 4.1) of several test drives. Exceeding the second threshold, the recorded steering wheel angle $\delta_{S,meas}$ is reduced by two subtractive portions

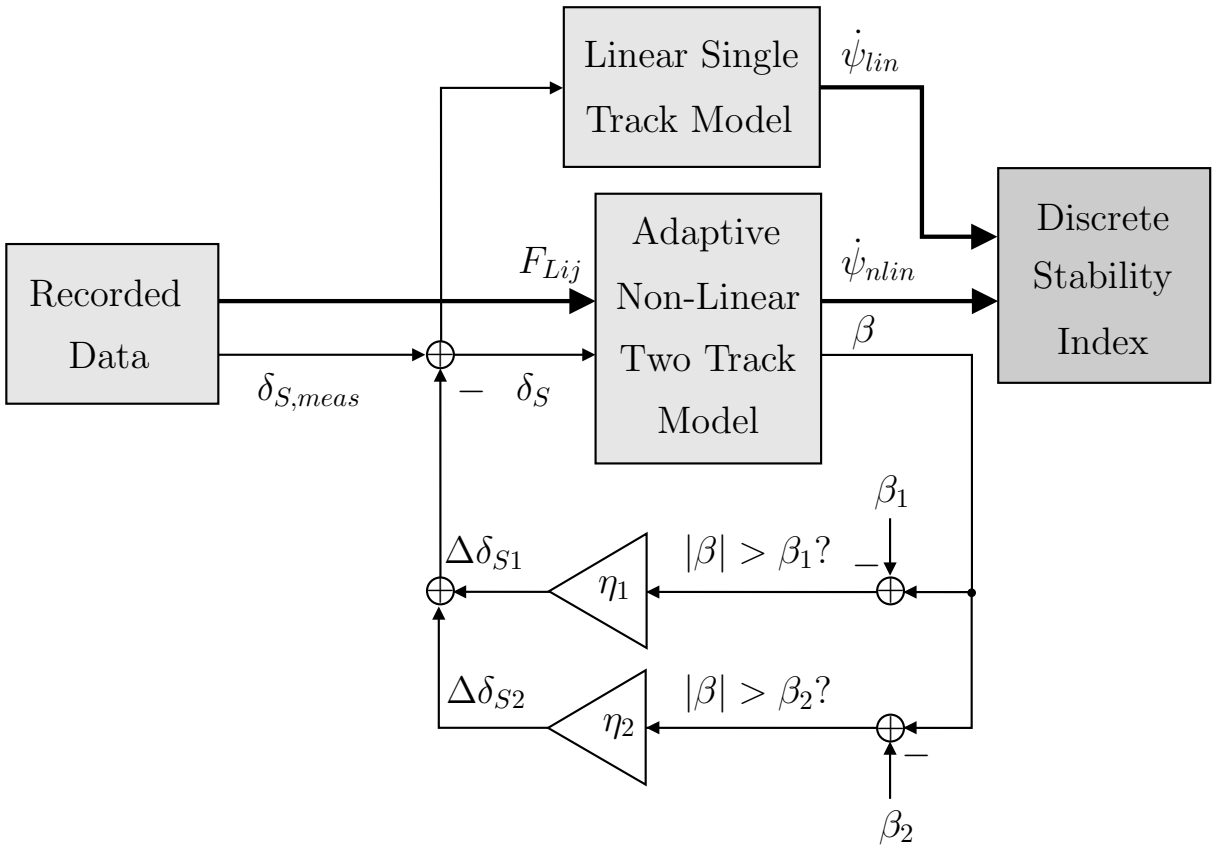

Figure 5.49: Structure of driver assessment by minimizing the VBSSA

$$\delta_S = \delta_{S,meas} - \underbrace{\eta_1 \cdot (\beta - \beta_1)}_{\text{if } |\beta| > \beta_1} - \underbrace{\eta_2 \cdot (\beta - \beta_2)}_{\text{if } |\beta| > \beta_2} \quad . \tag{5.126}$$

Actually, this simple control strategy can only be applied, if the vehicle body side slip angle and the steering wheel angle have got positive algebraic sign. It is assumed that the control law prevents the car from sliding and that therefore the algebraic sign will always be equal. Otherwise, different cases for varying algebraic signs of β and δ_S must be distinguished.
The new steering wheel angle is applied to the model and the updated state variables, including the estimated VBSSA, are calculated. This assumes that the adaptive non-linear two track model is capable to describe the real vehicle behavior to the stability limit. This was shown in Section 3.6. The updated steering wheel angle δ_S according to Eqn. (5.126) is applied to the linear single track model as well. Both the updated yaw rate from the linear and from the adaptive non-linear model are applied to the discrete stability index block. Using the yaw gain method it is analyzed, if the controlled steering angle is capable to stabilize the car. If this is the case, then the suggested and the measured steering angle can be compared in order to assess, whether the driver reacted appropriately to the situation or not.

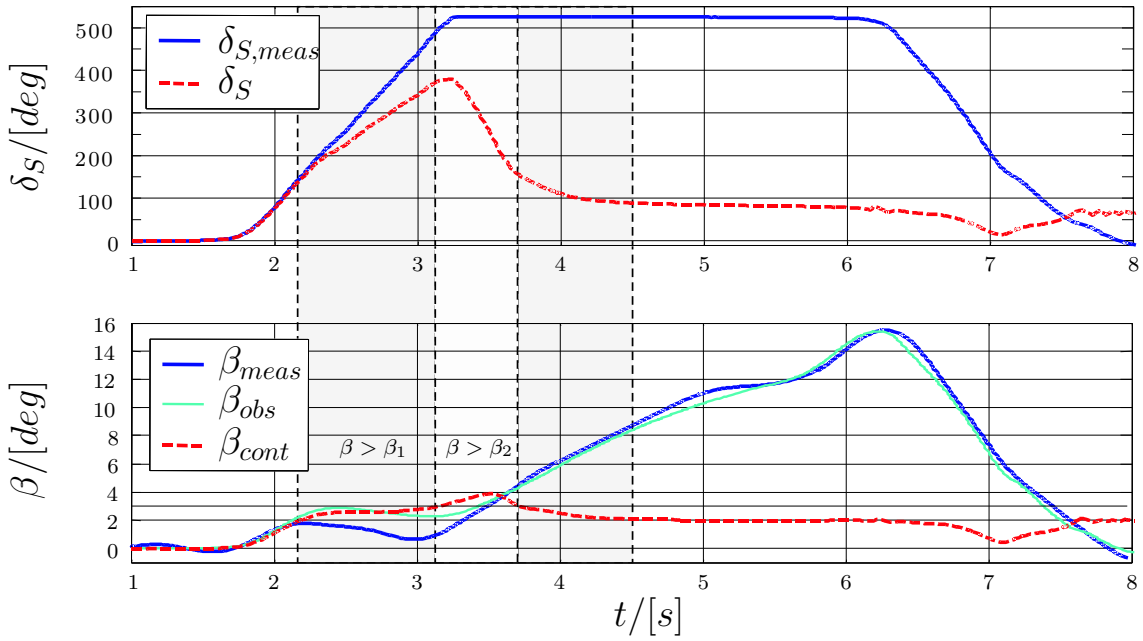

Figure 5.50: Effect of steering angle reduction based on side slip angle minimization

Fig. 5.50 shows the steering angle and the effect of steering control on the vehicle body side slip angle. Before $t \approx 2.2s$, the VBSSA β is below β_1. Therefore, the measured steering angle $\delta_{S,meas}$ and the controlled steering angle δ_S are equal. After exceeding the "recognition threshold" at $t = 2.2s$ the increase of the steering angle is reduced by the term $\eta_1 \cdot (\beta - \beta_1)$ in Eqn. (5.126). After $t \approx 3.2s$ the VBSSA exceeds the "risk threshold". Therefore, the second subtractive term $\eta_2 \cdot (\beta - \beta_2)$ in Eqn. (5.126) becomes active and the steering wheel angle is reduced significantly. The VBSSA stops growing at about $t = 3.7s$ and remains below the risk and later below the recognition threshold for the rest of the test drive.

Comparing the original test drive represented by DSI_{meas} with the controlled one (DSI_{cont}) in Fig. 5.51 shows, that both methods detect the critical situation approximately at the same time around $t = 2.1s$. The transition from understeer (area a.) to oversteer (area b.) is about $t_x = 0.8s$ earlier when controlling the steering angle. The critical state is finished after approximately $t = 3.7s$ whereas it ends for the original test drive at $t \approx 7s$. The bottom of Fig. 5.51 illustrates, that the real vehicle behavior (modeled by the adaptive non-linear vehicle model) converges against the linear reference model indicating that the driving situation is no more critical. After $t = 3.7s$, the linear and the non-linear model yaw rate are equal.

This example shows that the critical driving situation can be stabilized by steering wheel inputs. The deviation between the controlled and the original steering performance by the driver shows, that the driver should

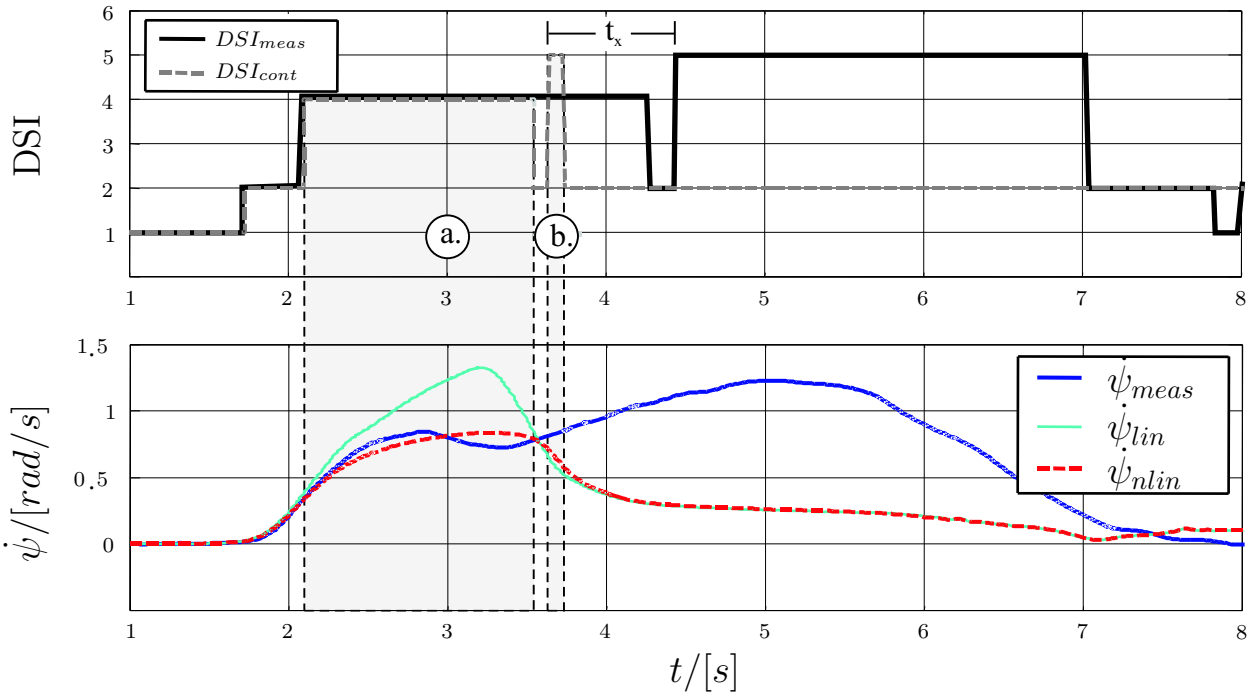

Figure 5.51: Stability index and yaw rate after steering intervention of the model

have reduced the steering angle at the latest at $t = 3.5s$. With the recorded steering performance, the driver has not tried to stabilize the car again. Therefore, the driving situation becomes critical.

5.10 Conclusion

The approaches for the reconstruction of road traffic accidents described in Chapter 5 provide information to support accident reconstruction experts. The main goal of accident reconstruction is to gain full knowledge about the vehicle motion and about influences of driver, environment and vehicle in the complete time interval around the accident situation.
For vehicle motion reconstruction a fuzzy system is used which processes the redundant information of the wheel speed sensors, the gyroscope and an acceleration sensor. The rule base contains knowledge about the reliability of these sensors in different driving situations. According to the respective driving situation, the sensors are weighted more or less to increase the accuracy of trajectory reconstruction.
Complete vehicle motion reproduction does not only mean the position of the center of gravity over time. It means also the vehicle heading, the direction of the vehicle's longitudinal axis and its direction of travel. To get this information, several non-linear state space observers were develo-

ped on basis of the adaptive non-linear state space model. These observers estimate the vehicle body side slip angle. In contrast to linear systems, the structure of a non-linear system significantly influences the different observer approaches. Therefore, the adaptive non-linear state space model is restructured. Finally, an extended KALMAN-BUCY-Filter was developed to explicitly consider model inaccuracies by choosing the respective noise covariance matrices appropriately. The presented non-linear observers and the extended KALMAN-BUCY-Filter are capable to estimate the vehicle body side slip angle accurately up to the stability limit.
The vehicle mass and the friction coefficient represent the most important time-varying parameters for accident reconstruction. Both parameters are gained by RLS-estimation. The vehicle mass can be estimated accurately only in certain driving situations which are selected by the suggested algorithm. Among other effects, the vehicle mass influences the model accuracy and the braking distance. The maximum friction coefficient provides information about the road surface. In hard braking situations, the friction coefficient can be estimated with a recursive estimator.
In order to detect braking situations with maximum friction with a high probability, a three step algorithm was described in this chapter in order to detect ABS-cycles by processing the wheel speed signals. Only when the friction is completely used, the assessment of the road surface characteristics is possible. Moreover, this method allows to check the proper operativeness of ABS in order to exclude a technical defect as an accident cause.
To gain more knowledge about the environment of the accident scene and to track a vehicle more accurately, a linear road gradient state space observer was developed. For public roads the estimation with this linear observer is sufficiently accurate.
Finally, in a theoretical approach the steering performance of the driver in a critical driving situation was assessed using the discrete stability index and by a control strategy to minimize the side slip angle. If the driver performance deviates significantly from the steering suggestions made by the system, then possibly the driver has not acted or reacted appropriately to the critical driving situation. However, this theoretical approach does not consider the vehicle trajectory.
All of the methodologies presented in this chapter help accident reconstruction experts to reproduce the facts leading to an accident. However, human knowledge, for example from eye witnesses or about the environment of the accident scene will still be required. An expert cannot be *replaced* but be *supported* by a model based event data recorder.

6 Test Vehicle and Measurement Environment

In order to validate the vehicle models and algorithms presented in Chapters 3 to 5 a test vehicle was equipped with the necessary equipment. The institute test car is a rear axle driven Ford Scorpio manufactured in 1987 (see also Appendix D.1). This chapter provides a brief overview of the test environment in the Ford Scorpio.

6.1 Overview

A model based event data recorder shall be hooked into the existing bus system of the car and act as a "listener" recording the data on the bus. The Ford Scorpio test car initially was not equipped with a CAN bus. Therefore, a 500 kBit CAN bus and three CAN nodes were installed in the car (see Fig. 6.1). These three microcontrollers acquire the analog and digital data from the sensors. Additionally, a CAN steering wheel angle sensor was integrated, as the steering angle is a key quantity for the employed models. In order to monitor and record the data on the CAN bus, a laptop with a PCMCIA CAN card and the CANalyzer™ software was added to the CAN bus. However, sophisticated calculations cannot be made with the CANalyzer™. Therefore, the dSPACE Autobox® was added to the CAN bus as well. The Simulink® models contain the algorithms specified in the previous chapters. They were developed in the laboratory and downloaded via LAN to the Autobox®. The calculated quantities can be monitored in the car by a laptop and the Control Desk™ Software. As a seventh CAN node, a dual processor board called "SAPS-RC" developed at the Institut für Industrielle Informationstechnik was added. Using the Target Link™ Rapid Prototyping Tool, Simulink® models can be downloaded to the μC/DSP board via the serial port or a USB port. The dual processor board represents a data logger as a kind of prototype for the model based EDR. It is capable to run linear reference models in real-time. With the data acquisition network shown in Fig. 6.1, most of the validation test drives were conducted.

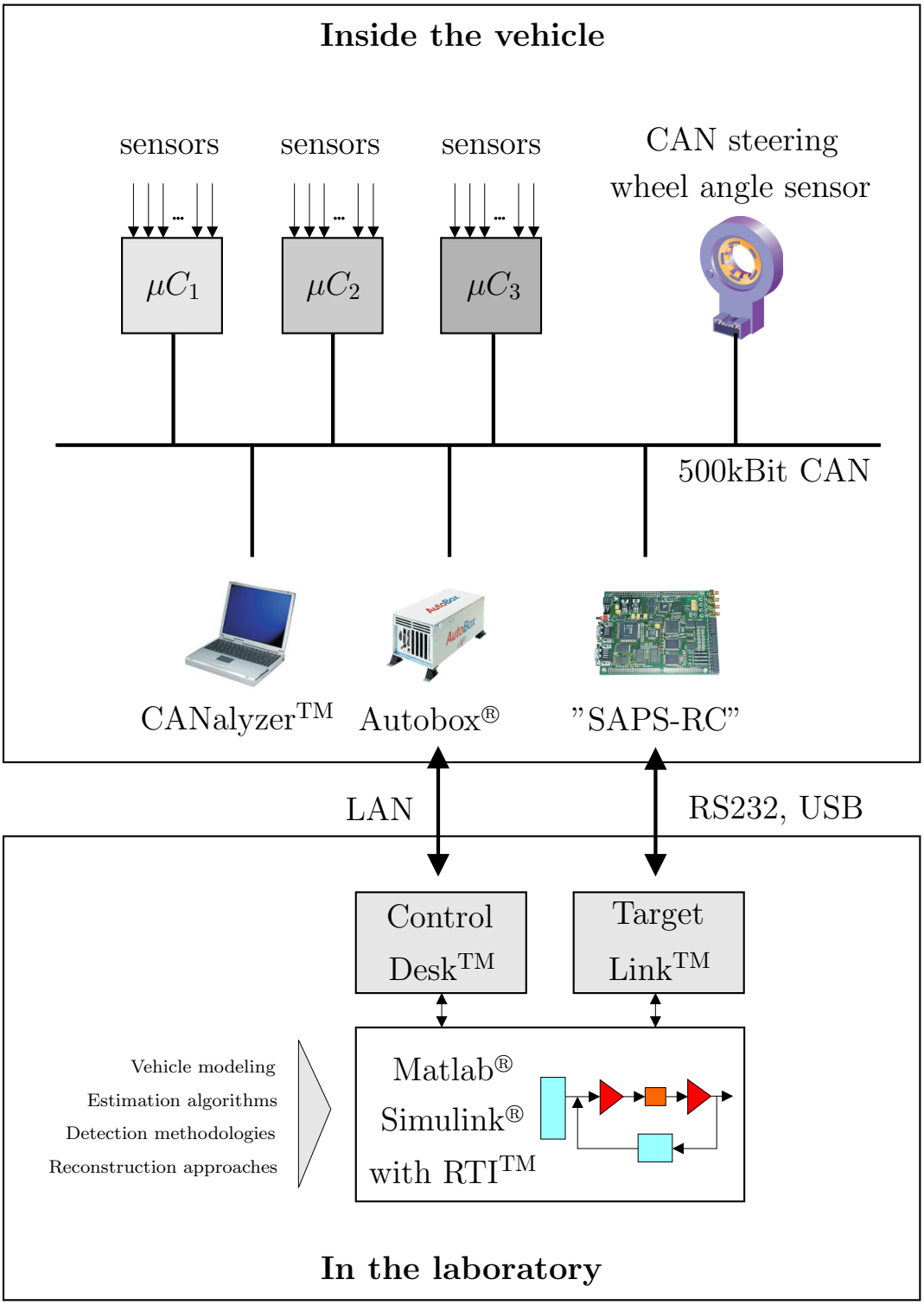

Figure 6.1: Overview over the data acquisition system

6.2 CAN Bus

The CAN bus installed in the test car has three CAN nodes. Each of them contains an 8bit Siemens SAB80C515C μController including a Philips CAN Transceiver PCA82C250. The CAN controller works in CAN 2.0B Full CAN mode. For performance reasons, CAN 2.0A was implemented in the software. The system is CAN 2.0B passive. It does not create error messages when receiving messages with a long identifier.
The CAN nodes acquire the data from the sensors. Analog sensor signals are 10bit A/D converted. Digital signals such as the edges from the ABS sensors are acquired with a capture and compare unit.
The bus load was kept low by means of an intelligent CAN-message format. To reduce the message overhead, several sensor signals were packed into one message. With this data structure, the bus load was limited to 27%. It is sufficiently low to avoid long latency times and jitter errors.

6.3 Sensors

By interfering into the ABS control unit, the sinusodial signals from the four inductive ABS sensors are acquired. An adaptation electronics converts the amplitude and frequency modulated ABS signals to rectangular signals. The rising edges of the rectangular signal are counted by the CAN μC units to calculate the rotational equivalent wheel speeds.
For the inertial sensors, a sensor block was mounted close to the center of gravity of the test car. With a water level, the horizontal orientation of the sensors can be improved. The sensor block contains three linear acceleration sensors for all degrees of freedom. Additionally, the yaw, roll and pitch rates are measured. For the models, only the yaw rate is required. The other two angular velocity sensors are used as reference sensors.
The steering wheel angle is a key quantity as it is the input of the linear single track model as well as the non-linear two track model. Therefore, two sensors were mounted in the car. The original sensor is a potentiometer. The other sensor uses the Anisotropic Magneto-Resistive (AMR) effect. It outputs a CAN signal and can simply be added to the existing CAN. The sensor can be reset and recalibrated during a test drive. This reduces the offset significantly.
The wheel torque angle sensor is an exception: it is not installed in serial production cars. During the development process, its signal is used as a reference input signal into the non-linear vehicle model. The torque sensor uses eight quartz sheer force sensors which are preloaded between two

Figure 6.2: Test vehicle with wheel torque sensor

flanges. The sensor consists of two disks. One disk is connected to the hub, the other one to the rim. That means, a special rim had to be installed where the sensor is screwed on. The rim had to be cranked in order to not change the distance of the rear wheels, see Fig. 6.2. The wheel torque angle sensor grips the electrical wheel torque signal with a slip ring and outputs an analog $\pm 5V$ signal which is acquired by the Autobox®. The torque signal is very accurate. It is transformed into a longitudinal wheel force signal and can afterwards be applied to the vehicle model.

6.4 Prototypes for a Model Based Event Data Recorder

6.4.1 CANalyzer™

The CANalyzer™ represents the simplest data logger type. It is capable to record the traffic on the CAN bus via a laptop with a PCMCIA card. The recorded ASCII file is evaluated in Matlab®. Furthermore, the CANalyzer™ was used as a development tool to analyze the traffic on the CAN bus or to initiate the communication with the prototype board "SAPS-RC". Apart from some basic arithmetical operations, the employed version of the CANalyzer™ software is not capable to run sophisticated vehicle models.

6.4.2 Autobox

On the modular Autobox® complex vehicle models can be implemented. It therefore represents the *model based* event data recorder. With the real-time interface (RTI) the Simulink® models are translated to C-Code. The C-Code is downloaded via an Ethernet connection and executed on the microprocessors in the Autobox®. The results of the real-time calculations on the Autobox® can be monitored with the Control Desk™ Software. Furthermore, simulation parameters can be changed easily here to increase the development speed. The models presented in Chapters 3 - 5 were implemented in the Autobox®.

6.4.3 SAPS-RC

In a last step, the target hardware "SAPS-RC" (Signal Analyzer for Pressure Sensor - Real-time CAN-interface) was integrated into the CAN. Originally, the board was designed for signal processing on a common-rail test bench as described in [72]. It is equipped with a microcontroller and a signal processor. As the board contains all the necessary features for a passive event data recorder, it was used as a "prototype" here. The board contains a 16bit Infineon C167CR μ-Controller with a clock frequency of 25MHz. The μC is the master and responsible for communication and for the execution of a main program. The signal processor is a Motorola XC56309 digital signal processor at a clock frequency of 100 MHz. The DSP acts as the slave. Both microprocessors communicate via a dual port RAM.
The signal processor filters the sensor signals before applying them to the linear models running on the microcontroller. The models were developed in Simulink®. Afterwards, the models were downloaded to the microcontroller using the following software tool chain:

- dSPACE Target Link™
- dSPACE Target Optimization Module™ for the C16x family
- Tasking™ C166/ST10 C-Compiler

On the microprocessor the linear single track model and two methods fpr detecting critical driving situations according to Chapter 4 are running successfully and in real-time. The triggering of accidents works properly with this prototype hardware. However, the non-linear models cannot be executed in real-time on this hardware platform.

7 Conclusions and Outlook

The amount of electronic control systems in modern vehicles has constantly grown during the past decade. Interventions by systems like ABS or ESP support drivers in critical driving situations. However, such systems still cannot avoid every accident. In case an accident has occurred, brake traces on the road surface are lacking due to ABS. Furthermore, it is hard to decide whether the driver or a technical component has failed. Country road accidents have an increased fatality rate, as these accidents occur at high speed with vehicle dynamics being often at the limit.
In order to assist accident investigators reconstructing such accidents, this thesis deals with the detection and reconstruction of road traffic accidents by means of model based event data recorders (EDR).

The underlying idea is to describe the vehicle motion and dynamics up to the stability limit by means of a vehicle model. Based on these models, non-measurable states and parameters can be determined. The linear single track model turned out to be insufficient for accident reconstruction. Therefore, an enhanced non-linear two track model was set up by means of the forces acting on the car. Several parameters of this model are time-varying. In order to achieve sufficient accuracy, especially the cornering stiffnesses of the tires have to be adapted. This adaptive non-linear two track model was then validated. It is capable to describe the vehicle dynamics up to the stability limit of the car.

The principle of a model based event data recorder is to record data continuously until a trigger event indicates an accident situation. The trigger procedure of existing EDRs is enhanced to the detection of laterally critical driving situations by using linear reference models. If the vehicle does not react proportionally to the driver desire, then the driving situation can become uncontrollable for an average driver. The field of experience of such drivers is covered by the linear single track model. The real vehicle behavior can be measured with sensors. The deviation of the measured signals from the linear single track model is evaluated to classify the driving situation with a discrete number called discrete stability index (DSI). In order to guarantee that a reliable trigger signal is generated, the DSI is calculated

with four different methods relying upon different sensor combinations. For inconvenient sensor configurations, though, the four methods can provide different stability results. Therefore, the discrete stability index was enhanced to a continuous stability index (CSI). The CSI represents a continuous number between one and six. The CSI values of the four methods were validated with test drives made with two different test cars and proved to be more coherent. The CSI were compared with the vehicle body side slip angle and with the cornering stiffnesses. Growing CSI indicate reduced cornering stiffnesses and increased side slip angles. This shows that the physical vehicle behavior can be described appropriately with the CSI-method. Knowing that the method provides reasonable results, it can be applied to trigger an EDR. A "two-of-four-method" generates an EDR trigger signal, if the continuous stability index gained from two of the four methods exceeds a certain threshold. This ensures robust and reliable triggering. The detection of accident situations must occur *online*.

After an accident was detected, accident relevant data are saved in a memory. Based on these data and using the vehicle model, the accident can be reconstructed *offline*. The goal of accident reconstruction is to reproduce the vehicle behavior and external as well as internal influences on the vehicle and the driver.
The vehicle motion in plane can be described by means of the center of gravity location and the vehicle heading. The center of gravity location is determined with a fuzzy trajectory estimator which consists of two fuzzy subsystems: one estimates the vehicle velocity whereas the other one determines the yaw rate. The redundant sensor signals are weighted according to their reliability to gain a more accurate trajectory estimate. The method was validated with test drives on public roads and a robustness analysis was conducted. The estimator results turned out to be accurate and robust against injected sensor failures.
The vehicle heading can be calculated by means of the vehicle body side slip angle. Furthermore, the side slip angle is a measure for vehicle stability. Therefore, a linearization observer and an observer with adaptation of a quality function were designed to determine the vehicle body side slip angle. The basis for these observers was the adaptive non-linear two track model. Existing model weaknesses were reduced by restructuring the vehicle model. Additionally, an extended Kalman-Bucy-Filter was designed. The appropriate choice of the covariance matrices allows to weight model components according to their reliability in the current driving situation. Restructuring the model is not necessary any more.
A road gradient observer was designed to extend trajectory reconstruction from the plane to the height. The vehicle motion can be reconstructed

completely knowing the vehicle's center of gravity location, its heading and its height over ground.
The mass of the car influences the brake distance as well as the accuracy of the vehicle models. Therefore, it is estimated with a recursive least squares method evaluating the longitudinal force balance of the vehicle. The quality of mass estimation varies extremely and depends significantly on the accuracy of the sensor signals. A situation based approach improves the mass estimation results.
The estimation of the friction coefficient provides valuable information for accident investigators. Therefore, the recursive least squares method was applied to a quarter vehicle model evaluating the torque balance on the wheels. In order to ensure that the maximum friction was used, an ABS-cycle detection method was implemented. If ABS-cycles are detected, then in most cases the maximum friction was reached and the friction value can be utilized to assess the road surface characteristic.
The majority of road traffic accidents are caused by driver mistakes. The described vehicle models allow to assess the driver performance. The underlying idea is based on a control strategy of the side slip angle. It assumes that a driver should keep the vehicle body side slip angle small by reducing the steering angle with a simple control strategy. The controlled steering angle is compared to the measured steering angle after an accident to see, if the critical situation could have been defused or not.

A test car had to be set up to validate the methodologies, models and estimation approaches. Therefore, the laboratory test car was equipped with state of the art sensor equipment and with a CAN bus to gain all the sensor information which was required. The models were implemented in Matlab®/Simulink®. They were tested with the Autobox® to prove that they run in real-time. The linear reference models were downloaded to a prototype hardware by means of automatic code generation tools and were validated in the car.

As an outlook, the detection of laterally critical situations may be further improved, when the employed detection thresholds are further parametrized with more test drives and different test cars.
The estimation values of the vehicle body side slip angle gained from the non-linear observers and from the extended Kalman-Bucy-Filter may also be used to set up a non-linear controller for the lateral vehicle dynamics. Radar or ultrasonic systems as well as video devices can additionally be introduced to combine vehicle dynamics with collision avoidance systems. With such improvements, the methodologies presented in this thesis may lead from accident *reconstruction* considered here to accident *avoidance*.

A Non-linear Two Track Model

A.1 Jacobian-Matrix

The elements of the JACOBIAN-matrix for the adaptive non-linear vehicle model read:

$$\begin{aligned}\frac{\partial \dot{v}_{CoG}}{\partial v_{CoG}} &= \frac{1}{m_{CoG}} \cdot \Big\{ -c_{WX} v_{CoG} \cos\beta - \frac{l_F \dot{\psi}}{v_{CoG}^2}(c_{FL}+c_{FR}) \sin(\delta_W - \beta) \\ &\quad -(c_{RL}+c_{RR}) \frac{l_R \dot{\psi}}{v_{CoG}^2} \sin\beta \Big\} \quad , \end{aligned} \tag{A.1}$$

$$\begin{aligned}\frac{\partial \dot{v}_{CoG}}{\partial \beta} &= \frac{1}{m_{CoG}} \cdot \Big\{ (F_{LFL}+F_{LFR}+c_{FL}+c_{FR}) \cdot \sin(\delta_W - \beta) \\ &\quad -\big(c_{RL}+c_{RR}+F_{LRL}+F_{LRR}-c_{WX} \cdot v_{CoG}^2\big) \sin\beta \\ &\quad +(c_{FL}+c_{FR})(\delta_W - \beta - \frac{l_F \dot{\psi}}{v_{CoG}}) \cos(\delta_W - \beta) \\ &\quad +(c_{RL}+c_{RR})(-\beta + \frac{l_R \dot{\psi}}{v_{CoG}}) \cos\beta \Big\} \quad , \end{aligned} \tag{A.2}$$

$$\begin{aligned}\frac{\partial \dot{v}_{CoG}}{\partial \dot{\psi}} &= \frac{1}{m_{CoG} v_{CoG}} \cdot \Big\{ l_F \cdot \sin(\delta_W - \beta) \cdot (c_{FL}+c_{FR}) \\ &\quad +l_R \cdot \sin\beta \cdot (c_{RL}+c_{RR}) \Big\} \quad , \end{aligned} \tag{A.3}$$

$$\begin{aligned}\frac{\partial\dot{\beta}}{\partial v_{CoG}} &= -\frac{1}{m_{CoG}v_{CoG}^2}\cdot\Big\{(c_{FL}+c_{FR})(\delta_W-\beta-2\frac{l_F\,\dot{\psi}}{v_{CoG}})\cos(\delta_W-\beta)\\ &\quad+(F_{LFL}+F_{LFR})\cdot\sin(\delta_W-\beta)\\ &\quad-\big(F_{LRL}+F_{LRR}+c_{WX}\cdot v_{CoG}^2\big)\cdot\sin\beta\\ &\quad+(c_{RL}+c_{RR})(-\beta+2\frac{l_R\,\dot{\psi}}{v_{CoG}})\cos\beta\Big\}\quad, \end{aligned}\tag{A.4}$$

$$\begin{aligned}\frac{\partial\dot{\beta}}{\partial\beta} &= \frac{1}{m_{CoG}v_{CoG}}\cdot\Big\{(c_{FL}+c_{FR})(\delta_W-\beta-\frac{l_F\,\dot{\psi}}{v_{CoG}})\sin(\delta_W-\beta)\\ &\quad-(c_{FL}+c_{FR}+F_{LFL}+F_{LFR})\cos(\delta_W-\beta)\\ &\quad-\big(c_{RL}+c_{RR}+F_{LRL}+F_{LRR}-c_{WX}v_{CoG}^2\big)\cos\beta\\ &\quad-(c_{RL}+c_{RR})(-\beta+\frac{l_R\,\dot{\psi}}{v_{CoG}})\sin\beta\Big\}\quad, \end{aligned}\tag{A.5}$$

$$\begin{aligned}\frac{\partial\dot{\beta}}{\partial\dot{\psi}} &= \frac{1}{m_{CoG}v_{CoG}^2}\cdot\Big\{l_R\,(c_{RL}+c_{RR})\cos\beta\\ &\quad-l_F(c_{FL}+c_{FR})\cos(\delta_W-\beta)\Big\}-1\quad, \end{aligned}\tag{A.6}$$

$$\begin{aligned}\frac{\partial\ddot{\psi}}{\partial v_{CoG}} &= \frac{1}{J_Z\,v_{CoG}^2}\Big\{l_F\,\dot{\psi}\,(c_{FL}+c_{FR})(l_F-n_{LF}\cos\delta_W)\cos\delta_W\\ &\quad+\frac{1}{2}\,l_F\,\dot{\psi}\,b_F(c_{FL}-c_{FR})\sin\delta_W\\ &\quad+l_R\,\dot{\psi}\,(c_{RL}+c_{RR})(l_R+n_{LR})\Big\}\quad, \end{aligned}\tag{A.7}$$

$$\frac{\partial \ddot{\psi}}{\partial \beta} = \frac{1}{J_Z} \cdot \Big\{ -(c_{FL} + c_{FR})(l_F - n_{LF} \cos\delta_W) \cos\delta_W - \frac{b_F}{2}(c_{FL} - c_{FR}) \sin\delta_W + (c_{RL} + c_{RR})(l_R + n_{LR}) \Big\} \quad , \quad \text{(A.8)}$$

$$\frac{\partial \ddot{\psi}}{\partial \dot{\psi}} = \frac{1}{J_Z\, v_{CoG}} \cdot \Big\{ -l_F\,(c_{FL} + c_{FR})(l_F - n_{LF} \cos\delta_W) \cos\delta_W - \frac{l_F b_F}{2}(c_{FL} - c_{FR}) \sin\delta_W - l_R\,(c_{RL} + c_{RR})(l_R + n_{LR}) \Big\} \quad . \text{(A.9)}$$

A.2 Coefficients of the Restructured Non-linear System

$$a_{11}(\dot{\psi}, \underline{u}) = \frac{1}{m_{CoG} v_{CoG}} \Big\{ (c_{FL} + c_{FR}) \left[\sin\delta_W \left(\delta_W - \frac{l_F \dot{\psi}}{v_{CoG}} \right) - \cos\delta_W \right] - (c_{RL} + c_{RR}) - (F_{LFL} + F_{LFR}) \cdot \cos\delta_W - \left(F_{LRL} + F_{LRR} - c_{WX} v_{CoG}^2 \right) \Big\} \quad \text{(A.10)}$$

$$a_{12}(\underline{u}) = -1 + \frac{l_R \cdot (c_{RL} + c_{RR}) - l_F \cdot \cos\delta_W \cdot (c_{FL} + c_{FR})}{m_{CoG} v_{CoG}^2} \quad \text{(A.11)}$$

$$a_{21}(\underline{u}) = \frac{1}{J_Z} \Big\{ -(c_{FL} + c_{FR}) \cdot (l_F - n_{LF} \cos\delta_W) \cos\delta_W - \frac{b_F}{2} \sin\delta_W \cdot (c_{FL} - c_{FR}) + (c_{RR} + c_{RL})(l_R + n_{LR}) \Big\} \quad \text{(A.12)}$$

$$a_{22}(\underline{u}) = \frac{1}{J_Z v_{CoG}} \Big\{ -l_F \cdot (c_{FL} + c_{FR})(l_F - n_{LF} \cos\delta_W) \cos\delta_W - \frac{l_F\, b_F}{2} \sin\delta_W (c_{FL} - c_{FR}) - l_R (c_{RR} + c_{RL})(l_R + n_{LR}) \Big\} \quad \text{(A.13)}$$

$$b_1(\underline{u}) = \frac{\delta_W \cdot \cos\delta_W \cdot (c_{FL} + c_{FR}) + \sin\delta_W \cdot (F_{LFL} + F_{LFR})}{m_{CoG} v_{CoG}} \tag{A.14}$$

$$\begin{aligned} b_2(\underline{u}) = \frac{1}{J_Z}\Big\{ & \delta_W \cdot \cos\delta_W \cdot (c_{FL} + c_{FR}) \cdot (l_F - n_{LF}\cos\delta_W) \\ & + \frac{b_F}{2}\cos\delta_W (F_{LFR} - F_{LFL}) \\ & + (F_{LFR} + F_{LFL}) \cdot \sin\delta_W \cdot (l_F - n_{LF}\cos\delta_W) \\ & + (c_{FL} - c_{FR}) \cdot \delta_W \cdot \frac{b_F}{2} \cdot \sin\delta_W + (F_{LRR} - F_{LRL}) \cdot \frac{b_R}{2}\Big\} \end{aligned} \tag{A.15}$$

A.3 Non-linear System Observability

A.3.1 Observability of the Non-linear System with Two Output Variables

For analysis of the observability of the system described by Eqns. (5.38) and (5.39), Eqn. (5.24) must be calculated

$$\underline{y}^{[2]} = \begin{bmatrix} \underline{y} \\ \underline{\dot{y}} \\ \underline{\ddot{y}} \end{bmatrix} = \begin{bmatrix} y_1 \\ y_2 \\ \dot{y}_1 \\ \dot{y}_2 \\ \ddot{y}_1 \\ \ddot{y}_2 \end{bmatrix} = \begin{bmatrix} v_{CoG} \\ \dot{\psi} \\ \dot{v}_{CoG} \\ \ddot{\psi} \\ \ddot{v}_{CoG} \\ \dddot{\psi} \end{bmatrix} = \underline{q}_{obs}(\underline{x}, \underline{u}) \quad . \tag{A.16}$$

These are six non-linear equations for three state variables. Therefore, three of these equations can be selected appropriately to prove unique reversibility by means of the reconfigured observability matrix $\underline{q}_{obs,r}$:

$$\begin{bmatrix} y_1 \\ y_2 \\ \dot{y}_2 \end{bmatrix} = \begin{bmatrix} v_{CoG} \\ \dot{\psi} \\ \ddot{\psi} \end{bmatrix} = \begin{bmatrix} v_{CoG} \\ \dot{\psi} \\ \beta \cdot g_{21}(\underline{u}) + g_{20}(\underline{u}, \underline{y}) \end{bmatrix} =: \underline{q}_{obs,r}(\underline{x}, \underline{u}). \tag{A.17}$$

The terms $g_{20}(\underline{u}, \underline{y})$ and $g_{21}(\underline{u})$ are derived from the third state space equation (3.65):

$$\ddot{\psi} = \beta \cdot g_{21}(\underline{u}) + g_{20}(\underline{u}, y) \quad . \tag{A.18}$$

The system of equations can be uniquely transformed to

$$\underline{x} = \begin{bmatrix} v_{CoG} \\ \beta \\ \dot{\psi} \end{bmatrix} = \begin{bmatrix} y_1 \\ \frac{\dot{y}_2 - g_{20}(\underline{u},y)}{g_{21}(\underline{u})} \\ y_2 \end{bmatrix} = \underline{q}_{obs,r}{}^{-1}(\underline{u}, y) \quad , \tag{A.19}$$

if $g_{21}(\underline{u})$ is non-zero. Then, the system is globally observable.

A.3.2 Observability of the Non-linear System with One Output Variable

For the analysis of the observability of the system (5.44) the observability transformation (5.24) is calculated:

$$\underline{y}^{[2]} = \begin{bmatrix} y \\ \dot{y} \\ \ddot{y} \end{bmatrix} = \begin{bmatrix} \dot{\psi} \\ \ddot{\psi} \\ \psi^{(3)} \end{bmatrix} = \underline{q}_{obs}(\underline{x}, \underline{u}) \quad . \tag{A.20}$$

The second and the third row depend on sin- and cos-terms of β. Without restrictions, they are not analytically invertible. Therefore, for this purposes the local observability is proven by using Eqn. (5.29). This provides

$$\underline{Q}_B(\underline{x}, \underline{y}^{[2]}) = \frac{\partial \underline{q}_{obs}(\underline{x}, \underline{u})}{\partial \underline{x}} = \begin{bmatrix} \frac{\partial \dot{\psi}}{\partial v_{CoG}} & \frac{\partial \dot{\psi}}{\partial \beta} & \frac{\partial \dot{\psi}}{\partial \dot{\psi}} \\ \frac{\partial \ddot{\psi}}{\partial v_{CoG}} & \frac{\partial \ddot{\psi}}{\partial \beta} & \frac{\partial \ddot{\psi}}{\partial \dot{\psi}} \\ \frac{\partial \psi^{(3)}}{\partial v_{CoG}} & \frac{\partial \psi^{(3)}}{\partial \beta} & \frac{\partial \psi^{(3)}}{\partial \dot{\psi}} \end{bmatrix} \quad . \tag{A.21}$$

The first row is trivial:

$$\frac{\partial \dot{\psi}}{\partial v_{CoG}} = 0, \quad \frac{\partial \dot{\psi}}{\partial \beta} = 0, \quad \frac{\partial \dot{\psi}}{\partial \dot{\psi}} = 1 \quad .$$

The partial derivatives of the second row can be found in Appendix A.1. The partial derivatives of the third row

$$\psi^{(3)} = \frac{d\ddot{\psi}}{dt} = \frac{\partial \ddot{\psi}}{\partial \underline{x}}\dot{\underline{x}} + \frac{\partial \ddot{\psi}}{\partial \underline{u}}\dot{\underline{u}} \quad \text{with } \underline{x} = \begin{bmatrix} v_{CoG} \\ \beta \\ \dot{\psi} \end{bmatrix}^T \text{ and } \underline{u} = \begin{bmatrix} F_{LFL} \\ F_{LFR} \\ F_{LRL} \\ F_{LRR} \\ \delta_W \end{bmatrix}^T$$

were calculated with Matlab®. The resultant terms are very complex and therefore not listed here. Using Matlab®, the full rank of Matrix $\underline{Q}_B$ can be checked numerically. It turns out that the system (5.44) is locally observable.

A.3.3 Observability of the Restructured Non-linear System

For the analysis of the observability of the system (5.51) the observability transformation (5.24) is calculated using the differential equation (3.65):

$$\underline{y}^{[1]} = \begin{bmatrix} y \\ \dot{y} \end{bmatrix} = \begin{bmatrix} \dot{\psi} \\ \ddot{\psi} \end{bmatrix} = \begin{bmatrix} \dot{\psi} \\ \beta \cdot g_{21}(\underline{u}) + g_{20}(\underline{u}, y) \end{bmatrix} = \underline{q}_{obs}(\underline{x}, \underline{u}) \quad . \quad \text{(A.22)}$$

In Eqn. (A.22), $\underline{x}$ can be uniquely isolated

$$\underline{x} = \begin{bmatrix} \beta \\ \dot{\psi} \end{bmatrix} = \begin{bmatrix} \frac{\dot{y} - g_{20}(\underline{u}, y)}{g_{21}(\underline{u})} \\ y \end{bmatrix} = \underline{q}_{obs}^{-1}(\underline{u}, y) \quad , \quad \text{(A.23)}$$

if $g_{21}(\underline{u}) \neq 0$. The system (5.51) is globally observable, if $g_{21}(\underline{u}) \neq 0$.

B Nomenclature

B.1 Physical Variables

Convention:
The following indices are wildcards:
$i : F, R$ - front/rear axle
$j : L, R$ - left/right side

Latin

Symbol	Unit	Meaning
A_L	m^2	vertical front area of vehicle
a_X	m/s^2	longitudinal acceleration
$a_{X,0}$	m/s^2	offset of longitudinal acceleration sensor
$a_{X,B}$	m/s^2	longitudinal vehicle body acceleration
$a_{X,C}$	m/s^2	corrected longitudinal acceleration
a_Y	m/s^2	lateral acceleration
$a_{Y,B}$	m/s^2	lateral vehicle body acceleration
a_Z	m/s^2	vertical acceleration
b_F	m	wheel track at front axle
b_R	m	wheel track at rear axle
b_{RA}	m	distance of roll axis from center of gravity
$c_1, \ldots, c_3$	1	tire parameters
c_4	s/m	tire parameter
c_5	N^{-2}	tire parameter
c_{aer}	1	long. air drag coefficient
c_{ij}	N/rad	cornering stiffnesses (generally)
c_F	N/rad	cornering stiffness of front axle
c_R	N/rad	cornering stiffness of rear axle

c_S	Nm/rad	steering stiffness
c_{WX}	kg/m	resultant long. air drag coefficient
c_{WY}	kg/m	resultant lat. air drag coefficient
e_{CoG}	m	distance: pressure point to CoG
F_A	N	acceleration force
F_{DH}	N	down hill force
F_{fric}	N	friction force
F_{Lij}	N	long. wheel forces
F_{LF}, F_{LR}	N	long. wheel forces of front/rear axle
F_R	N	rolling resistance force
F_{Res}	N	resultant long. resistance force
F_{Sij}	N	lateral wheel forces
F_{SF}, F_{SR}	N	lat. wheel forces of front/rear axle
F_{VL}, F_{VS}	N	long./lat. wheel force in v_W-direction
F_{WX}, F_{WY}	N	long./lat. wind resistance force
F_{WZ}	N	lift force
F_{Xij}	N	long. wheel forces in the CoG-coordinate system
F_{XF}, F_{XR}	N	long. wheel forces on the front/rear axle
F_{Yij}	N	lat. wheel forces in the CoG-coordinate system
F_{YF}, F_{YR}	N	lat. wheel forces on the front/rear axle
F_{Zij}	N	vertical wheel forces
F_{ZF}, F_{ZR}	N	vertical wheel force of front/rear axle
f_C	Hz	cut-off frequency of low pass filter
$f_{R,0}$, $f_{R,1}$, $f_{R,4}$	1	rolling friction coefficients
g	m/s^2	earth acceleration
$h_1, \ldots, h_3$	1	weighting factors: fuzzy yaw rate estimator
h_{CoG}	m	height of the center of gravity over ground
h_{PA}	m	height of the pitch axis over ground
h_{RA}	m	height of the roll axis over ground
i_S	1	steering transmission
i_Z	m	radius of gyration
J	$kg\,m^2$	mass moment of inertia (generally)
J_X, J_Y, J_Z	$kg\,m^2$	mass moment of inertia about x-, y-, z-axis
J_W	kgm^2	mass moment of inertia of wheel

k	1	threshold (method of char. speed)
$k_1, \ldots, k_5$	1	weighting factors: fuzzy velocity estimator
k_{redij}	1	wheel force reduction factor
l	m	wheel base
l_F, l_R	m	CoG distance of front/rear axle
l_{PA}	m	distance of pitch axle from CoG
$\max \Delta_v$	m/s	max. deviation of corrected wheel speeds
$\max \Delta_\omega$	m/s	max. deviation of wheel speeds
m_{CoG}	kg	vehicle mass
m_B	kg	vehicle body mass
m_F, m_R	kg	front/rear axle portion of the vehicle mass
N	1	number of samples
n_C	m	constructive caster
n_{LF}, n_{LFj}	m	wheel caster: front wheels
n_{LR}, n_{LRj}	m	wheel caster: rear wheels
p_{BM}	bar	main cylinder brake pressure
p_{BWij}	bar	individual wheel cylinder brake pressures
r, r_C	m	curve radius
r_{meas}	m	measured curve radius
r_{model}	m	model curve radius
r_{stat}	m	static tire radius
SSG	rad	self-steer gradient
SSG_m	rad	modified self-steer gradient
SSG_{l1}, SSG_{l2}	rad	lower self-steer gradient thresholds
SSG_{u1}, SSG_{u2}	rad	upper self-steer gradient thresholds
$s(n)$	m	distance driven by vehicle
s, s_{Res}	1	wheel slip
s_{Lij}	1	longitudinal wheel slip
s_{Sij}	1	lateral wheel slip
T_A	Nm	alignment torque
T_B	Nm	brake torque
T_D	Nm	drive torque
T_S	s	sampling time

t	s	time (generally)
t_0	s	initial point of time
t_x	s	time difference
$\bar{v}$	m/s	average rotational equivalent wheel speed
v_{Ch}	m/s	characteristic speed
$v_{Ch,t}$	m/s	parameter of the characteristic speed method
v_{CoG}	m/s	velocity of the center of gravity
$\hat{v}_{CoG}$	m/s	fuzzy estimate for the center of gravity velocity
v_F, v_R	m/s	wheel velocity front/rear wheel
$v_{R,est}$	m/s	predicted wheel velocity
v_{Rij}	m/s	rotational equivalent wheel velocity
$\dot{\bar{v}}_{Rij}$	m/s^2	averaged wheel accelerations
$v_{Rij,C}$	m/s	corrected rot. equivalent wheel velocities
v_{Wij}	m/s	wheel ground contact point velocities
v_{WY}	m/s	lateral wind velocity
v_X , v_Y	m/s	long./lateral velocity in CoG
$\underline{x}(t), \underline{x}(n)$		center of gravity position over time (trajectory)
x, x_{In}	m	x-coordinate in world coordinate system
$\underline{x}_F$		trajectory calculated with front axle sensors
$\underline{x}_{Fuz}$		trajectory calculated with fuzzy estimators
$\underline{x}_R$		trajectory calculated with rear axle sensors
$\underline{x}_S$		trajectory calculated with gyroscope
x_{CoG}	m	long. vehicle axis
x_{VW}	m	long. wheel velocity axis
$\underline{x}_W$		vector of the wheel plane direction
y, y_{In}	m	y-coordinate in world coordinate system
y_{CoG}	m	lat. vehicle axis
y_{VW}	m	lat. wheel velocity axis

Greek

Symbol	**Unit**	**Meaning**
α_{ij}	rad	tire side slip angles

α_F, α_R	rad	TSSA of front/rear axle wheels
β	rad	vehicle body side slip angle
β_0	rad	stationary vehicle body side slip angle
β_1	rad	recognition threshold of VBSSA
β_2	rad	risk threshold of VBSSA
β_{cont}	rad	controller output value of VBSSA
β_{meas}	rad	measured VBSSA
β_{obs}	rad	observed VBSSA
β_R	rad	equilibrium point of VBSSA
γ	rad	course angle
Δn_1, Δn_2	$1/m$	thresholds of curve radius method
Δp_1, Δp_2	$1/m$	thresholds of curve radius method
Δs, Δs_{ij}	m	distance traveled between successive sample points
Δs_{meas}	m	distance traveled (measured)
Δs_{model}	m	distance traveled (modeled)
ΔT	s	integration time for CRM
Δv_F	m/s	wheel speed difference of front axle
Δv_P	m/s	velocity prediction error
Δv_R	m/s	wheel speed difference of rear axle
Δv_{Rij}	m/s	wheel speeds difference from $\hat{v}_{CoG}$
$\Delta\beta$	rad	average VBSSA observation error
$\Delta\delta_{S1}$, $\Delta\delta_{S2}$	rad	steering angle control interventions
$\Delta\dot{\psi}_l$, $\Delta\dot{\psi}_u$	rad/s	tolerance band widths of $\dot{\psi}$
$\Delta\psi$	rad	yaw angle difference between two successive sample points
$\Delta\dot{\psi}$	rad/s	deviation of linear and nonlinear yaw rate
δ_A	rad	ACKERMANN angle
δ_S	rad	steering wheel angle
$\delta_{S,meas}$	rad	measured steering wheel angle
δ_W	rad	wheel turn angle
$\delta_{W,th}$	rad	wheel turn angle threshold for "cornering"
η_1, η_2	1	amplification factors
μ, μ_{res}	1	friction coefficient
μ_{Lij}, μ_{Sij}	1	long./lat. friction coefficients

ν	rad	curve angle
ξ_1, ξ_2	1	tire parameters
φ	rad	roll angle
χ	rad	pitch angle
χ_{Road}	rad	road gradient
$\dot{\psi}$	rad/s	yaw rate (generally)
ψ_F	rad	yaw angle from front axle sensors
$\dot{\psi}_F$	rad/s	yaw rate from front axle sensors
ψ_{Fuz}	rad	fuzzy yaw angle estimate
$\dot{\psi}_{Fuz}$	rad/s	fuzzy yaw rate estimate
$\dot{\psi}_l$, $\dot{\psi}_{l2}$, $\dot{\psi}_u$, $\dot{\psi}_{u2}$	rad/s	thresholds of continuous yaw gain method
$\dot{\psi}_{lin}$, $\dot{\psi}_{nlin}$	rad/s	linear/non-linear yaw rate model value
$\dot{\psi}_{max}$, $\dot{\psi}_{min}$	rad/s	upper/lower limit of $\dot{\psi}$-tolerance band
$\dot{\psi}_{meas}$	rad/s	measured yaw rate
$\dot{\psi}_{model}$	rad/s	model yaw rate
ψ_R	rad	yaw angle from rear axle sensors
$\dot{\psi}_R$	rad/s	yaw rate from rear axle sensors
ψ_S	rad	yaw angle from gyroscope sensor
$\dot{\psi}_S$	rad/s	yaw rate from gyroscope sensor
$\dot{\psi}_{th}$	rad/s	yaw rate threshold for "cornering"
ω_{Rij}	rad/s	angular wheel velocities
$\dot{\bar{\omega}}_{Rij}$	rad/s^2	average angular wheel accelerations
$\dot{\bar{\omega}}_{Rij,th}$	rad/s^2	average angular wheel acceleration threshold

Terms of System, Observer and Parameter Estimation Theory

Symbol	**Meaning**
$\underline{A}$	dynamic matrix
$\underline{A}_0$	dynamic matrix of linear reference model
$\underline{\hat{A}}$	JACOBIAN-matrix of EKBF

$\underline{B}$, $\underline{b}$	input matrix/vector
$\underline{B}_0$	input matrix of linear reference model
$\underline{C}$, $\underline{c}$	output matrix/vector
$\underline{\hat{C}}$	JACOBIAN-matrix of EKBF
$E\{\cdot\}$	expectation value
$\underline{F}$	dynamic matrix
$\underline{f}(\cdot)$	non-linear state vector function
$\underline{h}(\cdot)$	non-linear output vector function
$\underline{H}$	time-discrete output matrix
$\underline{I}, \underline{I}_n$	identity matrix
$\underline{K}, \underline{K}(t)$	KALMAN-matrix gain
$\underline{L}$	observer gain
$\underline{L}_{lin}$	observer gain for linear reference model
$N_{\underline{R}_L}$	norm
$\underline{P}, \underline{P}(t)$	covariance matrix of KALMAN-Filters
$\underline{P}_L$	matrix of LJAPUNOV-function
$\tilde{P}_{L,ii}$	positive weighting functions in $\underline{P}$
$\underline{Q}, \underline{Q}(t)$	covariance matrix of system noise
$\underline{Q}_B$	observability matrix
$\underline{q}_{obs}$	non-linear observability transformation
$\underline{q}_{obs,r}$	reconfigured non-linear observability matrix
$\underline{R}$	covariance matrix of measurement noise
$\underline{R}_L$	matrix of LJAPUNOV-function
$\underline{R}_{L,lin}$	matrix of the ideal LJAPUNOV-function
$\hat{r}_{xy}$	cross correlation function
$T(\cdot)$	threshold function

$\underline{u}$	input vector
$\underline{u}_{lin}$	input vector of linearized reference model
$\underline{u}_R$	input vector of equilibrium point
$\underline{w}_i$	left eigenvectors
$\underline{w}_k, \underline{w}(t)$	system noise
$\bar{\underline{w}}_i$	complex conjugate left eigenvectors
$\underline{v}_k, \underline{v}(t)$	measurement noise
$V(\underline{x})$	LJAPUNOV-function
$V_{lin}(\underline{x})$	ideal LJAPUNOV-function for linear estimation error
$\underline{x}$	state vector
$\hat{\underline{x}}$	observed state vector
$\tilde{\underline{x}}$	estimation error
$\underline{x}_0$	initial value of state vector
$\hat{\underline{x}}_0$	initial value of state space observer
$\underline{x}_{S,0}$	initial simulation value of state vector
$\underline{x}_{lin}$	state vector of linearized reference model
$\hat{\underline{x}}_{lin}$	observed state vector of linearized reference model
$\tilde{\underline{x}}_{lin}$	estimation error of linearized reference model
$\underline{x}_p$	expansion point of TAYLOR expansion
$\underline{x}_R$	state vector of equilibrium point
$\underline{y}$	output vector
$\underline{y}_{lin}$	output vector of linearized reference model
$\underline{y}_{model}$	model output vector
$\underline{y}_{meas}$	measured output vector
$\Delta\underline{y}$	deviation of measured and modeled output vector
δ_{ij}	KRONECKER-Symbol
Θ	RLS-estimation parameter
λ_F	forgetting factor
λ_ν	eigenvalues
$\underline{\Phi}(T_S)$	time-discrete dynamic matrix

B.2 Abbreviations

ABS : Antilock Braking System
AMR : Anisotropic Magneto-Resistive
AQF : Adaptation of a Quality Function

CAN : Controller Area Network
CC : Center of Curvature
CoG : Center of Gravity
CRM : Curve Radius Method
CS : Characteristic Speed
CSI : Continuous Stability Index
CSM : Characteristic Speed Method

DE : Differential Equation
DERM : Diagnostic and Energy Reserve Module
DSC : Dynamic Stability Control
DSI : Discrete Stability Index
DSP : Digital Signal Processor

EDR : Event Data Recorder
EEPROM: Electrical Erasable Programmable Read Only Memory
EHB : Electro-Hydraulic Brake
EKBF : Extended Kalman-Bucy-Filter
ESP : Electronic Stability Program

GM : General Motors (Corporation)
GPS : Global Positioning System

ICR : Inverse Curve Radius
IEEE : Institute of Electrical and Electronics Engineers

KBF : Kalman-Bucy-Filter

LS : Least Squares

NHTSA : National Highway Traffic Safety Administration
NL : Non-linear
NTSB : National Traffic Safety Board

OEM : Original Equipment Manufacturer
OV : Output variable

PP : Pressure Point
PSA : Peugeot Citroen S.A.

RAM : Random Access Memory
RLS : Recursive Least Squares
ROM : Read Only Memory

SAPS-RC : Signal Analyzer for Pressure Sensor - Real-time CAN-interface
SDM : Sensing and Diagnostic Module
SI : Stability index
SSG : Self-Steer Gradient
SSGM : Self-Steer Gradient Method

TCS : Traction Control System
TSSA : Tire Side Slip Angle

VBSSA : Vehicle Body Side Slip Angle
VDC : Vehicle Dynamics Control

WGCPV : Wheel Ground Contact Point Velocity

YGM : Yaw Gain Method

B.3 Angle and Coordinate Definitions

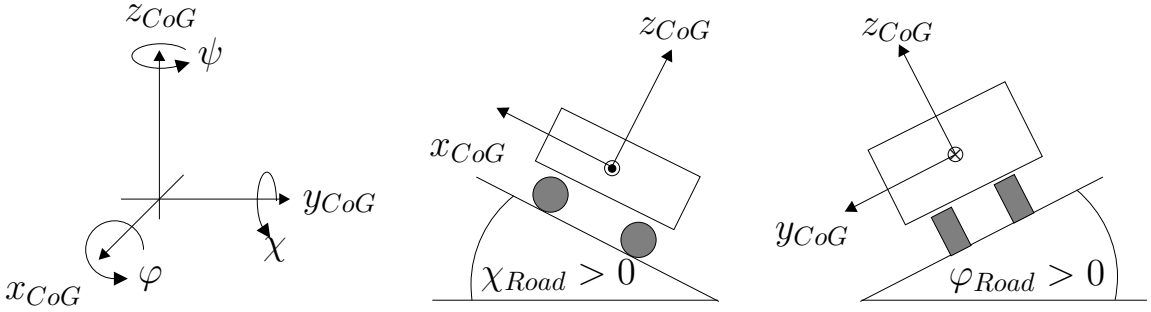

(a) Angles in the vehicle coordinate system (b) Longitudinally inclined road (c) Laterally inclined road

Figure B.1: Angle definitions

C Fuzzy Rule Base

C.1 Fuzzy Velocity Estimator

The individual rule bases listed in Tables C.1 to C.5 for the different subsystems were implemented in the fuzzy velocity estimator.

Strong Braking

Area of application: $a_{X,C} < -3m/s^2$
The velocity gained from the wheel speed sensor signals are weighted rather low due to brake slip. As the braking force on the front axle is large, the slip values are higher than on the rear axle. Therefore, the wheel speeds of the front axle are only considered for the velocity calculation if those of the rear axle are erroneous. The acceleration sensor's weight is increased in this driving situation (Table C.3).

Braking

Area of application: $-3m/s^2 < a_{X,C} < 0m/s^2$
The rule base for "Braking" does not differ a lot from the one of the subsystem "strong Braking". Only the linguistic terms and the slip thresholds of Δv_i have other limits and the slip values are generally reduced.

Rolling

Area of application: $-0.3m/s^2 < a_{X,C} < 0.3m/s^2$
If $\max \Delta_v$ is small in this drive situation, then the fuzzy system is not used at all. The estimated velocity is the average of the wheel speed signals.
If $\max \Delta_v$ is big, though, then the rolling wheels are weighted high, whereas those wheels not free rolling are weighted less.

Acceleration

Area of application: $0m/s^2 < a_{X,C} \leq 1.5m/s^2$
The rough structure is comparable to the subsystem "Braking" with the significant difference that in this case *drive* slip must be detected and the respective wheel speed signals must obtain reduced weight. Additionally, braking affects all the wheels, whereas acceleration only affects the wheels of the driven axle (for test car: the rear axle).

Strong Acceleration

Area of application: $1.5m/s^2 < a_{X,C}$
The rule bases of "Acceleration" and "Strong Acceleration" are similar. The basic difference is the selection of the linguistic terms of the different subsystems. The shape of the trapezes of the membership functions must be adapted, though. The increased drive slip must be considered. The values for Δv_i are larger and the linguistic terms "Front" and "Rear" of the membership functions are shifted to the left.

Δv_{RFL}	Δv_{RFR}	Δv_{RRL}	Δv_{RRR}	max Δ_v	k FL	k FR	k RL	k RR	k v(a)
-	-	-	-	small	zero	zero	middle	middle	middle
-	-	rear	rear	big	zero	zero	small	small	big
front	-	rear	-	big	zero	-	small	-	big
-	front	rear	-	big	-	zero	small	-	big
front	-	-	rear	big	zero	-	-	small	big
-	front	-	rear	big	-	zero	-	small	big
-	-	rear	-	big	-	-	small	-	big
-	-	-	rear	big	-	-	-	small	big
-	front	not rear	-	big	-	small	small	-	middle
front	-	not rear	-	big	small	-	small	-	middle
-	front	-	not rear	big	-	small	-	small	middle
front	-	-	not rear	big	small	-	-	small	middle
not front	-	-	-	big	zero	-	-	-	-
-	not front	-	-	big	-	zero	-	-	-

Table C.1: Rule base for the v-Fuzzy subsystem "Braking"

Δv_{RFL}	Δv_{RFR}	Δv_{RRL}	Δv_{RRR}	max Δ_v	k FL	k FR	k RL	k RR	k v(a)
-	-	-	-	small	big	big	big	big	zero
OK	OK	not OK	not OK	big	big	big	zero	zero	middle
not OK	not OK	OK	OK	big	zero	zero	big	big	middle
not OK	OK	OK	OK	big	zero	big	big	big	small
OK	not OK	OK	OK	big	big	zero	big	big	small
OK	OK	not OK	OK	big	big	big	zero	big	small
OK	OK	OK	not OK	big	big	big	big	zero	small
OK	OK	too high	too high	small	middle	middle	middle	middle	small
too high	too high	OK	OK	small	middle	middle	middle	middle	small
not too high	too high	too high	too high	big	zero	big	big	big	small
too high	not too high	too high	too high	big	big	zero	big	big	small
too high	too high	not too high	too high	big	big	big	zero	big	small
too high	too high	too high	not too high	big	big	big	big	zero	small
not too low	too low	too low	too low	big	zero	big	big	big	small
too low	not too low	too low	too low	big	big	zero	big	big	small
too low	too low	not too low	too low	big	big	big	zero	big	small
too low	too low	too low	not too low	big	big	big	big	zero	small

Table C.2: Rule base for the v-Fuzzy subsystem "Rolling"

Δv_{RFL}	Δv_{RFR}	Δv_{RRL}	Δv_{RRR}	max Δ_v	k FL	k FR	k RL	k RR	k v(a)
-	-	-	-	small	zero	zero	small	small	big
-	-	rear	rear	big	zero	zero	small	small	middle
-	-	not rear	rear	big	zero	zero	zero	big	middle
-	-	rear	not rear	big	zero	zero	big	zero	middle
front	-	not rear	not rear	big	small	zero	zero	zero	big
-	front	not rear	not rear	big	zero	small	zero	zero	big
ABS	ABS	front	front	big	zero	zero	small	small	big

Table C.3: Rule base for the v-Fuzzy subsystem "strong Braking"

C.2 Fuzzy Yaw Rate Estimator

The fuzzy yaw rate estimator is not explicitly partitioned into subsystems. Therefore, the complete rule base is given by Table C.6.

Δv_{RFL}	Δv_{RFR}	Δv_{RRL}	Δv_{RRR}	max Δ_v	k FL	k FR	k RL	k RR	k v(a)
-	-	-	-	small	middle	middle	zero	zero	big
front	front	rear	rear	big	middle	middle	zero	zero	big
front	-	rear	-	big	middle	-	zero	-	big
front	-	-	rear	big	middle	-	-	zero	big
front	-	rear	-	big	-	middle	zero	-	big
-	front	-	rear	big	-	-	middle	zero	big
front	not front	rear	rear	big	small	zero	zero	zero	middle
not front	-	rear	-	big	small	-	small	-	big
not front	-	-	rear	big	small	-	-	small	big
-	not front	rear	-	big	-	small	small	-	big
-	not front	-	rear	big	small	-	-	small	big
error	-	-	-	big	zero	-	-	-	-
-	error	-	-	big	-	zero	-	-	-
-	-	error	-	big	-	-	zero	-	-
-	-	-	error	big	-	-	-	zero	-
ABS	-	-	-	big	zero	-	-	-	-
-	ABS	-	-	big	-	zero	-	-	-
-	-	ABS	-	big	-	-	zero	-	-
-	-	-	ABS	big	-	-	-	zero	-
not front	not front	rear	rear	big	small	small	middle	middle	big
error	error	error	error	big	small	small	zero	zero	middle
ABS	ABS	ABS	ABS	big	small	small	small	small	small

Table C.4: Rule base for the v-Fuzzy subsystem "Strong Acceleration"

Δv_{RFL}	Δv_{RFR}	Δv_{RRL}	Δv_{RRR}	max Δ_v	k FL	k FR	k RL	k RR	k v(a)
-	-	-	-	small	middle	middle	zero	zero	big
front	-	rear	-	big	middle	-	small	-	big
front	-	-	rear	big	middle	-	-	small	big
-	front	rear	-	big	-	middle	small	-	big
-	front	-	rear	big	-	middle	-	small	big
not front	not front	rear	rear	big	zero	middle	small	small	big
front	not front	rear	rear	big	middle	zero	small	small	big
not front	not front	rear	rear	big	small	small	small	small	big
ABS	-	-	-	big	zero	-	-	-	big
-	ABS	-	-	big	-	zero	-	-	big
error	-	-	-	big	zero	-	-	-	big
-	error	-	-	big	-	zero	-	-	big
-	-	rear	-	big	-	-	zero	-	middle
-	-	error	-	big	-	-	zero	-	middle
-	-	-	rear	big	-	-	-	zero	middle
-	-	-	error	big	-	-	-	zero	middle

Table C.5: Rule base for the v-Fuzzy subsystem "Acceleration"

δ_W	a_Y	$a_{X,C}$	Δv_F	Δv_R	h_1	h_2	h_3
-	little	little	small	small	small	large	large
-	-	-	error	-	little	zero	-
-	-	-	-	error	little	-	zero
-	little	strong braking	small	small	average	small	average
-	little	strong braking	small	-	average	large	small
-	little	strong acc.	small	-	average	large	small
-	not little	strong acc.	small	large	average	average	small
-	not little	strong acc.	small	small	average	large	small
not little	little	little	small	-	small	large	-
not little	not little	little	small	-	average	average	-
not little	little	little	-	small	-	-	large
not little	not little	little	-	small	average	-	small
little	not little	little	small	-	average	small	-
little	not little	little	large	large	average	zero	average
little	not little	little	-	small	small	-	large

Table C.6: Complete rule base of the $\dot{\psi}$-Fuzzy estimator

D Vehicles, Parameters and Sensors

D.1 Vehicle 1: Ford Scorpio

Most of the test drives were conducted with the test vehicle of the Institut für Industrielle Informationstechnik (IIIT). Thereby, the sensors displayed in Fig D.1 were used:

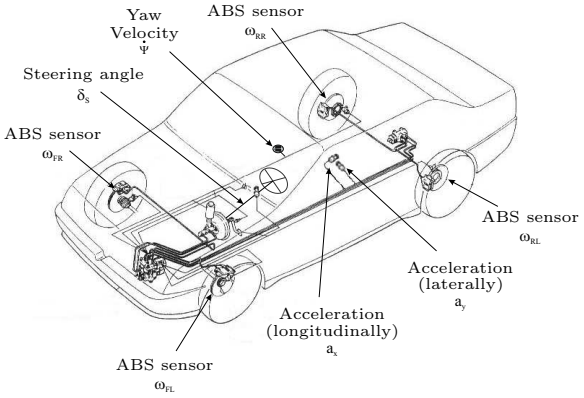

Figure D.1: Test car with employed sensors

Vehicle data:

Rear wheel driven, year of manufacture: 1987, 85kW

Distance of front axle from CoG	: l_F	=	$1,377\,m$
Distance of rear axle from CoG	: l_R	=	$1,383\,m$
Track front	: b_F	=	$1,476\,m$
Track rear	: b_R	=	$1,477\,m$
Height of CoG	: h_{CoG}	=	$0,47\,m$
Tire radius	: r_{stat}	=	$0,303m$
Mass (empty)	: m_{CoG}	=	$1350\,kg$
Vehicle mass moment of inertia	: J_Z	=	$1856\,kgm^2$
Cornering stiffnesses (approx.)	: c_{ij}	=	$58000\,\frac{N}{rad}$
Steering transmission	: i_S	=	16
Sampling Time	: T_S	=	$10ms$

D.2 Vehicle 2: Opel Vita

The test drives with side slip angle reference measurements were carried out with this test vehicle. It is an Opel Vita, front axle driven. Some important vehicle parameters and sensor positions are displayed in Fig. D.2.

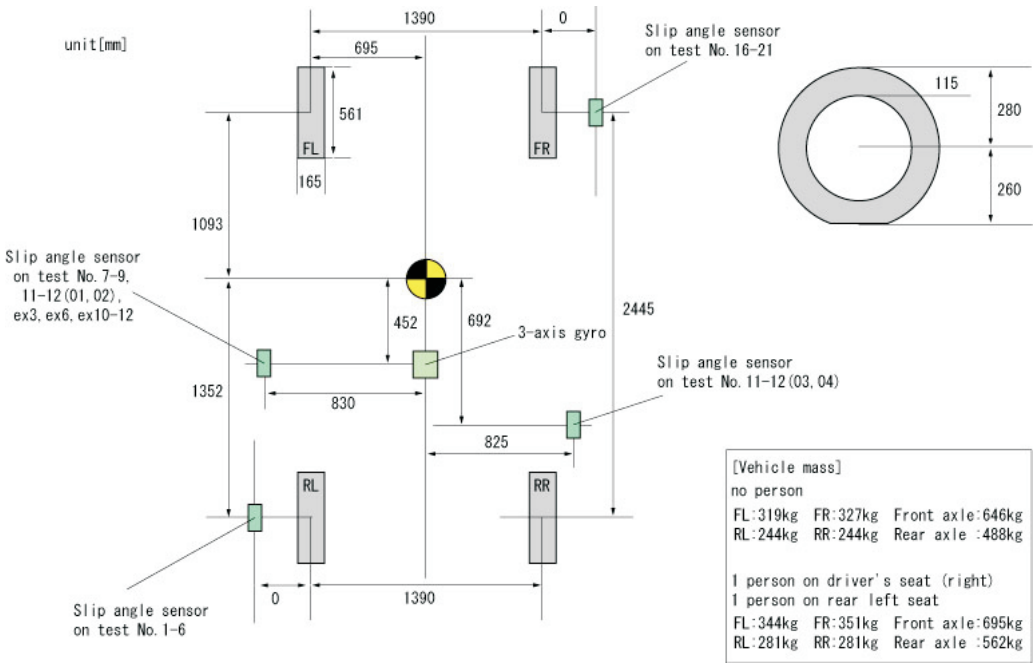

Figure D.2: Opel Vita

Vehicle data:

Front wheel driven

Distance of front axle from CoG	: l_F	=	$1,093\,m$
Distance of rear axle from CoG	: l_R	=	$1,352\,m$
Track front	: b_F	=	$1,39\,m$
Track rear	: b_R	=	$1,39\,m$
Height of CoG	: h_{CoG}	=	$0,47\,m$
Tire radius	: r_{stat}	=	$0,27m$
Mass (empty)	: m_{CoG}	=	$1257\,kg$
Vehicle mass moment of inertia	: J_Z	=	$1446\,kgm^2$
Cornering stiffnesses	: c_{ij}	=	$58000\,\frac{N}{rad}$
Caster front	: n_{LF}	=	0,06 m
Caster rear	: n_{LR}	=	0,06 m
Steering transmission	: i_S	=	16
Sampling Time	: T_S	=	$1ms$

D.3 Most Important Sensors

The sensors used for the measurements were mostly industrial automotive sensors. The analog and digital sensor signals were 10bit A/D converted in three CAN nodes of the Ford Scorpio (see also Chapter 6).

	Accelerations	Yaw rate	Steering angle	Wheel speeds
Sensor princicple	piezo-resistive	piezoelectric vibration	anisotropic magneto resistive	inductive
Manufacturer	FGP Instr.	MuRata GmbH	Robert Bosch GmbH	Robert Bosch GmbH
Signal Range	$-2g...+2g$	$-60\frac{deg}{s}...+60\frac{deg}{s}$	$-780°...+779.9°$	$\approx 0.5...177\frac{m}{s}$
Resolution	$\approx 0.04\frac{m}{s^2 \cdot \text{digit}}$	$\approx 0.002\frac{\text{rad}}{s \cdot \text{digit}}$	$0.1°$	$0.02\frac{m}{s \cdot \text{digit}}$
Cycle time	10 ms	10 ms	10 ms	10 ms
Variable name	a_X, a_Y	$\dot{\psi}$	δ_S	ω_{Rij}
Protection type	-	-	IP 50	IP 67
Temp. range	$-20°C...80°C$	$-30°C...80°C$	$-40°C...50°C$	$-40°C...+110°C$
Output signal	analog, $0.5V-4.5V$	analog, $0.5V-4.5V$	CAN, ISO 11898	freq. + ampl. modulated

Table D.1: Standard sensors used in test car

	VBSSA	Wheel torque
Sensor princicple	optical	piezoelectric
Manufacturer	Corrsys Datron	Kistler Instrumente AG
Measuring Range	$-40°...+40°$	$-3000Nm...+3000Nm$, $-300Nm...+300Nm$
Resolution	$< 0.1°$	$< 1.5Nm$
Cycle time	1ms	10 ms
Variable name	β	M_{YRL}
Protection type	IP 67	IP 65
Temp. range	$-25°C...+50°C$	$-25°C...+80°C$
Output signal	analog, $-10V...+10V$, or digital	analog, $-5V...+5V$
Internal filter delay	128ms	-
Overall time delay	75ms	-

Table D.2: Reference sensors used in test car

[58] describes the measurement procedure with these reference sensors very extensively and provides information about measurement error compensation. Detailed information about inertial reference sensors can be found in, [73], [74].

Bibliography

[1] M. Abe. *Vehicle dynamics and control.* Sankaido Publishing Co., LTD., Japan, 3rd edition, 1996.

[2] D. Ammon. *Modellbildung und Systementwicklung in der Fahrzeugdynamik.* Teubner Verlag, Stuttgart, 1997.

[3] D. Bevly, J. C. Gerdes, and C. Wilson. The use of GPS based velocity measurements for measurement of sideslip and wheel slip. *Vehicle System Dynamics*, 38(2):pp. 127–147, 2000.

[4] D. Bevly, R. Sheridan, and J. C. Gerdes. Integrating INS sensors with GPS velocity measurements for continuous estimation of vehicle sideslip and tire cornering stiffness. *Proceedings of the American Control Conference*, pages 25 – 30, June 25-27, 2001.

[5] J. Birk. *Rechnergestützte Analyse und Lösung nichtlinearer Beobachtungsaufgaben.* VDI-Fortschrittberichte, Reihe 8, Nr. 294. VDI-Verlag, Düsseldorf, 1992.

[6] J. Birk and M. Zeitz. Extended Luenberger observer for non-linear multivariable systems. *Int. J. Control*, vol. 47, 1988.

[7] K. Brammer and G. Siffling. *Kalman-Bucy-Filter. Deterministische Beobachtung und stochastische Filterung.* Oldenbourg Verlag, München Wien, 1975.

[8] K. Brammer and G. Siffling. *Stochastische Grundlagen des Kalman-Bucy-Filters: Wahrscheinlichkeitsrechnung und Zufallsprozesse.* Methoden der Regelungstechnik. R. Oldenbourg Verlag, München, Wien, 1975.

[9] M. Börner. *Adaptive Querdynamikmodelle für Personenkraftfahrzeuge - Fahrzustandserkennung und Sensorfehlertoleranz.* VDI-Fortschrittberichte, Reihe 12, Nr. 563. VDI-Verlag, Düsseldorf, 2004.

[10] Bundesanstalt für Straßenwesen (bast). *Charakteristika von Unfällen auf Landstraßen*. Wissenschaftliche Informationen der Bundesanstalt für Straßenwesen, info 08/01. Bundesanstalt für Straßenwesen, Bergisch Gladbach, 2001.

[11] Bundesanstalt für Straßenwesen (bast). *Volkswirtschaftliche Kosten durch Straßenverkehrsunfälle in Deutschland 1999*. Wissenschaftliche Informationen der Bundesanstalt für Straßenwesen, info 12/01. Bundesanstalt für Straßenwesen, Bergisch Gladbach, 2001.

[12] M. Burckhardt. *Radschlupf-Regelsysteme*. Vogel Fachbuchgruppe: Fahrwerktechnik. Vogel Buchverlag, Würzburg, 1st edition, 1993.

[13] A. Chidester, J. Hinch, and T. Roston. Real World Experience with Event Data Recorders. *National Highway Traffic Safety Administration*, (Paper Number 247), 2002.

[14] A. Daiß. *Beobachtung fahrdynamischer Zustände und Verbesserung einer ABS- und Fahrdynamikregelung*. VDI-Fortschrittberichte, Reihe 12, Nr. 283. VDI-Verlag, Düsseldorf, 1996.

[15] M. Danner and J. Halm. *Technische Analyse von Verkehrsunfällen*. Eurotax (International) AG, Pfäffikon, Switzerland, 1994.

[16] E. L. Ding. Modellgestützte Sensorüberwachung eines ESP-Systems. *Automatisierungstechnische Praxis atp*, 41(7):pp. 35 – 42, July 1999.

[17] H. B. Pacejka (Editor), J. J. van Oosten, and E. Bakker. The Magic Formula Tyre Model. *Proceedings of the first international colloquium on tyre models for vehicle dynamics analysis, Delft, Netherlands, October 21-22, 1991*, 21:pp. 19–29, 1993.

[18] P. Köhn et al. Active Steering - The BMW approach towards modern steering technology. *Proceedings of the SAE World Congress, Detroit, MI, USA*, (2002-01-1105), 2004.

[19] R. Fay et al. Using Event Data Recorders in collision reconstruction. *Proceedings of the SAE World Congress*, (2002-01-0535), 2002.

[20] S. L. Miller et al. *Calculating longitudinal and lateral wheel slip and tire parameters using GPS velocity*. Proceedings of the American Control Conference, Arlington, VA, USA, 2001.

[21] W. J. Flemming. Overview of automotive sensors. *IEEE Sensor Journal*, 1(4):pp. 296 – 308, 2001.

[22] O. Föllinger. *Lineare Abtastsysteme*. Methoden der Regelungstechnik. Oldenbourg Verlag, München, Wien, 5. edition, 1993.

[23] O. Föllinger. *Nichtlineare Regelungen, Band 2*. Oldenbourg Verlag, München, 7. edition, 1993.

[24] O. Föllinger. *Regelungstechnik*. Hüthig-Verlag, Heidelberg, 8th edition, 1994.

[25] Y. Fukada. Slip-angle estimation for vehicle stability control. *Vehicle System Dynamics*, (32):pp. 375 – 388, 1999.

[26] T. Gillespie. *Fundamentals of vehicle dynamics*. Society of automotive engineers, Warrendale, PA, USA, 1st edition, 1992.

[27] Robert Bosch GmbH. *Kraftfahrtechnisches Taschenbuch, 24. Auflage*. Vieweg Verlag, Braunschweig, Wiesbaden, 2002.

[28] J. Grehn. *Metzler Physik*. J. B. Metzlersche Verlagsbuchhandlung, Stuttgart, 2. edition, 1995.

[29] NHTSA EDR Working Group. Summary of findings. Technical report, National Highway Traffic Safety Administration (NTHSA), Washington D.C., August 2001.

[30] M. Guzek and Z. Lozia. Possible errors occurring during accident reconstruction based on car "black box" records. *Proceedings of the SAE World Congress, Detroit, MI, USA*, (2002-01-0549), 2002.

[31] A. Hac and M. D. Simpson. Estimation of vehicle side slip angle and yaw rate. *Proceedings of the SAE World Congress, Detroit, MI, USA*, (2000-01-0696), 2000.

[32] C. Halfmann. *Adaptive semiphysikalische Echtzeitsimulation der Kraftfahrzeugdynamik im bewegten Fahrzeug*. VDI-Fortschrittberichte, Reihe 12, Nr. 467. VDI-Verlag, Düsseldorf, 2001.

[33] J. Helling. *Vertikal-/Querdynamik von Kraftfahrzeugen*. Institut für Kraftfahrwesen RWTH Aachen, Aachen, 1991.

[34] M. Hiemer and J. Barrho. Observer design for road gradient estimation. *Reports in Industrial Information Technology*, Vol. 7, Shaker Verlag, Aachen:pp. 23–30, 2004.

[35] M. Hiemer, U. Kiencke, T. Matsunaga, et al. Cornering stiffness adaptation for improved side slip angle observation. *Proceedings of the First IFAC Symposium on Advances in Automotive Control, AAC*, 2004.

[36] M. Hiemer, S. Lehr, U. Kiencke, and T. Matsunaga. A fuzzy system to determine the vehicle yaw angle. *Transactions of the SAE World Congress*, (2004-01-1191), 2004.

[37] G. Himpert. Kfz-Sachverständigen-Dienstleistung im Wandel - polizeiliche und/oder private Verkehrsunfallaufnahme. *Der Verkehrsunfall*, 33(2), 1995.

[38] H. Holzmann. *Adaptive Kraftfahrzeugdynamik-Echtzeitsimulation mit Hybriden Modellen.* VDI-Fortschrittberichte, Reihe 12, Nr. 465. VDI-Verlag, Düsseldorf, 2001.

[39] P. Huang, H. Smakman, and J. Guldner. Design of a vehicle state observer for vehicle dynamics control systems. *Proceedings of 5th International Symposium on Advanced Vehicle Control*, August 22-24, 2000, Ann Arbor, Michigan.

[40] R. Isermann. *Identifikation dynamischer Systeme, Band II.* Springer-Verlag, Berlin Heidelberg New York, 1988.

[41] J. Kahlert. *Fuzzy Control für Ingenieure.* Vieweg Verlag, Braunschweig, Wiesbaden, 1995.

[42] H. Keller. *Entwurf nichtlinearer Beobachter mittels Normalformen.* VDI-Fortschrittberichte, Reihe 8, Nr. 124. VDI-Verlag, Düsseldorf, 1986.

[43] U. Kiencke and R. Eger. *Meßtechnik.* Springer-Verlag, Berlin, Heidelberg, New York, 5th edition, 2001.

[44] U. Kiencke and L. Nielsen. *Automotive Control Systems.* Springer-Verlag, Berlin, Heidelberg, New York, 2000.

[45] P. Koehn, A. Pauly, and M. Schnabel et al. Die Aktivlenkung - Das fahrdynamische Lenksystem des neuen 5er. *Automobiltechnische Zeitschrift extra*, 105(8):pp. 96–105, 2003.

[46] K. Kowalenko. IEEE to create standards for vehicle 'Black Box' devices. *The Institute*, 26(6):pp. 1,7, 2002.

[47] H. Kronmüller. *Digitale Signalverarbeitung*. Springer-Verlag, Berlin Heidelberg New York, 1991.

[48] J. M. Lawrence, C. C. Wilkinson, et al. The accuracy of pre-crash speed captured by event data recorders. *Proceedings of the SAE World Congress, Detroit, MI, USA*, (2003-01-0889), 2003.

[49] W.S. Levine. *The Control Handbook*. CRC Press LLC, Boca Raton, FL, USA, 1996.

[50] D. G. Luenberger. *Introduction to Dynamic Systems - Theory, Models and Application*. John Wiley & Sons, New York, 1979.

[51] H. Lutz and W. Wendt. *Taschenbuch der Regelungstechnik*. Verlag Harri Deutsch, Frankfurt am Main, 4. edition, 2002.

[52] M. Mitschke. *Dynamik der Kraftfahrzeuge*. Band A: Antrieb und Bremsen. Springer-Verlag, Berlin, Heidelberg, New York, 2nd edition, 1988.

[53] M. Mitschke. *Dynamik der Kraftfahrzeuge*. Band C: Fahrverhalten. Springer-Verlag, Berlin, Heidelberg, New York, 2nd edition, 1990.

[54] M. Mitschke and H. Wallentowitz. *Dynamik der Kraftfahrzeuge*. Springer-Verlag, Berlin, Heidelberg, New York, 3rd edition, 2004.

[55] M. Mitschke, H. Wallentowitz, and E. Schwartz. *Vermeidung querdynamisch kritischer Fahrzustände durch Fahrzustandsüberwachung*. VDI-Tagung: Reifen, Fahrwerk Fahrbahn, VDI-Berichte 916. VDI-Verlag, Düsseldorf, 1991.

[56] O. Nelles. *Nonlinear system identification*. Springer Verlag, Berlin, Heidelberg, New York, 1st edition, 2000.

[57] S. Nicodemus. Unfallgeschehen im Strassenverkehr 2003 - Presseexemplar. Technical report, Statistisches Bundesamt, Wiesbaden, April 2004.

[58] M. Nüssle. *Ermittlung von Reifeneigenschaften im realen Fahrbetrieb*. Dissertation, Universität Karlsruhe (TH), 2002.

[59] U.S. Department of Transportation. Traffic safety facts 2002 - a compilation of motor vehicle crash data from the fatality analysis reporting system and the general estimates system. Technical report, National Highway Traffic Safety Administration, 2002.

[60] H. B. Pacejka. *Tyre and vehicle dynamics.* Butterworth Heinemann, Oxford, Amsterdam, Boston, 2002.

[61] J. Paul, W. Klinkner, and A. Müller. Das elektronische Fahrsicherheitssystem ESP (Elektronisches-Stabilitäts-Programm) von Mercedes Benz. *VDI Berichte*, (1224):pp. 401–421, 1995.

[62] K. Popp and W. Schiehlen. *Fahrzeugdynamik.* Leitfäden der angewandten Mathematik und Mechanik, Band 70. Teubner-Verlag, Stuttgart, Leipzig, 1993.

[63] J. Reimpell. *Fahrwerktechnik: Grundlagen.* Vogel Fachbuchgruppe: Fahrwerktechnik. Vogel Buchverlag, Würzburg, 2nd edition, 1998.

[64] J. Reimpell and P. Sponagel. *Fahrwerktechnik: Reifen und Räder.* Vogel Fachbuchgruppe: Fahrwerktechnik. Vogel Buchverlag, Würzburg, 2nd edition, 1988.

[65] G. Rill. *Simulation von Kraftfahrzeugen.* Vieweg Verlag, Braunschweig, 1994.

[66] J. Ryu, E. J. Rossetter, and J. C. Gerdes. Vehicle side slip and roll parameter estimation using GPS. *AVEC 2002, 6th Symposium on advanced vehicle control, Hiroshima, Japan*, 2002.

[67] H. Schlitt. *Systemtheorie für stochastische Prozesse: Statistische Grundlagen, Systemdynamik, Kalman Filter.* Springer-Verlag, Berlin, Heidelberg, New York, 1992.

[68] E. Schwartz. *Erkennung und Regelung querdynamisch kritischer Fahrzustände bei der Kurvenfahrt von PKW.* Dissertation, Universität Braunschweig, Braunschweig, 1990.

[69] R. Schwarz. *Rekonstruktion der Bremskraft bei Fahrzeugen mit elektromechanisch betätigten Radbremsen.* VDI-Fortschrittberichte, Reihe 12, Nr. 393. VDI-Verlag, Düsseldorf, 1999.

[70] U. Sieber. *Ljapunow-Synthese nichtlinearer Systeme durch Gütemaßangleichung.* VDI-Fortschrittberichte, Reihe 8, Nr. 250. VDI-Verlag, Düsseldorf, 1991.

[71] T. Sticher, H. Fennel, and P. Gies. Strategien zur Software-Entwicklung für Kfz-Regelungssysteme. *Automobiltechnische Zeitschrift*, 104(12):pp. 1823–1836, 2002.

[72] D. Torkzadeh. *Echtzeitsimulation der Verbrennung und modellbasierte Reglersynthese am Common-Rail-Dieselmotor*. Logos Verlag, Berlin, 2003.

[73] E. v. Hinüber. Inertiale Messsysteme mit faseroptischen Kreiseln. *Automobiltechnische Zeitschrift*, 104(6):pp. 584–591, 2002.

[74] E. v. Hinüber and H. Janocha. Leistungspotential moderner inertialer Meßsysteme. *Automobiltechnische Zeitschrift*, 97(1):pp. 30–35, 1995.

[75] A. van Zanten, R. Erhardt, and G. Pfaff. FDR - Die Fahrdynamikregelung von Bosch. *Automobiltechnische Zeitschrift*, 96(11):pp. 674 – 689, November 1994.

[76] A. van Zanten et al. VDC, the vehicle dynamics control system of Bosch. *Proceedings of the SAE World Congress*, (SP-1075), 1995.

[77] J. Wiedemann and J. Neubeck. Fahrdynamikentwicklung jenseits der klassischen Systemgrenzen. *Automobiltechnische Zeitschrift*, 105(12):pp. 1194–1199, 2003.

[78] H. P. Willumeit. *Modelle und Modellierungsverfahren in der Fahrzeugdynamik*. Teubner-Verlag, Stuttgart, Leipzig, 1998.

[79] J. Y. Wong. *Theory of ground vehicles*. John Wiley & Sons, Inc., New York, Chichester, Brisbane, 1st edition, 1993.

[80] M. Würtenberger. *Modellgestützte Verfahren zur Überwachung des Fahrzustandes eines PKW*. VDI-Fortschrittberichte, Reihe 12, Nr. 314. VDI-Verlag, Düsseldorf, 1997.

[81] M. Zeitz. *Nichtlineare Beobachter für chemische Reaktoren*. VDI-Fortschrittberichte, Reihe 8, Nr. 27. VDI-Verlag, Düsseldorf, 1977.

[82] A. Zomotor. *Fahrwerktechnik: Fahrverhalten*. Vogel Fachbuchgruppe: Fahrwerktechnik. Vogel Buchverlag, Würzburg, 1991.

Patents and Publications

[83] Hiemer, M. and T. Matsunaga: *System to Analyze Vehicle and Driver Behavior.* Patent Application, Patent-No. 543456 JP 01 (Japan) and 543456 US 01 (United States of America), 2003.

[84] Hiemer, M. and T. Matsunaga: *Vehicle Dynamics Behavior Reproduction System.* Patent Application, Patent-No. 546787 JP 01 (Japan), 2004.

[85] Hiemer, M. and T. Matsunaga and J. Barrho: *Vehicle Accident Analyzing Apparatus.* Patent Application, Patent-No. 549783 JP 01 (Japan), to be applied in 2004.

[86] Hiemer, M. and T. Matsunaga: *Driving Situation Detection System.* Patent Application, Patent-No. 550761 JP 01 (Japan), to be applied in 2004.

[87] Hiemer, M. and T. Matsunaga and J. Barrho: *Road Gradient Determination System.* Patent Application, Patent-No. 550763 JP 01 (Japan), to be applied in 2004.

[88] Barrho, J. and M. Hiemer: *Integrated Safety Systems for Circular Saws: Concepts for Detection Systems of Human Limbs.* Reports in Industrial Information Technology, Vol. 7, 2004.

[89] Hiemer, M. and J. Barrho: *Determination of crash parameters for low speed crash reconstruction.* Reports in Industrial Information Technology, Vol. 7, 2004.

[90] Hiemer, M. and J. Barrho: *Observer design for road gradient estimation.* Reports in Industrial Information Technology, Vol. 7, 2004.

[91] M. Hiemer, U. Kiencke, T. Matsunaga, et al. Cornering stiffness adaptation for improved side slip angle observation. *Proceedings of the First IFAC Symposium on Advances in Automotive Control, AAC*, 2004.

[92] Hiemer, M., S. Lehr, U. Kiencke, and T. Matsunaga: *A fuzzy system to determine the vehicle yaw angle*. Transactions of the SAE World Congress, 2004.

[93] Jäkel, H. and M. Hiemer: *Calculation of a discrete event arma-structure*. Reports in Industrial Information Technology, Vol. 6, 2003.

[94] Nenninger, P. and M. Hiemer: *Observability of a reduced non-linear two-track model*. Reports in Industrial Information Technology, Vol. 7, 2004.

Supervised Academical Works

[95] Barrho, J.: *Reconstruction of Road Traffic Accidents by Means of Accident Data Recorders (ADR).* Diplomarbeit, Universität Karlsruhe (TH), 2003.

[96] Feist, A.: *Nichtlineare Regelung des Schwimmwinkels basierend auf einem extended Kalman-Filter.* Diplomarbeit, Universität Karlsruhe (TH), 2004.

[97] Jin, D.: *Identifikation von Parametern im Kraftfahrzeug.* Studienarbeit, Universität Karlsruhe (TH), 2004.

[98] Jin, D.: *Untersuchung der Kombination der Regelungssysteme ESP, EAS und EAR.* Diplomarbeit, Universität Karlsruhe (TH), 2004.

[99] Kumpakeaw, S.: *Implementierung und Optimierung eines Reifenmodells und Schätzung eines Reibbeiwertes.* Diplomarbeit, Universität Karlsruhe (TH), 2002.

[100] Lehr, S.: *Rekonstruktion der Trajektorie eines Kfz mittels Fuzzy-Logik.* Studienarbeit, Universität Karlsruhe (TH), 2002.

[101] Lehr, S.: *Modellvalidierung und Entwicklung eines Fahrermodells für die Unfallrekonstruktion.* Diplomarbeit, Universität Karlsruhe (TH), 2004.

[102] Märgner, M.: *Sensor-Datenkommunikation im Kraftfahrzeug mittels CAN.* Diplomarbeit (Zweitbetreuung), Universität Karlsruhe (TH), 2002.

[103] Patino, M.: *Non-Contact Vehicle Speed Measurement through Image Correlation Techniques.* Projektarbeit (Zweitbetreuung), Universität Karlsruhe (TH), 2002.

[104] Pazulla, P.: *Modellierung eines Ausweichmanövers in Matlab/Simulink.* Studienarbeit, Universität Karlsruhe (TH), 2004.

[105] Schmidt, R.: *Detektion und Beurteilung fahrdynamisch kritischer Zustände im Kfz.* Diplomarbeit, Universität Karlsruhe (TH), 2003.

[106] Sugg, R.: *Analyse der Fahrzeugquerdynamik zur Bestimmung kritischer Fahrmanöver.* Diplomarbeit, Universität Karlsruhe (TH), 2004.

[107] Unfried, M.: *Integration eines Dualprozessor Boards in ein Controller Area Network.* Diplomarbeit, Universität Karlsruhe (TH), 2004.

[108] Vietinghoff, A. von: *Beobachterentwurf zur Charakterisierung der Querdynamik eines Kraftfahrzeuges.* Diplomarbeit, Universität Karlsruhe (TH), 2004.

[109] Wolf, J.: *Untersuchung eines abstandsgeregelten Bremsassistenten.* Diplomarbeit, Universität Karlsruhe (TH), 2003.

[110] Zentai, A.: *Automotive sensor processing and accident reconstruction analysis.* Projektarbeit, Universität Karlsruhe (TH), 2004.

Index